Smart Material Actuator for Trailing Edge Thickening

Theunis Christoffel Botha

Electronic Systems Laboratory, Department Electrical and Electronic Engineering,
Stellenbosch University, Stellenbosch, South Africa, 7600

Supervisor:

Mnr. J.A.A. Engelbrecht

Prof. A.A. Groenwold

Thesis presented in partial fulfilment of the requirements for the degree of Master in Engineering at Stellenbosch University

March 2016

Declaration

I, the undersigned, hereby declare that the work contained in this thesis is my own original work and that I have not previously in its entirety or in part submitted it at any university for a degree.

T. C. Botha: ..... Date: .....

Abstract

The goal of the research project is to provide the conceptual, high level and subsystem level design of an actuation system that would achieve a shape change at the trailing edge of the rudder of a next generation Airbus aircraft. The shape change should be from blunt to a sharp form and vice versa. The purpose of the shape change is to increase the low-speed lift of the vertical tail wing: a strategy proposed by Airbus Future Programmes, following aerodynamic research conducted by them. The increased lift would allow for a reduction in the size of the vertical tail wing, but an increase in aerodynamic drag would result from the blunt trailing edge. This trade-off between the lift and the drag characteristics is what drives the need for bi-directional actuation. The challenge is to design an actuation mechanism that would fit inside the confined space at the trailing edge. Since the typically used hydraulic actuators and their supporting systems are normally too bulky for such a confined space, the use of alternative technologies such as smart materials is explored. The benefit of the research is that the reduction of the tail wing size would lead to lower in-flight drag as well as a reduction in the overall mass of the aircraft.

The research followed a systemic hardware development process, consisting of a requirements capture, conceptual design and detailed design, as well as implementation and verification phases. The design requirements were captured interactively with technical specialists from Airbus. Different system concepts were generated and compared in a pareto trade-off study, and Shape Memory Alloy (SMA) technology was identified as the technology most suited to the application. The feasibility of the concept design was then explored through the design, manufacturing and practical testing of a prototype actuator. The actuator design was based on a parallel arm architecture, and included special links that provided lateral stabilisation. Both the architecture and the stabilisers proved effective, but the manner in which the SMA wires are employed still needs to be refined.

Opsomming

Die doel van hierdie navorsingsprojek is om die konseptuele, stelsel-vlak sowel as substelsel-vlak ontwerp uit te voer vir n aktueringstelsel wat die sleepkant van n vliegtuig roer se vorm moet aanpas. Die verandering in vorm moet wissel tussen n verdikking aksie in een rigting, en n verdunning aksie in die ander. Die verdikking se funksie is om n verhoging in stygkrag te bewerkstellig, soos voorgestel deur Airbus Future Programmes. Hierdie voorstel het gevolg na aerodinamiese analises wat deur hulle voltooi is. Die gevolg van verbeterde stu-krag is dat die vlerke verklein kan word om sodoende die massa en brandstof verbruik van die vliegtuig verlaag. Alhoewel daar n verhoging in stygkrag geskied is dit slegs voordelig tydens lae-spoed vlug, siende dat die sleepkant-verdikking gepaard gaan met n verhoging in die ho-spoed sleurkrag van die vlerk. Hierdie teenstrydigheid in behoeftes tussen lae en ho-spoed vlug is die rede waarom die aktueerder in twee rigtings moet kan funksioneer.

Wat hierdie ontwerp uitdagend maak is die feit dat die sisteem in n baie beperkte volume moet pas, n volume wat moontlik te klein is vir die lomp hidroliese aktueerders wat oor die algemeen in lugvaart-sisteme gebruik word. Daar word vermoed dat moderne aktuerings-tegnologië , genaamd "smart materials", voordele kan inhou in hierdie verband. Dus word hierdie tegnologi tydens die navorsing as sterk kandidate beskou. Die navorsing volg n sistematiese, gestruktureerde benadering van hardeware ontwerp. Hierdie ontwerpsproses sluit in die bepaling van die sisteem se behoeftes, n konsep ontwerp en n gedetaileerde ontwerp, asook implimentering en verifiring van n aktueerder prototipe. Die behoefte bepaling is gedoen met insae van Airbus. In die konsep ontwerp is verskeie konsepte teen mekaar opgeweeg, waardeur bepaal is dat Shape Memory Alloys (SMA)die mees gepaste tegnologie is vir die betrokke projek. Deur die konsep te ontwikkel tot n fisiese prototipe, en hierdie prototipe aan n eksperimentele proses bloot te stel, is die lewensvatbaarheid van die konsep ondersoek. Tydens hierdie ontwikkeling is daar besluit op n parallele argitektuur vir die strukturele komponente, en dele van die struktuur is so uitgel dat dit die laterale stabiliteit van die meganisme bevoordeel. Daar is bevind dat die parallele argitektuur effektief die las versprei, en dat laterale stabiliteit wel deur die betrokke komponente bewerkstellig is. Die gebruik van die SMA materiaal moet egter verder ondersoek word indien daar gepoog wil word om dit optimaal te benut.

Acknowledgements

I would like to thank the Airbus Group and the South African National Aerospace Centre for funding this research. I would also like to thank Ian Whitehouse, Tim Slack and Ettienne Coetzee from Airbus Filton and Carsten Weber from Airbus Bremen for their technical guidance and feedback. Much gratitude is also extended to the project supervisor, Japie Engelbrecht, for his patient guidance, as well as Professor Albert Groenwold for his valuable insight into the mechanical aspects of the project. Special thanks are also extended to the technical staff at Central Mechanical Services and Central Electronic Services at the University of Stellenbosch for their assistance during the manufacturing and experimentation phases of the project.

Contents

List of Figures

List of Tables

Nomenclature

Abbreviations

4WB	*4 Wire Bundles*, SMA wire bundle that contains 4 loops of SMA wire
5WB	*5 Wire Bundles*, SMA wire bundle that contains 5 loops of SMA wire
A / D	Analogue to Digital
AC	Actuator Concept
AEA	All-Electric-Aircraft
AFM	Active Fibre Matrix
AM	Active Material
CNR	Customer Numerical Requirement
CPFS	Characteristic PerFormance Score
CQR	Customer Qualitative Requirement
DF	Design Factor
DS	Derived Specifications
DTR	Design Trend Requirement
E1,E2	Electrical interface 1 or 2 within the actuator
EHA	Electro-Hydrostatic Actuators
EMA	Electro Mechanical Actuators
EO	Electrical Output element
EO	Experimental Outcome
EP	Electrical Power element
ES	External Structure

FBL	Fly-By-Light
FBW	Fly-By-Wire
FEA	Finite Element Analysis
FTN	Force Transfer Node
IAP	Integrated-Actuator-Package
IFc	Importance Factor
IS	Internal Structure
LVDT	Linear Variable Differential Transducer
M1,M2	Mechanical interface 1 or 2 within the actuator
MEA	More-Electric-Aircraft
NiTi	Nickel-Titanium
NOL	Naval Ordnance Laboratory
O1,O2	Output interface 1 or 2 within the actuator
PBW	Power-By-Wire
PID	Proportional Integral Derivative
SME	Shape-Memory-Effect
T	Transmission
TE	Trailing Edge

Acronyms

Nitinol	Nickel-Titanium Naval Ordinance Laboratory
SATETH	Smart Material Actuator for Trailing Edge Thickening

List of Symbols

β	Wing sweep angle
ΔS_{full}	The amount of pre-stretch that was selected for the biassing spring
$\Delta y_{pre-stress}$	The displacement of the structural stiffness from its free length to its smallest operational length
Δ	The extent of the change in the relevant value
δ	Indicates a change in a value

ϵ	Strain
ν	Poisson's ratio
σ_s	Detwinning start stress
σ	Stress
σ	stress
σ_f	Detwinning finish stress
θ	An angle, the context of which is defined by subscripts and/or figures
A	An area of which the context is defined through subscripts and/or figures
A	Austenite
A	Cross-sectional of surface area, the context is provided by subscripts/figures
A, B, C, D	Quadrants within the local coordinate system of the actuator
A_f	Austenitic transformation finish temperature
A_f^σ	Austenitic transformation finish temperature at applied stress σ
A_s	Austenitic transformation start temperature
A_s^σ	Austenitic transformation start temperature at applied stress σ
A_w	Cross-sectional area of a single SMA wire
A_x	Normalised coefficient for x_z as a percentage
a_x	Coordinate with context defined by subscript
a_x	Normalised coefficient for x_z as a fraction
A_y	Normalised coefficient for y_s as a percentage
a_y	Normalised coefficient for y_s as a fraction
$A_{subscript}$	Arms/links, with susbscripts A, B, C, D referring to the quadrants in which they lie
AF	Amplification Factor
c	Chord length
C^A	Slope of A_s and A_f versus σ curves
C^M	Slope of M_s and M_f versus σ curves
C_p	Pressure coefficient

D	Flexural Rigidity
d	Pin diameters
d_w	Diameter of a SMA wire
E	Modulus of elasticity
E_{stroke}	Stroke work
E_w	Displacement error in w-direction
F	A force, the context of which is defined by subscripts and/or figures
f	Distributed force
h	Plate thickness
I	Electrical current
I	Moment of Inertia
k	Structural stiffness
L	A length, the context of which is defined by subscripts and/or figures
l	Indicates a variable length
M	A moment of which the context is defined through subscripts and/or figures
m	Distributed moment
M^d	De-twinned martensite
M^t	Twinned Martensite
M_f	Martensitic transformation finish temperature
M_f^σ	Martensitic transformation finish temperature at applied stress σ
M_s	Martensitic transformation start temperature
M_s^σ	Martensitic transformation start temperature at applied stress σ
N	Integer quantity of which the context is indicated the a subscript
p	Pressure loading
P_{act}	Power of actuation
P_{atm}	Atmospheric pressure
$P_{subscript}$	Pins, with susbscript AB, AD, BC, CD referring to the quadrants of the arms that meet at this pin

R	A lever length
R	Electrical resistance
s	Path length
$S_{subscript}$	Stabiliser arms/links, with susbscripts A, B, C, D referring to the quadrants in which they lie
T_{act}	Actuation period
T_{atm}	Environmental air temperature
$T_{turnaround}$	Turnaround time, the elapsed time between landing and take-off
V	Volume
V_{air}	Air speed of aircraft
V_{air}	Density of air
w	Lateral displacement on a plate
x_z	Chord-wise coordinate in a cross-section parallel to the xz plane
x_{attach}	The chord-wise placement of the actuator line of action
$x_{subscript}$	Coordinate with context defined by subscript
x_{TE}	Chord-wise placement, with the start of the trailing edge as reference point
y_s	Thickness coordinate in a cross-section parallel to the xz plane
$y_{subscript}$	Coordinate with context defined by subscript
z	Vertical direction in an aircraft coordinate system
$z_{subscript}$	Coordinate with context defined by subscript

List of Subscripts

act	Actuator/Actuation
$aero$	Aerodynamic
$aero, eq$	Aerodynamic equivalent
AL	Attachment Line
$allow$	The allowable limit of a variable
$attach$	Refers to the line of action of the actuator
b	Bundle or bundles

cl	Closed/Un-thickened state i.e. the sharp form of the trailing edge
$design$	The design value of a variable
err	Error
f	Flat plate coordinate system
G	Global coordinate system, i.e. that of the aircraft
i	Integer identifier for an element within a set
in	Direction specifier indicating an input
k	Integer identifier for an iteration within a procedure
$k, 0$	Refers to a state of where the structural stiffness is completely unloaded.
lbs	Large bundle set
max	Maximum value
min	Minimum value
out	Direction specifier indicating an output
REF	Indicates a reference value
req	Indicates a requirement
RR	Compliant Region
RR	Rigid Region
sbs	Small bundle set
$skin$	This refers to the outer skin of an air-foil
$struct$	Structural
T	Total
TE	Trailing Edge
TER	Trailing Edge Region
th	Open/thickened state i.e. the blunt form of the trailing edge
w	Refers to wire/wires

Chapter 1

Introduction

The following chapter is intended to introduce the problem, the proposed solution and the process that was followed to apply the suggested solution. The structured overview of the proceedings as presented by this document is also discussed.

To start with, Section 1.1 provides some background information as well as a description of the problem. The projects objectives are identified, as set out in Section 1.2, and the project scope and thesis layout are discussed in Section 1.3 and Section 1.4.

1.1 Problem Description

The sizing of control surfaces such as the vertical and horizontal tail wings, are often dominated by the need to achieve sufficient lift at low air speeds. If the profile of the wing is manipulated in a way that low-speed lift is increased, the low-speed requirements could be met with smaller wings. The high-lift profiles would, however, tend to increase the aerodynamic drag associated with the wing, which would in turn increase fuel consumption during high-speed flight. The result is that the profile of a wing has contradictory requirements in the low- and high-speed flight regimes, and compromises often have to be made to meet both requirements.

If the profile of the wing could, however, be altered between low- and high-speed flight, these compromises could be reduced and more optimal wing sizes could be achieved for both the low- and high-speed flight. Such a practice would lead to fuel savings at high speeds while maintaining the low-speed controllability of the aircraft. Airbus has shown that a blunt trailing edge such as is shown in Figure 1.1 increases the lift at low speeds, while the sharp-edged variant also shown has good drag characteristics at high speeds. The suggested profiles thus provide a good basis for such a fuel-saving strategy.

Actuation is, however, required to facilitate the change in profile. Such an actuator does not exist, and the requirements thereof are not known. The problem space thus needed

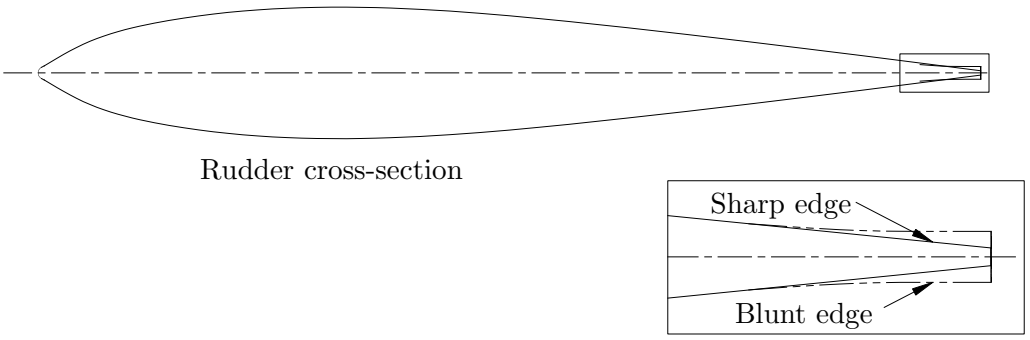

FIGURE 1.1: Blunt trailing edge illustration as suggested by Airbus

to be explored by performing a first iteration of system and subsystem level design, and testing a functioning actuator within the system. The design required the exploration of different actuator technologies, the derivation of typical requirements and the detailed design of an actuator that could meet the requirements. An actuator also needed to be built and tested to show that the derived requirements could be met.

The problem statement below summarises the identified need and serves as a starting point for the project.

Problem Statement:

To design a system that can thicken the trailing edge of the rudder to a value specified by the client. The system needs to achieve stable functionality in the full range of aerodynamic forces expected to act upon it, and is required to fit within the confines of the aircraft skin and rudder, preferably even within the trailing edge itself. A prototype also needs to be built and tested to illustrate the technical feasibility of the suggested design.

1.2 Objectives

The following are the objectives (O) set out for this project:

O1 . Explore the problem of incorporating a low frequency actuator in the trailing edge of a rudder in order to thicken it.

O2 . Generate a concept system by which this could be achieved.

O3 . Identify a theoretically suitable technology for use in the proposed system by studying and comparing different technology options.

O4 . Estimate the requirements for a system that would effectively solve the problem stated in Section 1.1.

O5 . Assess the practical feasibility of using the selected technology by designing, constructing and testing a prototype.

O6 . Communicate the lessons learnt and make recommendations regarding future work.

1.3 SATETH Project, Execution and Thesis Layout

For the Smart Material Actuator for Trailing Edge Thickening (SATETH) project, the V-model was adapted as is shown in Figure 1.2. The parts enclosed in blue indicate the scope of the project within the wider systems-engineering framework. Those parts enclosed in red are the higher level tasks, which would typically be included in the parent program but fall outside the current scope. The SATETH scope included the conceptual design, as well as system and subsystem level design, which was mainly centred around the eventual testing of a functional actuator.

Note that while all the subsystems would be specified as well as emulated/simulated during testing and simulation of the prototype, the detailing of such subsystems was beyond the scope of the project. The detailed design in the current project was centred on the actuator itself. The problem was treated as a blank slate with all the opportunities that would go along with that. The systems-engineering approach was then applied to the problem, by which the scope was gradually reduced from system to subsystem, and then to component level. On the system level, a full range of alternative technologies were compared with one another by developing candidate concepts that were traded off against each other. By doing so Shape Memory Alloy (SMA) technology was identified as the ideal technology for current application.

Based on the high level SMA concept, a more complete system concept was generated. The concept includes subsystem definitions, layout decisions and subsystem requirement specifications. In order to assess the feasibility of the proposed system on a practical level, a prototype was built and tested, and shown to function reasonably well.

The project report is concluded by considering its positive and negative aspects and making recommendations for future work.

1.4 Project and Thesis Structure

The project and this written account thereof follows the same structure as that of the V-model, and the work is presented in roughly the same order as it was done.

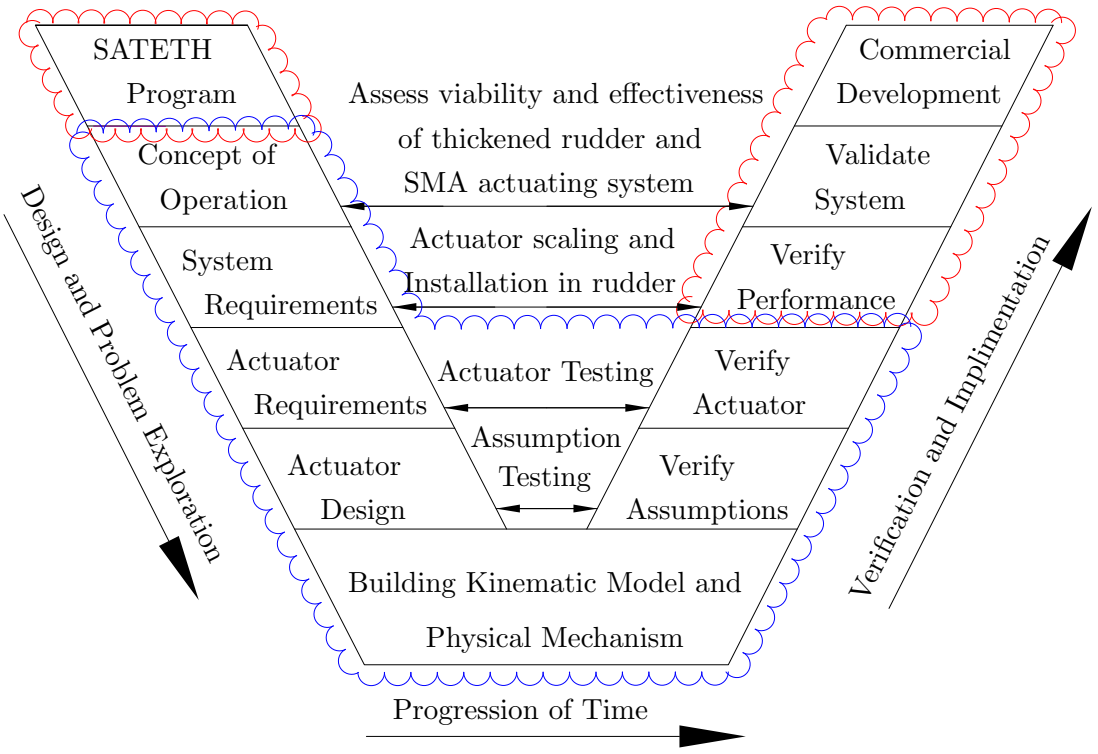

FIGURE 1.2: V-model of systems engineering

Chapter 2 serves to inform the reader on SMA technology, how it functions and some of its uses. It also includes a section on the actuators and smart materials that are generally used in aerospace applications.

Chapters 3 and 4 are dedicated to the process by which the proposed solution was developed into a complete concept. In the V-model, this would correspond to *Concept of Operation* and *System requirements*. In Chapter 3 the requirements are introduced, as well as a list of existing actuator technologies. The requirements are then used to narrow the options down to a specific short-list of candidate technologies. A more detailed trade-off study is documented in Chapter 4. The trade-off starts with a functional breakdown of the proposed system and the specification of candidate subsystems to perform each function, thereby specifying reasonably complete system concepts. These concepts are then traded off against each other in a pareto analysis to yield the top three concepts. These are the concepts which were presented to the client, and from which the final concept was chosen: an SMA-driven car-jack mechanism.

Chapter 5 discusses the detailed design on system level. It is dedicated to details such as system layout and generalised actuator requirements. The chapter corresponds to the *Actuator Requirements* block in the V-model.

Chapter 6 deals with the actuator design. This included not only the sizing of components, but also architectural decisions, such as kinematic relations and the specification

of some supporting subsystems. One such specification is the stiffness of the biassing spring.

There is no chapter explicitly dealing with the building of the simulation models and prototypes. These two processes should become sufficiently apparent in the sections dedicated to their use, which are Chapters 7 and 8.

The simulation model is used in a kinematic simulation, discussed in Chapter 7, to test the effectiveness of some of the design decisions that were made.

The prototype, on the other hand, was experimented upon to assess the success of the design and the viability of constructing such a mechanism. This *Experimental Verification* is discussed in Chapter 8, followed by Chapter 9, which includes concluding remarks on the project, lessons learnt and some suggestions for future work.

Chapter 2

Literature Review

In the SATETH project an actuator was designed, which would be able to thicken the trailing edge of a vertical tail wing. The actuator was based on SMA technology, a widely used smart material with several competitors within the aeronautical industry.

A study of the actuators typically used in aerospace, both conventional and unconventional, provided some insight into the aerospace context and highlighted some of the technologies that SMA competes against within the aerospace industry. It also highlighted the properties of the technologies that make them well suited to their respective applications. This study is presented in Section 2.1.

The SMA technology itself is also considered. It is first discussed at a high level in Section 2.2 to provide more insight into how its unique properties provide advantages in a wide range of industries. This is followed by the more detailed information on its physical behaviours, which were needed during the design. These details, provided in Section 2.3, will also inform the reader better on how the material is used to perform work.

2.1 Actuators and Smart Materials in Aerospace

In a project such as is presented in this document, it is always valuable to develop a frame of reference before more detailed work is attempted. For the current project an exercise in aeronautical design this meant that typically used actuators would need to be studied. During the initial study it was found that actuation in the aeronautical industry was still largely centred around hydraulic and pneumatic technologies. These systems, while being robust and well understood, have significant influence on the weight and design of an aircraft. Filters, valves, connections, and primary and backup piping systems are all a reality of these large and interconnected systems; not to mention the additional mass added by filling all the piping with hydraulic fluid.

In recent years the trend has been to move away from these centralised actuation systems through the commercial development of suitable alternatives [13]. This is not a simple matter of substitution, but a complete change in the philosophy behind the design of a typical aircraft. In its most extreme form, this philosophy aims at the eventual development of an *All-Electric-Aircraft(AEA)* [14] , with the more modest *More-Electric-Aircraft(MEA)* design strategy serving as a stepping stone to reach this goal. Both philosophies centre around the same core design theme, which is to make use of distributed actuation rather than centralised systems. The actuators would then be electrically driven a strategy referred to as *Power-By-Wire(PBW)* [15] - and controlled using *Fly-By-Wire(FBW)* or *Fly-By-Light(FBL)* systems. It was considered imperative in the current project that similar design approaches be followed, in order for the resulting actuation system to be in line with current trends.

The first movement towards these distributed systems saw Electro-Mechanical Actuators (EMA) and Electro-Hydrostatic Actuators (EHA) replacing the distributed systems in secondary flight controls, such as landing gear deployment. These actuators are currently considered state of the art when it comes to distributed actuation.

EMAs generally take the form of ball screws, driven by brushless DC motors and packaged into a self-contained unit. Such a device is shown in Figure 2.1a. EHAs such as the one shown in Figure 2.1b, on the other hand, takes the form of a self-contained, electrically driven hydraulic system. An EHA would typically make use of a fixed displacement pump, driven by a variable speed electrical motor. An alternative, yet similar, actuator, referred to as an *Integrated-Actuator-Package(IAP)*, makes use of a fixed speed electrical motor with control being applied by varying the displacement of the pump [14].

While these actuators hold some advantages when used in primary and secondary flight controls, they are complex mechanical machines. They are thus subject to the drawbacks typically associated with such machines: their moving parts and filters require substantial maintenance, making them not well suited for hard-to-reach places; their inertias limit their response time a characteristic that is becoming increasingly important, due to fast-developing control and comfort requirements on aircraft; their noise negatively impacts passenger perceptions; and their bulk puts them at a disadvantage when it comes to low aspect ratio applications.

Some of these issues meant that these technologies were possibly not the best option for the project at hand. Even though speed was not considered crucial in the current context, space was, as was the required maintenance. In applications with such requirements, smart materials such as shape memory alloys and piezoelectrics excel. Their intrinsically low aspect ratios and solid state nature make them very well suited for confined spaces. They can often be embedded within structures, or even integrated into the actual aircraft skin [16]. They are also considered fairly simplistic, and designs based on them often have low mass compared to competing technologies. Piezolectrics have the additional

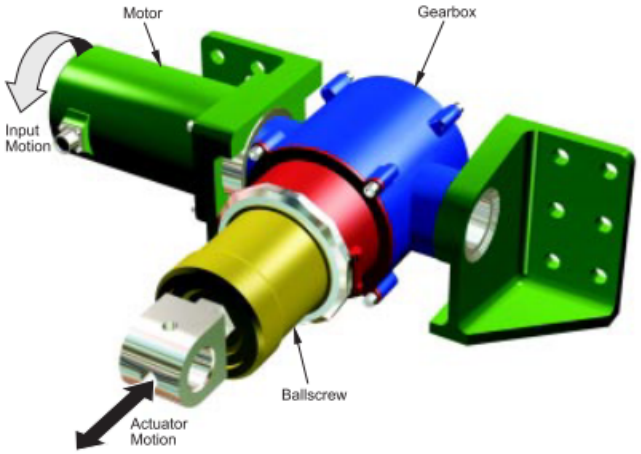

(a) Electro-mechanical actuator [14]

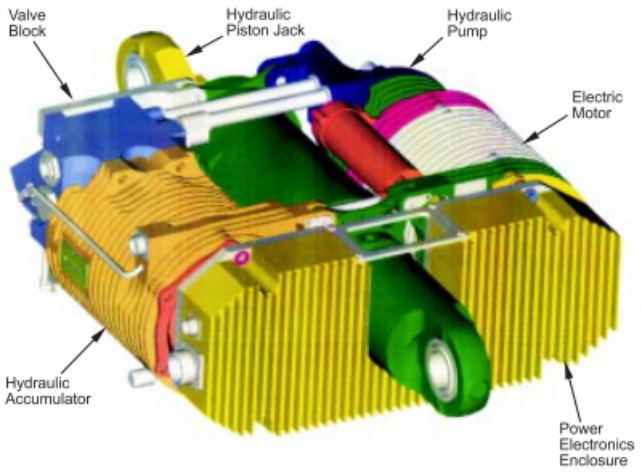

(b) Electro-hydrostatic actuator [14]

FIGURE 2.1: State-of-the-art self-contained actuators

advantage of having extremely short response times and high power density. This makes them ideal for active vibration control [17] or other high frequency applications, such as blade pitch control in helicopters [18].

When it comes to shape memory alloys, the attainable frequencies are lower, but substantially higher stroke than that of piezoelectric materials can be realised. This is often used in single-stroke mechanisms, or for low frequency actuations in very confined spaces. Bolt shearing collars, passive vibration control by tuning beam stiffness [19] and trailing edge actuation are some of the uses it has seen [20]. A previous project in this program (Actuation in confined spaces by Airbus) aimed to lower the force requirements of aileron actuation by using trailing edge tabs [3]. This was a more dynamic application than that in the current project, and the frequency limitations proved a burden. For the

trailing edge actuation, once per flight, as is currently being considered, such limitations in the attainable frequency would not be considered overly problematic.

Many other types of actuators exist and are used both inside and outside the aerospace industry. This section was dedicated specifically to actuation in aerospace, for which the most relevant concepts have already been mentioned. A quick summary is, however, in order.

It was found that the design of aerospace actuation systems currently tends toward self-contained, electrically driven devices. Within this trend, EMAs, EHAs and IAPs are considered state of the art. In spite of the widespread application of these technologies, the use of new actuator types based on SMAs and piezoelectrics are considered advantageous in some applications. These include applications that are space limited, necessitate the use of low maintenance devices or require extremely high frequency actuation (piezoelectrics only).

2.2 Applications of SMA's

Early in this project, a rigorous selection process led to the selection of SMA technology as the basis for further design. It would thus play a central role in the execution of the project, and a high level discussion on the technology was considered important. Such a discussion is the purpose of this section, which allows the reader to be informed, while later sections are more focussed on the design and analysis of the system. The section is presented in the form of a discussion on application areas for the technology, and the characteristics that made it well suited to said applications. A variety of such applications were discussed by Lagoudas [4],who is one of the major sources on this topic.

Lagoudas mentioned that in home appliances temperature control is often achieved using the high temperature dependent displacements that can be realised with SMAs. It has, for instance, been used to open the steam-vent in a rice cooker, set the louvre positions on air-conditioning systems and adjust the hot/cold water mixing in a shower head. It has even been used to create textiles that can be dynamically tailored.

The medical industry is another major application area for SMA technology, as discussed by Duerig et al. [21]. Although bio-compatibility is a major consideration in these applications, it also holds other advantages over conventionally used metals, such as stainless steel. Its super-elasticity means that prosthetics, bone-clamps and stents that make use of SMA material tend to allow more movement without losing contact with the biological materials to which they are coupled. It also allows for the design of highly flexible surgical equipment, such as is needed in minimally invasive surgery. Examples of such equipment include endoscopic tubes, scissors and graspers.

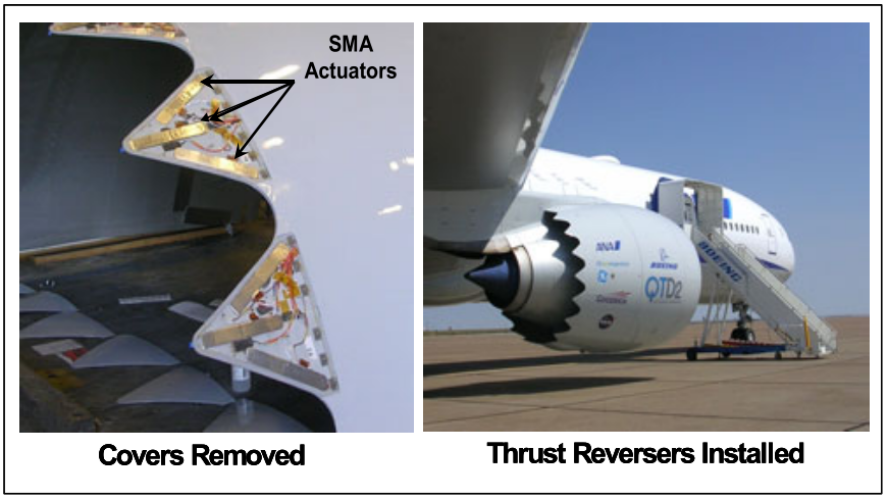

FIGURE 2.2: Noise-suppressing chevrons on Boeing 777 [1]

Aerospace applications have also been substantial. Aeronautical applications have been largely experimental, but functional mechanisms have made their way into many satellite and other space applications. In the former, one of the largest projects was the smart wing program. It focussed on increasing the performance of lifting bodies through the creative use of the shape memory effect. The program included outputs such as twisting wings, and ailerons with no hinges. The respective physical formats of SMA in these devices were torque tubes and contracting wires. SMA beams were also used to straighten noise suppression chevrons on the engines of a Boeing 777. The chevron can be seen in Figure 2.2. The SMA beams, making use of a simple PID controller, would induce bending in the chevrons in such a way that the engine noise would be minimised.

In space and satellite applications it was largely used in low-shock release mechanisms. Here the controllable, but powerful, stroke delivered by SMA material was found to be very useful compared to alternatives, especially when compared to pyrotechnic release mechanisms, which have been known to damage the spacecraft. One example of such a deployment mechanism was used to open a solar collector on a satellite. The solar array, shown in Figure 2.3a unfolded using flexible hinges(Figure 2.3b), which would extend to their full length when powered.

Many more examples of applications can be found in literature, but those that were discussed provide an overview of the extent to which SMA technology is commercially utilised and indicate some of the characteristics that make it well suited to those applications.

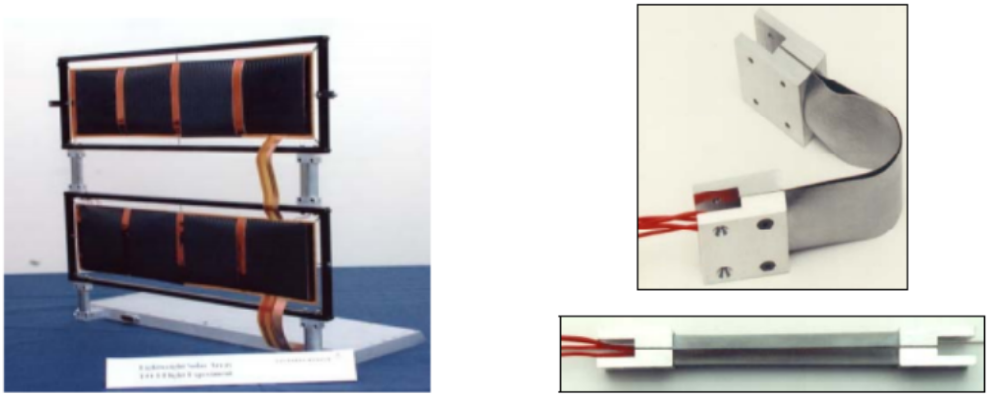

(a) The extended solar array (b) The SMA-driven flexible hinge

FIGURE 2.3: Solar array deployment using a flexible SMA-driven hinge [2]

2.3 Shape Memory Alloy Behaviours

Understanding the function of the SMA material within the designed actuator requires more detailed knowledge of the behaviour of the material and how this behaviour can be applied towards producing work. This section discusses some of the history of the material and highlights some of the useful physical characteristics thereof. The one- and two-way shape memory effects are introduced, as well as pseudo-elasticity. The main focus is, however, on the one-way shape memory effect itself and some of the material chemistry associated with it. For the remainder of this section, unless explicitly stated otherwise, the term *Shape-Memory-Effect(SME)* will refer only to the one-way SME.

According to Lagoudas [4], a significant research effort in the early 1900's was sparked by a discovery in the 1890's that steel could exist in a martensitic form. This was considered at the time to be irreversible. This changed in 1949 when Kurdjumov and Khandros [22] showed that a reversible thermo-elastic transformation could occur. This thermoelastic transformation was seen first in CuZn and CuAl, followed shortly after by other Alloys. The behaviour of these first alloys, while intriguing was not on a scale that was useful in engineering applications. This changed in the early 1960's when the Naval Ordnance Laboratory(NOL) discovered that Nickel-Titanium(NiTi) alloys exhibited significant, thermally-driven shape recovery [23] referred to as the Shape Memory Effect.

On a practical level, the SME presents itself as is indicated in Figure 2.4. Unstressed, annealed material would have a specific shape. For the wire shown, the shape in question would be its length. The application of sufficient force (the addition of the mass), would then result in a large strain being induced in the material. A part of this strain would be the typical elastic strain that other materials would also experience; the majority thereof would, however, be due to a change in the crystal structure of the material. This strain can be recovered by heating the material up to a sufficiently high temperature;

the strain recovery would coincide with an induced force that can be used to perform work (lifting of the mass). Note the elastic component of the strain is not recovered in this process. Upon cooling, the applied force would once again strain the material, and the process can be repeated. The maximum strain typically ranges between 3% and 10% of the initial material length, and the recovery stresses can reach up to 600 MPa. These cycles can be repeated a finite amount of times, with typical lifespans ranging from 1 to 100 000 cycles depending on the operating conditions. For 50 000 repeatable cycles for instance, Nitinol could be stretched to about 4% with a moderately high stress applied(around 200 MPa). Note that this is an estimate and that the exact lifespans of different materials under specific operating conditions would have to be determined experimentally.

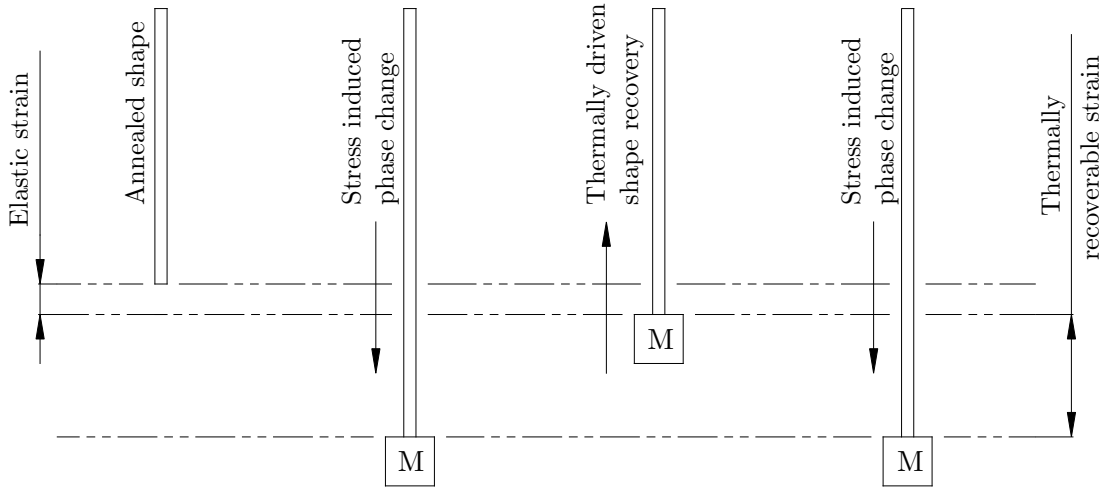

FIGURE 2.4: Practical representation of the Shape Memory Effect [3]

Chemically, the SME results from the transformation within the material between different phases. These are the high temperature Austenite phase and the low temperature Marteniste phase. Austenite can exist only with a cubic structure; this is thus the fixed shape phase to which the material reverts upon heating.

Martensite on the other hand, can exist in more than one stable form. One of these, twinned Martensite (M^t), is also referred to as self-accommodated, and is spontaneously formed upon cooling from the Austenite phase. Twinned Martensite crystals have a similar macroscopic shape to that of ustenite due to the existence of up to 24 martensite variants, which are spontaneously orientated within the same macroscopic boundaries as that of the Austenite phase. This phenomenon is shown in Figure 2.5. Note that the phase transformation can occur in both directions without a macroscopic change in shape. It does, however, occur only in the absence of applied stress.

Another Martensitic form which exits, the detwinned form, is formed when sufficient stress is applied to the material. This is also referred to as reoriented Martensite, due

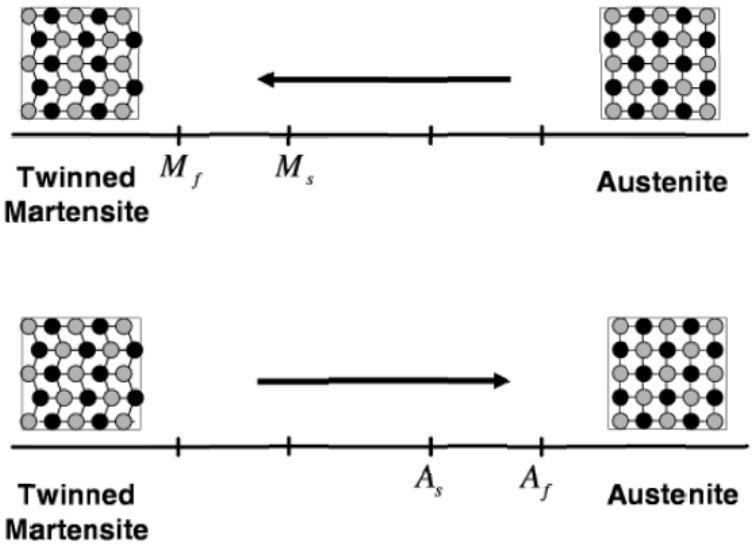

FIGURE 2.5: Thermally-induced phase transformation at zero stress [4]

to the stress-induced reorientation of the crystal structure to a favoured variant (Figure 2.6). The reorientation process occurs together with a macroscopic change in shape such as was discussed in the practical example. Note that this strain also has an elastic component, as was previously mentioned.

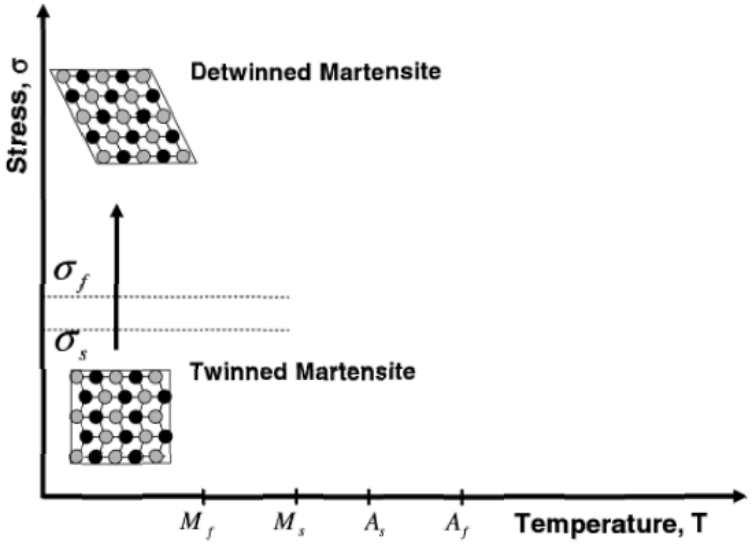

FIGURE 2.6: Stress-induced detwinning [4]

When the load is removed, only the elastic strain will be recovered while the strain associated with detwinning becomes permanent. The word permanent is placed between quotation marks to indicate that while the shape could be maintained indefinitely, it is still reversible through the application of sufficient heat. Such a shape recovery would

return the material the austenitic phase as is shown in Figure 2.7. Macroscopically this would coincide with a return to its initial shape.

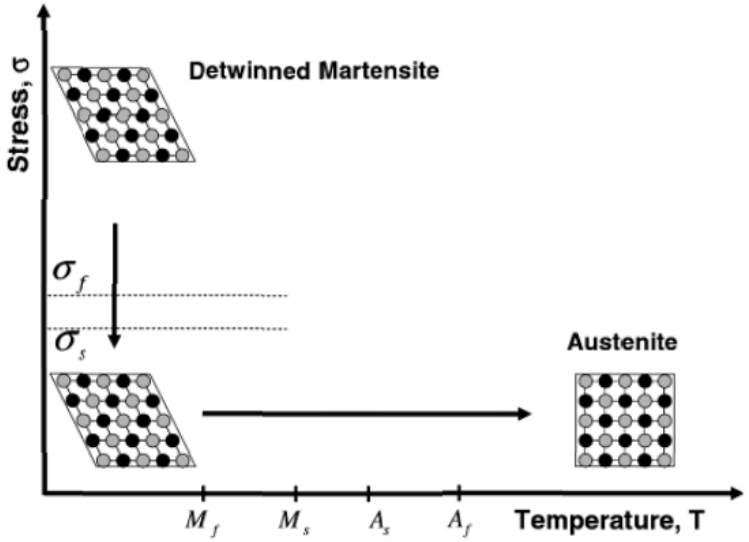

FIGURE 2.7: Thermally-driven shape recovery [4]

The shape memory effect is generally classified and studied using phase diagrams. On these diagrams, transformation regions can be indicated, as well as boundaries at which phase transformations begin and end. Such a diagram, duplicated here from a book by Lagoudas [4], is shown in Figure 2.8.

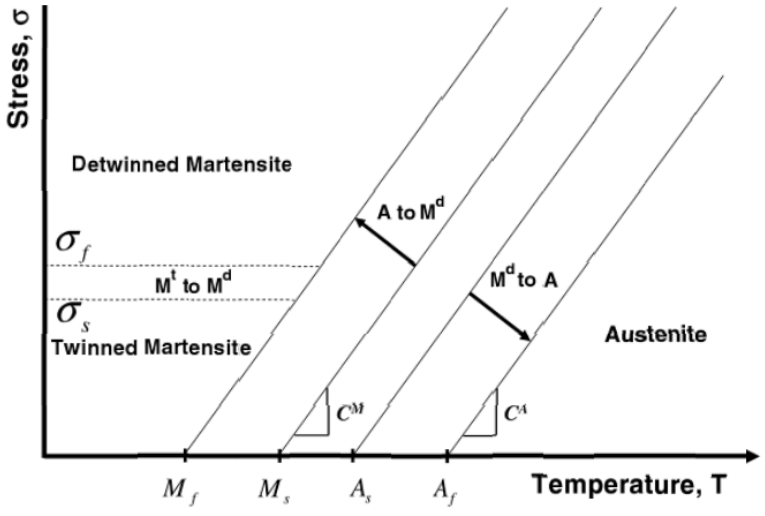

FIGURE 2.8: SMA phase diagram [4]

The transformation temperatures (M_s, M_f, A_s, A_f) are also shown in the figure and can be defined as follows:

- A_s - The temperature at which phase transformation to Austenite starts.
- A_f - The temperature at which phase transformation to Austenite finishes(material is fully Austenitic).
- A_s - The temperature at which phase transformation to Martensite starts.
- A_f - The temperature at which phase transformation to Martensite finishes(material is fully Martensitic).

They indicate the transformation temperatures in a state where no external stress is applied to the material. Transformation temperatures do, however, vary with applied stress, as is indicated by the linear curves that extend upwards from the temperature axis (M_s^σ, M_f^σ, A_s^σ, A_f^σ). The superscript σ is used to indicate a stress-specific transformation temperature. Their gradients(C^M and C^A) are material-specific parameters which are determined experimentally for different materials. They quantify the stress dependence of the transformation temperature.

The remaining variables seen in the phase diagram, σ_s and σ_f indicates the stresses at which stress-induced reorientation starts and finishes. For SME to be used in actuation, the applied stress would need to be, at the very least, above σ_s in order to achieve transformation strain during cooling. Only a stress above σ_f would result in full detwinning of the material and full utilisation of the stroke capability thereof.

Typical material parameters are shown in Table 2.1:

TABLE 2.1: Typical SMA material parameters [3]

Parameter	Unit	Value
M_s	C	18.4
M_f	C	9
A_s	C	34.5
A_f	C	49
C_m	MPa	8
C_a	MPa	13.8
σ_f^{cr}	MPa	100
σ_s^{cr}	MPa	170

It is useful to note that the SME is not the only phenomenon associated with the phase transformation in SMAs. While these phenomenons are not used in this project, and as such not discussed in detail, they are still worth mentioning.

The additional effects are referred to as the two-way shape memory effect, and pseudoelasticity.

The two-way shape memory effect is similar to the shape memory effect, the difference being that the shape recovery happens spontaneously upon cooling. According to

Lagoudas [4] this effect occurs when a material has been conditioned to "remember" its shape by repeated actuation cycles along the same loading path a process referred to as training. This effect occurs due to defects introduced during cycling. The mentioned defects cause a residual stress in the material; this in turn, biases the Martensitic phase transformation towards a preferred shape. The preferred variant would be that which is associated with the original macroscopic shape of the material.

Pseudo-elasticity, on the other hand, occurs when the stress cycles applied to the material occur in a different temperature region. With a temperature above the Austenite finish temperature, detwinning can occur only with the application of very high stresses [4]. When the detwinning load is removed, the shape recovery (Marteniste to austenite transition) occurs spontaneously. The strains exhibited during this behaviour are orders of magnitude larger than the recoverable elastic strains of conventional metals; as such, this phenomenon is also referred to as super-elasticity.

Another difference between the pseudo-elasticity and conventional elasticity, is that the strain/displacement return path is different to the forward path(Figure 2.9). The hysteresis that results coincides with the dissipation of energy - a characteristic usefully employed in vibration control applications. The hysteresis curve can also be altered by controlling the material temperature; this results in vibration absorption that can be tuned.

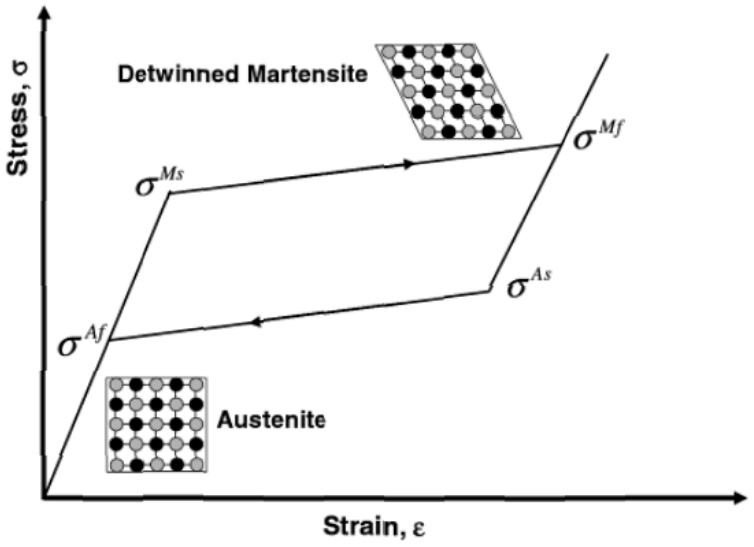

FIGURE 2.9: Hysteresis curve of pseudoelastic behaviour[4]

Chapter 3

Requirements and Technology Down-Selection

This chapter is dedicated to the derivation of design requirements as well as the process followed to identify a list of existing actuator technologies. The list served to guide the conceptualisation and design of the trailing edge actuation system.

A physical description of the problem is first given in Section 3.1. The description provides detailed geometrical requirements for the systems operation in the form of a thickness for the blunt and sharp configurations that the trailing edge would have to assume. The rudder and trailing edge is also defined mathematically, using the same normalising strategy generally used to define wing geometries in the aeronautical industry. This convention, which makes use of concepts such as the wing sweep angle and air-foil thickness distribution, is explained in some detail.

Additional system requirements, which were taken from various sources, are then communicated in Section 3.2. The requirements include qualitative and numerical requirements that were received from Airbus, as well as design trends in the aeronautical industry.

Section 3.3 draws on the numerical information contained in the identified requirements. Through high level mathematical operations, the requirements were used to derive preliminary specifications that could be used in later trade-off studies. The specifications given are energy, power, volume and actuation period limits as well as goal values, which fell within the set limits.

An extensive list of existing technologies is compiled in Section 3.4; the list is also somewhat shortened by disqualifying those technologies that were considered ill-suited for use in the current application. The disqualified technologies and the reasons for their exclusion from the final list are briefly discussed.

The remainder of the chapter discusses the reduction of the list to a list of the most suitable candidates. Detailed discussions on the technologies can be found in Section 3.5, followed by a discussion on known configurations and mechanism types typically used with such technologies in Section 3.6. Finally, the identified specifications are used for a numerical down-selection of the potential technologies (Section 3.7), using two-dimensional graphs.

The most promising candidates were identified to be: Polymer-based as well as high- and low-strain piezoelectric materials, hydraulics, pneumatics, magnetostrictive materials, shape memory alloys, fluid muscles and high temperature thermal expansion elements.

3.1 Physical Description

Airbus originally stated that an actuation mechanism was required to actuate the trailing edge of the rudder control surface. The actuation requirement was to thicken the trailing edge into a blunt form during the low-speed flight regime, and return it to its sharp edge form during the high-speed regime. The application would not require high speeds, nor would it require precise control of the thickening process. A low-frequency, on-off type device would be sufficient. The mechanism would be required to fit inside the volumetric constraints of the rudder. This volumetric requirement was a statement of the maximum space that the actuator could occupy, with the trailing edge cavity itself being the preferred installation volume. Preliminary studies, based on the energy and power densities of common actuator technologies, showed that designs that could fit within the trailing edge cavity would likely be achievable. The author thus set the volumetric requirement for this project to be that of the trailing edge cavity.

To provide a more precise definition of the space requirements as well as the required deflection, geometrical descriptions were provided. In order to understand these descriptions better, consider Figure 3.1, which illustrates the manner in which swept wing sections are typically defined. Note that the coordinate system is defined for a vertical wing, with the span of the wing being in the z-direction. The x-direction would then typically be aligned with the horizontal axis of the aircraft fuselage, and the y-direction would be horizontally orientated and perpendicular to the x-axis.

The wing sweep would be defined by the angle between the z-axis and the leading edge of the wing section(β), and the wing taper would be defined by the distribution of the chord length c in the z-direction($c(z)$). The skin of the wing would have a specific profile, which is referred to as the thickness-distribution. The thickness-distribution refers to the lateral offset from the chord-line at a given value for x_z denoted as $(y_s(x_z))$. Values for y_s and x_z are generally normalised in terms of c as shown in Equations 3.1 to 3.4, which provide the basis for stating generalised dimensions as a percentage of c, for example: $x_z = a_x * c$ or $x_z = A_x\%c$.

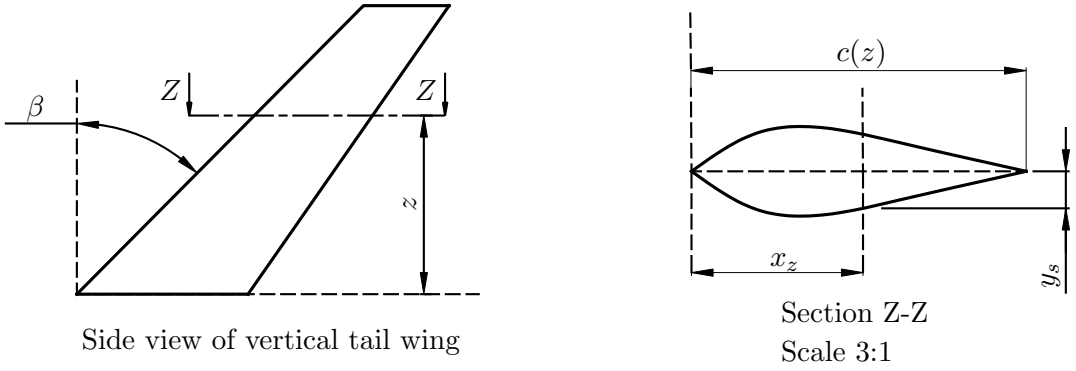

FIGURE 3.1: Geometrical definition of a wing sections

$$a_x = x_z/c(z) \tag{3.1}$$

$$A_x = 100 * x_z/c(z) \tag{3.2}$$

$$a_y = y_s(x_z)/c(z) \tag{3.3}$$

$$A_y = 100 * y_s(x_z)/c(z) \tag{3.4}$$

Given these conventions, the rudder and trailing edge are defined as shown in Figures 3.2 and 3.3. Note that Figure 3.3 is a scaled representation of a portion of Figure 3.2 as indicated by the red boundary box. The rudder was specified by the Airbus to consist of the rearmost 30% and the trailing edge the rearmost 5% of the vertical tail wing. The illustration in Figure 3.3 includes both the blunt and sharp trailing edge forms, with the thickened state requirement being defined as 2%c by Airbus' future projects division. The lateral limit of the installation space is defined by the aircraft skin, of which the thickness distribution is shown in Equation 3.5 as approximated from a CAD model thereof. This distribution corresponds to a trailing edge thickness of 0.0862%c in its "sharp" form.

$$a_y = 0.1044 - 0.104 * a_x \quad with \quad 0.95 \geq a_x \geq 1 \tag{3.5}$$

In summary, an actuation system would need to be designed in such a way that it could fit within the trailing edge of the rudder. The trailing edge is defined as the last 5% of the vertical tail wing, with the lateral physical constraint being equal to the thickness distribution of the wing, which can be approximated as $a_y = 0.1044 - 0.104 * a_x \quad with \quad 0.95 \geq a_x \geq 1$. The function of the actuator would be to alter the trailing edge thickness from a value of 0.0862%c to a value of 2%c and back again. The system would also need to hold the trailing edge in either one of these two positions for extended periods of time.

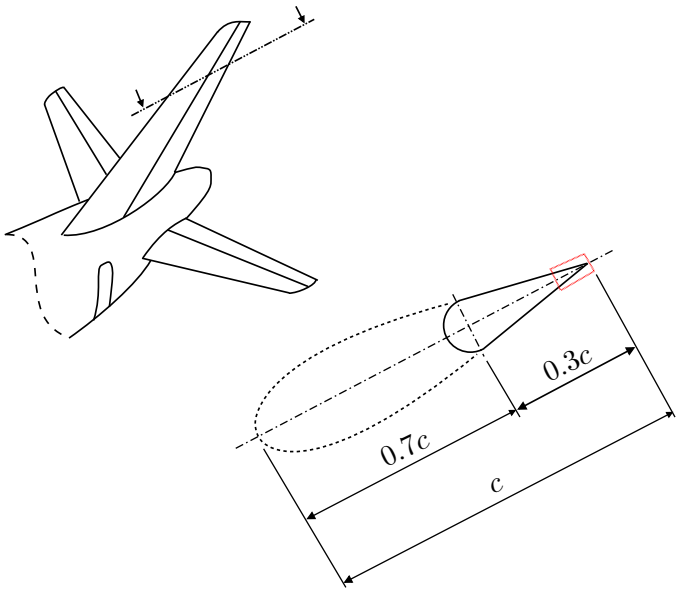

FIGURE 3.2: Rudder cross-section and trailing edge definition

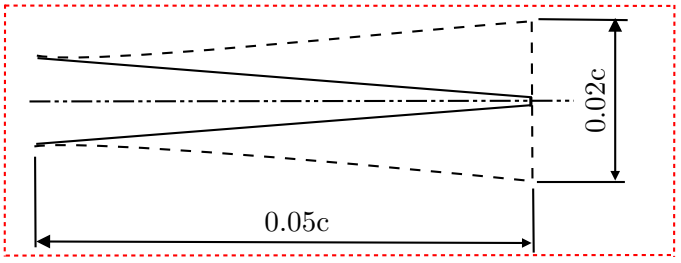

FIGURE 3.3: Trailing edge thickening description

3.2 System Requirements

An actuator was required for the thickening of the trailing edge on a vertical tail wing. In addition to the geometrical requirements discussed in Section 3.1, some operational requirements were specified by Airbus, as well as qualitative design requirements. The current section is dedicated towards a discussion on these requirements, as well as some additional requirements that were identified from design trends in literature.

The qualitative requirements are summarised in Table 3.1. The first requirement stated that no structural damage should occur if the system failed; this could refer to either loss of actuation or if a jam of some kind were to occur. With distributed actuators, for instance, functional actuators should not overstress the structure if a single actuator were to lock. The second requirement namely that of low-mass, is typical of aerospace applications and need not be elaborated upon. In addition to this requirement, an open

failure state was specified. This requirement is based on the need for a blunt trailing edge during landing in order to maintain sufficient lift for control purposes.

Another requirement stated was that the mechanism had to have low complexity. This referred to both complexity of operation and complexity of construction. Complex operation would mean that expensive control systems would be needed, or that it could prove taxing on existing flight controls and pilot operations. A high complexity in construction, on the other hand, would mean that expensive fabrication facilities and personnel would be required for its commercialisation.

The final qualitative requirement was that the system would require little or no maintenance. This was in part due the hard-to-reach position in which it would operate, and in part to maintaining short turn-around times in airports and maintenance facilities.

TABLE 3.1: Customer Qualitative Requirements(CQR)

Number	Requirement description
CQR1	No structural damage to occur upon system failure
CQR2	To revert to thickened state during failure
CQR3	To be of low complexity
CQR4	To require little or no maintenance

The operational requirements are summarised in Table 3.2. The aerodynamic forces that would be acting on the outer skin of the trailing edge were given as pressure coefficients. Even though the pressure distribution on a wing section generally varies in a chord-wise direction, the largest gradients exist further upstream on the wing. As a result, the pressure on the trailing edge itself can be treated as a constant over its entire surface area.

The minimum flight speed and atmospheric conditions are given, since they would be needed for the calculation of a dimensional value for the pressure acting on the surface. The atmospheric conditions could also play a role in the selection of technologies/materials were they to prove limiting. The temperature was originally given as 0 $^{\circ}C$; it was, however, altered to be more closely related to the climate of the region wherein the experiments would be conducted. This was deemed acceptable by stakeholders of the project. The maximum actuation period would be the time within which the actuation would need to be completed in both directions. The value, which was received from stakeholders at Airbus, was chosen to be sufficiently quick for post-take-off and pre-landing procedures. It was also slow enough for inertial effects to be neglected during the design.

The identified customer requirements needed to be studied further before they could provide the foundation for a design. This is provided here together with some "trend requirements" which aimed at establishing a design framework similar to that found in

TABLE 3.2: Customer Numerical Requirements(CNR)

Number	Description	Expression
CNR1	Minimum aerodynamic pressure	$C_{p,min} = -0.5$
CNR2	Maximum aerodynamic pressure	$C_{p,max} = 0.2$
CNR3	Minimum flight speed at landing	$V_{air,min} = 200\ kts = 102.9\ m/s$
CNR4	Atmospheric conditions during landing	$\rho_{air} = 1.2\ kg/m^3$ $T_{atm} = 20\ °C$ $P_{atm} = 1\ atm$
CNR5	Maximum period of actuation	$T_{act,max} = 19\ s$

relevant literature. It was attempted to identify trends from both industry and academic sources.

Current design trends towards electrically powered actuators; these would also be discrete units which would be distributed throughout the system, as opposed to cables, pipes and wires that stretch over long distances within the aircraft. These trends fall under the More Electric Aircraft(MEA) concept, which is discussed in Section 2.1. The decision was made to keep to this trend in the current design, leading to the first three requirements in Table 3.3.

TABLE 3.3: Design Trend Requirements(DTR)

	MEA conceptual requirements
Number	Requirement description
DTR1	Use discrete, self-contained actuators
DTR2	Actuators to be electrically driven
DTR3	Make use of distributed actuation
	Requirements for mass-efficient design
Number	Requirement description
DTR4	Limit the amount of coupling mechanisms
DTR5	Avoid bending moments as force transfer mechanism
DTR6	Bias active materials effectively
DTR7	Use simple mechanisms
DTR8	Optimally stress all material within the mechanism, and use active material as far as possible
DTR9	Avoid compliant hinges or bending force transfer, use rigid parts instead
DTR10	Use actuators with suitable form and with ideally orientated line of actuation

As an extension of this, and with the understanding that aerospace applications are mass critical, *mass-efficient* design practices were investigated. It was then identified that Precht and Hall [12] had compiled a list of design axioms that facilitate mass-efficient designs. These axioms were incorporated in the design by adding the remaining items in the list of design trend requirements. Note that many of these overlap with

the customer numerical as well as qualitative requirements. Note also that not all of the axioms in the article were included in the table. The complete list of axioms can be seen in Table 3.4, and is followed by a discussion on those which were excluded.

TABLE 3.4: Design axioms for optimal discrete actuators[12]

Axiom	Used	Description
Planar actuators	✗	Planar actuators such as piezo-benders present manufacturing difficulties and poor centre of gravity characteristics.
Coupling mechanisms	✓	Coupling mechanisms such in multi-stage actuators are considered to reduce the efficiency of amplification significantly.
Flexures	✓	This is considered an inefficient means of obtaining degrees of freedom.
Bending	✓	Structures that carry load in bending have compliance which absorbs some of the stroke produced by active materials.
Compressive pre-load	✗	Compressive pre-load allows for higher force output by piezo-electric materials without damaging said material.
Self-reacting actuators	✓	Replacing inactive/inert structures by active material reduces the material that does not actively contribute to the output of the mechanism.
Simplicity	✓	Simple mechanisms are easier to construct and provides for easier fault finding and optimisation.
Form factor	✓	The actuator should be compact and produce displacements in the desired direction.
Thermal stability	✗	Actuator performance should vary greatly with temperature.
Linearity	✗	Linearity improves the ease with which an actuator can be modelled, which holds advantages for feedback control systems.

The axioms that were excluded are the following: Planar actuators, compressive pre-load, thermal stability and linearity. Planar actuators, while not ideal in the context of the article, could potentially hold advantages in the trailing edge actuator and were not considered unfeasible. The compressive pre-load was specified for piezoelectric material;

it was altered here to *effective biassing*, since some technologies might require biasing other than compression. This is for instance the case with SMA wires, which would need to be biased in tension rather than compression. Thermal stability was considered a level of detail that would not be reached in this project, due to its exploratory nature, and linearity was considered to be a control system requirement, which was not relevant to the problem at hand.

The section can be summarised by stating that 3 lists of requirements were identified. These were the qualitative and numerical requirements by Airbus, as well as some requirements taken from design trends in literature. The design trend requirements were centred around the MEA concept and design axioms that allow for the design of optimal discrete actuators. The requirements are summarised in Tables 3.1, 3.2 and 3.3.

3.3 Preliminary System Specifications

The presented project dealt with the design of an actuation system that would alter the shape of a vertical tail wings trailing edge. The design of such a system required the selection of a suitable technology on which to base the design. By this phase in the project, the high level requirements were already known. These included a list of qualitative requirements, a list of numerical requirements and a list of design trend requirements. The numerical list provided hard constraints, which could be used for the down-selection of candidate technologies. The list is shown in Section 3.2 in tabular form. Table 3.2 was, however, not sufficiently detailed for such a down-selection to be conducted. This required the derivation of more useful specifications, based on the originally specified numerical requirements as well as the geometrical requirements in Section 3.1. The derivations and their results are discussed in the remainder of this section.

The specifications were found through application of the calculations shown in Appendix A. See Table 3.5 for a list of the results.

TABLE 3.5: Derived Specifications(DS)

		Opening		Closing	
Parameter	Unit	Calculated	Goal	Calculated	Goal
V_{max}	$[m^3]$	1.34	<0.65	1.336	<0.65
$E_{stroke,max}$	[Nm]	219.7	220	549.25	550
T_{act}	[s]	18.97	10	18.968	10
P_{act}	[W]	11.58	22	28.96	55
$T_{turnaround}$	[min]	>30	5	>30	5

In order to do these calculations, the trailing edge thickening was treated as the angular deflection of a rigid plate. An integration was performed through the identified displacement angle against the aerodynamic pressures given, this yielded $E_{stroke,max}$, which is the estimated stroke work for an actuation. The C_p values used for each case(opening or closing) were those that represented the worst case scenario for the case in question. For the closing case, suction would prove most restrictive; this would coincide with C_p, min. The opposite would be the case for opening(thickening), where the highest positive pressure, C_p, max, was associated with the strongest resistance.

P_{act} was then calculated using the 10 s goal time and $E_{stroke,max}$ and assuming that the energy would be expended at a constant power level. The 10 s was chosen arbitrarily to be shorter than the maximum specified by Airbus, while still being of the same order of magnitude. The other time value $T_{turnaround}$ the time expected between actuations. The minimum grounded time of the aircraft would be the time between actuations after landing, and the time between actuations after lift-off would be the typical flight time of a short flight. The reasoning behind these turnaround times was that the actuator would be open and preparing to close while it is on the ground, and while in flight it would be closed and preparing to open again. The goal values of turnaround time are thus the period within which, following an actuation, the actuator needs to be reset in order for the direction of actuation to be reversed.

To find the maximum available space, the cross-section of the trailing edge was integrated over its length. The result, shown in the table, is 1.34 m^3 which refers to the total volume inside the trailing edge. The goal volume is smaller than this by half. The reason for the reduction from the full volume, was that wires and structural components inside the trailing edge were expected to take up some of the space. A 50% reduction in available space due to other clutter was considered a reasonable estimate.

With the original statements of requirements converted into a more suitable format, a numerical basis was gained for the down-selection of actuator technologies. The derived specifications came in the form of calculated constraints, and goal values were selected to fall within the stated constraints. The performance indicators used are stroke work, power output, actuation period and maximum volume. These are all common high level descriptors in engineering applications.

3.4 Potentially Viable Technologies

The design of an actuator/actuators used for trailing edge thickening required the selection of a technological basis. This led to a study of literature dedicated to the design and analysis of actuator technologies. From the study, without considering the suitability of a technology option, an exhaustive list of candidate technologies could be compiled.

A high level study of each technology then very quickly highlighted certain technologies as being wholly unsuited for the current application. The technologies that were considered ill-suited, were excluded from more detailed trade-off studies. Since they did form a part of the original list, however, it was considered important that they enjoyed a brief mention in this document, with some consideration given to the reason for their disqualification. The full list is first presented, followed by a brief discussion on the disqualification and the resulting short-list of viable technologies.

The initial list of technology that was identified is shown in Table 3.6. The first technologies to be disqualified were oxygen pumps and electrolytic actuators. These technologies make use of pressurised gas in manners similar to that used in pneumatic actuators as discussed by Janocha [24] and Cameron and Freund [25]. The pressure is, however, generated through chemical reactions at very low rates. These slow processes/actuations happen over periods of hours or even days, and the frequencies cannot be boosted or traded off by any means known to the author. It is due to these frequency limitations that the use of the mentioned technologies was considered unfeasible.

Photostrictive materials, both semiconductor and polymer based, produce strain when exposed to light [24, 28]. This occurs when the light intensity is such that a certain bandgap energy is exceeded, similar to what occurs in photovoltaic semiconductors during the production of an electrical charge. Only the surface of a material can, however, receive the light necessary for this to occur, and extremely thin layers of material need to be used (thickness on the scale of micrometers [28]). These thin layers would not be able to sustain/generate the levels of stress needed for actuation of the trailing edge.

Electrostatic actuators rely on the attractive forces between charged particles [29]. Since the force is inversely proportional to the square of the distance between particles, it does not scale well to a macroscopic level.

Polymeric piezo is a fairly new type of material, and while remarkable characteristics can be achieved, the highly customisable nature thereof makes it difficult to classify. The study and development of such materials constitute a distinct specialist field.

The metal hydride actuators rely on the reduction in hydrogen absorptivity of some metals upon heating , as well as the reverse thereof [30]. It might be better classified as a pressure source for pneumatic actuation, since it is used in conjunction with bellows [30] and pneumatic muscles [31]. It is said to be small, light and noiseless [30] and to achieve high actuation stresses [32]. The fact that this is a pneumatic source rather than a stand-alone technology negates its explicit inclusion in the study, including it, rather, implicitly in the form of pneumatics.

The fluid-based actuator, referred to as a "fluid mass flow", is included in an article by one of the prominent authors. In this article, however, no information is given on the exact nature of the actuator. A wide search to identify such a technology also did not

TABLE 3.6: Full list of actuator technologies

Class	Type	[24].	[26]	[9]	[27]
Electromagnetic	Solenoid	x	x	x	x
	Magnetostriction	x	x	x	x
	Moving Coil (Voice Coil)	x		x	x
	Swinging Magnets	x			
	Various Rotary Motor Types	x			
Electromechanical(EMA)[1]	Linear Drive (Electric Cylinder)		x		
Electrohydrostatic(EHA)[2]	Hydraulically amplified electrical motor				
Electrostatic	MEMS Comb Drive	x	x		x
Fluidic	Hydraulic	x	x	x	x
	Rotary Hydraulic	x			
	Pneumatic	x	x	x	x
	Rotary Pneumatic	x			
	Fluid mass flow				x
	Fluid Muscle				
	Bellows				
Piezoelectric	High Strain (Polycrystalline ceramics)	x	x	x	x
	Low Strain (Natural Crystals)	x	x	x	
	Polymer	x		x	
	Photostrictive				
Shape Memory Alloys	Shape Memory Alloy	x	x	x	x
	Magnetic SMA	x			x
Thermal Expansion	Bimetallic	x	x	x	x
	Metallic	x			
	Phase Change Materials	x			
Electrochemical	Fuel Cells (Electrolysis)	x			
	Oxygen Pump	x			
	Solid State Reaction	x			
Thermo-chemical	Metal Hydride Actuator	x			

1 This technology was not included explicitly in the given references, since it is essentially a self-contained electrical/hydraulic hybrid. It is given here to emphasise its consideration for the design.

2 This technology is not included explicitly in the technology selection, but is listed here to emphasise its relevance to the project. It is a widely studied technology, often taking the form of a worm-screw powered by an electrical motor.

yield any results. The end result was exclusion from the list, based on the assumption that this was actually a variant of hydraulics or pneumatics rather than a stand-alone technology: likely a turbine type device, where momentum transfer is utilised to produce work rather than confined pressure.

The final list to be studied/discussed is summarised in Table 3.7. For the technologies contained in the list, no immediately apparent reason could be found for considering said technologies infeasible. This was thus the list that was studied in more detail.

TABLE 3.7: List of actuators warranting further study

Class	Type
Electromagnetic	Solenoid
	Magnetostrictive
	Moving Coil (Voice Coil)
	Swinging Magnets(Limited angle motors)
	Various Rotary Motor Types
Electromechanical(EMA)	Linear Drive (Electric Cylinder)
Electrohydrostatic(EHA)	Hydraulically amplified electrical motor
Fluidic	Hydraulic
	Rotary Hydraulic
	Pneumatic
	Rotary Pneumatic
	Fluid Muscle
	Bellows
Piezoelectric	High Strain (Polycrystalline ceramics)
	Low Strain (Natural Crystals)
Shape Memory Alloys	Shape Memory Alloy
	Magnetic SMA
Thermal Expansion	Bimetallic
	Metallic
	Phase Change Materials
Electrochemical	Solid State Reaction

3.5 Review of Selected Technologies

In Section 3.4 an extensive list of actuator technologies was reduced to those that could potentially prove viable in the current application. The current section is dedicated to conveying more information on all these previously listed technologies. The discussions are short and serve to convey the essence of each technology before a more mathematical selection process is communicated in the section that follows. The discussions are grouped in the categories which are shown in Table 3.7, and the within each category its constituents are discussed in a type of point format.

3.5.1 Electromagnetic Actuators

Electromagnetic actuators do work through the interaction of two magnetic fields. The misalignment of the magnetic field of a movable object(rotor) from that of a stationary object(stator) causes a force that seeks to align the two fields. The generated force is then used in a variety of ways to do mechanical work. One or both of the magnetic fields are generally created by the flow of current through a coil, with the former of the two scenarios making use of permanent magnets instead. The most common types of electromagnetic actuators are as follows:

Solenoids - These are limited motion drives that apply the previously discussed magnetic force in a linear fashion [33]. Although large forces can be generated, the iron cores are generally heavy and the stroke capabilities tend to be small. They generally are used for on/off type applications [24] such as relays.

Magnetostricitve - This according to Janocha [24], is a technology in which materials such as Terfenol-D experiences a macroscopic shape change when exposed to an external magnetic field. It is caused by the reorientation of magnetic domains within the material to align itself with the magnetic field. The materials retain this ability for long periods of time and are thus considered stable. The voltage requirements are quite low [34], but the susceptibility to electromagnetic interference [27] is quite high. The material is also extremely expensive [24], giving them little commercial application. Common applications of this technology includes sonar, vibration absorption [24] and precision automation [35].

Moving coil - This is a coil and a permanent magnetic field, with either possibly being the mover. Its stroke is said to have high accuracy and repeatability, as well as high customisability, with the possibility of infinite strokes if the track used forms a closed loop [36]. It is however heavy [33] and requires current to hold its position [36]. These actuators are normally used where high frequency and high accuracy motion control are required [24].

Limited angle motors - These are limited rotation devices that function on a principle similar to solenoids. They are very robust [24], as well as small, light, cheap and can provide large torques [37]. Disadvantages include low starting forces and small motion capability [24]. They have been applied in aerospace in optical scanning systems, fuel control systems and other limited rotation mechanical applications [37]. Throttle and control valves [24] are other common applications.

Electrical motors - This is similar to a voice coil in that magnetic fields attempt to align. In these devices, however, the magnetic fields are continuously commutated to provide infinite motion. They are stated to have a good power-to-weight ratio [38], and in aerospace can be applied directly in power-by-wire and fly-by-wire systems [14] as well as provide better fault finding in flight control systems compared to traditional hydraulic systems [14]. The disadvantages of this technology generally refers to the mechanical systems they need to be coupled to, such as worm-screws and gearboxes. Examples of such disadvantages include high maintenance and large backlash.

3.5.2 Fluid-Based Actuators

According to Parr [39], enclosed fluids can be used to distribute energy. By appropriate means this energy can be used to produce forces and displacements of either a linear or a rotational nature. The fluid-based actuators can be subdivided into pneumatic and

hydraulic, depending on the characteristics of the fluid. Hydraulics refers to the use of incompressible fluids, with the term pneumatic being reserved for those fluids that are compressible. Discussed below are some of these fluid-based actuators.

Hydraulic - This is mostly applied in linear actuators, due to its inherent suitability. Rotary versions (piston, vane and gear motors) [24] do, however, exist. It uses pressurised, incompressible fluids to exert very high forces very efficiently and with well understood physics. High resolution, highly repeatable control is also possible [24]. The viscosity of the hydraulic fluids is disadvantageous in such systems and causes energy losses where large volume flow is required(such as is required for rotary variants). Alciatore and Histand [33] also stated that it is noisy and that large, heavy infrastructure is required. The applications area of this technology is very wide, including its application in aerospace and, as such, will not be listed here.

Pneumatic - According most sources, including Janocha [24], this technology is very similar to hydraulic. The main differences are higher speed capability due to lower fluid viscosity, lower resolution control due to compressibility and lower actuation force capability [24].

Fluid muscle - According to Festo, they are one-directional actuators that mimic real muscles. A rubber hose wrapped in strong fibres is pressurised, the radial displacement of the hose then causes the fibres to pull the ends of the hose closer together. See Figure 3.4 for an illustration of this concept. The devices are pneumatic, with similar advantages and disadvantages to other pneumatic variants. According to Daerden and Lefeber [40], it can often be directly applied (without additional mechanisms), due to its good stroke capabilities. The dry friction that results from the displacement of the bladder however leads to loss of energy. The technology is mostly applied in humanoid robotics due to the similarity with skeletal muscles [40].

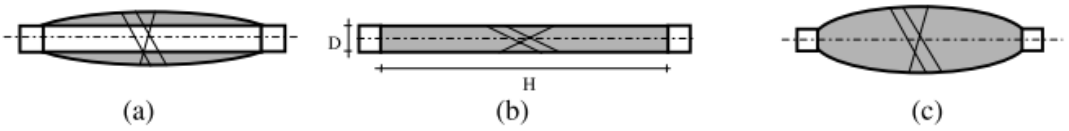

FIGURE 3.4: Fluid muscle illustration[5]:
a - resting condition. b - stretched condition. c - pressurised condition

Bellows - This is another pneumatic device, which is in some ways the compressive counterpart to fluid muscles. It possess the same characteristics as other pneumatic devices and, as such, will not be discussed in detail.

3.5.3 Piezoelectric Actuators

Piezoelectric materials are those where a relationship exists between mechanical force and electric charge [24]. Actuation with these materials is achieved by the direct application of a voltage to the material; this induces strain in the material, which can be used to perform work. The effects can be seen in naturally occurring crystals such as quarts (low strain piezo), or polycrystalline materials with enhanced characteristics (high strain piezo). Both these variants are discussed further below.

Low strain piezo - These are naturally occurring crystals in which a relationship exists between charge and mechanical force as was previously stated. It produces small displacements and very large forces, and can do so at extremely high frequencies. They are brittle materials, however, and are susceptible to creep, as well as changes in polarisation [24]. The changes in polarisation would generally result from excessively high voltage application.

High strain piezo - These materials are similar to the low strain variants but come in the form of customised polycrystalline materials with higher strains. Other than this they have similar advantages and disadvantages to the low strain variants. They are widely applied in high frequency applications, as well as those requiring high resolutions such as optics [41]. In aerospace they are arguably the most widely studied smart material technology, with applications including tuneable vibration absorbers [17], active vibration absorption and active control of blade aerodynamics through flap deflection and wing morphing [42].

3.5.4 Shape Memory Alloys

Shape memory alloys produce strains and stresses due to changes in the orientation of its crystal structure. The changes in orientation can be driven either by temperature change, or by the application of a magnetic field. The shape memory effects are normally stable at different orientations, requiring stimulus or the application of stress to be changed. This is very different to other solid state effects such as thermal expansion and magnetostriction, which spontaneously revert to its original shape when the stimulus is removed. See more information below on both the thermally and magnetically driven materials. Note also that several sections in Chapter 2 are dedicated to discussing the thermally activated SMA in detail.

Thermally activated SMA - This technology consists of materials that present high temperature dependent strains. The high strain capability results from solid state phase transformation in the material and the crystal orientations that go along with it [43]. The strain is reversible with temperature decrease if the material has been trained to do so resulting in a two-way shape memory effect; however, more commonly used is

the one-way shape memory effect where the reverse transformation needs to be stress induced [24]. The material possesses high energy densities, diverse deformation possibilities, mechanical simplicity and cleanliness, as well as the possibility to be heated electrically [24]. Disadvantages include actuation frequency limitations(due to cooling requirement), expense, design complexity and fatigue [24], as well as high non-linearity [43]. Janocha [24] and Copra [43] listed a variety of applications, such as surgical tools, stents, bone anchors, gripping devices and natural frequency tuning. The reader is encouraged to refer to Chapter 2 for more detail on this material.

Magnetic SMA - This technology consists of materials such as Ni-Mn-Ga, which changes its crystal structure, similar to the previously mentioned SMA [44]. In this case, however, the driver is a magnetic field(usually a ferromagnetic core) rather than a change in temperature. The application of said field causes the reorientation of some twin variants within the crystal structure [45](illustrated in Figure 3.5). This results in strain as well as stress being induced in the material. Biassing or antagonistic design is required for reorientation after the removal of the field. These materials show large strains and extremely fast response time [24] as well as very good cycle life characteristics [45]; they are, however, extremely expensive [24] and show large hysteresis, which results in losses [45]. Closed loop control [45] is required if repeatability and accuracy are required. Applications of the technology include linear motors, fluid control valves and pulsating pumps [45].

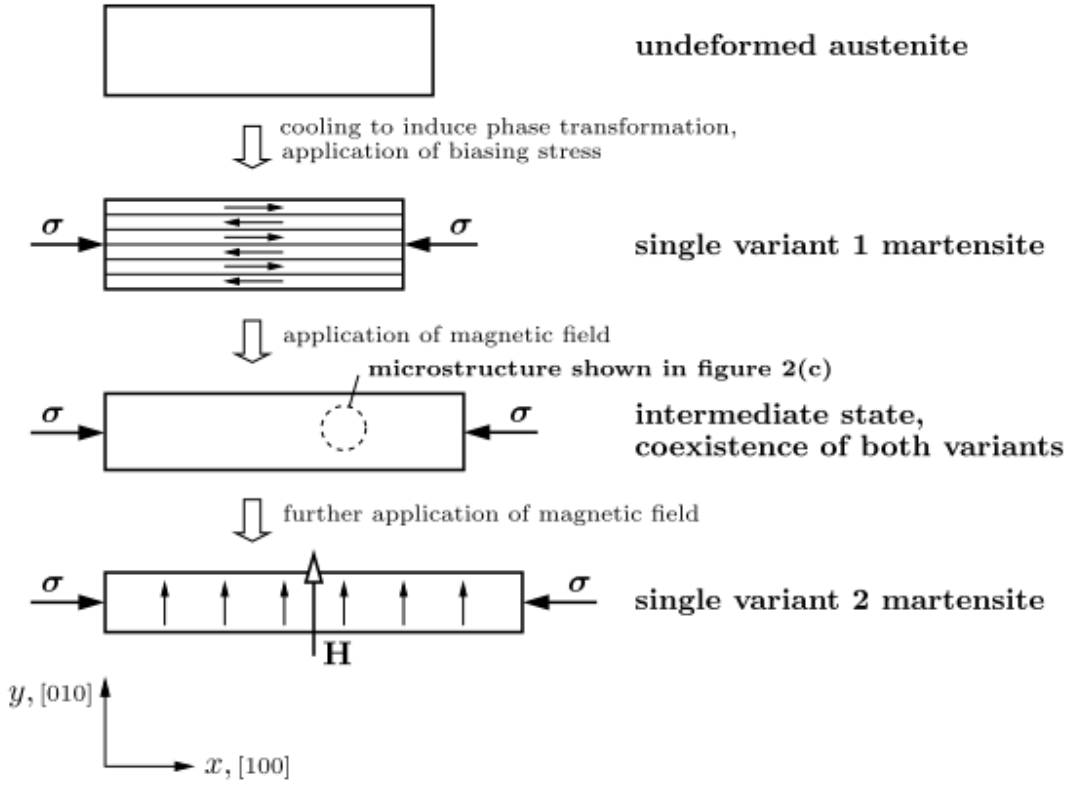

FIGURE 3.5: Illustration of the functionality of MSMA's [6]

3.5.5 Thermal Expansion

These technologies rely on the volumetric expansion of materials due to the application of heat. More details are given below on different ways in which thermal expansion can be used.

Bimetallic - This consists of metals with different thermal expansions layered on top of each other [9]. It is a widely available, well-priced technology with linear temperature dependence and very high repeatability throughout its life [24]. While possible strains are high, the output forces are generally low and require fairly large temperature differences [24]. They are mostly used for temperature sensing or in temperature-based control systems [9].

Metallic - This is similar to the bimetallic, but consists of a single metal, and instead of being used in bending they are generally applied in a linear fashion. The application areas are similar although the actuation forces are higher and strokes lower.

Phase change - Many materials exhibit large volume changes during phase transition a phenomenon that can be used in conjunction with pistons, bellows etc. to achieve actuation [24]. The required temperature differences are much lower than in those technologies that rely on single phase expansion, however, the energies involved tend to be higher. The main application area is in thermostats.

3.6 Supporting Systems and Configurations

The technology selection would be done on the basis of high level descriptors such as power and energy. In order to account for the possibility of trading off lower level characteristics such as stroke/force/frequency within this energy boundary, output mechanisms and configurations needed to be considered. To this end, a study was conducted on the possible trade-off mechanisms that could be used, as well as different configurations that could be employed.

3.6.1 Actuator Configurations

Actuators, structural members and active material elements can all be placed in either series or parallel. Parallel configuration shares the load between neighbouring members; this increases the stiffness of the relevant subsystem and increases its capacity to carry load [27]. Series configuration, on the other hand, reduces the stiffness and increases the stroke capacity [27].

3.6.2 Output Mechanisms

The general approach taken was that the possible design variants and applications for any mechanism are vast. The creative use of such mechanisms can lead to effective and interesting solutions to a great many problems. A wide study of mechanism types was therefore conducted to acquire background knowledge and ideas, rather than a list of possible candidates to select from. This knowledge would prove valuable in the generation of concepts when a solution was sought for the problem statement in the current project. In the discussion that follows, no strict grouping strategy is followed, with grouping done to improve readability rather than context.

It is still, however, useful to consider some of the characteristics often used to distinguish between different types of mechanism.

The purpose of a mechanism is to condition a certain input in such a way that it meets a certain output requirement. If this were not the case, why could the active material not just be applied directly? In any event, this conditioning of the input signal comes down to trade-offs between the different characteristics that define mechanical work.

For the purpose of this discussion, consider the characteristics to be effort that is applied (force/torque), the extent to which it is applied (displacement) and the rate at which it can be applied (frequency/speed). These characteristics provide perhaps the most general categorisation of mechanism types, and that is the type of trade-off that the mechanism facilitates. The trade-offs can be force/stroke, frequency/stroke or a combination of force/stroke/frequency.

Another characterisation is often the physical law employed by the mechanism to perform its function. It basically comes down to leverage (gears, pulleys, levers, cranks and even, to some extent, benders), the exploitation of trigonometric relations (linkages, cams) or pressure relations (hydraulic, pneumatic, bellows, etc.). The physical laws that were mentioned above actually apply to force/stroke trade-off only. It is through the successive application of high frequency actuation cycles that frequency is traded off against either force or stroke, or both.

In this document such a trade-off is referred to as a frequency-based trade-off. In frequency-based trade-offs, three methods are often used. These are stepping, ultrasonic and the pumping of fluid. Stepping actuators make use of two clamps, which take turns to open or close, or of a stick-slip method, which will be explained further in due course. The stepping methods can, very literally, be likened to the steps taken by a human, or the "inching" forward of certain types of worms. Ultrasonic actuators make use of moving waves, which create friction through motion similar to the movement strategies employed by snakes and earth worms.

More information on this is given in the paragraph dedicated to such mechanisms. In the meantime, some discussions on mechanisms that were found in the literature follow below.

Conventional mechanisms:

Conventional, rotational mechanisms are gears, pulleys, cranks and cams(Figure 3.6). Gears(Figure 3.6c) and pulleys(Figure 3.6d) in actuation are used in conjunction with rotary motors, mostly electrical, but also hydraulic and pneumatic variations. Here the leverage principle, i.e. the ratio between moment arms, is used to scale between rotational speed and torque. Cranks(Figure 3.6a), on the other hand, use the same principle to convert linear motion into rotational or vice versa. In cams(Figure 3.6b), the trigonometry between the cam and a "follower" is exploited to achieve complex relationships between the output speed/force and a simple rotational input. Examples of these types of mechanisms in engineering applications are endless and will not be discussed here in more detail.

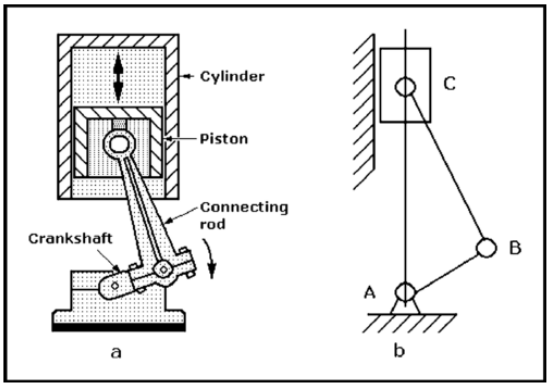

(a) Crank mechanism

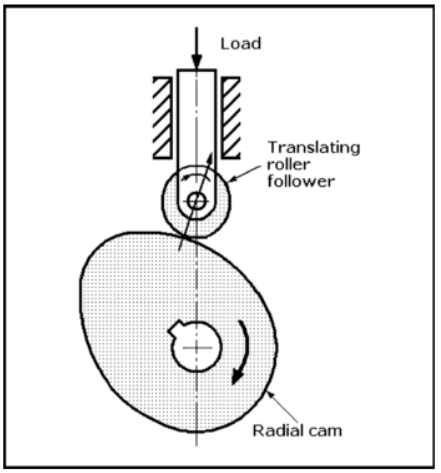

(b) Cam mechanism

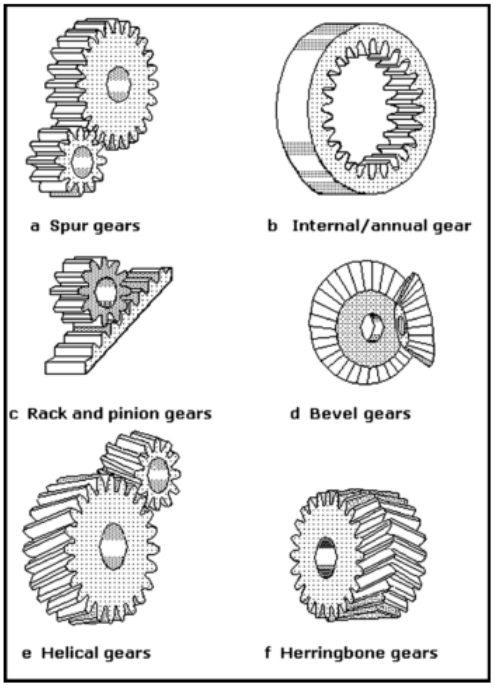

(c) Gear mechanisms

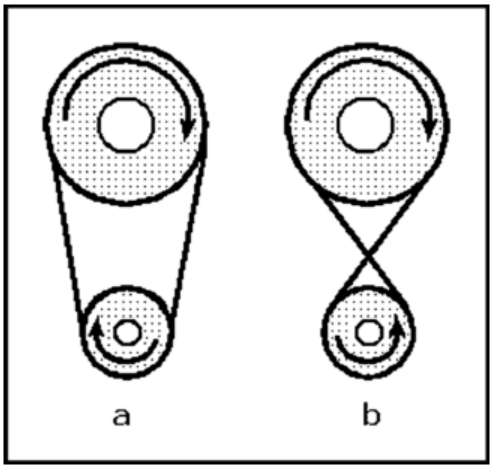

(d) Belted pulleys

FIGURE 3.6: Conventional mechanical devices(figures taken from *Mechanisms and mechanical devices sourcebook* [7])

Linkage type mechanisms:

Another category of output mechanisms are called linkages. This is a blanket term for a very wide range of mechanisms that make use of rigid links of various lengths, interconnected with hinged joints. A wide array of input/output relationships can be realised though the creative applications of such multi-link machines. They are, for instance, used to convert rotational input into straight lines (Figure 3.7a), ellipsoids and figures of 8 to name just a few. More simplistic linkage types can be recognised by looking at old car-jacks, also known as a 7-or 5-bar linkage type (Figure 3.7b). The 5-bar linkages actually function as two back-to-back applications of a 3-bar linkage, where

one link has a variable length. The 7-bar linkage operates in largely the same manner. The 5-bar type is a mechanism very commonly used in smart material applications, and can yield highly mass-efficient designs due to the axial nature of forces inside the mechanism. Often, in smart material applications the pin-type hinges are replaced with flexural hinges, as was done in the RACT actuator [18](Figure 3.7c).

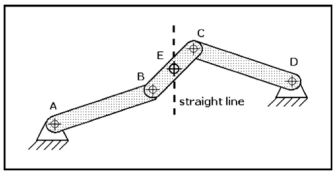

(a) Straight line generator [7]

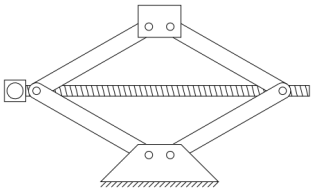

(b) Car-jack mechanism [46]

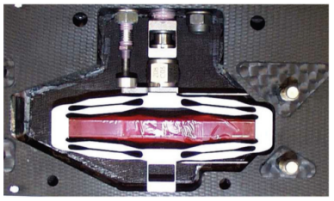

(c) RACT, flexural hinge linkage type actuator [18]

FIGURE 3.7: Linkage mechanism examples

Similar concepts are used in the Moonie [47] and fish-mouth actuators [48]. In these actuators, however, the strain is distributed throughout a compliant frame, as opposed to the localised rotational movement in hinged connections. See Figure 3.8 for a graphical representations of these actuators.

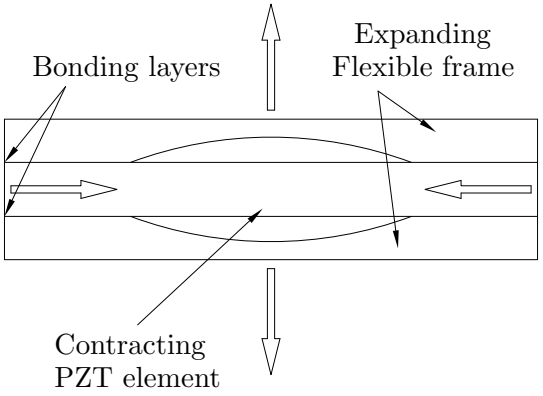

(a) Moonie actuator [47]

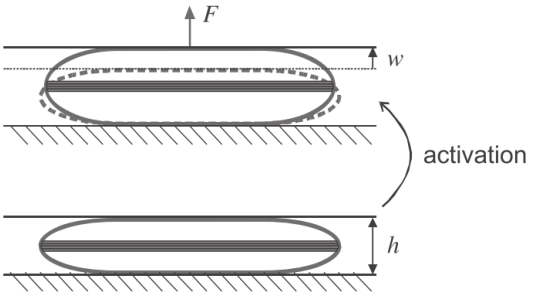

(b) The "fishmouth" actuator [48]

FIGURE 3.8: Actuators that use flexible frame structures for stroke amplification

Single and dual layer benders:

Benders use, inside the material, something akin to the lever principle. A strain, either positive or negative, is induced in material, which is offset from the neutral plane. A neutral layer or, alternatively, neutral material in the same layer, does not take part in the extension/expansion that is taking place in the active material. The difference in length between the active and passive parts of the material then causes macroscopic bending to take place, resulting in high values of stroke for a small strain in the active material. Examples of bi-layer benders are the C-BLOCK (Figure 3.9a), CERAMBOW

(figure 3.9b) and THUNDER (Figure 3.9c) actuators, as well as conventional bi-metal beams.

Examples of single layer bending would be SMA actuators such as helical springs and beams which are trained to produce bending deflections.

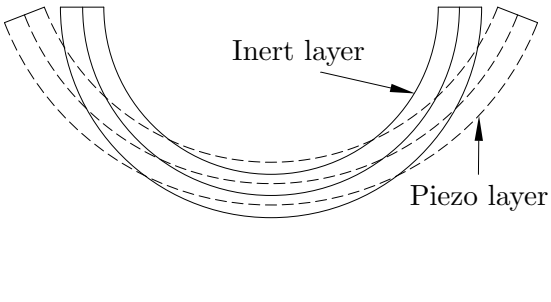

(a) C-block pre-bent actuator

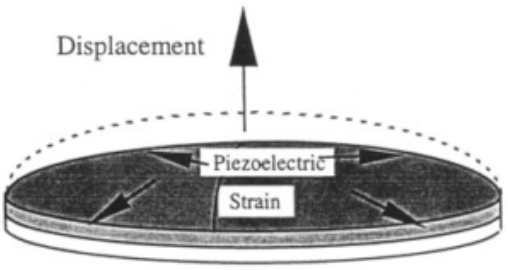

(b) CERAMBO disk actuator[49]

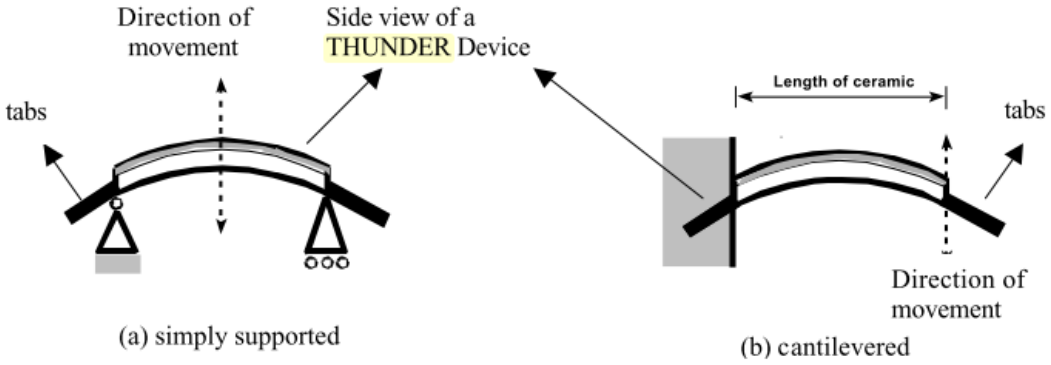

(c) THUNDER, beam type actuator[49]

FIGURE 3.9: Bi-layer type bending actuators

Mechanisms that facilitate frequency-based trade-off:

These mechanisms use stepping strategies, ultrasonic vibration(waves) or the pumping of fluid to create movement.

The stepping strategies follow a similar order of events as that indicated in Figure 3.10. Here, Zhou et al. [50] likened the movement of a mechanism to that of the worm that inspired such mechanisms.

The stepping cycle works as follows:

1. The rear is "clamped" in position and the front free to move.
2. The active material extends, moving the front further from the rear.

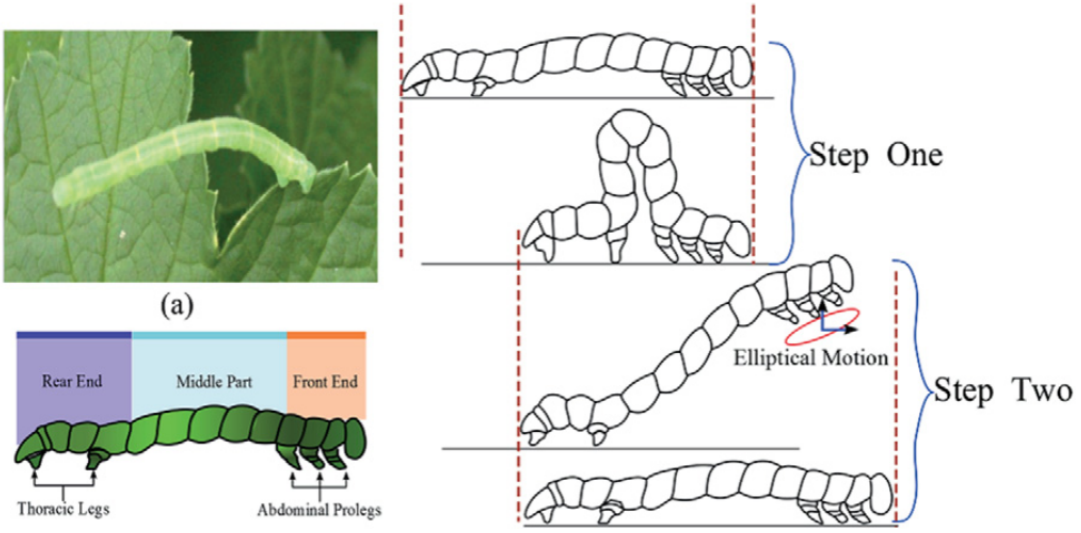

FIGURE 3.10: The walking movement of a worm that inspired stepping mechanisms

3. The front is "clamped" and the rear released.

4. The active material contracts and moves the rear closer to the front.

Repetition of this cycle would move the actuator further in the same direction. Also, by alternating the clamping sequence, the direction in which the actuator "walks" can be changed.

Clamps can be either static or passive in nature, with the clamps in both cases mimicking the function of the rear and front ends of the worm. The difference between the two variants are that in the case referred to as the active variant the clamps themselves are actuated to open and close, while for the passive variant some or other type of self-locking clamp is used.

A similar stepping technique, the stick-slip technique, uses a single friction clamp rather than the 2-clamp strategy as discussed above. The successive forward and reverse strokes then alternate their speed. A slow actuation draws the mechanism to a specific side, and a quick actuation then overcomes the static friction of the clamp and slides the clamp one step in the direction of movement. The inertia of the moving object stops it from being moved back to its original position during the jerk, earning one such mechanism the name "inertia drive". Figure 3.11 illustrates the working principle of the inertia drive.

Ultrasonic actuators make use of waves to create linear or rotational movement; it could be seen as a snake or worm-like movement of continuous harmonic excitation. The ultrasonically vibrating members can take many shapes, including warping plates, linear peristaltic devices, and "fingers" or "legs", similar to the legs of a millipede. A travelling wave is illustrated in Figure 3.12a and a similar device making use of oscillating beams "legs" is shown in Figure 3.12b.

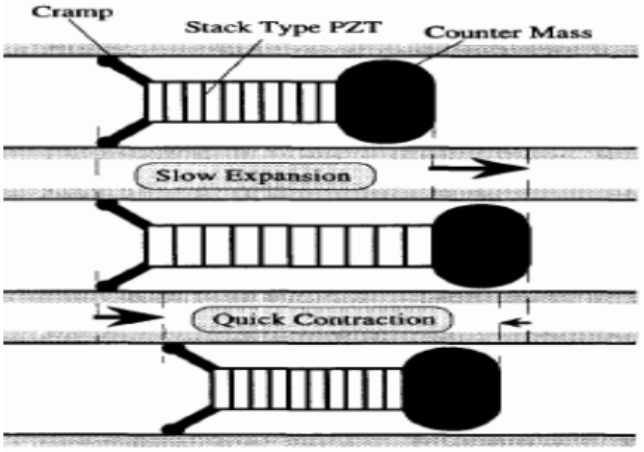

FIGURE 3.11: Inertia drive linear motor [8]

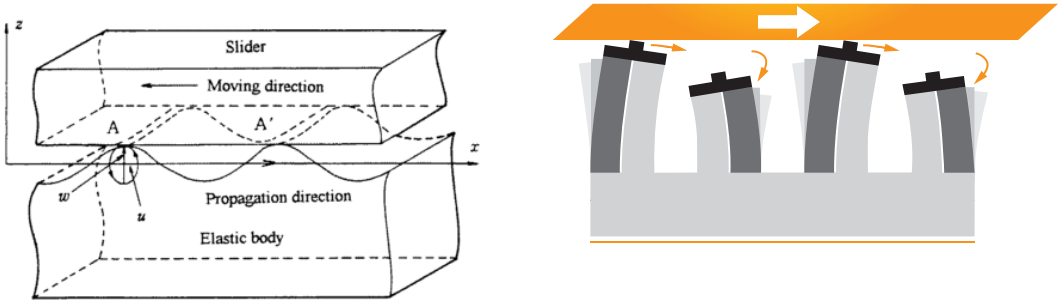

(a) Travelling wave on a plate [51] (b) Piezo legs illustration [52]

FIGURE 3.12: Some ultrasonic actuation strategies

Fluid-based actuators (hydraulic, pneumatic) are well known, and therefore the conventional versions are not discussed in detail. They do, however, enjoy quite a number of new application areas, including miniature actuators. In terms of smart material applications, it is usually used in the form of a piston type hydraulic pump, with valves that control the direction of fluid flow. A cyclically applied stroke by a magnetostrictive, piezo-electric or similar type of active material provides the reciprocating movement required for the piston to pump the fluid. There have also been other interesting pumps, which made use of diaphragms, bellows or peristalses. The fluid pressure that is generated can then be used to perform work, also using pistons/diaphragms/bellows or any other pneumatic or hydraulic-compatible mechanism.

3.7 Initial Technology Selection

This section discusses the initial selection process followed to reduce the initial list of candidate technologies to a more manageable amount of considered options.

This section discusses the selection process followed to reduce the initial list of candidate technologies to a more manageable number of options considered. The selection was performance based, keeping in mind the theoretical suitability, and high level optimality of the selected options. The performance indicators that were used are discussed in Section 3.7.1 This is followed by Section 3.7.2, in which the selection strategy is explained. The eventual application of the discussed method is then documented in Section 3.7.3, which culminates in the list of technologies that were carried over into the next project phase. A separate selection was conducted for single and multi-stroke (those making use of frequency-based trade-offs) options, as their selection criteria would be very different.

The selected technologies were hydraulic, pneumatic, SMA, fluid muscles and high temperature thermal expansion in the single-stroke case. The best multi-stroke options, on the other hand, were dominated by piezoelectric options, with polymeric as well as low and high strain variants being selected. Other technologies that were considered to be viable options for multi-stroke actuators were the hydraulic and magnetostrictive technologies.

3.7.1 Performance indicators

The numerical selection in this project was made using charts of combined primary variables. This procedure was suggested by Huber et al. [9] and is discussed in more detail here. The list of performance characteristics in the mentioned article included the minimum as well as maximum stress and strain, and also the density, modulus, volumetric power (related to frequency), efficiency and resolution of the actuator.

For the purpose of this design, the resolution was considered irrelevant, due to the open/closed nature of the required movement. The modulus was temporarily disregarded, as this would be determined through design. The efficiency was also temporarily disregarded, which seemed reasonable, since the expected periods for which the device would be operated was expected to be negligible compared to overall flight time. A low efficiency might lead to high power losses, but the small actuation period should mean that this would amount to small overall energy losses.

By disregarding the above-mentioned parameters, one is left with the following performance indicators:

Actuation stress: Actuation force divided by actuator cross-section.

Maximum actuation stress: The maximum stress in any given stroke.

Actuation strain: The nominal length change of the actuator divided by its length.

Maximum actuation strain: The maximum possible actuation strain.

Actuator density: Actuator mass divided by its volume at the start of actuation, excluding supporting systems.

Volumetric power density:

Other than these characteristics that are explicitly listed by Huber et al. [9], the following also appeared, either resulting from calculations based on the parameters listed above or as inputs for calculating them.

Mass power density: This is the power output capability divided by the mass of the actuator.

Volumetric energy density: The stroke energy capability divided by the actuator volume.

Mass energy density: The stroke energy output divided by the mass of the actuator.

Maximum frequency capability: The maximum cyclical frequency that can be achieved, often limited to a quarter of the first resonant frequency of a material.

The parameters are seemingly simple and similar to the force, stroke etc. used by other authors. When they are, however, used in combination charts, additional system level selection variables result, which can be very useful when trade-offs between performance characteristics are considered. By including possible trade-offs in the selection process, active materials can be selected independently from the specific mechanisms that would facilitate the necessary trade-off. Some examples of such additional variables are the -1 slopes of stress/strain or specific actuation stress/strain charts. These slopes represent, respectively, volumetric energy density and mass energy density. The selection process is discussed conceptually in Section 3.7.2, followed by the actual application thereof in Section 3.7.3.

3.7.2 Selection strategy

The selection of actuators, similar to any other component in engineering systems, is done in such a way as to meet certain performance criteria; in this the current strategy is no different. Often then, the viable options listed can be compared to each other and the performance criteria by indicating their performance limits on a single graph. In two-dimensional graphs this generally means that two distinguishable variables can be considered at the same time. The current strategy, however, as suggested by Huber et al. [9], allows for additional information to be assessed on the same graph by selecting the performance indicators in such a way that their product forms a third useful variable. In

such graphs the possible trade-off's between the variables can then also be considered. The performance indicators borrowed from the article by Huber et al. [9] were already discussed in Section 3.7.1.

Consider, for instance, the $\sigma\epsilon$ graph shown in Figure 3.13, which contains exactly the kind of performance limits that were mentioned. The horizontal and vertical lines for any given envelope represent the maximum values of the relevant performance indicator that can be achieved by that given technology. For Figure 3.13 this would mean that the horizontal limit of an envelope indicates the maximum actuator stress for the relevant technology, and the vertical limit indicates the maximum strain. The diagonal limits, on the other hand, indicate the maximum values for the additional variable that was previously mentioned; this additional variable is found by taking the first two. For the current example the diagonal lines would then indicate the maximum value of the product $(\sigma_{max} * \epsilon_{max})$, which is the maximum volumetric energy density.

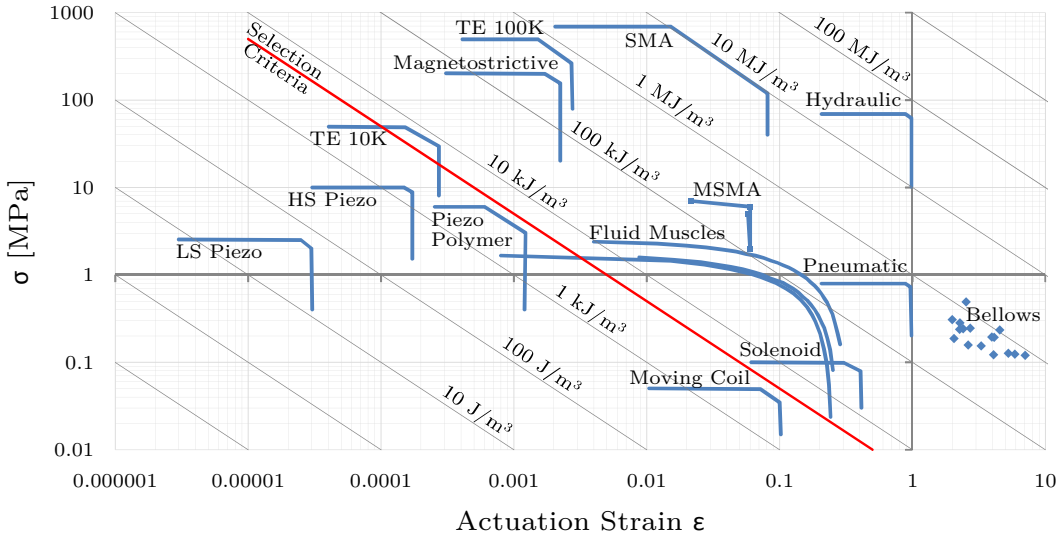

FIGURE 3.13: Stress/Strain selection chart (adapted from Huber et al. [9])

The shape of the operational envelopes suggests that during low strain applications, a certain maximum stress is reached and vice versa. Note that in such applications one of the performance indicators saturates, and the full volumetric energy density capability of the relevant technology is not utilised. Once application reaches the maximum, volumetric energy (the diagonal line) has not been exceeded. Once the maximum volumetric energy density is reached, the operation of the device would fall on the diagonal line, and the two performance indicators would have to be traded off against each other. If a technology is used in such a way that its performance falls on such a diagonal line, the output can theoretically be shifted along this line using some of the mechanisms that were discussed in Section 3.6.2. It is easy to see that using this selection process gives three possible selection parameters on a single graph, and that the possible mechanical

trade-off's can be considered already in the selection process. The application of this selection strategy within the current project is discussed in section 3.7.3. Note that while the selection strategy is discussed in terms of the $\sigma\epsilon$ graph(Figure 3.13), the concept can be directly applied to similar graphs, provided that suitable performance indicators are selected.

3.7.3 Selection process

The selection process, which consisted of the methods discussed in Section 3.7.2, was conducted using the previously estimated system requirements. These requirements, discussed in Section 3.3, are repeated in Table 3.8 for convenience.

TABLE 3.8: Numerical requirements for technology selection

		Opening		Closing	
Parameter	Unit	Calculated	Goal	Calculated	Goal
V_{max}	$[m^3]$	1.34	<0.65	1.336	<0.65
$E_{stroke,max}$	[Nm]	219.7	220	549.25	550
t_{act}	[s]	18.97	10	18.968	10
P_{act}	[W]	11.58	22	28.96	55
$t_{turnaround}$	[min]	>30	5	>30	5

Both energy and power values are specified in this table; the first would be used to select technologies that could provide the necessary actuation in a single stroke. Such technologies would likely be simple and require little maintenance. The power, on the other hand, would be used for the selection of technologies with high frequency capabilities. Such devices, while maybe not capable of providing the necessary stroke in a single stroke, could be applied cyclically to yield the same result. By making full use of their high power densities, the possibility would exist for weight savings compared to single stroke options. For each of the two strategies (single and multi-stroke), five candidate technologies were chosen to provide a broad basis for further conceptual development. The single selection was considered first.

For a technology to be viable in the current application, it would need to be capable of providing the necessary stroke and force. It would, furthermore, need to fit inside the available space a requirement that can be considered to be a hard limit. An additional, broadly stated, requirement was that the actuator needed to be as light as possible. The spatial requirement was the first to be selected for; this way only technologies that did not violate this hard limit would be considered further. The next step was to select from the remaining options those that proved to be the lightest. In doing this, the second requirement was enforced.

Volumetric energy density is a useful performance indicator when it comes to space-limited, single stroke applications. This is, in fact, the selection variable that was already seen in Figure 3.13 Note that a red line is also indicated on this figure. The red line serves to communicate, graphically, the selection criteria that were estimated from the performance requirements in Table 3.8. The following calculation was done to estimate the selection criteria:

$$e_{req} = E_{stroke,max}/((1/3) * V_{max}) \tag{3.6}$$

Note that the estimated available volume was divided by three in the calculation. The reason for this was that the available volume would need to house all the necessary supporting equipment. This would include power-supplies, moving parts and fasteners. It was then assumed that two thirds of any system would need to be dedicated to such supporting components, and that only a third would be available to house the primary mover. The energy density of a primary mover selected from Figure 3.13 would thus need to be larger than e_{req}, as is indicated by the red line. Any technology below or to the left of this line, was considered to be unable to fit into the available space, and could thus be immediately disqualified.

With the list of viable technology options now reduced to only those that could fit into the required space, the lightest of the remaining options needed to be found. This was done at the hand of Figure 3.14, which shows the volumetric power density as well as the mass density of the different technologies. The diagonal lines indicated on this figure correspond once again to the product of the mentioned performance indicators, resulting in mass-based energy densities as indicated by the annotations on said lines. It can be seen that a progression towards the upper right hand corner of the graph would lead to higher mass-based energy densities. Thus the selection of the five lightest technologies came down to picking those that were the highest up in this direction.

The results of the selection are summarised in Table 3.9. Also indicated in this table are crude estimates of the mass and volume of such a primary, given its output was the stroke work that was required.

Next, the technologies were selected that, while possibly not being able to provide the actuation energy in a single stroke, had high enough frequency capabilities to warrant a trade-off between frequency and stroke. Piston pumps in hydraulics, piezo-steppers and travelling wave actuators are example mechanisms in which such trade-off's are in fact made. The graph used for selection is shown in Figure 3.10. The specific volumetric power density and mass density appear on the respective axes. On this graph, +1 slope lines represent the mass density of the technologies. Using this graph, the volumetric constraint could be enforced by selecting a technology that was high enough on the graph in the y-direction. The lightest option could then be identified by determining

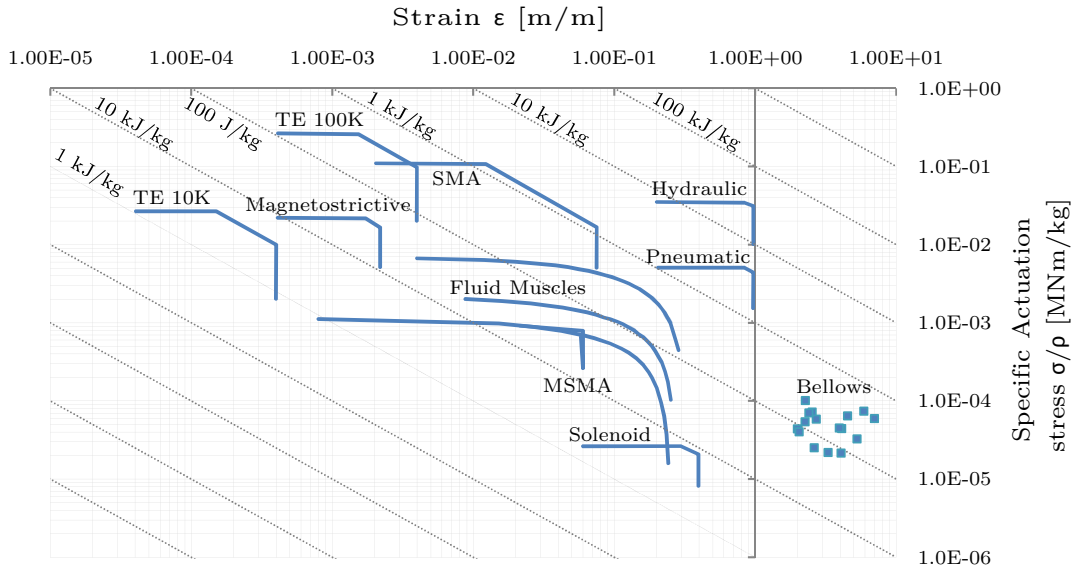

FIGURE 3.14: Stress/Strain selection chart (adapted from Huber et al. [9])

TABLE 3.9: Single stroke actuator shortlist

	Max Specific Stroke Work $[kJ/kg]$	Max Volumetric Stroke Work $[MJ/m^3]$	Min Mass $[kg]$	Min Volume $[m^3]$
Hydraulic	30.33	61.12	3.627E-02	1.800E-05
Pneumatic	4.257	0.7034	2.584E-01	1.564E-03
SMA	1.317	10.44	8.352E-01	1.054E-04
Fluid muscles	0.4087	0.1465	2.691E+00	7.509E-03
Thermal expansion (100K)	0.3978	0.7034	2.765E+00	1.564E-03

which of the viable options were higher up in a direction perpendicular to the +1 slopes. The frequency capability did not need to be explicitly considered here, since the power-based selection included, implicitly, both the single stroke energy capabilities and the frequency.

When the selection criteria were plotted, it fell outside the region shown in the graph. This meant that all the technologies presented in the graph were theoretically viable; therefore, the chosen options were identified on the basis of mass power density to select the technologies that would have the lowest mass. The selected technologies can be seen in Table 3.10. Note that, once again, based on the available power densities and estimated actuator requirements, possible performance values for the prime mover were calculated and are indicated in the table.

It might be noted that the mass and volume values for these technologies are substantially lower than those of the single stroke actuators in Table 3.9. This is due to the more complete utilisation of material capabilities. The estimates would, however, not

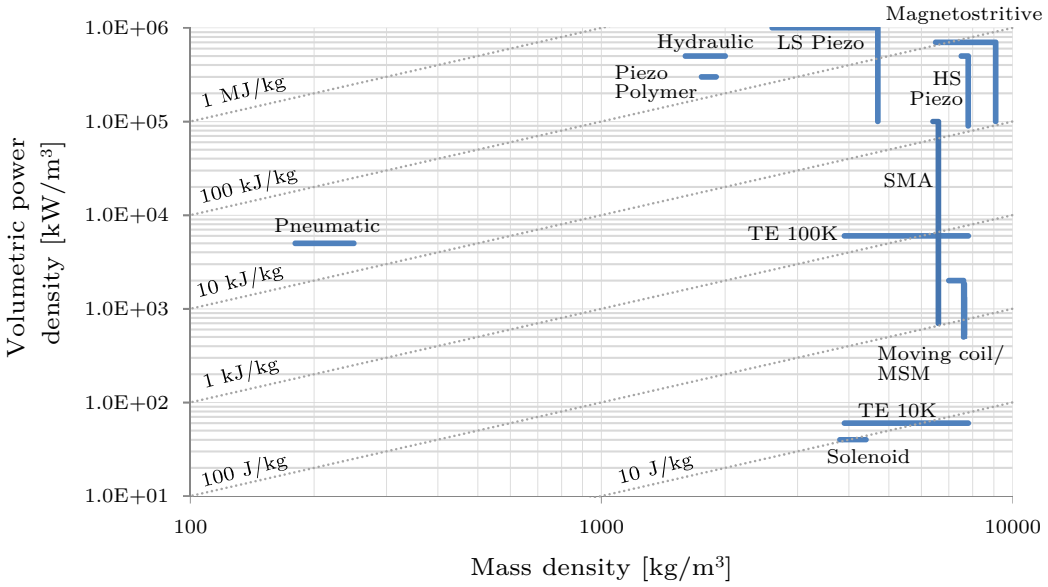

FIGURE 3.15: Power-based selection chart (adapted from Huber et al. [9])

TABLE 3.10: Multiple stroke selection results

	Maximum mass power density (kW/kg)	Maximum Volumetric power(kW/m3) (kW/m^3)	Minimum mass (kg)	Minimum volume (m^3)
Piezo- polymer	171	300 000	4.288E-04	2.444E-07
Hydraulic	313	500 000	2.343E-04	1.467E-07
HS piezo	66.7	500 000	1.099E-03	1.467E-07
Magnetostrictive	108	700 000	6.790E-04	1.048E-07
LS piezo	385	1 000 000	1.905E-04	7.333E-08

include the mass and volume of various supporting systems. In the multi-stroke mechanisms, due to their higher complexity, such supporting systems may prove to be heavier and larger than those of the single stroke variants. Without a more detailed trade-off study, it would prove difficult to choose between the various options included in these short-lists. To this end, exactly such a study was conducted as is communicated in the next chapter.

Chapter 4

Functional Diagram and Final Selection

The design of an actuation system required the selection of a suitable core technology upon which to base the design, as well as suitable subsystems, which would support the core technology in performing its function. The manner in which such selections are typically conducted is discussed in several literary sources ([9, 26, 27, 53]); all of these authors followed similar selection processes (qualitative $->$ quantitative $->$ pareto), varying mostly in the scope of the selection (which subsystems to include) and the performance characteristics used. The qualitative and quantitative selections are discussed in Sections 3.4 and 3.7 respectively, with two technology short-lists identified by the end of Section 3.7. This section is dedicated to the next step in the selection, i.e. the pareto analysis.

The previous selections considered mainly the core technologies, and not the supporting subsystems that would be needed for them to operate. This was deliberate, since the purpose was to find the best core technologies rather than becoming bogged down in a study of its peripherals. In the pareto selection more attention was, however, paid to the effect of peripheral systems on the performance of the technology in a functional application. This was done by performing the pareto analysis on complete concepts rather than stand-alone technologies. This then served as the final selection, after which a complete system concept was known.

The final selection is presented as follows:

1. A functional breakdown of the system to provide a framework for the generation of concepts(Section 4.1).

2. The generation of several alternative concepts by specifying subsystems to perform the identified functions(Section 4.2).

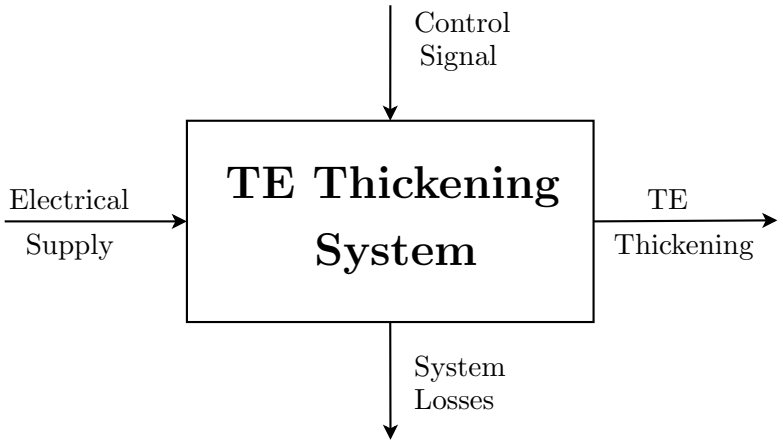

FIGURE 4.1: Black box system representation

3. A pareto analysis to select the best 3 concepts(Section 4.3).

4. Presentation of the chosen concepts to Airbus for a final decision(Section 4.4)

This process resulted in the selection of a concept that makes use of SMA wires, which is driven electrically by a switching power supply, and is coupled to the trailing edge skin through a simple mechanical linkage.

4.1 Functional Breakdown

In the current chapter, a concept is generated/selected for a system that can alter the shape of a vertical tail wing between a blunt and a sharp form. The system would need to have low mass and fit within the confines of the trailing edge. The concept is chosen from several alternative concepts, all making use of several subsystems that would allow it to perform its overall function. The structure of the proposed system is defined by the functional breakdown that is presented in this section.

The functional breakdown started from the blackbox representation of the system as shown in Figure 4.1. The system should take energy from an electrical supply, and at the command of a control signal convert this energy into mechanical work in the form of a thickening of the trailing edge. As with any system, some energy losses were also expected.

The functions that the system needed to perform to provide this functionality were considered to be the following:

- ***Control*** the energy from the electrical supply to drive the active material.

- ***Convert*** the energy from electrical to mechanical.
- ***Condition*** the mechanical energy to the required form by trade-offs between frequency, stroke and driving force, as well as converting between linear and rotational motions.

A complete system concept would then possess subsystems that could perform each of the mentioned functions. The following subsystems were suggested:

Energy Controller:

This is a driver, which conditions the electrical energy to be suited for the active material that it drives. It also initiates/stops actuation when such a command is received/required. It consists of an amplifier stage, as well as an output element. The purpose of the amplifier stage is to supply the electricity in the required form. It can perform step up/step down functions, pulse width modulation, rectification or any other type of transformation that may be needed. The output element is the element that provides the physical stimulus that the energy converter requires.

Energy Converter:

This is the active material, i.e. the actual physical process by which the electrical energy is transformed into mechanical energy. This can include SMA, piezo-electric, electromagnets etc.

Energy Conditioner:

These are the output stages of the actuator. It would include any such system element that ensures the mechanical energy supplied to the load is well suited to the task. Three stages are suggested for this subsystem.

The first stage is a transmission element; this is the mechanism that takes the mechanical energy provided by the energy converter (hydraulic/pneumatic/rotational), and converts it into a force and a stroke as required.

The second stage, called the internal structure, consists of structural elements that connect the mechanism to the aircraft skin. This element may serve purely as a mechanical connection, or a second stage of mechanical amplification after the transmission stage.

The final stage, which is the external structure, refers to the aircraft skin itself, it is considered to be a part of the energy conditioner, since the type of deflection (compliant or rigid) would affect the thickening characteristics of the trailing edge itself. It can also be used as a third stage of mechanical amplification in the form of angular deflection.

The final block diagram representation of the proposed system can be seen in Figure 4.2. This concludes the functional breakdown, and provides a framework for further conceptualisation.

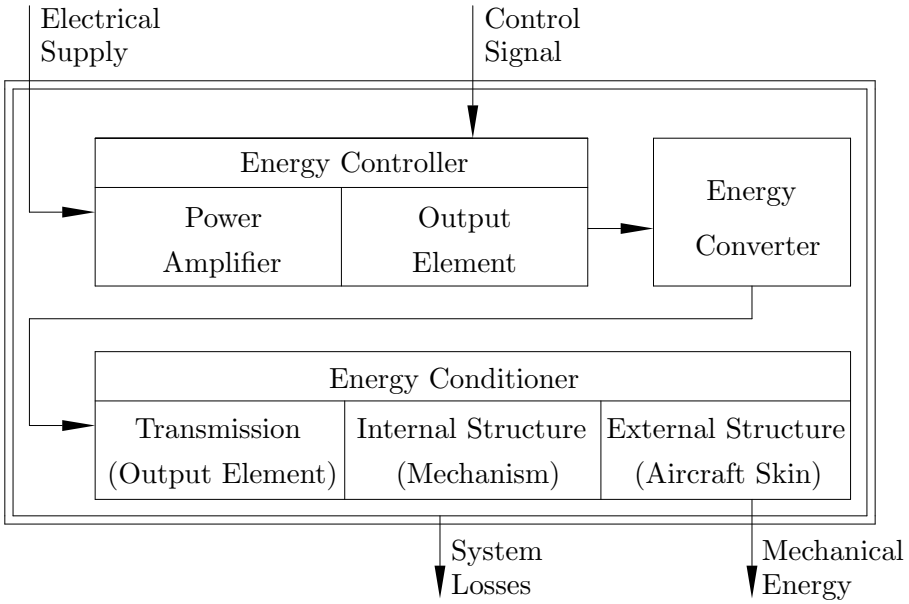

FIGURE 4.2: Functional diagram

4.2 Generating Alternatives

Alternative concepts were needed for further down-selection from the original list of actuator technologies, which would result in a final conceptual starting point for detailed design. The concepts were generated using Figure 4.3, here referred to as the alternatives generation diagram. As can be seen from the diagram, candidate technologies/components were given for each functional block in the functional diagram (Figure 4.2). Note also that for several of the functional blocks, *direct connection* equivalents were given. This was done to provide for the possibility that some systems could function without the explicit use of one or more of the functions. The Active Fibre Matrix (AFM), an SMA embedded composite material [54], for instance, spans several functional blocks, since all these functions are integrated within the same system element. By selecting one of the alternatives provided for each functional block, while considering its compatibility with every other selected block, the entire structure of Figure 4.2 was populated, thereby generating concepts for a complete system.

An alternatives table(Table 4.1)shows several concepts generated in this manner. These were the system concepts that would be weighed up against each other in the pareto analysis.

4.3 Pareto Analysis

Following the generation of alternative system concepts, a quantitative selection method was needed to determine which of these concepts should be developed further. Pareto

TABLE 4.1: Alternatives table

	Energy Contoller		Energy Converter	Energy Conditioner		
Concept	Power amplifier	Output Element	Active material	Stage 1	Stage 2	Stage 3
AC 1	EP2 (switching)	EO1 (direct)	AM5 (SMA active fibre composite)			
AC 2	EP3 (direct)	EO1 (direct)	AM5 (SMA active fibre composite)			
AC 3	EP2 (switching)	EO1 (direct)	AM2 (Motor)	T1 (pump-hyd)	IS1 (linkage)	ES1
AC 4	EP3 (direct)	EO1 (direct)	AM2 (Motor)	T3 (Screw)	IS1 (linkage)	ES1
AC 5	EP2 (switching)	EO1 (direct)	AM3(Serie piezo)	T2 (hydraulic)	IS1 (linkage)	ES1
AC 6	EP2 (switching)	EO1 (direct)	AM3(Serie piezo)	T6 (stepper)	IS1 (linkage)	ES1
AC 7	EP2 (switching)	EO1 (direct)	AM4 (chemical)	T4 (pist-pnuem)	IS1 (linkage)	ES1
AC 8	EP3 (direct)	EO1 (direct)	AM4 (chemical)	T4 (pist-pnuem)	IS1 (linkage)	ES1
AC 9	EP2 (switching)	EO1 (direct)	AM4 (chemical)	T5 (fluid muscle)	IS1 (linkage)	ES1
AC 10	EP3 (direct)	EO1 (direct)	AM4 (chemical)	T5 (fluid muscle)	IS1 (linkage)	ES1
AC 11	EP2 (switching)	EO3 (resistor)	AM6(SMA coil)	T7 (Direct)	IS1 (linkage)	ES1
AC 12	EP3 (direct)	EO3 (resistor)	AM6(SMA coil)	T8 (Direct)		ES1
AC 13	EP2 (switching)	EO1 (direct)	AM8 (piezo-paral)	T2 (hydraulic)	IS1 (linkage)	ES1
AC 14	EP3 (direct)	EO1 (direct)	AM7 (SMA wire)	T7 (Direct)	IS1 (linkage)	ES1
AC 15	EP2 (switching)	EO1 (direct)	AM 8 (piezo-paral)	T6 (stepper)	IS1 (linkage)	ES1
AC 16	EP3 (direct)	EO3 (resistor)	EM 9 (SMA bend)	T8 (Direct)		ES1

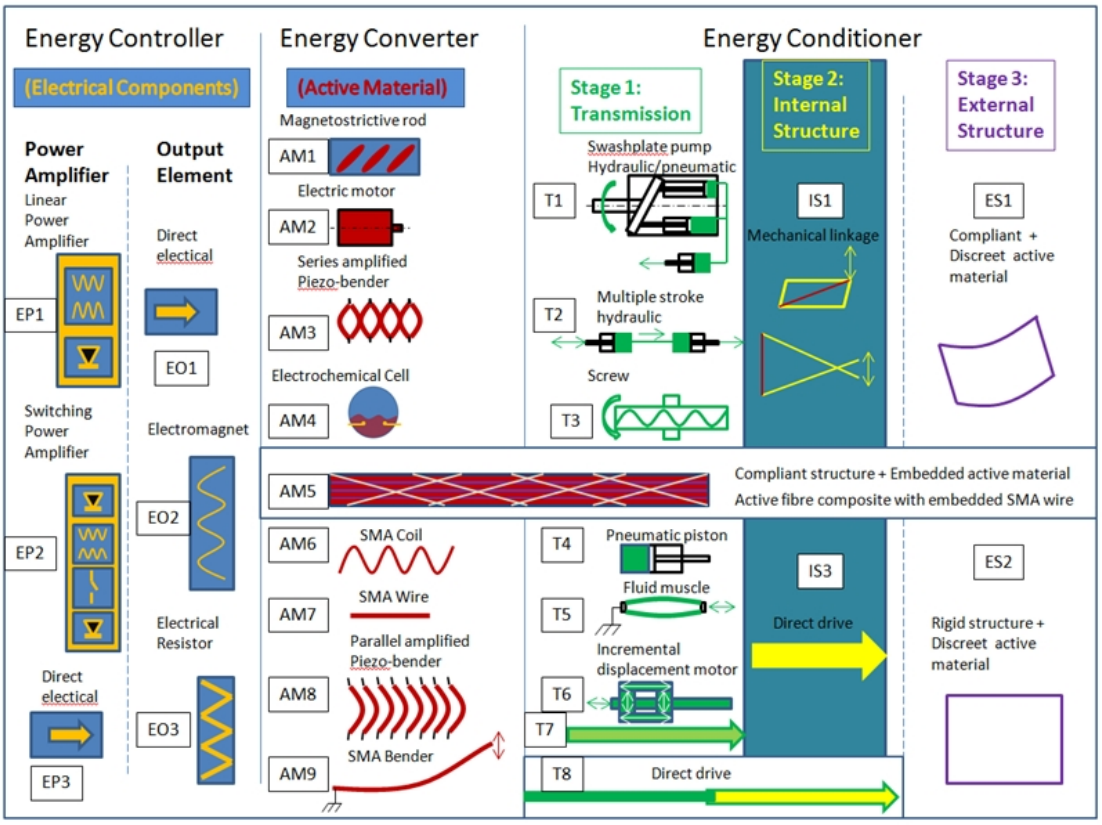

FIGURE 4.3: Alternatives generation diagram

analysis, a common high level selection tool used in system design, was judged an appropriate method for the current application. The first step in comparing alternatives through this method was to determine a scoring strategy which was based on the relative importance of a list of system characteristics.

Such a scoring strategy was developed for this project in collaboration with Airbus and can be defined by the following steps:

1. Determine the characteristics by which the suitability of the concepts would be judged.
2. Determine how marks would be allocated for each of the characteristics. This would mean a scale would have to be identified as well as details on how the score would be calculated.
3. Determine the relative importance of each characteristic by assigning an ***Importance Factor*** or ***IFc*** to it. The performance factor would be a fraction, with the IFc's of all the characteristics adding up to 1.
4. Determine the performance of each concept by calculating the ***Characteristic PerFormance Score's(CPFS's)*** in the manner that was prescribed in step 2.

5. Scale the CPFS's according to the relative importance of each performance characteristic by multiplying it with the IFc of each characteristic.
6. Add the different CPFS's to determine an overall pareto score for each concept.
7. Select the final concept based on the overall pareto scores.

By following the proposed process as discussed in subsections 4.3.1 to 4.3.4, the three best-scoring concepts were identified. All three of these concepts are SMA based, showing the overwhelming theoretical suitability of the technology for an application such as this.

4.3.1 Performance Characteristics

The following performance characteristics were determined to be important;

- Supply
- Mass
- Power Requirements
- Volume
- Maintenance
- Risk

Supply refers to the feasibility of sourcing the necessary subsystems. The commercial availability of the subsystems were considered, as well as the availability of academic information about such systems. The availability of academic information would become important if such a system were to be designed. The complexity of the system was also considered, as it would be an indicator of the relative ease with which the designed system could be assembled.

Mass, power requirements and volume are physical characteristics, which can be estimated for complete systems. It was assumed that no explanation was required regarding these characteristics.

Maintenance was considered to be important, due to the confined space within which the system would need to function. The system would very likely be hard to reach, and maintenance could prove difficult; therefore, low maintenance systems or those with low frequencies of maintenance would be preferred.

The risk score focussed on the probability that a system would break down to the extent that it could no longer sufficiently perform its function. Consideration was given to the reliability of technologies, with reliable systems being less likely to fail. Other considerations were based on the assumption that all engineering systems can fail; in such an event, it would be imperative that such a failure could be detected as well as mitigated. The detectability of failures and the possibility of mitigating them was, therefore, given high priority within the risk scoring.

4.3.2 Mark Allocation for CPFS's

For each of the determined characteristics a strategy was developed by which to allocate scores for it. The relevant strategies are communicated below through a short discussion in point form. Note that the maximum marks that could be achieved for any given characteristic was a value of 5.

Supply - The supply score quantified the availability and complexity of systems. Complexity countws for 3 marks and availability for 2. The mark allocation was based on component count, and scoring was done relative to the complexity of other systems. The system with the highest estimated part count received a score of 0 and the lowest part count a score of 3. A linear scaling between the part counts of these two systems provided the scores for every other system. The availability score was determined as follows: 2 marks were given to systems that could be bought off the shelf, 1.5 was given to systems that had to be custom made, but for which suppliers could be identified, a maximum of 1.2 was given to completely new systems. For the new systems, 1.2 was the score given to a technology for which abundant design resources were available. For systems with comparatively fewer available resources, the score was reduced. A score of zero was allocated to any subsystem for which the design was considered to be infeasibly complex.

Mass - The score for mass was calculated in relative terms, similar to what was already discussed for complexity. After mass estimates were calculated for each system, the heaviest concept received a score of 0 and the lightest a score of 5. The remaining systems received their scores based on a linear scaling between these two.

Power Requirements - The score for power requirements was also calculated relative to other systems. The full score of 5, in this case, was given to the system with the lowest power requirements, and the score of 0 to that with the highest. Power requirements were estimated using the efficiencies listed in Table 4.2. The power output of the system was assumed to be that which was calculated in Section 3.3; this power was then propagated backwards through the system by dividing it by the efficiency of each subsystem.

Volume - This scoring was done relative to the available space. A linear scaling was done between a volume of 0 m^3 and the goal volume which was determined in Section

TABLE 4.2: Efficiencies used in the calculation of power requirement estimates

Origin	Device	Efficiency
Huber et al. [9]	Piezo-electric	0.945
	Magnetostrictive	0.895
	SMA	0.015
	Hydraulic cylinder	0.94
Estimates based on reading	Ball-Screw	0.9
	Switching power supply	0.9
	Hydraulic pump	0.85
	Electric motor (small)	0.56
	Piston pump	0.91

3.3. A score of 5 corresponded to a zero volume, and a score of zero was given to a system that would occupy the entire allocated space. Volume estimates were based on the power and energy requirements of the system and the energy and power densities of each technology.

Maintenance - The maintenance score was split into two components. The first component, which counted for half of the overall marks, was the complexity of maintaining the system. A hypothetical maintenance procedure was given a score from 0 to 2.5, with 2.5 being given to a system that could easily be maintained from outside. This may seem farfetched, but a simple example would be greasing, or the changing of oil, which could potentially be done via piping. An active fibre matrix, on the other hand, would need to be replaced completely, since it forms an integral of the structure. This would then earn it a score of zero. The second component of the maintenance score was the maintenance frequency. A linear scaling was done from 0 and 2.5, with 1/1000 cycle maintenance frequency being allocated a zero mark. The 2.5 score was given to systems with maintenance frequencies of less than 1/100 0000 cycles. It must be noted that the estimated life-span requirement for the system was set at 50 000 cycles. A system with a 1/100 000 cycle maintenance frequency estimate would thus be very likely never to need maintenance during the commercial life-span of the aircraft. The maintenance estimates were based on intuition and documented sources such as maintenance manuals.

Risk - The risk score was based on the perceived risk of complete failure, the perceived likelihood of detecting such a failure and the relative ease with which mitigation strategies could be envisioned. The score contributions were: 1 for likelihood of failure, 1.7 for detectability and 2.3 for the possibility of mitigation.

4.3.3 IFc's used for CPFS scaling

The IFc's were determined in collaboration with Airbus, as a way of further quantifying their needs. The results of this process were as follows:

- Supply - 0.25
- Mass - 0.35
- Power Requirements - 0.15
- Volume - 0.1
- Maintenance - 0.09
- Risk - 0.06

These values together with those that were discussed throughout this section are summarised in Table 4.3, which should serve as an overview of the entire scoring strategy.

4.3.4 CPFS scoring and concept selection

By following the guidelines set out in Table 4.3, pareto scores were found for the complete system concepts. Details on these calculations are not provided here, as they were not believed to add value to this document. It should be noted, however, that the scoring was not only done at system level; instead, the scoring strategy was applied on subsystem level. This ensured a fairly detailed understanding of the relative performance of different concepts, and, hopefully, a good practical and theoretical basis for most of the scores.

The results of the scoring process can be seen in Figure 4.4. Note that only the highest-scoring concepts are shown, due to limited space. The stacked bar chart that was used provided a convenient way of comparing the overall scores of systems, as well as the performance of said systems in the different areas of interest. This provided a basis for further collaboration with Airbus to determine the best-suited system concept. The 3 best-scoring concepts were all SMA based. The fact that the material could be used in different ways and still remained one of the best-suited options, indicated that it was inherently very suited for applications such as the one for which it is currently considered.

One can clearly see that the power consumption of the SMA-based concepts is higher than for most of the other technologies, due to its low efficiency. This would probably make it unsuited to higher frequency applications, but was not considered to be a disqualifying trait in the current project. In all other performance characteristics the concepts seemed to be either on par with or superior to other concepts.

The supply scores were high, since it is a fairly widely studied technology and the material is available commercially in a variety of formats. It was also considered a low risk technology, since it has measurable material characteristics that can be used to detect a failure. Catastrophic failure was, however, considered unlikely. Rather

TABLE 4.3: tab:Pareto scoring strategy

Characteristic	Weight	Component	Scoring strategy	Max Value
Supply	0.25	Complexity	Component count normalised in terms of the system with the minimum count	3
		Availability	Standard systems = 2 Custom systems = 1.5 Novel systems = maximum 1.2 based on development risk	2
Mass	0.35	Subsystem wt's	Complete systems are scored,	5
Power consumption	0.15	Subsystem cons's	0 = least desirable and 5 = most desirable	5
Volume	0.1	Subsystem vol's	5-5*Volume/(rudder volume)	5
Maintenance	0.09	Complexity	Maintained system = 2.5 Maintenance free system = 5	5
Risk	0.06	Reliability	Risk of total breakdown is judged based on literature study (based on the individual actuators)	1
		Detection possibility	If possible ways of detecting this can be perceived	1.7
		Mitigation possibility	A good score will mean that mitigation strategies can be perceived	2.3

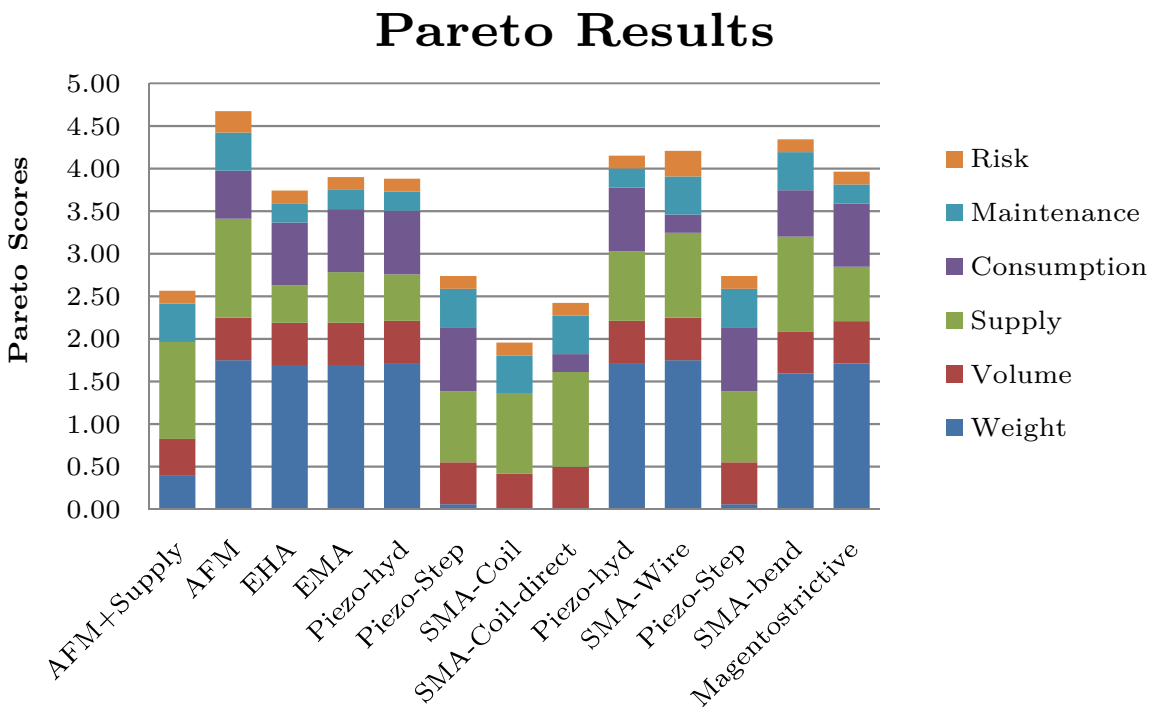

FIGURE 4.4: Pareto analysis results

than failure being of a catastrophic nature, failure of the material would most likely occur gradually or partially, with some actuation capability remaining even after damage occurred. The fact that the materials force capabilities are far larger than that which it would normally be used for, meant that even if some of the material completely lost its actuation capability, the remaining material would be capable of sustaining a higher level of performance for at least one more cycle. By doing so, the remaining material would, very literally, pick up the slack. There even existed the possibility that, by creative design, the system could be capable of re-annealing/reconditioning any damaged material in its installed state.

The maintenance score was good for SMA technology, since it is potentially maintenance free. This applied to both the active material, due to its solid-state nature, and the linkage that it would be connected to. By the use of appropriate hinging materials, lubrication or maintenance-free bushes, such a mechanism could be designed for a cycle-life that was sufficiently high.

The SMA-based concepts all had high scores for their mass. The main drivers behind their low mass estimates was their relative simplicity, the comparatively high stroke capability of the material and the high energy density of the SMA material itself.

It is interesting to note that no significant difference could be identified between the different concepts as far as volume was concerned. Since the scoring was done relative

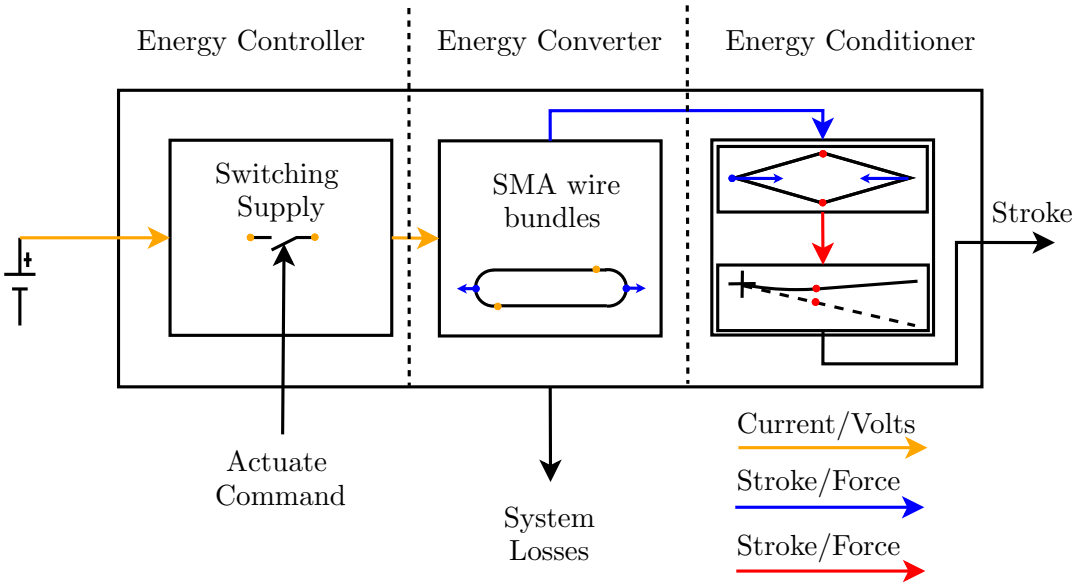

FIGURE 4.5: Conceptual view functional diagram

to the available volume, this meant that the available space was not as limiting as was initially thought. It did not, however, indicate whether or not the aspect of the available space could still prove restrictive.

4.4 Selection Results

The three SMA-based concepts were presented to Airbus for a final decision. In this process it was decided that for the active fibre matrix, the design risk was too high, since it is a fairly new application for SMA materials. Concern also existed over the possibility that SMA benders would not allow for the design of a system with a pre-defined failure state. Such a failure state is considered a crucial part of getting the aircraft safely grounded in the event of failure. The winning concept was thus the SMA wires, coupled to a mechanical linkage and driven by a switching power supply. The concept is illustrated diagrammatically in Figure 4.5.

Chapter 5

System Level Design

The leading concept for a trailing edge actuation system was one based on mechanical linkages that would be driven by SMA wires. The actuators would be self-contained, discrete units and would be distributed along the span of the trailing edge. It would also fit within the trailing edge boundaries. Figure 5.1 provides an overview of the actuators installed inside the trailing edge. A spring biassed actuator would be used, with the stiffness provided by the aircraft skin or some other discrete biassing element, for which the detailed design fell outside the scope of this project. The trailing edge skin would be compliant, with the lateral deflection being accommodated through the bending thereof rather than through a hinge.

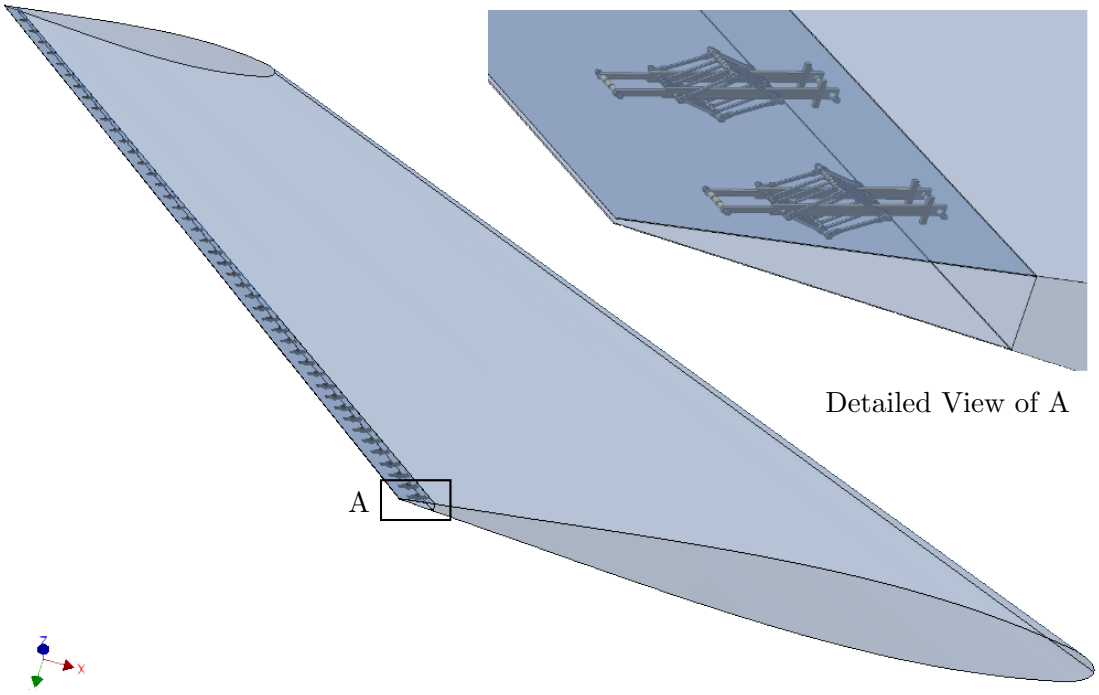

FIGURE 5.1: Illustration of the installed system

Preliminary specifications were derived for the system in Section 3.3, and was sufficiently detailed for the selection of the concept. This did not, however, provide a sufficient basis for the design of the necessary subsystems. This chapter deals with the derivation of a more complete set of requirements, and the architectural decisions that were needed for the subsystems to be designed.

The first specification that was determined was the *chord-wise placement* of the actuator, also know as the *line of action* or *attachment line*. Section 5.1 deals with the placing of the actuators. The actuator/skin combination was treated as a two-stage stroke amplifier, the first stage being the mechanical linkage and the second being a rigid plate. The rigid plate provides amplification by acting as a hinged lever, an assumption that underestimated the stroke amplification of the skin, the extent of which was estimated and compensated for as shown at the end of Section 5.1.

With the actuator placement known, more accurate stroke requirements were determined as discussed in Section 5.2. In order to do this, a detailed analysis of the trailing edge skin in its blunt form was conducted using Finite Element Analysis. In this iterative procedure, arbitrary forces are applied along the attachment line in a distributed manner. The forces are adjusted until the trailing edge reaches the desired lateral position. The trailing edge thickness that is achieved by doing so, together with the skin shape that goes along with it then allows for a detailed analysis of the skin in its deflected form. The actuator stroke that would produce this shape is then equal to the stroke requirement of the actuator.

The final unknown requirement was the aerodynamic component of the force that would act against the system. The derivation thereof is communicated in Section 5.3. The derivation was hampered by the lack of detailed structural information, the design of which was not included in the scope of the project. The need for structural information was circumvented by decoupling the aerodynamic and structural components of the force. To do so, the compliant portion of the trailing edge was treated as an infinite rectangular plate with evenly distributed loads applied to it. Such a plate deforms cylindrically, a state of deflection for which Kirchoffs plate equations can be solved analytically. The analytical expressions were then solved for two different load cases, the aerodynamic loading being one, and the actuator force being the other. By equating the two solutions, the structural terms of the equations were cancelled, and the actuator load requirement was found purely in terms of geometrical and aerodynamic descriptors. The final parts of Section 5.3 discusses the assumptions made in some more detail, and validates their use in the current context.

A final note on the system requirements found in this chapter is that they are of a generalised nature. They are not derived for a specific actuator within the system, but rather take on the form of normalised geometrical expressions or, in the case of the force

requirement, a distributed line load. They can then be used to find the requirements for a specific actuator by making use of a suitable discretisation strategy.

5.1 Actuator Placement

For the trailing edge thickening system to be designed, the stroke that it would need to achieve was required. The stroke was found in this section by treating the trailing edge and the skin deflection as individual stages in a two-stage stroke amplifier. This is shown in Figure 5.2, together with the associated parameters. With the stroke amplification goals set to 5 times for the mechanical linkage and 20 times for combined effect, this meant that the skin deflection would need to produce an amplification of 4 times for these goals to be reached. The placement for the actuator was then chosen in such a way that the angular deflection produced a displacement at the trailing edge that was estimated to be 4 times larger than the stroke that would be received from the actuator. An actuator placement of $x_{attach} = 1.25\%c$ was found to produce this amplification if the trailing edge was treated as a lever. This was then adjusted to a value of $1.5\%c$ by assuming that a compliant deflection would produce larger angular deflections, which, in turn, would produce amplifications approximately 20% larger than that of the rigid lever estimate.

The Amplification Factor (AF) is defined as the ratio between input and output stroke, such as is shown in Equation 5.1, and, as such, is basically the reciprocal of the mechanical advantage.

$$AF = (s_{out}/s_{in}) \tag{5.1}$$

Here s_{in} refers to the stroke into a mechanism and s_{out} to the stroke out of a mechanism.

By applying this definition to each output stage, and substituting the relevant parameters from Figure 5.2 into Equation 5.1, three amplifications factors could be identified. These were the mechanical linkage(Equation 5.2), the trailing edge skin(Equation 5.3) and the coupled amplification of the entire structure (Equation 5.4).

Four bar linkage(actuator):

$$\begin{aligned} s_{act,out} &= \Delta y_{act} \\ s_{act,in} &= \Delta x_{act} \\ AF_{act} &= \Delta y_{act}/\Delta x_{act} \end{aligned} \tag{5.2}$$

Skin:

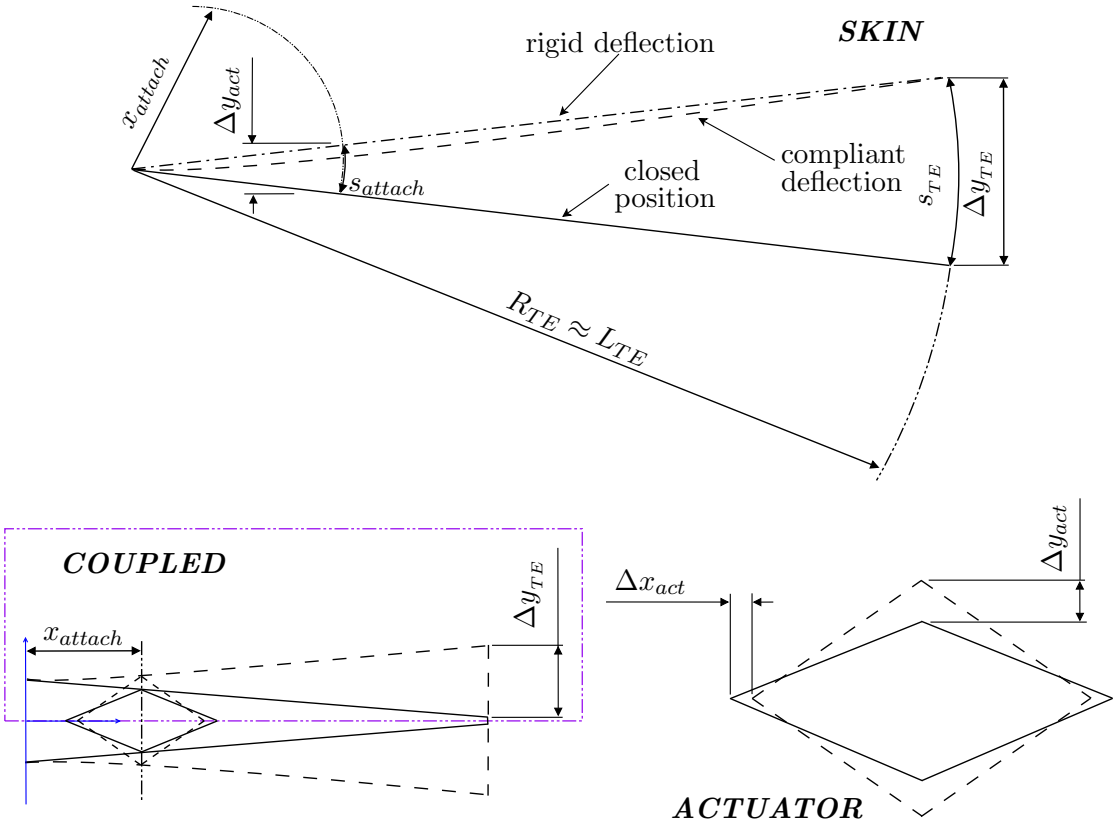

FIGURE 5.2: Rigid deflection simplification

$$\begin{aligned} s_{skin,out} &= \Delta y_{TE} \\ s_{skin,in} &= \Delta y_{act} \\ AF_{skin} &= \Delta y_{TE}/\Delta y_{act} \end{aligned} \tag{5.3}$$

Coupled:

$$\begin{aligned} s_{coup,out} &= \Delta y_{TE} \\ s_{coup,in} &= \Delta x_{act} \\ AF_{coup} &= \Delta y_{TE}/\Delta x_{act} \\ &= AF_{skin} * \Delta y_{act}/\Delta x_{act} \\ &= AF_{skin} * AF_{act} \end{aligned} \tag{5.4}$$

The AF of 5 was set for the actuator after some exploration of the design space. Larger amplification than this would not be feasible in the small physical space available. For the coupled mechanism the AF of 20 was selected, since this was the largest amplification

for which efficient actuators were considered possible [12]. The main factor affecting the efficiency at higher amplifications is the reduction in actuator stiffness. Given these values, the objective value for the skin was set to a value of 4 by rearranging Equation 5.4 as is shown in Equation 5.5.

$$AF_{skin} = AF_{coup}/AF_{act} = 20/5 = 4 \tag{5.5}$$

With the design objective determined, the actuator positioning could easily be found by using a small angle assumption. By this assumption the length of the arc (s_{TE}) followed by the end of the rigid plate during deflection was almost equal to its vertical deflection Δy_{TE}. Similarly, the arc travelled by the attachment point had a length (s_{attach}) nearly equal to Δy_{attach}. And since they circumscribed the same movement angle, they could be related to each other using the radii of their motions as follows:

$$\theta_{skin} = R_{attach}/s_{attach} = R_{TE}/s_{TE} \tag{5.6}$$

given that:

$$R_{attach} = x_{attach} \tag{5.7}$$

and R_{TE} is equal to the full chord-wise length of the trailing edge.

$$R_{TE} \approx L_{TE} = 0.05 * c \tag{5.8}$$

thus:

$$x_{attach}/\Delta y_{act} = 0.05 * c/\Delta y_{TE} \tag{5.9}$$

and remembering that $\Delta y_{TE}/\Delta y_{act} = AF_{skin}$ and $AF_{skin} = 4$:

$$x_{attach} = 0.05 * c/4 = 0.0125 * c \tag{5.10}$$

This meant that according to the assumptions made, the actuator would need to be placed 1.25%c away from the trailing edge's starting point. This value was adjusted to 1.5%c to compensate for an estimated 20% error in the calculated Δy_{TE}. The source of error was the fact that a compliant deflection of the plate, rather than the assumed rigid deflection, would result in a comparatively higher amplification of the stroke, due

to the additional angular deflection produced by its curvature. A more detailed study of the compliant deflection is discussed in Section 5.2.

5.2 Stroke Requirements

The actuation system being designed for the thickening of the trailing edge was placed using a rough estimate of the stroke amplification provided by the angular deflection thereof. While the assumptions made to do this were sufficient for high level decision making and estimation, it did not prove sufficient for determining the exact actuator displacement values which would be needed(Δy_{act}).

A more accurate estimate of this stroke requirement was found by finding a higher fidelity geometrical description of the deflected shape. The deflected shape was found through a non-linear Finite Element Analysis (FEA) of the trailing edge skin. In this analysis, hypothetical actuator forces were distributed along the $x_{attach} = 1.5\%c$ line of action. The forces were then adjusted iteratively until the trailing edge deflection was such that it produced the desired trailing edge deflection. With the trailing edge in position, the position of the attachment line, relative to its original position, gave the stroke that the actuator would need to produce. Since the detailed design of the trailing edge skin was not available, the FEA was based on an arbitrary thin plate (1 mm thick) of homogeneous elastic material(aluminium in this case). This produced the required shape in geometrical terms, but no information could be gained from the forces that were used to produce the deflection.

The different regions and dimensions in a cross-section of the system are shown in Figure 5.3. Downstream from this, i.e. further to the right on the figure, resides the *rigid region*, this is the region that experiences no bending, but rotates due to the bending in the compliant region. The parameters relevant to this section are the required actuator stroke Δy_{act} and the difference in lateral position of the trailing edge between its *thickened* and *un-thickened* forms Δy_{TE}.

Of the variables shown in the figure, x_{attach} and Δy_{TE} are already known (1.5%c and 0.957%c respectively). The first was found in Section 5.1, and the second was found by comparing the $2\%c$ thickened and $0.0862\%c$ un-thickened trailing edge thickness's.

The process followed to determine this shape is henceforth referred to as *shape prediction*. This is based on the observation that two thin plates of elastic material will deform in a geometrically equivalent manner if the placement of loads are geometrically equivalent. Thus, if the trailing edge was modelled using an arbitrary, thin elastic material, and could be deflected to the desired position by a geometrically equivalent load (i.e. applied at $x_{TE,att} = 1.5\%$), the resulting bent shape would be the bent shape we require. In reality, a plate of specific thickness and material would require a different force than

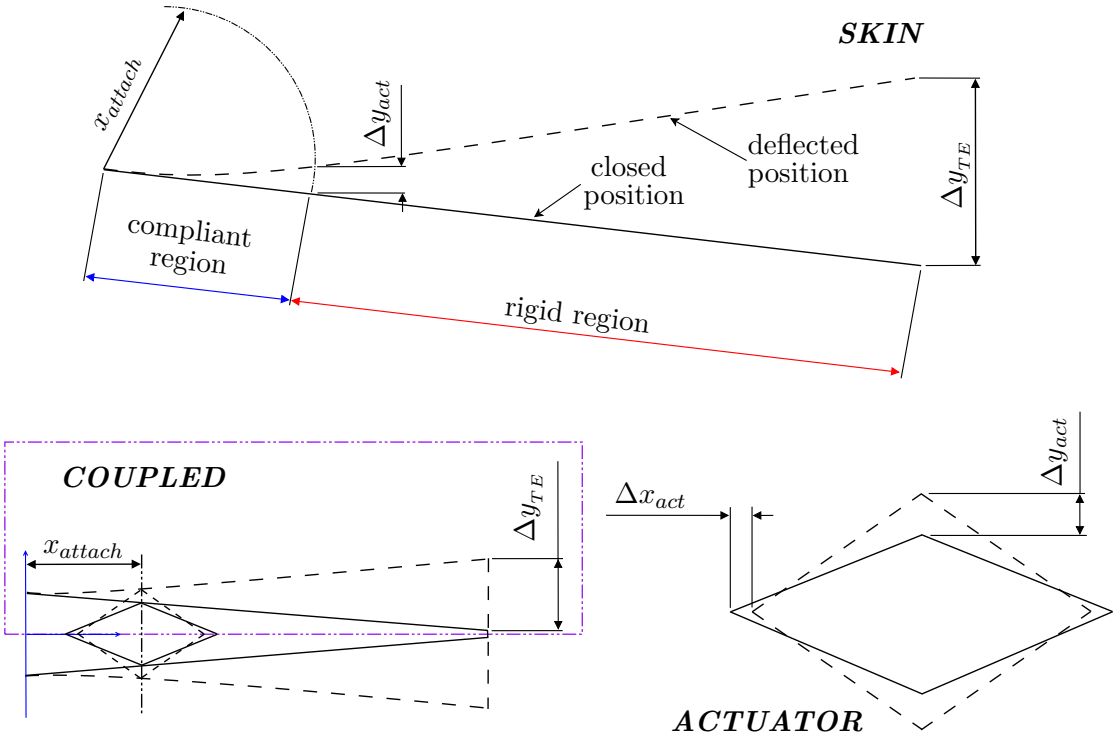

FIGURE 5.3: Definitions, compliant and rigid regions

the arbitrarily selected plate. The mid-plane of the two plates in their deflected shape would, however, have the same geometry.

To explain this further, see the mid-plane displacement of a centrally loaded beam shown in Figure 5.4:

$$v(x) = \frac{F}{EI}\left(\frac{lx^2}{2} - \frac{x^3}{6}\right) \quad for \quad 0 \leq x \leq l \tag{5.11}$$

$$v(x) = \frac{F}{EI}\left(\frac{l^3}{3} + xlL - \frac{x^2 l}{2} - xl^2 + \frac{x^2 L}{2}\right) \quad for \quad l \leq x \leq L \tag{5.12}$$

One can see that most of the equation is purely geometrical and that the loading and stiffness (F/EI) has a scaling effect. It would thus be possible to achieve the exact same shape for a beam of different size/material by altering the amplitude of load. A similar geometrical equivalence in mid-plane geometry is currently being exploited.

Whereas the beam deflection could be described by simple analytical equations, this was not the case for the aircraft skin, the loading/geometry of which deviated from most of the known analytical solutions to the plate equations. This provided the motivation for using FEA to find the deflected shape. The model, boundary conditions, analysis and results used for this production are discussed next.

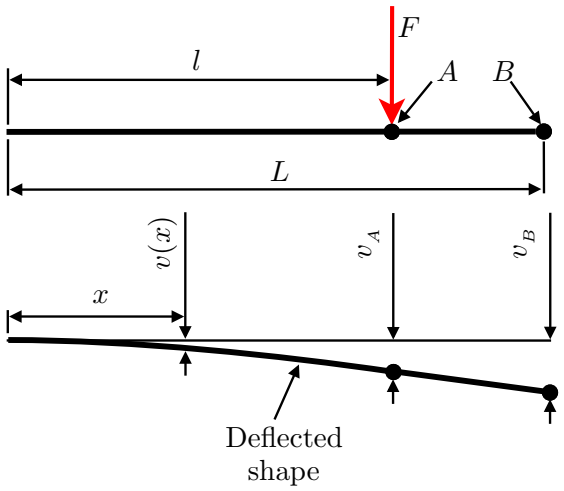

FIGURE 5.4: Deflected shape of a loaded beam

The model

The un-deflected shape of the trailing edge was recreated using measurements taken directly from a CAD model of the vertical tail wing. This CAD model is shown in Figure 5.5. Also indicated on the model, is the portion thereof that represents the tail wing itself, as well as the rudder and the trailing edge. The trailing edge was the plate that was analysed. The mesh used on the plate is shown in Figure 5.6.

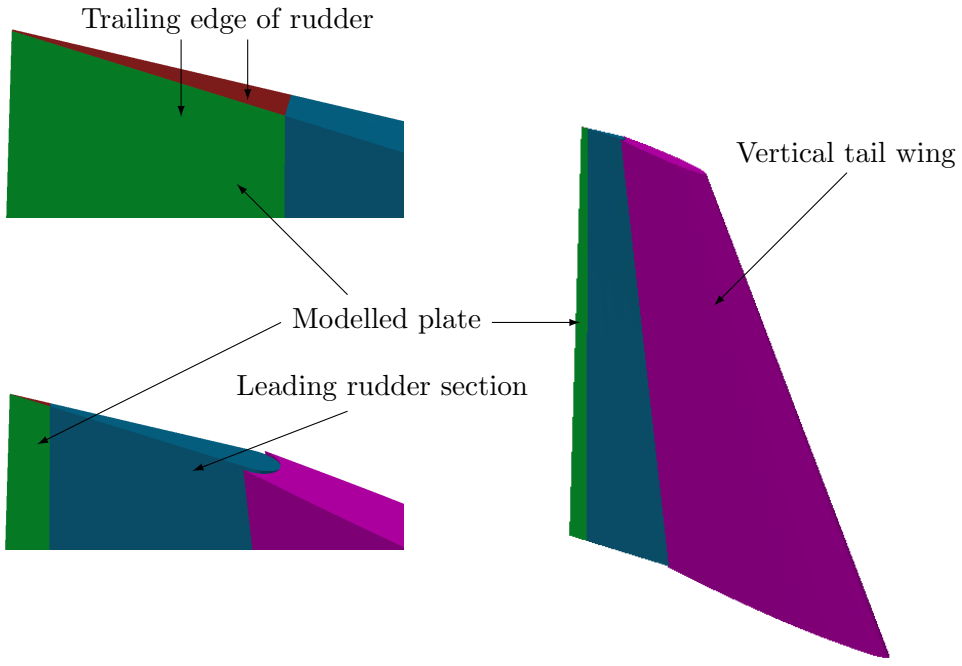

FIGURE 5.5: Vertical tail CAD model showing TE plates

The trailing edge is meshed with eight-node shell elements as shown in Figure 5.6. This, after some initial studies, showed that a fairly coarse mesh of quadratic elements was sufficient. In the mentioned study, different mesh sizes of both linear and quadratic

elements were compared, and the quadratic elements were found to capture the deflected geometry better with a reasonably coarse mesh.

The thickness of the elements was 1 mm, with generic aluminium properties used for the material $E_{alu} = 79\ GPa$ and $\nu_{alu} = 0.33$. In three span-wise positions(top, middle and bottom) nodes were constrained to lie on a plane parallel to the chord-line. This simplified the capturing of data related to the geometry of the deflection.

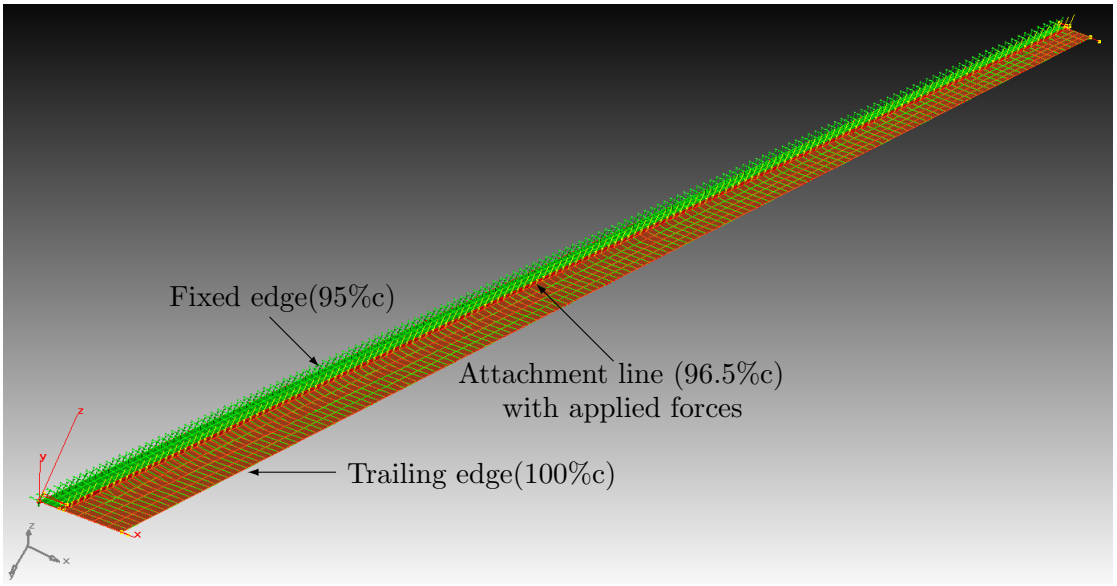

FIGURE 5.6: Full view of shape prediction FEA model

Boundary conditions

A more detailed view is shown in Figure 5.7; here the forces and constraints can be seen. All the nodes along the leading edge are fully constrained, while forces are applied in a distributed manner. As was discussed in Section 5.1 the normalised position for force application is at 96.5 % of the chord length(measured from the leading edge of the vertical tail-plane). Since the trailing edge is considered to be the trailing 5 % of the rudder, this meant that the forces had to be offset 1.5%c from the fixed edge. A total of 157 forces were applied along this line and arbitrarily initiated at force values of 50 N.

Analysis

A non-linear analysis needed to be used, due to the large displacement; therefore, the Nastran based sol400 solution algorithm was applied, with large deflection and follower forces enabled. These options forced the solution to be implemented incrementally, with the position of the force being updated to avoid geometrical errors in load placement. The solution was set up in this manner so that the angles of the forces remained constant relative to the global coordinate system, rather than local coordinate systems at which

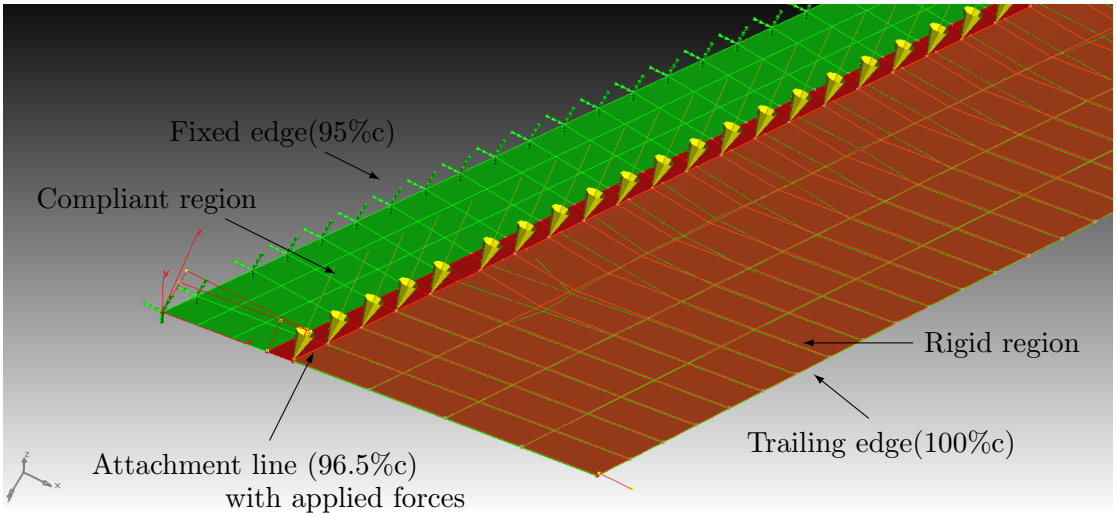

FIGURE 5.7: Close up view of trailing edge of FEA model

they were applied. This approached the behaviour of a real actuator more closely. Another source of non-linearity in large deflection problems, the skin-effect was not considered a problem. This was due to the cantilevered nature of the plate, as well as the fact that the starting and end positions were symmetrically distributed either side of a plane perpendicular to the loads.

Since the initial geometry was known, as well as the lateral position of the thickened trailing edge ($(y_{TE})_{req}$), the distance of the trailing edge from this required position after each iteration was considered to be an error. Externally to the Nastran solution procedure, another iteration scheme was followed to adjust the force in such a way that this error in deflection of the trailing edge approached zero. Once this error was sufficiently small, the thickened geometry of the trailing edge would be known.

Equation 5.13 shows the error definition used.

$$(E_{\Delta y_{TE},i})_k = \frac{[\Delta(y_{TE,i})_k - (\Delta y_{TE,i})_{req}]}{(\Delta y_{TE,i})_{req}} \tag{5.13}$$

with i being the forces 1 to 157 and k being the number of the current iteration.

The force update was done as follows:

$(F_i)_{k+1} = F_{k,i} + F_{k,i} * E_{w,TE}$

While this is a crude search algorithm, convergence is fairly quick (15 iterations). At the end, the maximum error at any node was below 0.5 %, which is considered sufficiently small.

Results

The normalised displacements for the top, middle and bottom node-sets are given in Figure 5.8.

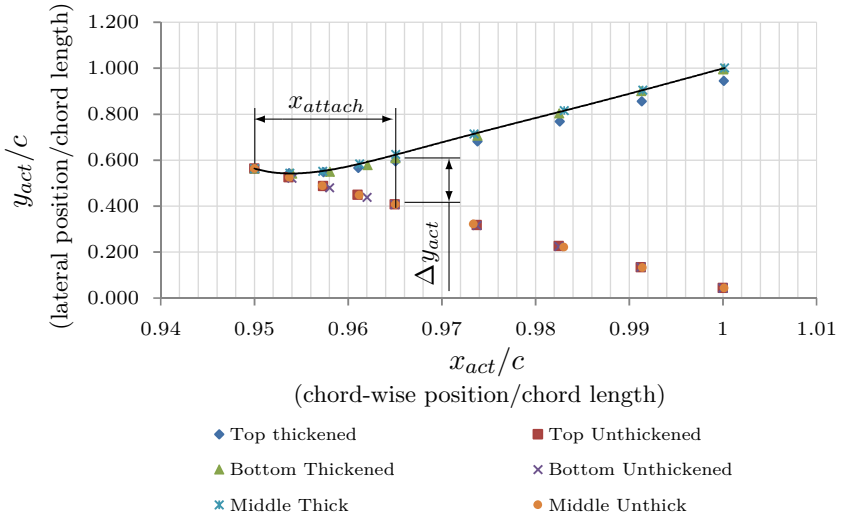

FIGURE 5.8: Shape prediction results

This normalised curve provided the basis for further design, since from it the stroke requirement of the actuator Δy_{act} could be determined. The normalised shape of the middle node-set had the smallest trailing edge deflection error($E_{\Delta y_{TE}} = 0.001\%$). This was thus the preferred normalised curve for use in further predictions. Based on this, the actuator would need to provide a stroke of:

$$\Delta y_{act} = 0.2176\%c \tag{5.14}$$

5.3 Equivalent Aerodynamic Force

In this section the force acting on the trailing edge actuation system is analysed. It was found that two forces act upon the actuation system, namely the aerodynamic and structural components thereof. With the structural component, as well as the structural design unknown, fluid-structure interactions could not be studied. This presented a need for a decoupling of the two force components, so that the aerodynamic component of

the force could be known, while postponing the structural stiffness selection to a more convenient design phase.

The two force components can be seen in Figure 5.9. The force would consist of a structural force which would bias the SMA material, as well as an aerodynamic component that could be either positive or negative. This is indicated in equation form below(Equation 5.15).

$$F_{act} = F_{struct} + F_{aero,eq} \tag{5.15}$$

With:

F_{act} - The full actuator force
F_{struct} - The structural component of the force acting on the actuator
$F_{aero,eq}$ - A concentrated, equivalent representation of the aerodynamic force

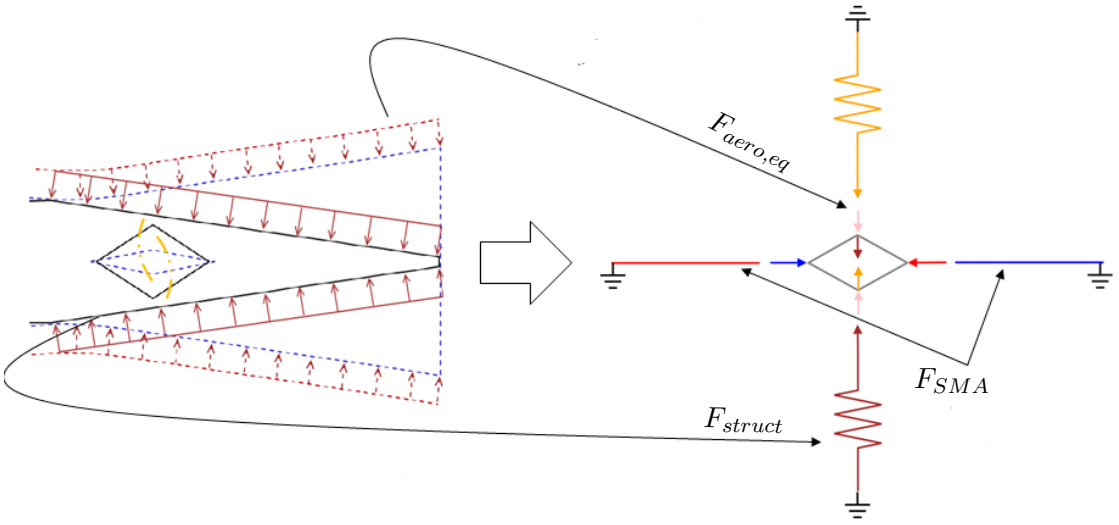

FIGURE 5.9: Equivalent mechanical model

This decoupling procedure is communicated in the remainder of this section, but can be summarised as follows:

1. Split the trailing edge into its rigid (non-bending) and compliant (bending) regions.
2. Convert the pressure acting on the rigid region into boundary conditions acting on the compliant region.

3. Assume that the compliant region can be treated as an infinite rectangular plate with constant load distribution, and that the resulting displacement would thus be cylindrical in nature (discussed in Section 5.4).

4. Integrate the plate equations, given the assumptions and the defined boundary conditions (edge force, edge moment and surface pressure applied). The resulting expression being the *general load displacement expression.*

5. Integrate the plate equations again, this time for the application of a distributed force $f_{aero,eq}$ only. The resulting expression being the *edge load displacement expressions.*

6. Assume that a distributed edge load that could produce the same edge displacement as the full aerodynamic loading is equivalent to the full load (equate general load displacement and edge load displacement expressions)

7. Solve for $f_{aero,eq}$, and consider this to be the edge load that would yield $F_{aero,eq}$ through the application of a suitable discretisation strategy.

By this project phase the rigid and compliant regions have already been defined. This discussion thus starts at point two in the process discussed above, which is to convert the pressure acting on the rigid region into boundary conditions for the compliant region integration. This translation of load is illustrated in Figure 5.10. The pressure was calculated using Equation 5.16, and Equations 5.17 and 5.18 indicated the resulting boundary conditions. The derivation of these expressions was fairly straight forward, and will not be considered in more detail.

$$p = C_p * \rho V_{air}^2/2 \tag{5.16}$$

$$f_{L_{CR}} = p * L_{RR} \tag{5.17}$$

$$m_{L_{CR}} = (1/2)p * L_{RR}^2 \tag{5.18}$$

The variables used are as follows:

p - The evenly distributed pressure acting on the trailing edge skin.
C_p - The pressure coefficient of the flow over the trailing edge.
ρ - The density of air.
V_{air}^2 - The air speed of the aircraft.
L_{RR} - The length of the *Rigid Region (RR)*, assumed to be close to an ideal rectangular shape.

L_{CR} - The length of a *Compliant Region (CR)*, assumed to be close to an ideal rectangular shape.
f_L - The distributed force on the CR/RR interface due to the presence of aerodynamic pressure on the rigid region.
m_L - The distributed moment on the CR/RR interface due to the presence of aerodynamic pressure on the rigid region.

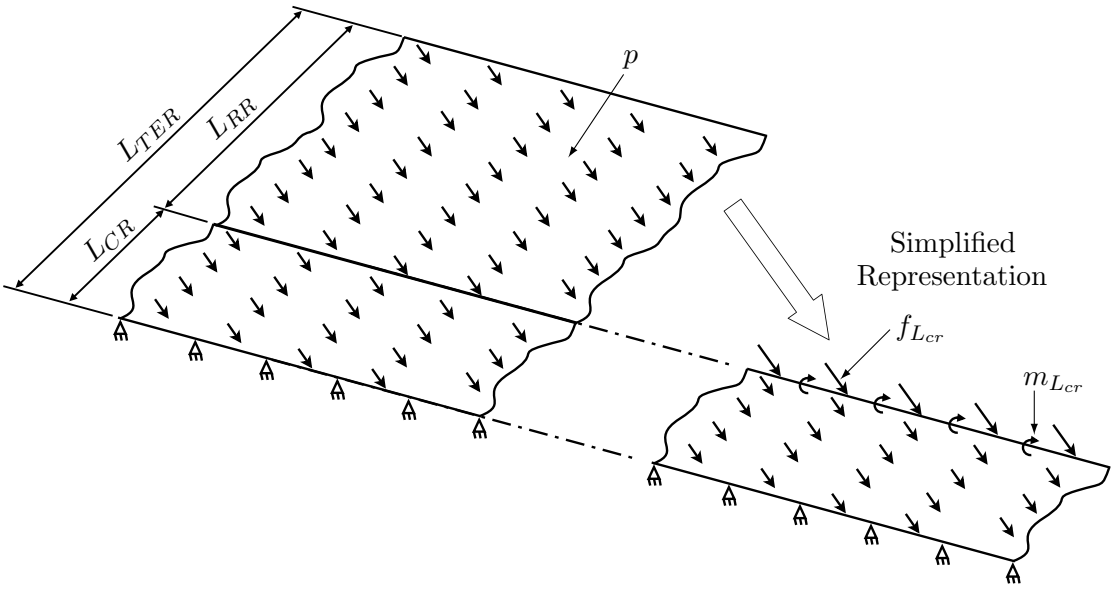

FIGURE 5.10: Simplified TE aerodynamic loading

With the boundary conditions defined, the rectangular plate and cylindrical bending assumptions were to be applied, in order to reduce the full plate equations(Equations 5.19 and 5.20) [55] into a more manageable form.

$$M_x = -D\left(\frac{\partial^2 w}{\partial x^2} + \nu\frac{\partial^2 w}{\partial y^2}\right)$$
$$M_y = -D\left(\frac{\partial^2 w}{\partial y^2} + \nu\frac{\partial^2 w}{\partial x^2}\right) \tag{5.19}$$

$$D = \frac{Eh^3}{12(1-\nu^2)} \tag{5.20}$$

ν - Poisson's ratio
w - Lateral displacement
h - Plate thickness
E - Modulus of elasticity
D - Flexural rigidity

Under the mentioned assumptions, this reduced to the cylindrical bending expressions (Equations 5.21 and 5.22), which could be solved analytically for several different boundary conditions, including those discussed earlier.

$$M_y = -D * \left(\frac{\partial^2 w}{\partial y^2}\right) \tag{5.21}$$

$$M_x = -D * \left(\nu \frac{\partial^2 w}{\partial y^2}\right) = \nu M_y \tag{5.22}$$

The problem to be integrated was that of a surface pressure acting directly on the compliant region (Figure 5.11). The bending of such a plate (a rectangular plate under uniform pressure loading) can expressed by the modified version of Equation 5.21 shown in Equation 5.23.

$$\partial^4 w(y)/\partial y^4 = p/D \tag{5.23}$$

Since cylindrical bending means that w does not vary in x, the partial derivative equation can be replaced by the normal derivative given in Equation 5.24, which, given suitable boundary conditions, can be solved with normal integration procedures.

$$d^4 w(y)/dy^4 = p/D \tag{5.24}$$

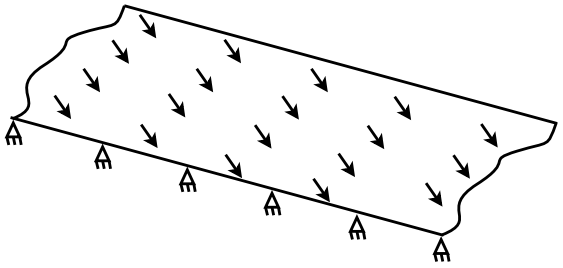

FIGURE 5.11: Infinite rectangular plate with pressure loading

The boundary conditions used were as follows:

- Fully constrained on the leading edge of the compliant region.
- A distributed force acting on the CR/RR interface.
- A distributed moment acting on the CR/RR interface.

Full constraint of the leading edge of the compliant region meant that displacement $w(y)$ and rotation $dw(y)/dy$ was zero at this edge. This is expressed mathematically in Equations 5.25 and 5.26.

$$w(0) = 0 \tag{5.25}$$

$$dw(0)/dy = 0 \tag{5.26}$$

The free edge was exposed to a distributed force and moment as already mentioned. Such a distributed force, shown in an isolated form in Figure 5.12, could be related to the third derivative of the displacement (Equation 5.27).

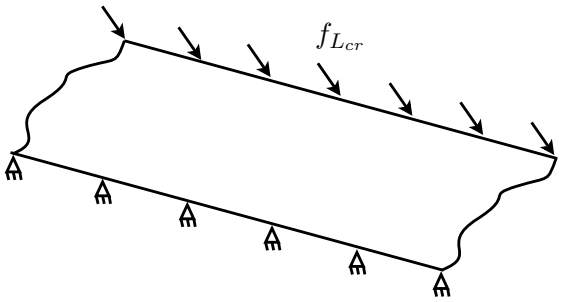

FIGURE 5.12: Infinite rectangular plate with distributed force end loading

$$d^3w(L_{cr})/dy^3 = f_{L_{cr}}/-D \tag{5.27}$$

The edge moment, on the other hand, could be related to the second derivative as shown in Equation 5.28. Figure 5.13 shows this moment graphically.

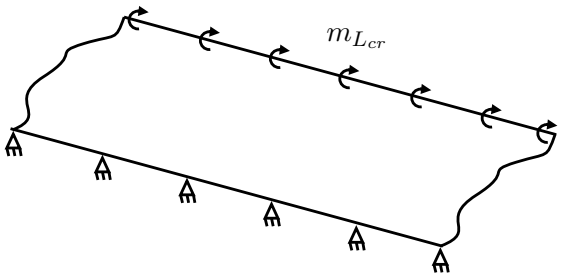

FIGURE 5.13: Infinite rectangular plate with distributed moment end loading

$$d^2w(L_{cr})/dy^2 = m_{L_{cr}}/-D \tag{5.28}$$

Integration of the original fourth derivative yielded a fourth order polynomial with three unknown coefficients. By substituting the boundary conditions, the coefficients could be found. Equation 5.29 shows the resulting *general load displacement expression.*

$$w(L_{cr}) = (1/D)(f_{L_{cr}} * L_{cr}^3/3 - m_{L_{cr}} * L_{cr}^2/2 + p * L_{cr}^4/8) \tag{5.29}$$

This edge displacement was to be equated to that of an unknown equivalent line load $f_{aero,eq}$. The needed expression, the *edge load displacement expression*, was found by integrating Equation 5.24 once again. This time the boundary conditions included only the fixed edge and distributed force boundary conditions. The fixed boundary conditions were given in Equations 5.25 and 5.26, and the edge load boundary condition would be similar to Equation 5.27, this time with $f_{L_{cr}}$ being replaced by $f_{aero,eq}$. The results of this integration can be seen in Equation 5.30.

$$w(L_{cr})_{f_{aero,eq}} = (1/D) * (f_{aero,eq} * L_{cr}^3/3) \tag{5.30}$$

Since $w(L_{cr}) = w(L_{cr})_{f_{aero,eq}}$ if f_{aero} is indeed equivalent to the complete load case, Equations 5.29 and 5.30 could be equated to each other. The structural characteristic, D, could then be cancelled. Solving then for $f_{aero,eq}$ led to an expression (Equation 5.31) that did not contain any structural terms. And, as such, effectively decoupled the aerodynamic and structural components of the actuator force requirement as was desired. This estimate for the aerodynamic component of the force seen by the actuator was also an analytical expression, which would simplify later discretisation of the design space.

$$f_{aero,eq} = (3/L_{cr}^3)(f_{L_{cr}} * L_{cr}^3/3 - m_{L_{cr}} * L_{cr}^2/2 + p * L_{cr}^4/8) \tag{5.31}$$

5.4 Validity of Simplifying Assumptions

The process discussed in Section 5.3 required certain simplifying assumptions to be made. The assumed scenario was not strictly accurate in the design problem at hand, but was considered reasonable, as is discussed in this section. What was assumed was that the plate was rectangular and could be considered to be infinitely long. The load acting on this plate was also considered to be evenly distributed, a load case which would result in cylindrical bending. The validity of these assumptions was then considered. The infinite rectangular plate assumption was shown to be valid (see Section 5.4.1). The validity was based on its 195:1 aspect ratio as well as a mathematical test that was used to assess the taper of elements in finite element models. The test showed that the taper between the edges of the compliant region was negligible, a statement that was strongly

supported by the small angle that exists between these edges (0.353°). The cylindrical bending assumption was proven valid (see Section 5.4.2) by considering the nature of the deflection seen in Section 5.2. The minimum principle curvature of the deflected plate was zero, a condition that is associated with cylindrical bending. In addition to this, the minimum principle curvature is orientated parallel to the edges of the compliant region, while the maximum principle curvature is perpendicular to it and both of these were constant. This further proved the cylindrical nature of the deflection, and also showed that the axis of the "cylinder" is parallel to the edges of the compliant region.

5.4.1 Rectangular plate assumption:

For the proof that the compliant region of the trailing edge could be considered to be rectangular, the nature of a rectangle was considered. A rectangle has parallel sides and 90°angles between these sides. For rectangles of infinite length, however, the effect of the corner angles becomes irrelevant and the requirement is reduced to only that of parallelism on the infinitely long sides. The comparatively large aspect ratio of the compliant region (approximately 195:1) meant that it could be treated as just such an infinitely long plate. The 90°corner requirement was thus ignored, and only the angle between the two edges considered. This angle was calculated to be 0.353°, which seems very small, but acceptably so. It was not, however, considered sufficient proof, since what an "acceptable" value would be was unknown. Also, no geometric check could be found for assessing the "rectangularity" or parallelism in any case similar to this. There are, however, mathematical checks for element quality in finite element models. One such criterium that considers the taper of edges was explained by Gokhale [56]. According to this source, a quadrilateral is to be divided into four distinct triangles using the diagonals thereof. The suggested triangles are shown in Figure 5.14.

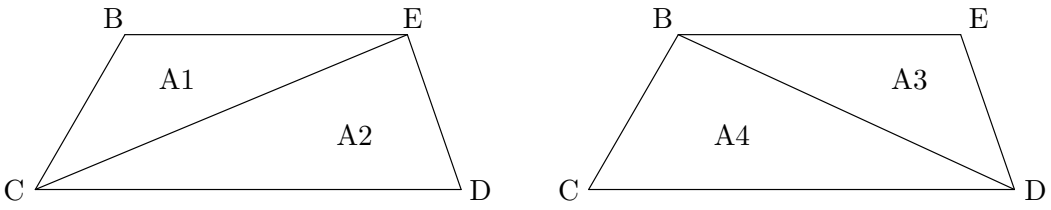

FIGURE 5.14: Triangle definitions for taper test

The taper is then calculated, using the areas of these triangles as is shown in Equations 5.32 and 5.33:

$$Taper = \sum \left| A_i - A_{avg} \right| / A_{avg} \tag{5.32}$$

$$A_{avg} = \sum |A_i| / 4 \tag{5.33}$$

The requirements set on this taper value was that it be smaller than 0.5, or ideally 0 for a quadrilateral with no taper at all. This criterium is expressed in Equation 5.34.

$$\begin{aligned} &Taper\ Requirement: \\ &Taper < 0.5 \end{aligned} \tag{5.34}$$

The compliant region on which this test needed to be conducted is shown in Figure 5.15 as a part of the trailing edge. Note that in this figure, the aspect ratio had to be reduced in order to view the rudder in the confined space of the page. This reduction in aspect ratio distorted the view in a way that made it seem less rectangular. To illustrate this, four reference points are indicated in blue on the figure and repeated in Figure 5.15 with a realistic aspect ratio. Note that no definitive deviation from parallel could be distinguished between these two lines. The triangles used in the taper test, with reference to the points marked in Figure 5.15, are as follows:

- $A_1 = A_{BCE}$
- $A_2 = A_{CDE}$
- $A_3 = A_{BCD}$
- $A_4 = A_{BDE}$

By applying Equations 5.32 and 5.33 to these areas, no deviation from zero could be identified for the value of $Taper$. This suggested that the two edges of the compliant region were indeed, for all intents and purposes, parallel. This, in turn, validated the rectangular plate assumption, and justified its use in the preceding prediction.

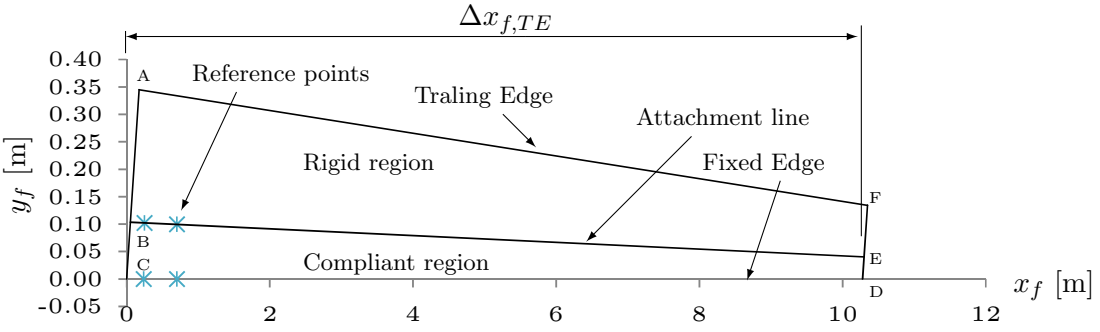

FIGURE 5.15: Global to flat plate axis rotations

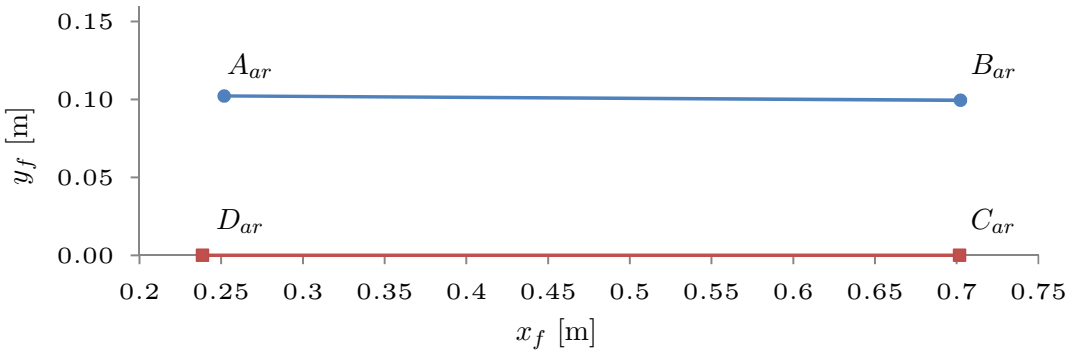

FIGURE 5.16: Enlarged view of a portion of the compliant region, with realistic aspect ratio

5.4.2 Cylindrical bending assumption

One of the assumptions on which requirement estimation was based was the existence of cylindrical bending. This type of bending is discussed in the current section and compared to the deflection that was seen in the shape prediction results (Section 5.2).

Cylindrical bending is the state of deflection that is expected when a short and wide beam is subjected to an evenly distributed load; a condition shown in Figure 5.17 (considering).

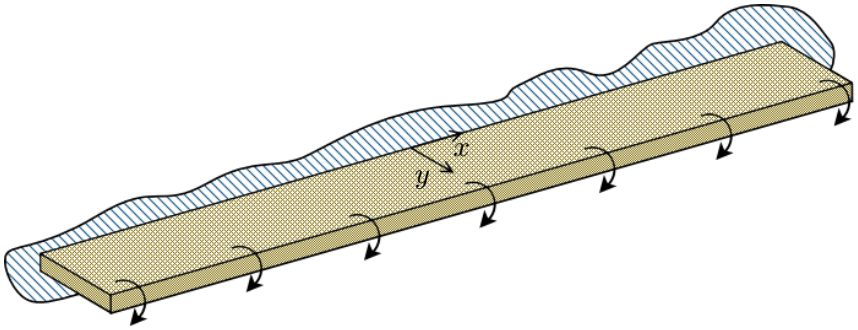

FIGURE 5.17: Short wide beam under constant distributed edge loading

Mathematically, a state of cylindrical bending is characterised by a deflected state for which the twist is zero as is shown in Equation 5.35:

$$\frac{\partial}{\partial y}\left(\frac{\partial w}{\partial x}\right) = 0 \tag{5.35}$$

Furthermore, the minimum principle curvature (shown in Equation 5.36) is zero. This indicates that there is a direction in which this the radius of curvature is zero.

$$\frac{\partial^2 w}{\partial x^2} = 0 \tag{5.36}$$

To avoid multiple analyses, the zero twist can also be found from the minimum principle curvature by showing that its direction does not change throughout the plate, and that this direction is parallel to the edges of the plate.

To confirm that these requirements were met in the displacement field of the compliant region, the results of the shape prediction in Section 5.2 were revisited. Figure 5.18 shows a close-up view of a part of the compliant region in the shape prediction model with the minimum principle curvature plotted. From this figure it can be seen that the minimum principle strain is consistently zero or very close to it, and that it remains consistently parallel to the fixed edge of the plate. This confirmed that the cylindrical deflection assumption was indeed reasonable.

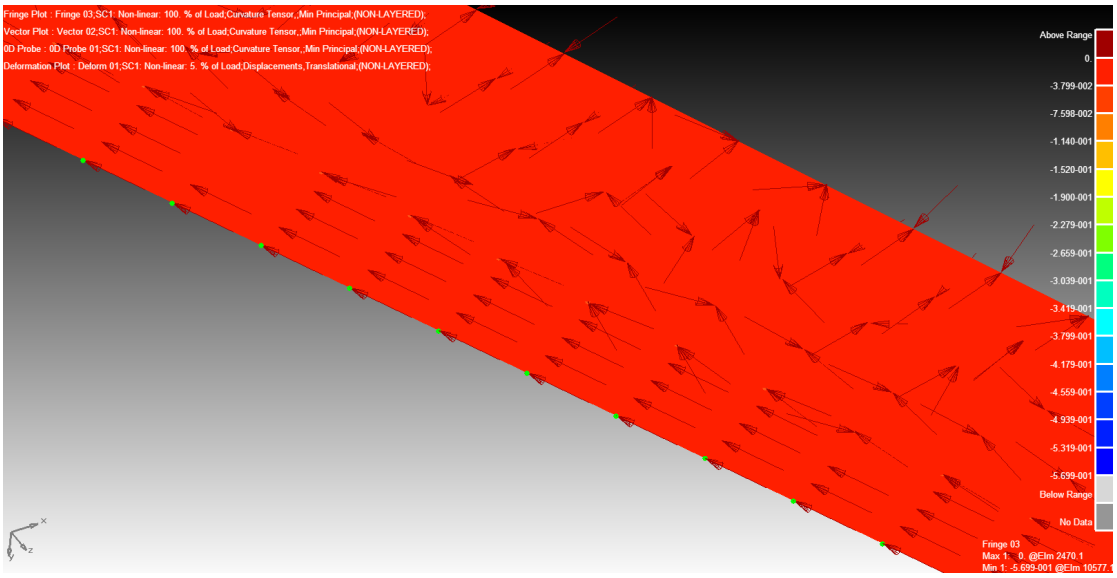

FIGURE 5.18: Minimum principle curvature, fringe and direction vector

One last comment on the results is to ignore the random direction vectors in the rigid region. These direction vectors are meaningless, since this plate region is not actually bent as seen by the zero value for maximum principle curvature in Figure 5.19.

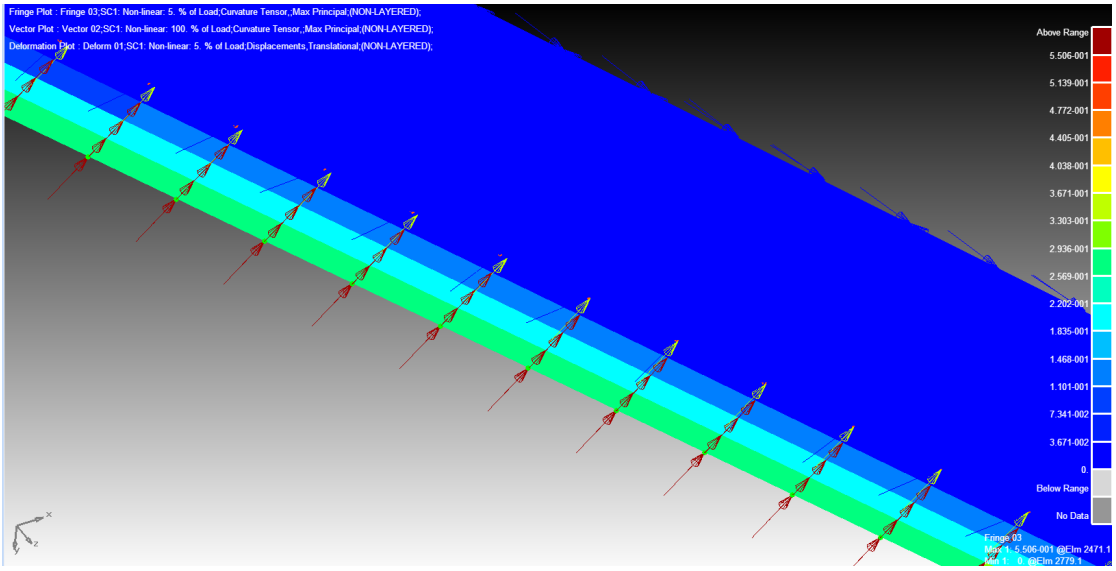

FIGURE 5.19: Maximum principle curvature, fringe and direction vector

Chapter 6

Actuator Design

This project dealt with the design of an actuation system that would allow for a change in the shape of the trailing edge of an aircraft rudder. The shape change would be from a blunt to a sharp edge and vice versa. The proposed system would make use of distributed actuators, each consisting of an SMA driven mechanical linkage that formed a self-contained unit. For the proposed system concept to be considered feasible, it needed to be shown that its fundamental element, the actuator, could be built and operated. The operation would also need to meet the requirements set for it, or it had to be evident that they could be met after further iterations of the project. This chapter discusses the detailing of the prototype actuator through which this feasibility could be assessed. An overview of the resulting actuator is given in Section 6.1

In Chapter 5, a high level design of the system was conducted. In this design, the detailed stroke and force requirements of the system were found, as well as the placement of the system within the trailing edge. The exact distribution of actuators was not specified, and the requirements were presented in the form of generalised expressions. These expressions could be used, together with a suitable distribution/discretisation strategy, to find the exact requirements for a specific actuator within the system, as is discussed in Section 6.2. The strategy was based on 40 actuators, an arbitrarily chosen quantity, being placed along the span of the trailing edge at equal intervals.

This was followed by decisions on the architecture of the actuator in Section 6.3. The parallel arm, load-sharing architecture was introduced. This was followed by a discussion on the floating design, which ensured that the actuator was unconstrained along its mid-plane; a strategy that would ensure that the actuator would exert forces only in the lateral direction. Other considerations included the balancing of wire forces to minimise the moments transferred in the mechanism and cross-over devices that would convert the expansion of the actuator into a tensile force.

Some high level structural decisions are presented in Section 6.4. The first decision was to use arms in such a way that triangles were formed between them, since this

would ensure the lateral stability of the actuator. The second, and final, decision was to support the stationary pins of the actuator with web-plates to keep the size of the pins down.

Sections 6.5, 6.6 and 6.7 are related to the sizing of the actuator components. First the arm lengths were found by defining the actuator kinematics. This was followed by the "sizing" of the biassing springs: essentially this is the selection of a suitable stiffness for the structure/spring that would be needed to bias the actuator. Finally the cross-sectional sizes of the arms were determined from the loads that they are expected to experience.

The final section, Section 6.8, is a brief discussion on the construction of the SMA wire bundles that were used to drive the actuator. It discusses how the crimps needed to secure the wire ends effectively to each other were too large to fit into the limited available space, and how the problem was circumvented by looping the wire ends back over each other and using smaller crimps.

6.1 Design Overview

This section provides an overview of the finalised actuator, the design of which is shown in Figure 6.1. The *parallel four bar linkage* basically comprises parallel stainless steel arms that when seen from the side resemble a diamond shape (Figure 6.2). The stainless steel arms(annotated in Figure 6.1) hinge on stainless steel pins that pass through their ends, forming an equilateral four bar linkage with two actuating and two sliding pins, which are also shown in the figure. The four bar linkage is driven by the application of the actuation force and stroke from electrically heated SMA wire bundles; the bundles act on the previously mentioned sliding pins.

Several SMA bundles were used, performing their work at points that were distributed along the lengths of said sliding pins. Neighbouring SMA bundles actuated pins on the opposite sides of the "diamond"; this is indicated in Figure 6.2. The SMA bundles are said to *cross-over* the mechanism, since the fixed end of each bundle is on the opposite side of the mechanism. The actuating capacities of the wire bundles were arranged symmetrically about its mid-plane; this can be seen on the right of Figure 6.2 in the form of unequal bundle quantities (red versus blue). The bundles were grouped as *sets*, with the collection of bundles indicated in red being referred to as "bundle set 1" and the blue grouping being called "bundle set 2". Set 1 consists of 5 wire bundles, each containing 4 loops of the wire. Wire set two, on the other hand, consists of 4 bundles, each of which contains 5 loops of the wire. It can be seen that the total amount of wire loops contained in each bundle set adds up to 20, which means that the total actuating capacity of the two sets are equal even though they are not identical.

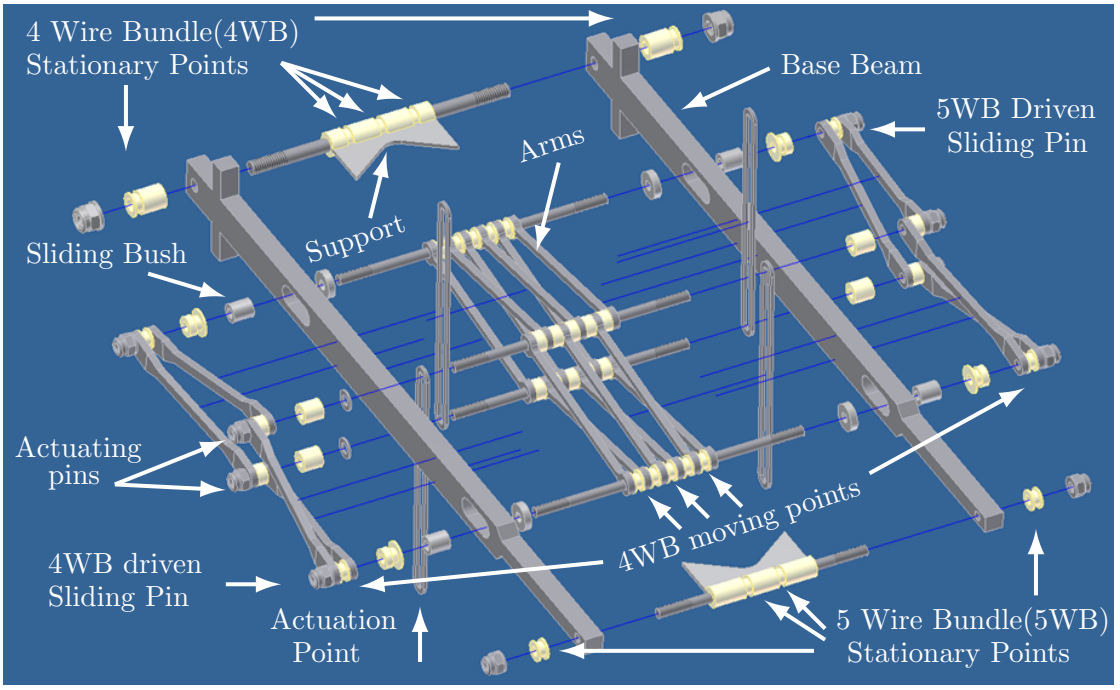

FIGURE 6.1: Exploded view of actuator(add arm and sliding pins)

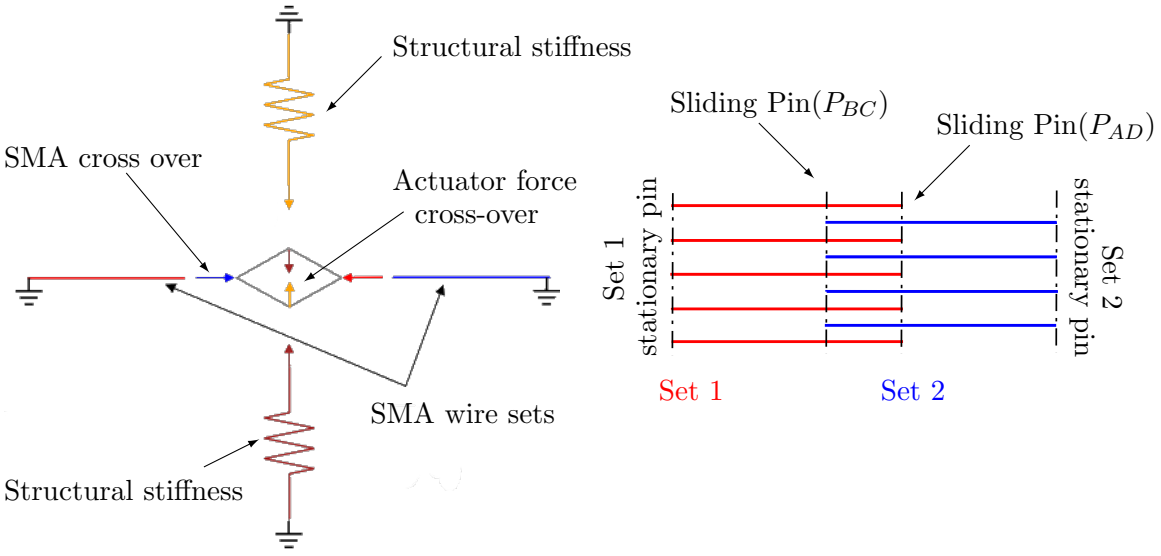

FIGURE 6.2: Actuator overview, bundle placement (add annotations)

The loads between the two stationary pins are carried by two base beams (Figure 6.4), thus keeping the distance between the pins fixed. Slots in these beams also constrain the movement of the sliding pins to the desired plane. Plastic sliding bushes served as spacers between the sliding pins and the slot surfaces. The bushes also provided spacing between some of the arms. The remainder of the plastic bushes served as insulators between the structural components and the SMA wires. The mentioned insulation was required due to the series electrical connection of the wire bundles to each other. In the bundles themselves, however, the individual loops of wire are connected in parallel.

The entire system, when electrically powered, provided usable motion and force at the actuating pins. Since the actuation points were located on the opposite side of the mechanism they were connected to the actuating pins via a second cross-over in the form of slender tensile members.

To reinforce the highly stressed stationary pins, supports were welded onto them, providing the opportunity to select more compact and lighter pins. Lateral stabilisation was also provided in the form of *stabiliser arms* that, due to their increased length, formed triangular linkages.

A photo of the assembled prototype(Figure 6.3) may provide additional insight on some of the topics discussed.

FIGURE 6.3: Full view of bundle construction

6.2 Discretised Requirements

In preceding sections, generalised positions/requirements were determined for the chordwise actuator placement, as well as the actuator stroke and force requirements.

These are repeated here for convenience.

Variables:

$L \rightarrow length \quad x_{act} \rightarrow localcoordinate \quad P \rightarrow Pin \quad S \rightarrow Stabaliserarm \quad A \rightarrow Arm$

$y_{act} \rightarrow localcoordinate$

Subscripts:

$A,\ B,\ C,\ D \rightarrow\ Quadrant\ identfiers\ for\ arms$

$AB,\ BC,\ CD,\ AD \rightarrow\ Arm\ Interfaces$

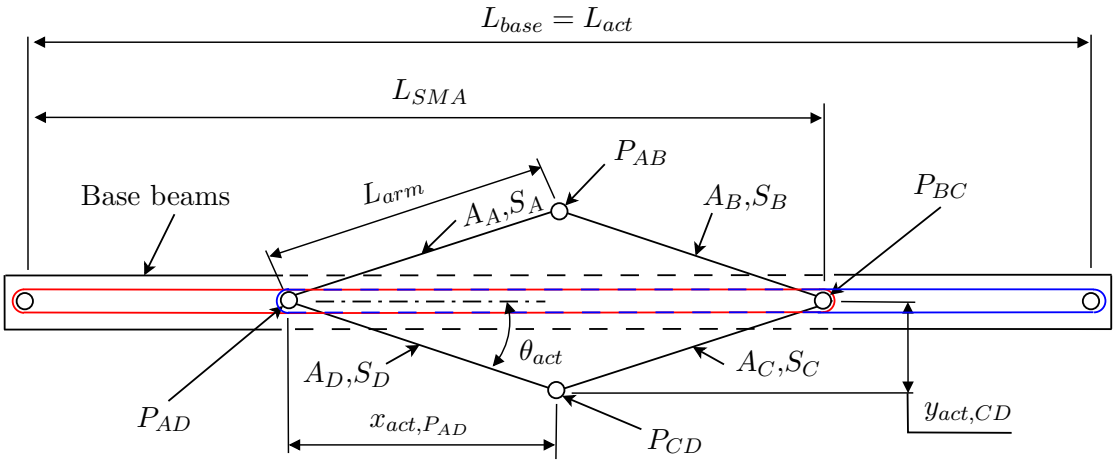

FIGURE 6.4: Actuator variable definitions

Actuator chord-wise placement:

$$x_{attach} = 1.5\%c \tag{6.1}$$

Actuator stroke:

$$\Delta y_{act} = 0.2176\%c \tag{6.2}$$

Equivalent aerodynamic load:

$$f_{aero,eq} = (3/L_{cr}^3)(f_{L_{cr}} * L_{cr}^3/3 - m_{L_{cr}} * L_{cr}^2/2 + p * L_{cr}^4/8) \tag{6.3}$$

In order to convert these generalised expressions into the requirements for a specific actuator, the trailing edge region needed to be discretised. The purpose of this section is to discuss the discretisation used in the current project. The discussion starts with geometrical definitions of the trailing edge in a flat plate coordinate system. This is followed by the definition of discrete intervals on the trailing edge and discrete lengths used to describe the different regions within each interval as perfect rectangles. The discrete dimensions are then substituted into Equations 6.1, 6.2 and 6.3 to find expressions for the requirements at each interval.

The geometrical definitions of the trailing edge were based on Figure 6.5, in which it was viewed as a flat plate. Indicated on this figure is a typical discrete interval, accompanied by some variable definitions, which are used throughout this discussion.

Important mathematical descriptions for the geometry of this flattened plate are shown in equations below. Equation 6.4 expresses the chord-line in terms of the global z-coordinates (span-wise position on the vertical tail). Equations 6.5 and 6.6 on the other hand, express the geometry of the Attachment Line (AL) and Trailing Edge (TE) in terms of the flat plate coordinates in the figure. Equation 6.7 shows the length ratio the between z_G and x_f which could be used to map the chord-line $c(z_G)$ onto the flat plate coordinate system.

$$c(z_G) = 0.51372 * z_G + 7.7 \quad [m] \tag{6.4}$$

$$y_{f,AL} = -0.0062 * x_f + 0.1038 \ [m] \tag{6.5}$$

$$y_{f,TE} = -0.0207 * x_f + 0.3486 \ [m] \tag{6.6}$$

$$z_G/x_f = 0.89 \tag{6.7}$$

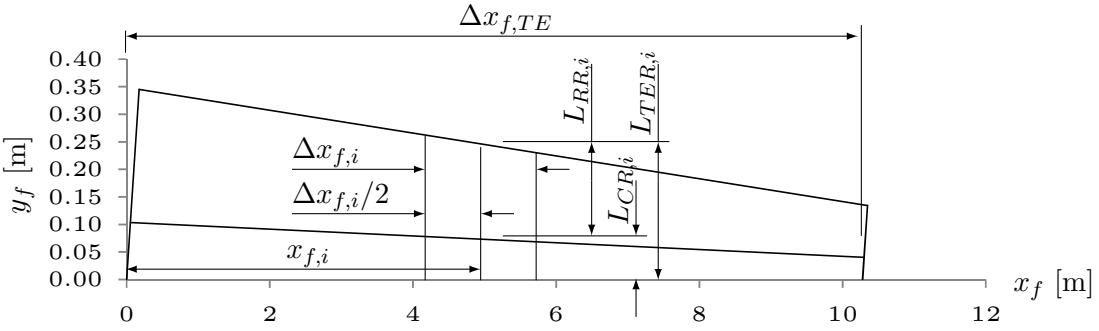

FIGURE 6.5: Flat plate variable definitions for the trailing edge discretisation

For the discretisation, the length of the stationary edge $\Delta x_{f,TE}$, was subdivided into the desired number of discrete intervals, with N intervals of equal length. The span of each interval is defined in Equation 6.8, and its placement in the coordinate system in Equation 6.9

$$\Delta x_{f,i} = \Delta x_{f,TE}/N \tag{6.8}$$

$$x_{f,i} = (i - 0.5) * \Delta x_{f,i} \tag{6.9}$$

The following are the variables used in these equations:

$\Delta x_{f,i}$ - The span of interval i in the flat plate coordinate system.
$\Delta x_{f,TE}$ - The span of the complete trailing edge in the flat plate coordinate system.
N - The number of discrete intervals.
$x_{f,i}$ - The location of the geometrical middle of interval i.
i - The numerical identifier for a given interval.

The geometry of different regions inside each interval could then be defined further by treating each interval as a perfect rectangle with its remaining dimension as shown in Equations 6.10 and 6.11. The defining dimensions were taken as the length of the region at the geometrical middle thereof.

$$L_{CR,i} = y_{f,AL}(x_{f,i}) = -0.062 * x_{f,i} + 0.1038 \ [m] \tag{6.10}$$

$$L_{RR,i} = y_{f,TE}(x_{f,i}) - y_{f,AL}(x_{f,i}) = -0.0145 * x_{f,i} + 0.2448 \ [m] \tag{6.11}$$

The dimensions used are defined as follows:

$L_{CR,i}$ - The defining length of the compliant region at interval i.
$L_{RR,i}$ The defining length of the rigid region at interval i

The chord-length c, which was already known in terms z_G from Equation 6.4, was related to x_f by mapping it though z_G using the length ratio in Equation 6.7. The resulting relation is shown in Equation 6.12.

$$\begin{aligned} c(x_{f,i}) &= -0.513172 * z_G(x_{f,i}) + 7.7[m] \\ &= -0.513172 * (0.89 * x_{f,i}) + 7.7 \ [m] \end{aligned} \tag{6.12}$$

This completed the definition of the geometric variables needed for discretisation. By substituting the geometric variables together with the load definitions in Equations 5.16, 5.17 and 5.18 into the generalised requirement definitions(Equations 6.1, 6.2, 6.3), the following set of discrete specifications could be determined:

$$x_{attach,i} = 0.015 * [-0.513172 * (0.89 * x_{f,i}) + 7.7][mm] \tag{6.13}$$

$$\Delta y_{act,i} = 0.002176 * [-0.513172 * (0.89 * x_{f,i}) + 7.7][mm] \tag{6.14}$$

$$f_{aero,eq,i} = \left[\frac{3}{(-0.062 * x_{f,i} + 0.1038)^3}\right] * ... \left[p * L_{RR,i} * \frac{L_{CR,i}^3}{3} - \frac{p * L_{RR,i}^2}{2} * \frac{L_{CR,i}^2}{2} + p * \frac{L_{CR,i}^4}{8}\right] \tag{6.15}$$

To find the concentrated load representation of $f_{aero,eq,i}$, the line-load was multiplied by the span of the relevant interval $\Delta x_{f,i}$. The resulting load, $F_{aero,eq,i}$, was the aerodynamic component of the force that the actuator needed to be designed for. The dimensional values used as the requirements for the design of the prototype are summarised in Table 6.1. These are the values calculated for the bottom-most actuator of the 40 actuators.

$$F_{aero,eq,i} = f_{aero,eq,i} * \Delta x_{f,i} \tag{6.16}$$

TABLE 6.1: Discretised requirements for the prototype actuator

Variable	Magnitude	Unit
$\Delta x_{f,1}$	257	mm
$x_{f,1}$	128	mm
c_1	7.64	m
$x_{attach,1}$	115	mm
$y_{attach,1}$	16.6	mm
$F_{aero,1}(C_{p,min})$	-136	N
$F_{aero,1}(C_{p,max})$	68	N

6.3 Layout Decisions

This section discusses some of the architecture of the mechanism. First discussed is the parallel nature of the actuator, and how it is an architecture born from the need to distribute the transferred loads. Next it is explained how the mechanism was allowed to *float* inside of the structure housing to allow for the movement of the sliding pins. Finally a cross-over method is discussed, by which the outward expansion of the car-jack mechanism is converted into a tensile force that can be applied to the aircraft skin.

Parallelism:

The design philosophy relevant here was the *Design Axioms for Optimal Discrete Actuator Design*: according to these axioms, in order to achieve mass optimised designs under-utilised materials should be avoided. This was achieved by using axially or shear loaded rigid materials. With conventional car-jack mechanisms, the singular arms of the mechanism would result in high shear forces, which would drive up the size of mechanism components. The large mechanism components, in turn, would mean that the axes of the mechanisms arms would be removed from each other laterally; this would result in load transfer by way of bending moments, a scenario that should be avoided.

In order to reduce the size of the actuator components, and distribute the shear force that would be transferred, a parallel configuration was used such as is shown in Figure 6.6.In this configuration the force was shared among the neighbouring shear-planes. It was not necessarily divided exactly equally, but for design purposes an even load distribution was a reasonable assumption to start from.

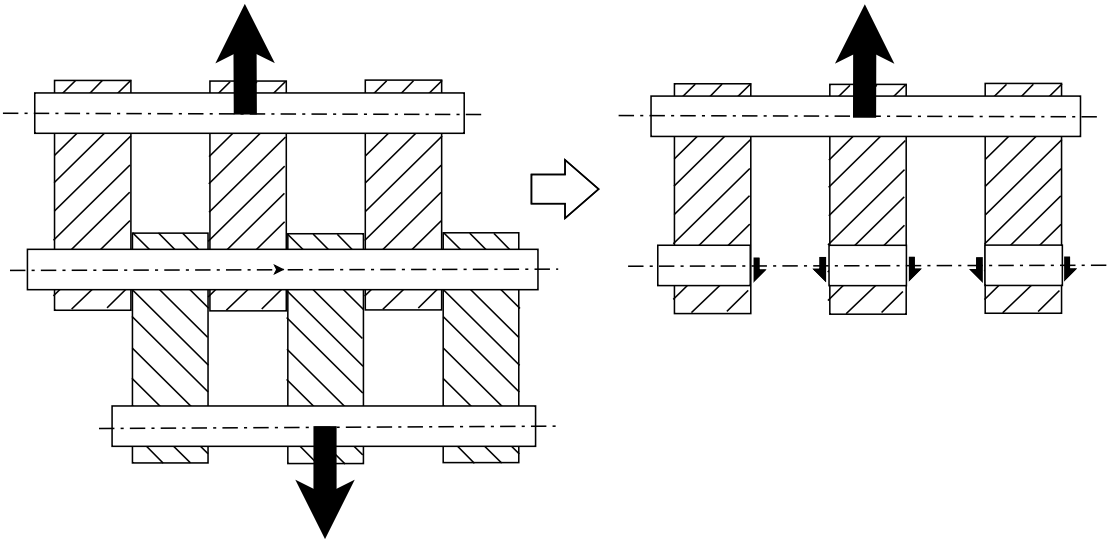

FIGURE 6.6: Parallel arrangement force distribution example

Another reason for the parallel design was the tendency of moving stainless steel parts to self-lock at stress concentrations, or excessive stress occurring at such locations. Such stress concentrations are caused by misalignment of the pin-and-hole axes, such as is shown in Figure 6.7b. In order to avoid this happening the pins needed to remain co-axial to the holes, with forces being transferred through sliding surfaces rather than along hole edges. A parallel configuration such as is shown in Figure 6.7b would go a long way towards forcing the axes into alignment.

Floating design:

The movements wanted/needed in the mechanism were those of the pins relative to each other. This would, however, result also in movement of some or all of the pins relative

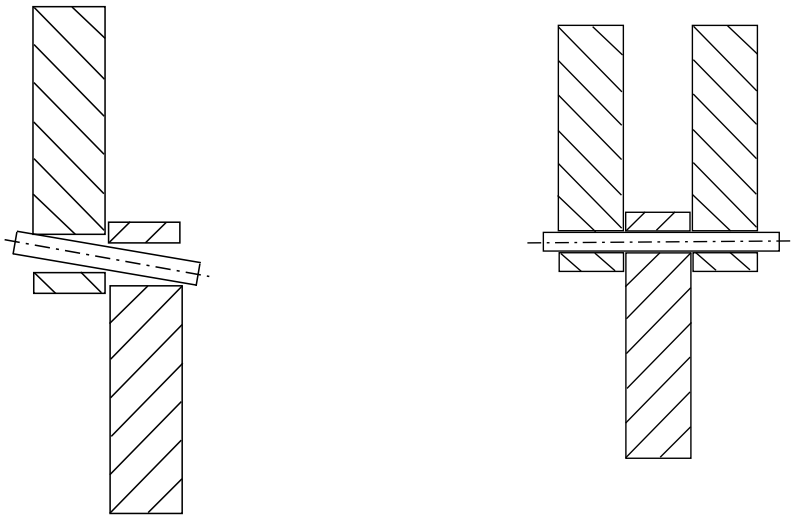

(a) Axial misalignment (b) Axial alignment enforced

FIGURE 6.7: Axial alignment of different arm arrangements

to the static parts of the actuator such as is shown in Figure 6.8. A readily achievable design would be one where a single pin was fixed and the others sliding (Figure 6.8a). This would lead to significant axial movement of the point of attachment, such as is indicated in the figure. A mismatch in movement between the attachment points on the actuator and that on the aircraft skin would result, causing forces in directions other than what was intended in the design. To avoid this, all pins needed to be allowed to move relative to the actuator base. Slots for each pin allowed for this. The resulting actuator would "float" within these slots as is shown in Figure 6.8b.

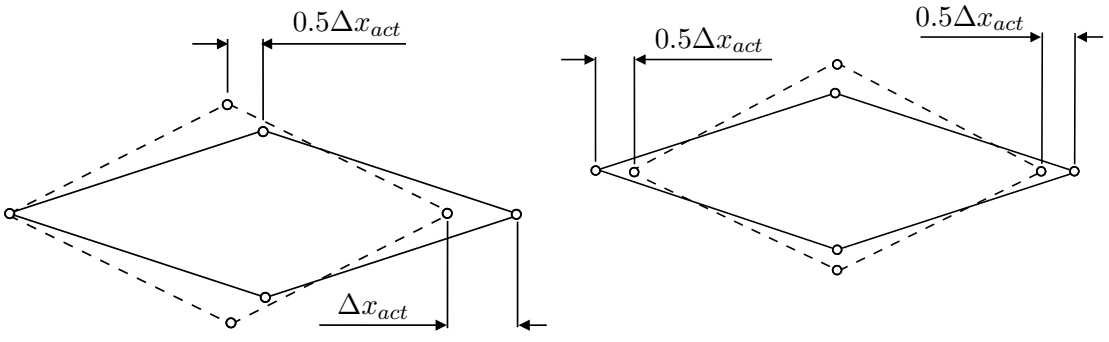

(a) Single fixed pin (b) Sliding pins

FIGURE 6.8: The movement of pins relative to inert reference frame

This floating design caused some difficulties, such as the necessity for individual actuation of each pin. Other arrangements, however, caused problems of their own, and

this was selected as the layout with the fewest "necessary evils". It was also one of the aspects of the current design which left the most scope for future changes.

Balanced wire bundles:

An unfortunate result of the floating design, coupled with the parallel architecture, was that actuator wires would need to act on both actuating pins. If equal bundle quantities were used on each side, it would lead to the situation showed in Figure 6.9. In this figure it can be seen how the forces would not be arranged in a symmetrical manner, and that moments would result. Such moments are undesirable for several reasons.

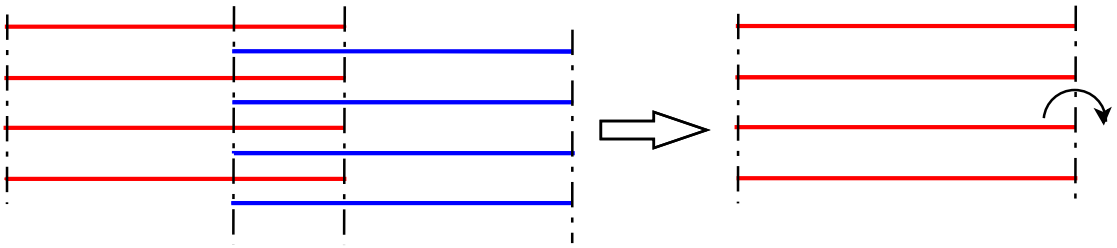

FIGURE 6.9: Moment generation by identical SMA wire bundle sets

The current solution to this problem was to distribute the actuating forces symmetrically about the mid-plane of the actuator, as shown in Figure 6.10. In this configuration the unwanted moments would be minimised.

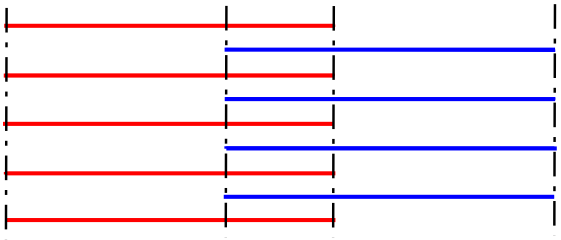

FIGURE 6.10: Parallel arrangement force distribution example

Cross-over mechanism:

A high level decision was made to allow for an open failure state for the trailing edge. This led to a situation where the actuator skin had to be "pulled" closed rather than being "pushed" open. This was to be achieved by a car-jack mechanism, which is traditionally associated with the action of pushing, especially so with the primary mover being wires that are only effective in tensile loading.

This meant that for the actuator to work, it needed to transform the pushing action into a pulling force. Rather than using a complex mechanism, it was decided that simple tensile units would be used to achieve this. These units, which somewhat resemble paperclips, were capable of transferring the pushing action of one pin to the other side of the mechanism. The result was the pulling action that is illustrated in Figure 6.11.

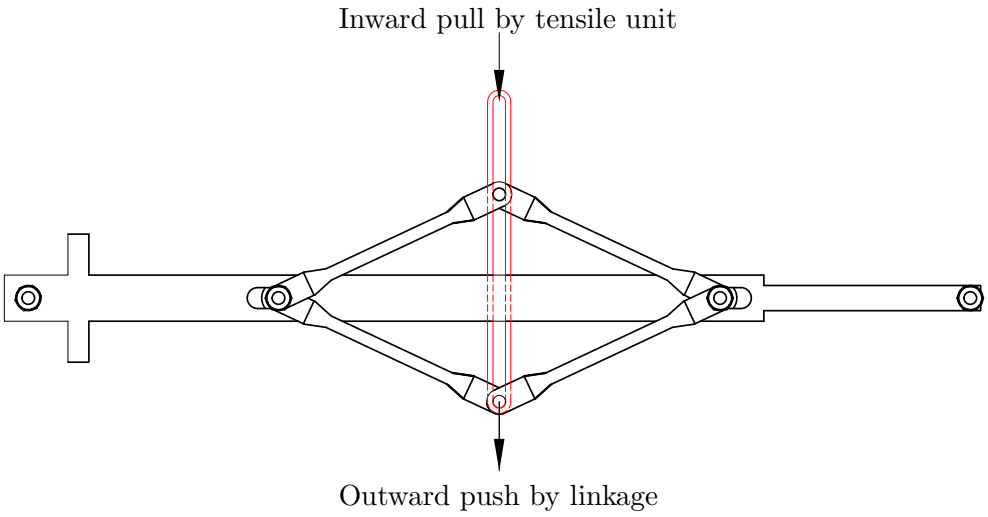

FIGURE 6.11: Tensile unit illustration example

In summary, several improvements to the basic car-jack mechanism were suggested in this section. Parallel arms would distribute the load, thereby minimising moments and stress Inward pull by tensile unit concentrations in the mechanism. The actuator would also "float" to avoid forces other than those that participate directly in the actuation. The wires, which would then be applied to both actuating pins, would be distributed symmetrically about the mid-plane in an additional attempt to avoid moment transfer within the mechanism. The resulting actuator, which would only allow for pushing action, was converted to a pull-type actuator by using simple tensile units that cross over the mid-plane of the actuator.

6.4 Stabilisers and Supports

With the basic layout of the actuator in place, some needs were identified in terms of lateral stabilisation and bending moment transfer within the mechanism. These additions did not change the initial concept in any way but served as improvements, which would result in more optimal design and improved stability during operation.

First a method is discussed by which unbalanced forces were negated through the use of triangular, inherently stable linkages. Next it is discussed how a reduction in the size of the static pins was realised by supporting them in a way that facilitated more effective force transfer within the mechanism.

Stabilisers:

At this point a lot of effort had been put into the design of a mechanism that operated symmetrically in many ways. Some imperfections in manufacturing and operation were, however, bound to occur, as well as the possible breaking of some of the wires in the life-span of the mechanism. This would lead to some asymmetric forces such as depicted

in Figure 6.12. In such an event the actuator would be prone to "falling over sideways", since no mechanism had been included by which to resist such imbalances effectively.

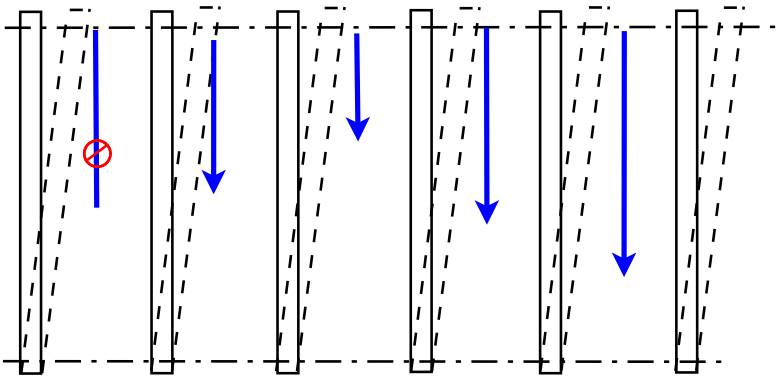

FIGURE 6.12: Mechanism "fall-over" concept

In order to provide resistance against any such source of lateral imbalance, stabilising arms were used on the outside of the parallel mechanism. The triangular linkage that these arms formed, as well as their effect, is shown in Figure 6.13. It can be seen that these arms would serve to stabilise the mechanism laterally, while also serving as force-transferring structural members, similar to the straight arms.

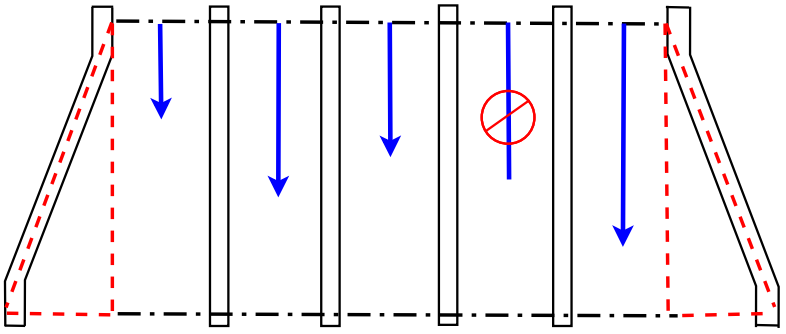

FIGURE 6.13: Laterally stabalised mechanism using stabiliser arms

Supports:

A major consideration in the design was to keep the size of the pins small. Due to the counteracting forces and lack of moments on the moving pins, this was not a problem.

The stationary pins, however, of which the arrangement is shown in Figure 6.14, required a method by which the forces would be transferred to the base beams. If only a pin was used, it would lead to very large moments and the need for very large pins to be used. Such pins would also not be optimally stressed, resulting in a large amount of under-utilised material. A better way of transferring the forces was to weld supports to

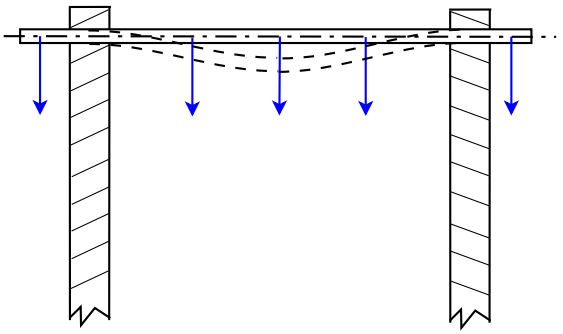

FIGURE 6.14: Stationary pin, force and deflection arrangement

the pins as depicted in Figure 6.15. The supports would be an effective means by which to transfer the forces from the wire sets to the base beams without the use of large, moment-carrying pins.

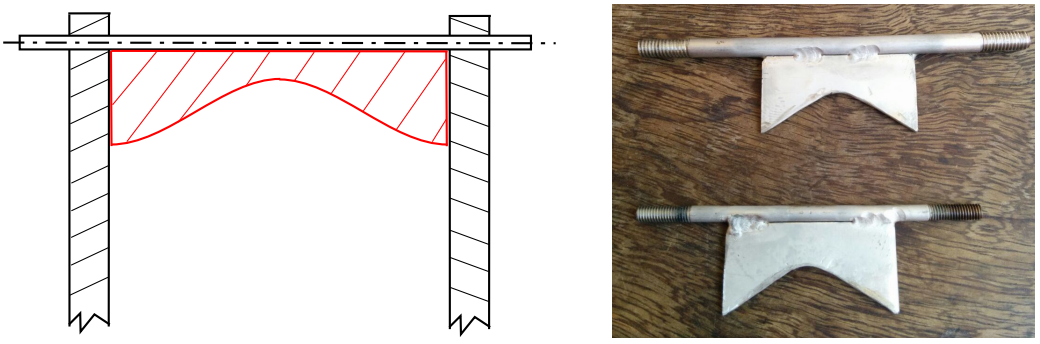

FIGURE 6.15: Stationary pin, support configuration

6.5 Actuator Kinematics

A car-jack type mechanism was to be used for the actuation of the rudders trailing edge. This section deals with the selection of component lengths by studying the kinematics of the actuators movement.

The study of the actuator kinematics revolved around geometrical specifications for the arm lengths, as well as the relative movements that they would experience during operation. The nature of the actuator requirements was such that the minimum and maximum positions were of interest rather than the complete motion paths. The actuator kinematics could thus be defined sufficiently by selecting values for the relevant variables at the two extreme positions of the actuator.

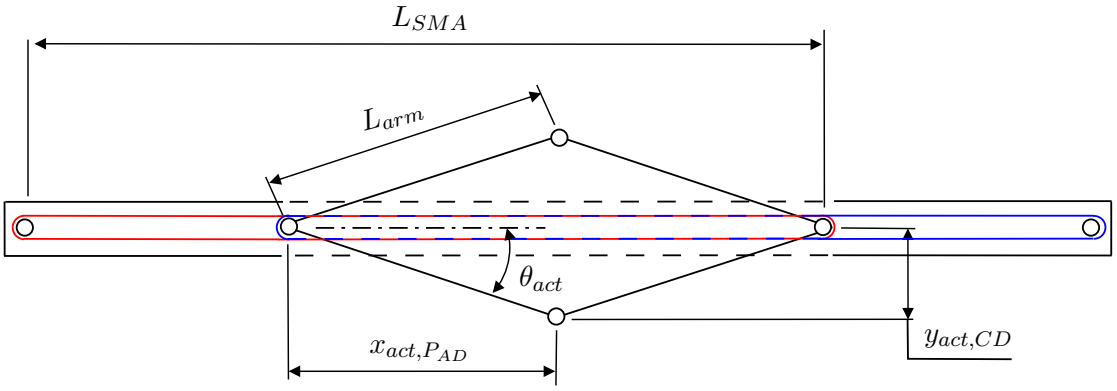

FIGURE 6.16: Actuator kinematic variables

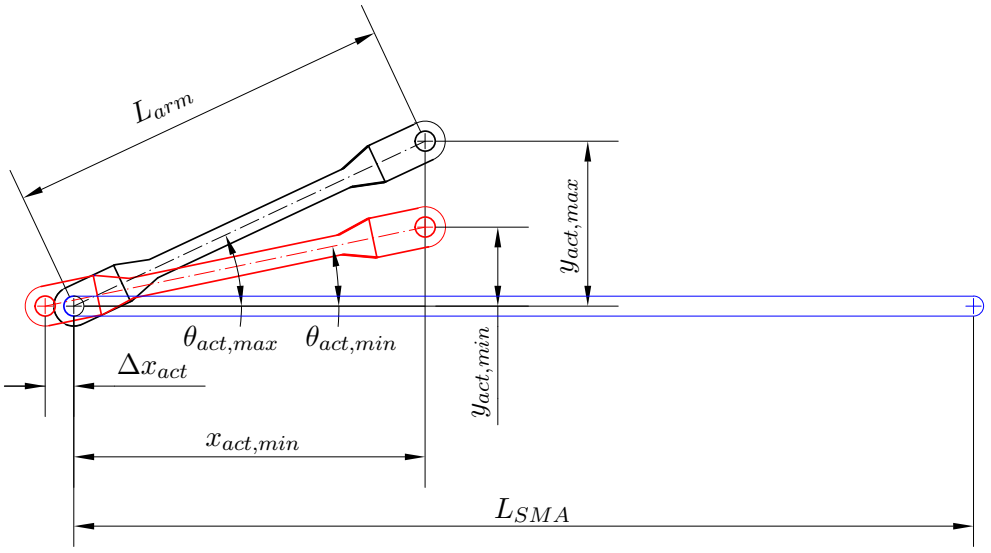

FIGURE 6.17: Quarter actuator model for selection of kinematics

The relevant variables are shown in Figure 6.17 together with a quarter actuator model, indicating their definitions in the extreme actuator positions. The given definitions served as the basis for the design equations, which were derived as follows:

$$\Delta x_{act} = \Delta L_{SMA} \tag{6.17}$$

With x_{act} being the stroke at the sliding pins and ΔL_{SMA} being the change in the length of the SMA to provide this stroke.

$$\Delta L_{SMA} = 0.03 * L_{SMA} \tag{6.18}$$

With L_{SMA} being the shortened length of the SMA wires, and the 0.03 being the 3% strain that would be experienced by the SMA material.

$$y_{act,max} = L_{arm} * sin(\theta_{act,max}) \tag{6.19}$$

With $y_{act,max}$ the maximum lateral position of the actuating pin, L_{arm} the length of the actuator arms and $\theta_{act,max}$ the maximum angle between the actuator arms and the mid-plane of the actuator.

$$(\Delta y_{act})_{th \to cl} = y_{act,max} - y_{act,min} \tag{6.20}$$

With $(\Delta y_{act})_{th \to cl}$ being the change in lateral position when the trailing edge switches between its blunt and its sharp forms.

$$AF = (\Delta y_{act})_{th \to cl} / \Delta x_{act} \tag{6.21}$$

The identified equations provided the basis for an iterative design study, which resulted in the selection of suitable kinematics for the actuator in question. As in most designs, some trade-offs were required. The trade-offs were between the long arm lengths required by stroke amplification requirements and the low arm length requirements set by space constraints and favourable force transfer characteristics. For the selection to occur, a specific design space was needed within which to explore the detailed selection. After some initial exploration of the design problem/requirements, the following constraints were selected as the limits of the design space.

- $(\Delta y_{act})_{th \to cl} = 16.63\ mm$
- $y_{act,max} \leq 25\ mm$
- $AF \leq 20$
- $\theta > 8°$
- $L_{SMA} - (x_{act,min} + \Delta x_{act}) < 267\ mm$

The origin of the preceding constraints were as follows:

- $(\Delta y_{act})_{th \to cl}$ - This was determined through stroke prediction in the high level design.

- $y_{act,max}$ - Space constraints within the trailing edge.
- AF - A rule of thumb, higher amplification rates result in low stiffness actuators which tend to have low mass efficiencies.
- θ - Set to limit the force required for initiating actuation.
- L_{SMA} - Space constraint within the trailing edge.

The design space proved fairly tight, with narrow bands of acceptable values for the design variables. Initially θ was chosen to be higher; however, a systematic reduction thereof was required before space constraints of a successful combination of variable values could be identified. While 8° was considered to be a small angle, and the SMA forces required for actuation high as a result thereof, it was still considered to be viable. Given the selected architecture, a larger angle could not be realised without L_{SMA} violating its constraints.

The final design variables are summarised in Table 6.2 together with the specifications which were driven by it.

TABLE 6.2: Kinematic specifications for the actuator prototype

Design Variable	Specification	Unit
$\theta_{act,max}$	25.15	°
$\theta_{act,min}$	8	°
$x_{act,max}$	57.61	mm
$x_{act,min}$	52.66	mm
L_{SMA}	165	mm
ΔL_{SMA}	4.95	mm
epsilon max	3.5	%
epsilon min	0.5	%
L_{arm}	58.18	mm
$y_{act,max}$	24.72	mm
$y_{act,min}$	8.1	mm

6.6 Biassing Stiffness Selection

The prototype actuator being designed made use of SMA wires to provide the necessary stroke. The material, when used in this format, upon heating, reduces in length and is capable of producing a usable force in the process. The reverse actuation is, however, not spontaneous when the one-way shape memory effect is utilised, as is the case in this design. A biassing force was thus needed to stretch the wire back to its full length in order to provide a return stroke. In this project, the biassing force was produced by a structural force that acted against the actuator. With the actuator kinematics

defined, the stage was set for the selection of the stiffness of the biassing structural, as is discussed in this section. The selection was based on the ratio between the maximum and minimum stresses that would be experienced by the SMA material. The selected stiffness was chosen in such a way that the stiffness was both small enough for the SMA wire to overcome while coupled to the minimum aerodynamic force, and large enough to stretch the material, even when the maximum aerodynamic force was acting against it.

The selection was based on the quarter model of the actuator shown in Figure 6.18. The quarter model shows quadrant A of the actuator, the position/definition of which can be seen in Figure 6.4.

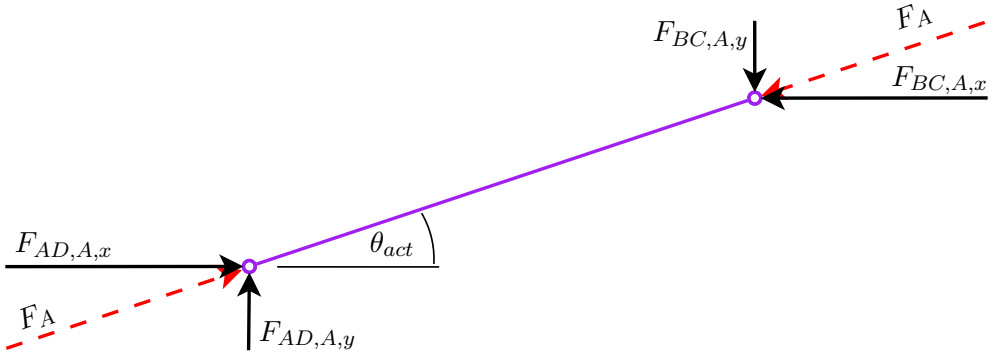

FIGURE 6.18: Quadrant A total arm forces

The horizontal force at pin AD originates from the SMA bundles, the total force applied by these bundle sets was $F_{SMA,T}$. The vertical force at pin BC on the other hand was that experienced by the actuator due to the load acting on it F_{act}. The symmetry of the actuator meant that these forces were shared by the neighbouring quadrants; as such, the forces on a single quadrant shown in this figure were:

$$F_{AD,A,x} = F_{SMA,T}/2 \tag{6.22}$$

$$F_{BC,A,y} = F_{act}/2 \tag{6.23}$$

With:

$$F_{AD,A,x} = F_{BC,A,x} \tag{6.24}$$

$$F_{BC,A,y} = F_{AD,A,y} \tag{6.25}$$

F_A is the resultant force; the orientation of the force will always be aligned axially with the arm due to the pin connection, which cannot transfer moments. This helped with the identification of the following trigonometric relationships based on Figure 6.19:

$$F_{SMA} = \frac{F_{act}}{\tan(\theta_{act})} \tag{6.26}$$

$$F_A = \frac{1}{\sin(\theta_{act})} * \frac{F_{act}}{2} \tag{6.27}$$

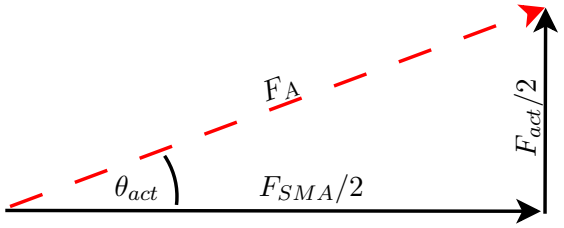

FIGURE 6.19: Trigonometric force relations within actuator

The spring stiffness selection would necessitate a trade-off between the maximum stress on the SMA wire sets and the amount of strain achieved by the stressing of these wires. The stress in the wire is the force per unit area of SMA wire. This area was unknown at the time of this study, and therefore the stiffness had to be selected based on the ratio between the maximum and minimum stresses. By using a ratio, the area could be cancelled from the selection as is shown in Equation 6.28.

$$\frac{\sigma_{SMA,max}}{\sigma_{SMA,min}} = \frac{F_{SMA,max}A_{SMA}}{F_{SMA,min}A_{SMA}} = \frac{F_{SMA,max}}{F_{SMA,min}} \tag{6.28}$$

The function of the structural force was to achieve reverse actuation, so it needed to overcome any positive aerodynamic pressure($C_{p,max} = 0.2$) while still achieving a minimum stressing of the SMA material $\sigma_{SMA,min} = \sigma_f^{cr} = 100\ MPa$ needed to complete the de-twinning of the martensitic SMA material. The force associated with this is shown in Equation 6.29:

$$F_{act}(F_{aero,max}) = k_{struct} * [(\Delta y_{act})_{k,0\rightarrow th} + (\Delta y_{act})_{th\rightarrow cl}] - F_{aero}(C_{p,max}) \tag{6.29}$$

With $(\Delta y_{act})_{k,0\rightarrow th}$ being the difference in actuator position from a hypothetical state where the structure would have been unstressed, to its un-actuated(TE thickened) state. The parameter $(\Delta y_{act})_{th\rightarrow cl}$, on the other hand, is the difference in actuator position between the un-actuated(TE thickened) to the actuated(TE closed) state, and k_{struct} was the hereto unknown structural stiffness.

This would place a fairly definite lower limit on the structural stiffness. The upper limit, which would be associated with the largest negative aerodynamic pressure ($C_{p,min} = -0.4$), would be set by a fairly arbitrary specification of σ_{max}. The associated force was as follows:

$$F_{act}(F_{aero,min}) = k_{struct} * [(\Delta y_{act})_{y_{k,0} \rightarrow y_{act,th}} + (\Delta y_{act})_{th \rightarrow cl}] - F_{aero}(C_{p,min}) \tag{6.30}$$

The yield stress of austenitic SMA is generally around 600 MPa and theoretically this would be the maximum recovery stress that could be achieved by the material. High stresses, however, reduce the cycle life of actuating SMA material and a different value had to be chosen. The design value selected for the actuator was $\sigma_{SMA,max} = 280$. Initially designs were attempted with values closer to 200 MPa, but in the process of design iteration it was however found that the current kinematics did not allow stresses this low without the minimum stresses dropping beneath the desired value of σ_f^{cr}. In the end the design requirements were set to:

$$\frac{\sigma_{SMA,max}}{\sigma_{SMA,min}} = \frac{280\ MPa}{100\ MPa} = 2.8 = \frac{F_{SMA,max}}{F_{SMA,min}} \tag{6.31}$$

F_{SMA} had already been related to the actuator force in Equation 6.26. Substituting into the associated aerodynamic force values, led to the following expression for the SMA forces:

$$F_{SMA,min} = min : \left[\left(\frac{1}{\tan(\theta_{act})} \right) * F_{act}(F_{aero,max}) \right] \tag{6.32}$$

$$F_{SMA,min} = min : \left[\left(\frac{1}{\tan(\theta_{act})} \right) * F_{act}(F_{aero,min}) \right] \tag{6.33}$$

The structural pre-stress was set to:

$$(\Delta y_{act})_{y_{k,0} \rightarrow y_{act,th}} = 0.5 * (\Delta y_{act})_{th \rightarrow cl} \tag{6.34}$$

With this value, the preceding equations could be solved to yield a value of:

$$k_{struct} = 21.82\ N/mm \tag{6.35}$$

The resulting maximum and minimum SMA forces are plotted below (Figure 6.20) as a function of θ_{act}. The maximum and minimum values were found to be:

$$F_{SMA,max} = 2260\ N \tag{6.36}$$

$$F_{SMA,min} = 807\ N \tag{6.37}$$

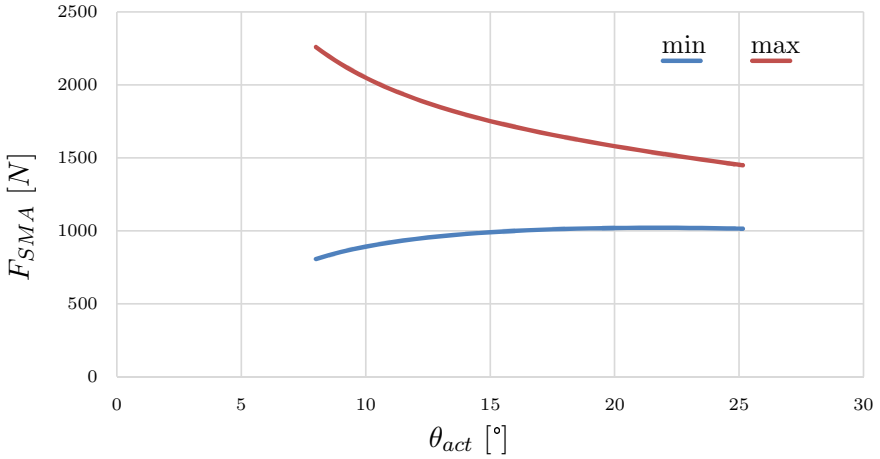

FIGURE 6.20: Minimum and maximum SMA forces vs. θ_{act}

6.7 Sizing

The sizing of the components mostly referred to cross-sectional sizes, since the geometrical decisions that related to kinematics had, at this point, been finalised to a large extent. The kinematics were used to determine the force relationships within the actuator in Section 6.6, and provided most of the information needed to estimate the forces on parts and their required sizes. The exception to this rule being the actuating pins, these were selected based on space limitations. The rest of the selections were as follows. F_A was for the selection of arm quantities as well their sizes, F_{SMA} was used to determine the cross-sectional area needed for each wire bundle, the rear stationary pin and the base beams. Lastly, F_{act} was used to determine the size of the tensile units. This section presents more information on each of these sizing procedures. Note that the sizing of the base beams and the tensile units are omitted from the discussion for the sake of brevity.

Actuating and sliding pin sizes:

The actuator would be used to pull, rather than push as is common for equilateral four bar linkages. The pulling was necessitated by an open failure state. This pull led to the crossing over of the working stroke from the actuating pin to the attachment point. Due to the cross-over, an opening action from the actuator would produce a closing action

on the skin of the trailing edge region. As a result, an outward moving attachment pin would actuate towards an inward moving skin, causing possible lock-up or even damage. The lateral(y_{act}-direction) size contributions from any part thus had to be kept as small as possible. This concept is shown in Figure 6.21, and, more specifically its relevance to the pin, and pin hole sizing.

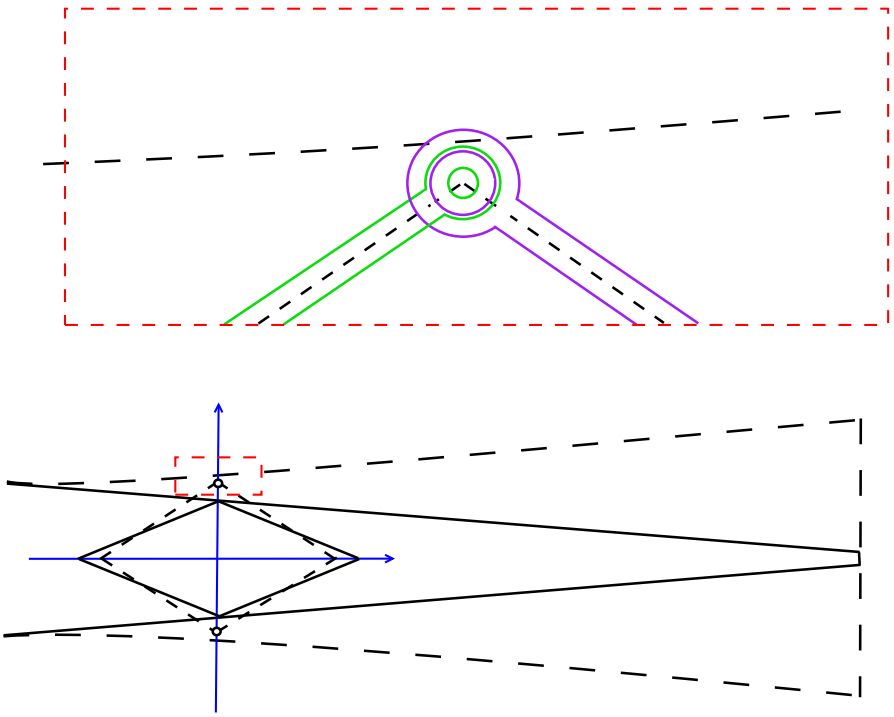

FIGURE 6.21: Actuator pins sizing concept

It was clear that a large pin, while in itself also a contributor to unwanted lateral size, was not the sole problem. The parts that work with these pins to form the hinges that allow movement (arms) and enforce proper spacing of arms (spacers) were required to fit around the pins, and possessed some thickness themselves. This could quickly increase the lateral size to unacceptable values, even for small pins.

After some trial and error it was found that for the current kinematic design, 3 mm pins would provide a tight but acceptable lateral fit. This diameter is shown in Equation 6.38.

$$d_{P_{AB}} = d_{P_{CD}} = 3\ mm \tag{6.38}$$

The sizing of the sliding pins were set to the same value for the purpose of easing the design and part sourcing. This is shown in Equation 6.39

$$d_{P_{AD}} = d_{P_{BC}} = 3\ mm \tag{6.39}$$

Arm quantities:

The parallel arms of the actuator served as a mechanism for distributing load transfer and, in doing so, reducing or completely removing moments as a method for the transferral of work effort. It was, however, difficult to determine the appropriate level of parallelism, i.e. the number of parallel arms to use in the design. Since, in Section 6.3 it was deemed necessary to use bundle sets of which the number of wire bundles N_b were not equal, it turned out that one of the major drivers behind the level of parallelism was the relative sizing of the different wire bundles. The other driver was the width of the mechanism. Higher levels of parallelism decreased the difference in bundle size, since the bundle sets became more and more equal in size. The high levels of parallelism would, however, make it more difficult to construct a mechanism of reasonable width. This is explained further in Figure 6.22.

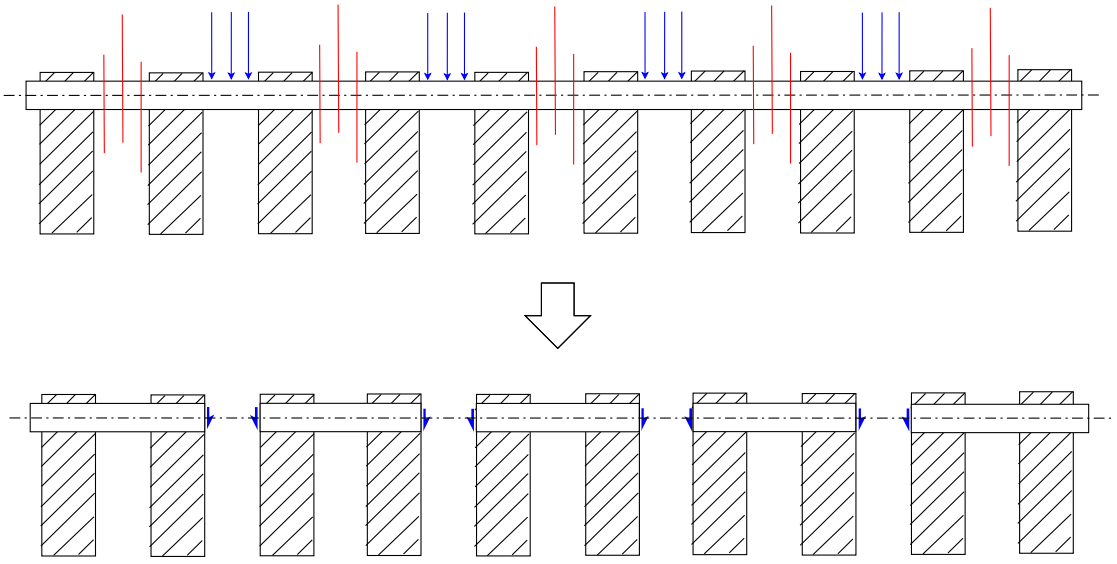

FIGURE 6.22: Actuator pins sizing concept

It is seen that two bundle sets(subscript *bs*) exist, each with a different amount of wire bundles. The sets were named based on the amount of wire bundles(subscript *b*). The set with the larger amount of bundles was called *l*-arge *b*-undle *s*-et(subscript *lbs*), the smaller set was similarly, called *s*-mall *b*-undle *s*-et(subscript *sbs*). The number of bundles contained in each bundle set was then denoted by $N_{b,lbs}$ and $N_{b,sbs}$. The sum of these two bundle sets gave the total number of bundles($N_{b,T}$) within the actuator and could be, in terms of the number of parallel arms(N_{arms}), as follows:

$$N_{b,T} = N_{arms} - 1 \tag{6.40}$$

With bundle quantities then:

$$N_{b,lbs} = N_{b,T}/2 + 0.5 \tag{6.41}$$

and

$$N_{b,sbs} = N_{b,T}/2 - 0.5 \tag{6.42}$$

Note that $N_{b,T}$ is not the number of arms in each quadrant, but rather the total number of arms that interface with a specific pin, as is indicated in the figure. $N_{b,T}$ will also be an even integer greater than 4 and N_{arms} will then always be an uneven integer. Based on these quantities the forces transferred by each wire bundle could be calculated as follows:

$$F_{b,lbs} = F_{SMA}/N_{b,lbs} \tag{6.43}$$

$$F_{b,sbs} = F_{SMA}/N_{b,sbs} \tag{6.44}$$

Equation 6.45 then estimated the percentage difference in force contributed by the bundles in each set.

$$F_{b,err}\% = \frac{F_{b,sbs} - F_{b,lbs}}{F_{b,lbs}} * 100\% \tag{6.45}$$

This error was plotted for different arm quantities in Figure 6.23.

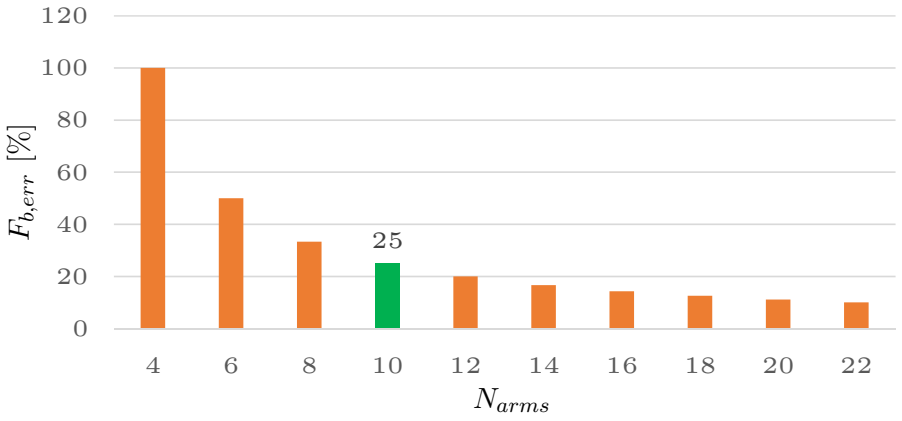

FIGURE 6.23: Wire bundle force difference for different levels of parallelism

A value of 10 was selected for N_{arms}; this was considered a good compromise between the force difference and the design effort for an actuator with higher parallelism. Note

that the design difficulty encountered refers to architectural decisions etc., which formed a part of the iterative procedure of generating a viable design and cannot be quantified.

Arm sizes:

The force F_A in Equation 6.27 is referred to as a quadrant force, due to its location in the actuator coordinate system. The subscript A was given to all the arms that were located in the second quadrant as can be seen from the Figure 6.4. The number of parallel arms in a quadrant would be 5, following the specification of 10 arms per pin in the previous paragraph. These 5 arms included 3 normal, and 2 slightly bent stabiliser arms. The reader is referred to Section 6.1 for an overview of the design.

It was then assumed that the stiffness of the stabilizer arms were comparable to that of the straight arms, resulting in an equal distribution of the load between these 5 arms. The design load carried by the individual arms was then one fifth of the maximum quadrant force. Since the maximum F_A could correspond to the largest negative value for aerodynamic force, this design load can be expressed as seen in equation 6.46.

$$F_{arm,design} = F_{A,max}/5 = F_A\ (F_{aero,min})/5 \tag{6.46}$$

This force was plotted against θ_{act} in Figure 6.24 allowing a maximum value of $(F_{arm,design})_{max} = 228\ N$ to be identified

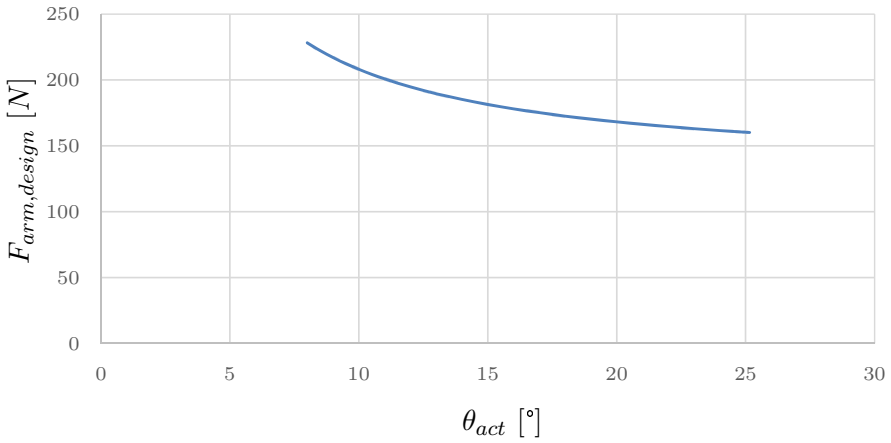

FIGURE 6.24: Axial forces in arms as a function of θ_{act}

The 2% proof stress of stainless steel 304L is 241 MPa, and 240 would thus be taken as the maximum allowable stress σ_{allow}. Setting the design factor(DF) to 4, to ensure a good safety margin under the uncertainty of the assumptions such as the equally shared load. By applying the design factor to the maximum stress, the design stress was found, as shown in Equation 6.47:

$$\sigma_{design} = \sigma_{allow}/DF = 240/4 = 60\ MPa \tag{6.47}$$

With a minimum cross-sectional area then defined as shown in Equation 6.48:

$$A_{min} = (F_{arm,design})_{max}/\sigma_{design} \tag{6.48}$$

The minimum cross-sectional area was then found to be 3.8 mm^2, which was rounded of to 4 mm^2 for a convenient 2 mm $\times$ 2 mm arm shape, which increased the design factor to 4.2:

SMA bundle sizes:

The SMA bundle sizes are related to their parent sets in the same way that the arms are related to the quadrant force through the assumption that the load is shared equally among them. Using this assumption, the required SMA cross-section was identified, using the maximum expected SMA force together with the maximum allowable SMA stress.

The stress was already set to $\sigma_{SMA,max} = 280\ MPa$ in Section 6.6, while the maximum value of the force experienced by the SMA was set to $F_{SMA,max} = 2260\ N$ in the same section. From these values, the required SMA cross-section was be found by the simple division in Equation 6.49.

$$A_{SMA,T} = \frac{F_{SMA,max}}{\sigma_{SMA,max}} = \frac{2260\ N}{280\ MPa} = 8\ mm^2 \tag{6.49}$$

The minimum stress($100MPa$) requirement can be used as a quick check of the design up to this point; equation 6.50 shows that with the selected cross-sectional area, and with the application of the minimum force, this design constraint was indeed met.

$$\sigma_{SMA,min} = \frac{F_{SMA,min}}{A_{SMA,T}} = \frac{807\ N}{8\ mm^2} = 101\ MPa \tag{6.50}$$

Within each set the force F_{lbs} is shared by the different numbers of bundles, which meant that the size of the bundles they contained would not be the same. The force per bundle in each bundle set was found by dividing by the amount of bundles in the set. This is shown in Equations 6.51 and 6.52.

$$F_{b,lbs} = F_{lbs}/N_{b,lbs} \tag{6.51}$$

$$F_{b,sbs} = F_{sbs}/N_{b,sbs} \tag{6.52}$$

Since these forces are related to stress through the cross-sectional area of the SMA bundles, the area of each bundle could be found by the dividing the bundle set by the same number as is shown in Equations 6.53 and 6.54.

$$A_{b,lbs} = \frac{A_{SMA,T}}{N_{b,lbs}} = \frac{8}{5} = 1.6\ mm^2 \tag{6.53}$$

$$A_{b,sbs} = \frac{A_{SMA,T}}{N_{b,sbs}} = \frac{8}{4} = 2\ mm^2 \tag{6.54}$$

A wire dimension of $d_w = 0.51\ mm$, since its cross-sectional area was such that multiples thereof would closely match the total cross-sectional areas required for each bundle. The number of wires that would be needed in each bundle was found in Equations 6.55, 6.56 and 6.57.

$$A_w = \frac{\pi d_w^2}{4} = 0.204 \tag{6.55}$$

$$N_{w,b,lbs} = \frac{A_{b,lbs}}{A_w} = 7.83 \approx 8 \text{ wires} \tag{6.56}$$

$$N_{w,b,sbs} = \frac{A_{b,sbs}}{A_w} = 9.79 \approx 10 \text{ wires} \tag{6.57}$$

6.8 Bundle Construction

The bundle construction proved to be a very important factor in the performance of the actuator, and, as such, required some attention as presented next. Both the mechanical and electrical connections are considered.

Mechanical connection:

In order for the wires/bundles to do their job, a strong mechanical connection was required. While pre-crimped constructions could be ordered from suppliers, the few ferrules/crimps used were all very bulky and heavy. While they undoubtedly would provide the necessary clamping force, they proved too large to be used in the available space, and other methods of connection needed to be explored. Copper and aluminium piping, as well as bootlace ferrules were tried in different configurations. The first

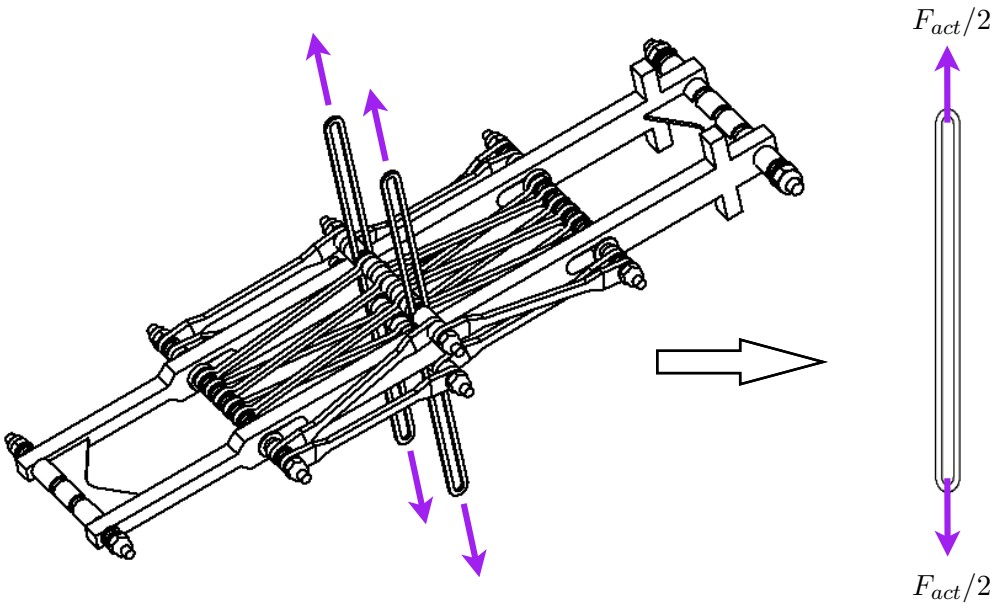

FIGURE 6.25: Tensile unit forces

attempt crimping the far ends of a continuous length of wire together proved not to provide the necessary clamping force. This led to the wires crimped ends pulling out of the crimped material. The next attempt was to crimp a larger pipe around the entire coil, hoping it would distribute the force transfer. This proved similarly ineffective.

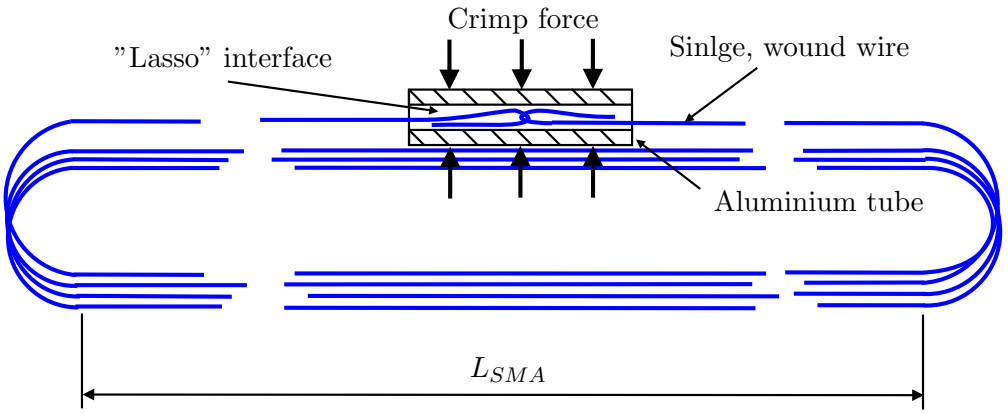

FIGURE 6.26: Wire bundle, series crimping strategy

Some way had to be found to transfer the force from the one end to the other directly, rather than relying on the friction between the ferrule and the SMA wire. Looping the ends round each other here called a "lasso" interface (Figure 6.26) proved an effective way of doing so. This lasso interface could be crimped either in a parallel manner, or in a series manner (Figures 6.26 and 6.27). The series construction of crimping the wires ends would distribute the force through the length of the wire. It could, however, lead to the unwanted bending at the rounded ends of the bundle, causing fatigue and eventual breaking of the wire. Some other thoughts on the matter were that if the wire broke,

the bundle would become useless, and that some uncertainty would exist regarding the effective electrical behaviour of the bundle (series vs parallel wires).

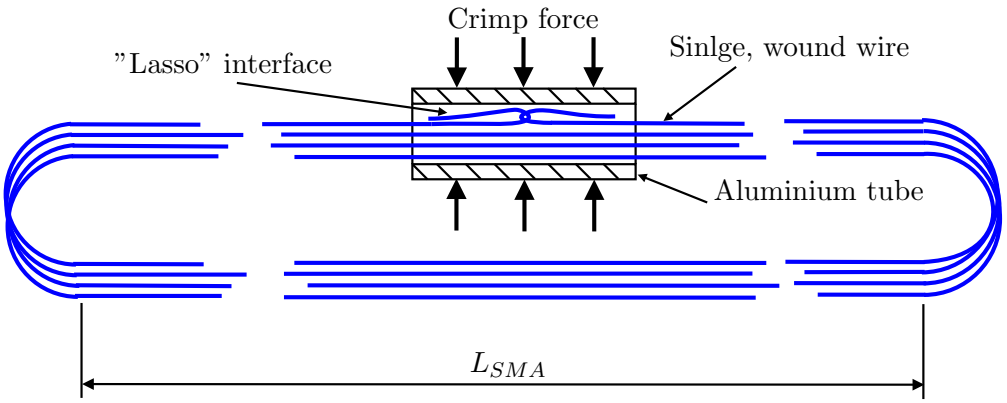

FIGURE 6.27: Wire bundle, parallel crimping strategy

It was decided to follow the parallel approach: there would possibly be some redundancy in terms of single loops that may fail, it was also easier to construct and electrically it would definitely present parallel behaviour. The result of this construction can be seen in Figures 6.28 and 6.29.

Electrical connection

FIGURE 6.28: Partial view of bundle construction(Crimping)

With the electrical connection, similar difficulties were encountered to those of the mechanical connection. The available crimp sizes proved too large for the available space. The mechanical construction at this stage had also been completed and therefore the crimps were required to have an open side. The pins from electrical connectors in computers provided such a function; they were made to be crimped to power supply wires

of a similar size. These pins were also expected to allow for the slight movement that the SMA wire would require inside them without loosening; in other words, they were expected to function similar to spring-loaded connections. The crimping was done over the entire bundle, similar to the mechanical connection in Figure 6.27, exuding obviously the lasso interface shown. The electrical connections can also be seen in Figures 6.28 and 6.29.

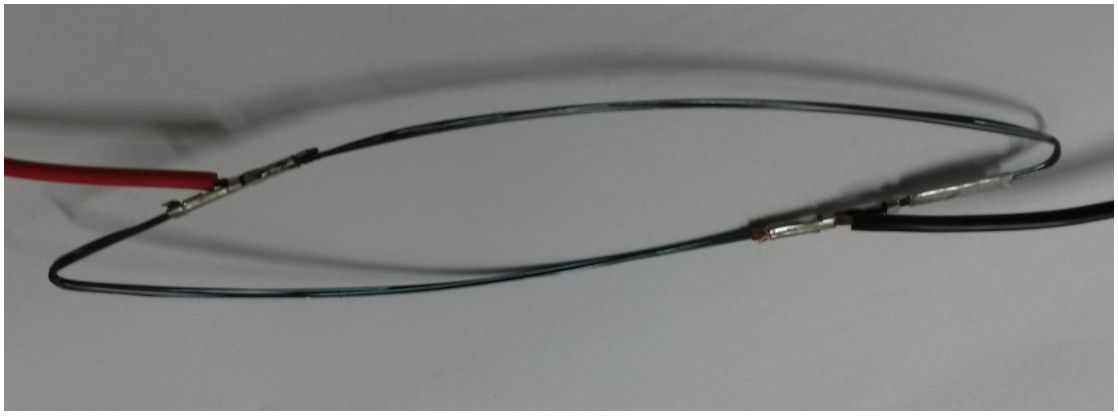

FIGURE 6.29: Full view of bundle construction

Chapter 7

Simulation

Many of the design decisions were based on the assumption that forces were distributed equally among the actuator arms. Although this significantly simplified the design, it was, without doubt, not completely accurate. To compensate for the uncertainty, the design included the use of safety factors, which would allow for operation without failure even when operating in conditions different from the assumed scenario. In spite of these safeguards, there would be a limit to the extent of the deviations that could be tolerated. As a result, it was necessary to test the load distribution within the actuator against the assumed conditions to confirm that the safety factors were sufficient. It would also be useful to assess the impact of the stabiliser arms, which were added for lateral stability.

These design checks would not be possible through simple structural calculations, due to the static indeterminate nature of the parallel arms. The small size of the arms also made the measurement of strain during the experiments impractical. It was thus decided to determine the load distribution using computer simulation.

The model and approach to simulation is discussed in this chapter, starting in Section 7.1 by a quick look at the use of NASTRAN super-elements. This is followed by Section 7.2, discussing the standard kinematic connections available in ADAMS. The kinematic model used for simulation in this project is then discussed in Section 7.3, and the results of said simulation follows in Section 7.4.

The first aim of the simulation was to assess whether or not the parallel arms did share the load equally, or in a manner close enough to it. This aim was met by applying realistic loading to the simulation model and showing that the resulting loads on the arms were sufficiently close in value. The second aim was to see if the stabiliser arms could indeed provide lateral stabilisation as was the intention. This was achieved by considering the largely unequal load distribution between stabiliser arms. The magnitude of the variation in load when compared to the much smaller load variation between the straight arms suggested that the stabiliser arms contributed much more significantly to the lateral stability of the actuator.

7.1 NASTRAN Super-elements

The super-element approach is an extension of the conventional Finite Element Methods(FEM). FEM can be used to solve the mechanics of complex structures. It is a discretisation method used to find approximate solutions to differential equations [57]. A physical analogy of the method would be breaking the structure up into small pieces or "elements" and solving simultaneously the physical law equations for all the elements that make up the structure. Conventional FEM however is highly computationally expensive, especially so in models that experience large displacements due to the need for non-linear analysis rather than the lighter, linear solving methods. The kinematic nature of the actuator in this project meant that this was exactly such a large displacement model.

To reduce computational requirements, conventionally meshed regions are replaced by super-elements. Boundaries are defined for these regions, as well as the interactions between these regions and their neighbours. The super-element then serves to include in the high level analysis the structural properties of the region as seen at its boundaries rather than a detailed analysis inside the region, much like a Thevenin equivalent circuit would do in electrical engineering.

The super-structure is broken up into substructures, which can be meshed individually. By subjecting the substructure to a modal analysis, reduced stiffness and mass matrices can be generated for it. This is stored in the form of a modal neural file (mnf), which can be reused within the super-structure, were there are multiple occurrences of a part. The stiffness matrices of all super-elements can be assembled into what is referred to as a *residual structure*. The behaviour of the residual structure is described by a largely reduced set of equations to be solved. During the high level simulation, this means that a reduced set of equations are solved at every iteration step.

The simple example given in the NASTRAN super elements user guide [10] is that of a linear set of springs, shown in Figure 7.1

Defining two super-elements such as those shown in Figure 7.2 results in a residual structure, shown in Figure 7.3. As is indicated in the figure, the reduced stiffness matrix for this residual structure contains a single displacement and stiffness for high level solution. The resulting displacement and stiffness seen is thus only that which is seen at the defined boundary node.

The reader is referred to the super-element guide for details on the generation of stiffness matrix and data recovery.

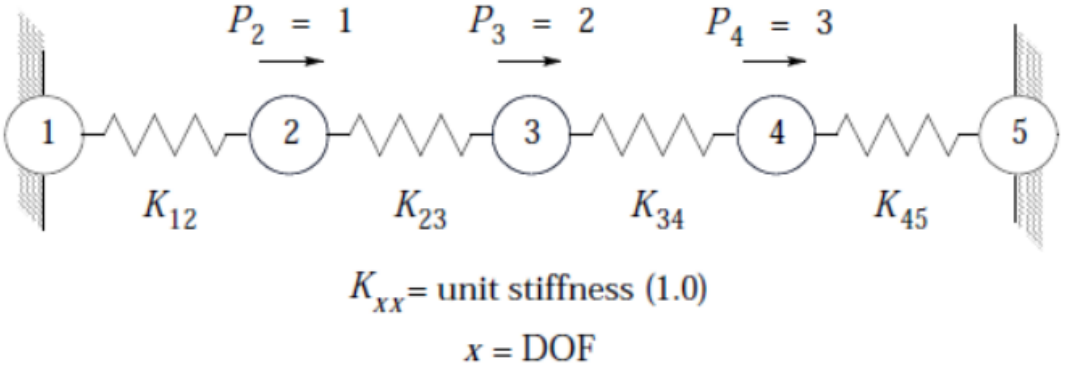

FIGURE 7.1: NASTRAN super-element example: super-structure [10]

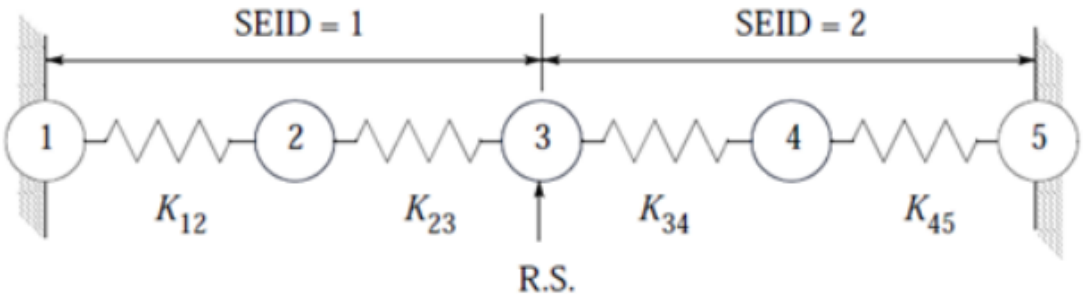

FIGURE 7.2: NASTRAN super-element example: super-element grouping [10]

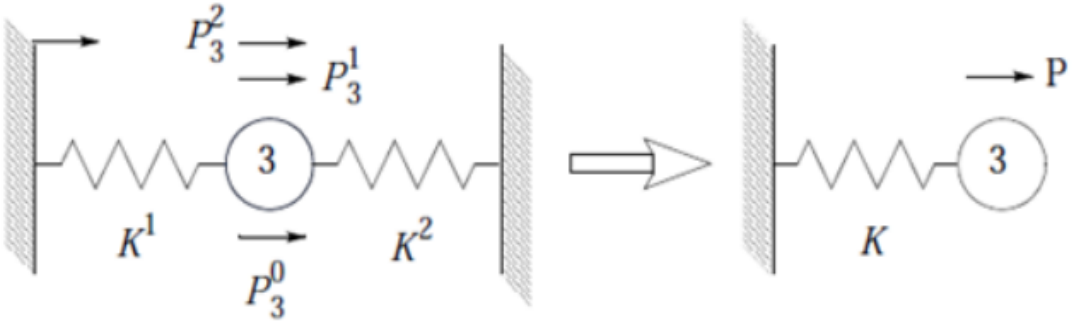

FIGURE 7.3: NASTRAN super-element example: residual structure [10]

7.2 Kinematic Connections

SimXpert motions workspace, like ADAMS, allows for mathematical relations to be defined between different parts of a mechanism. This, however, is a tedious process with some potential pitfalls. It is also numerically less refined than the connector capabilities in ADAMS, which are predefined. This meant that one needed to select from a multitude of options, the connection that was most representative of the physical operation of the actuator. To facilitate the choice, some connector variants are now briefly discussed. Note that the information in this section is taken from the Motions Workspace Guide by MSC Software [11].

The most basic and, often, useful connectors are referred to as "joint primitives". These are not generally aimed at representing an actual physical mechanism, but rather a numerical behaviour. Higher order joints are then formed by superimposing the primitives on each other. It is these higher order joints that are then meant to represent the connections found in real mechanisms such as hinges.

The joint primitives defined in the motions workspace are as follows:

- Atpoint - The origin of two coordinate systems always remain coincident, no rotations are contained.
- Inline - A part can move only in such a way that a point defined on it remains coincident with a line defined on another part.
- Inplane - A part can move only in such a way that a point defined on it remains coincident with a plane defined on another part.
- Orientation - Two parts will always have the same orientation even though they can translate relative to each other.
- Parallel axes - An axis defined on one part will always remain parallel to one which is defines on another part.
- Perpendicular Axes - The axis defined on ne part will always remain perpendicular to one defined on a second.
- Planar - A plane on one part can slide and rotate on a plane in another part.

The joint primitives are assembled into some interesting combinations. Some of these are fairly self-explanatory, and irrelevant in the current context, hence they will merely be named. These include constant velocity, rack-pin, screw, fixed and universal joints. All of which are obviously aimed at representing connections commonly found in machinery.

The remaining connectors(revolute, spherical, translational, cylindrical and hooke) had either less self-explanatory behaviours or were relevant in the current context, and thus warranted more attention in the current discussion.

The revolute joint, shown in Figure 7.4, allows rotation about a single axis. It constrains against all relative rotations, as well as relative translations between the two parts.

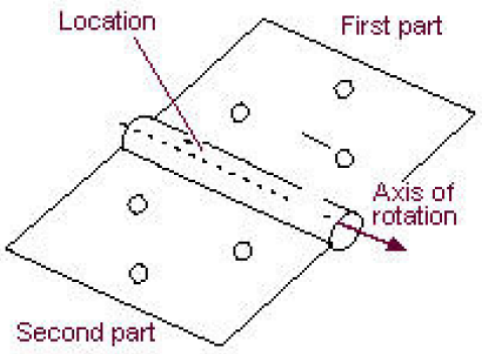

FIGURE 7.4: Kinematic Connections: Revolute joint [11]

The spherical joint(Figure 7.5) allows for free rotation in all directions between the two parts. It also constrains against any relative translation.

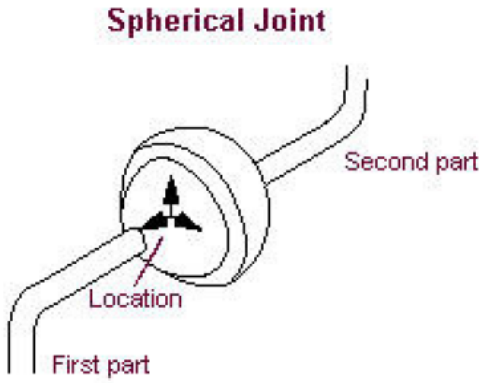

FIGURE 7.5: Kinematic Connections: Spherical joint [11]

The translational joint(Figure 7.6) constrains against any rotation, and allows translation only in a single direction.

The cylindrical joint constrains against two relative translations and two rotations. The remaining translational degree of freedom is directed along the axis of rotation that is left without constraint. See Figure 7.7 for more detail on this.

The final joint which to mentioned is the hooke joint. This joint is shown in Figure 7.8. Its functionality can be seen from the figure: this consists of constraints against

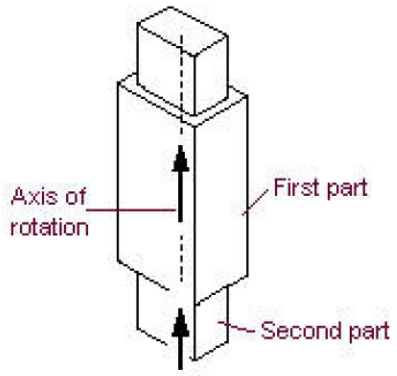

FIGURE 7.6: Kinematic Connections: Translational joint[11]

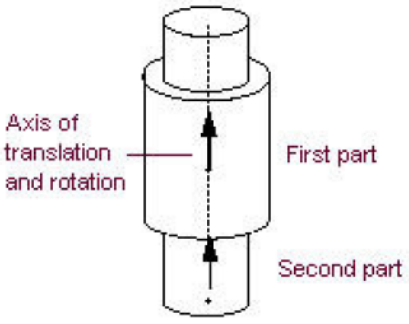

FIGURE 7.7: Kinematic Connections: Cylindrical joint[11]

relative translation and against a single rotation. This results in free rotation about two perpendicular axes.

While it is easy to identify which types of mechanisms While it is easy to identify which types of mechanisms are emulated by the different joints, the selection of the correct joint wass not as straightforward as it seems. The cylindrical constraint seemed most similar to the pin/arm interface found in the mechanism. The lateral sliding movement that it simulates was however at odds with the bushes in the mechanism that kept the arms at fixed distances from each other. The bushing suggested that the revolute joint may be more realistic. This joint, similar to the cylindrical joint would, however, keep the arm perpendicular to the pin axis. This constraint was not considered to be realistic, since the manufacturing tolerances of the mechanism was not so tight as to create in the mechanism a rigid connection between these degrees of freedom. Note that this did not

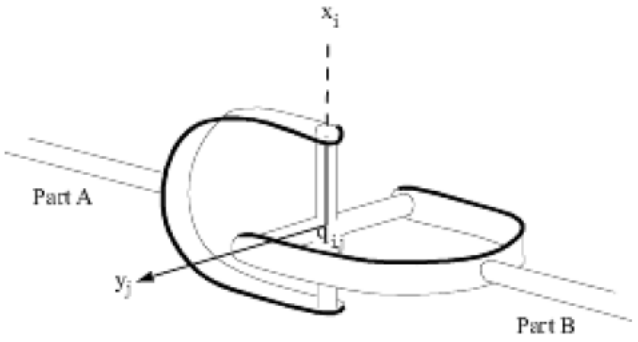

FIGURE 7.8: Kinematic Connections: Hooke joint[11]

apply to the stabiliser arms, which would be wedged against the pin by the tightening of the bolts against them, thus allowing moments to be transferred at this interface.

It seemed, then, that the hooke joint, while not actually being representative of the actual geometry of the mechanism, would likely yield the most realistic numerical behaviour. These joints, however, led to modelling issues that could be circumvented by the use of revolute joints instead. To make sure that their use did not violate the physics to any significant extent, the simulation results were checked for moment transfer at these joints. The moment transfer was found to be negligible, removing any concern about their numerical suitability.

7.3 Kinematic Model

The model was based on the CAD model discussed in Section 6.1. It was imported into SimXpert motions workspace where the arms were replaced with flexible bodies. Here the static indeterminate problem could be solved by replacing the rigid body representation of the actuator arms with flexible body representations. The flexible bodies came in the form of NASTRAN super-elements of which the generation and implementation is automated within SimXpert.

Figure 7.9 illustrates how this concept was applied in the current project.

The arms' solid model, on which the flexible body generation was based, used 1235 tetrahedral elements each with ten nodes. That of the stabaliser arms consisted of 1138 such elements.

10 Node tetrahedral elements(CTETRA10) are known for a reasonable accuracy under a variety of conditions. It can be used to represent full 3D linear strain, but it is not suited for second order strains, which would not be seen in this simulation.

The material parameters were defined as follows:

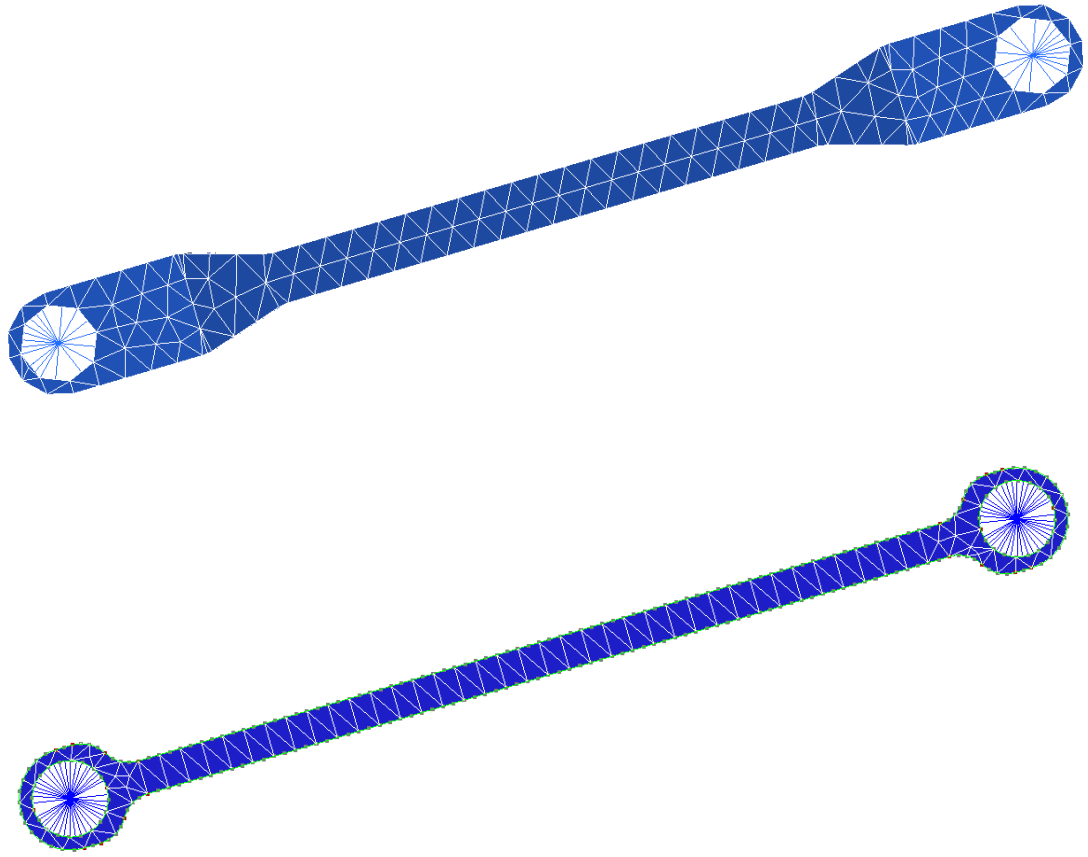

FIGURE 7.9: The meshed super-element used to represent actuator arms

- $E_{SS} = 207\ GPa$
- $v = 0.29$
- $\rho_{SS} = 7.801 * 10^{-6}\ kg/mm^2$

The first ten vibrational modes were used for the flexible body representation in order to capture its stiffness in all necessary directions.

The boundary nodes for the super-elements were set at a point in the centre of the "pin-holes". These nodes can also be seen in the figure. The boundary nodes were attached to the mating surfaces of the pin-holes using rigid RBE2 elements(visible in Figure 7.9).

The flexible arms were assembled in the complete actuator as shown in Figure 7.10. It was connected to a rigid representation of the pins, via revolute connections(Figure 7.11). The revolute joint fixed the translational as well as lateral rotational degrees of freedom relative to the pin.

Some effort was made to include friction between the pins and the arms. The computational requirements of this, however, was not worth the negligible difference seen in the results. Well lubricated stainless steel on stainless steel interfaces, as it happens,

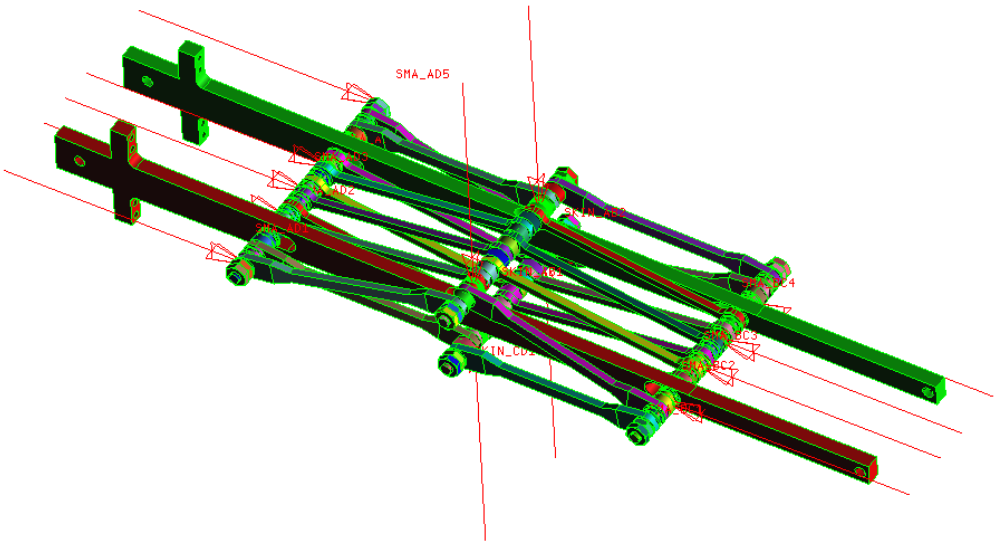

FIGURE 7.10: Kinematic model: Assembled actuator

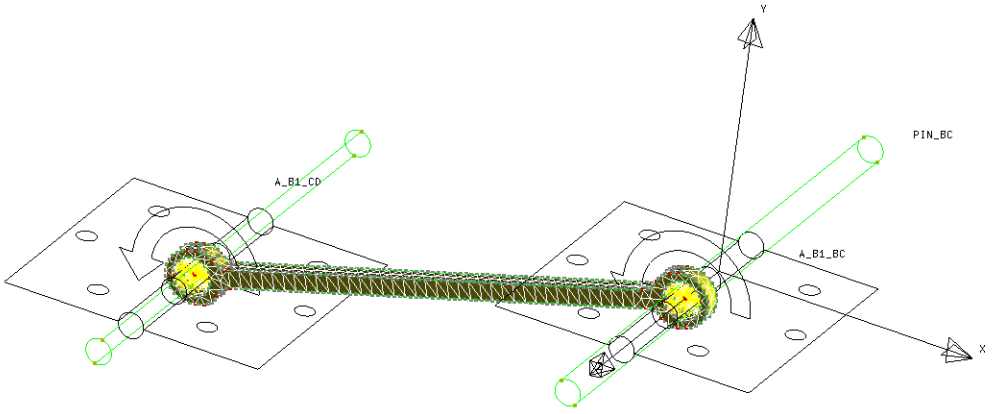

FIGURE 7.11: Kinematic model: revolute joint connections

have very low coefficients of friction(0.1-0.3 [58]). This meant that the frictional forces would be orders of magnitude lower than any other force in the system, and that their exclusion from the model was reasonable.

Forces were applied to the centrelines of the pins as shown in Figure 7.12, and the structural stiffness was simulated using a simple linear relationship, including pre-stretch, as follows:

$$F_{struct,i} = k * (\Delta y_{pre-stress} + \Delta y_{act,i}) \tag{7.1}$$

With the displacement for each stress measured at the relevant point of application.

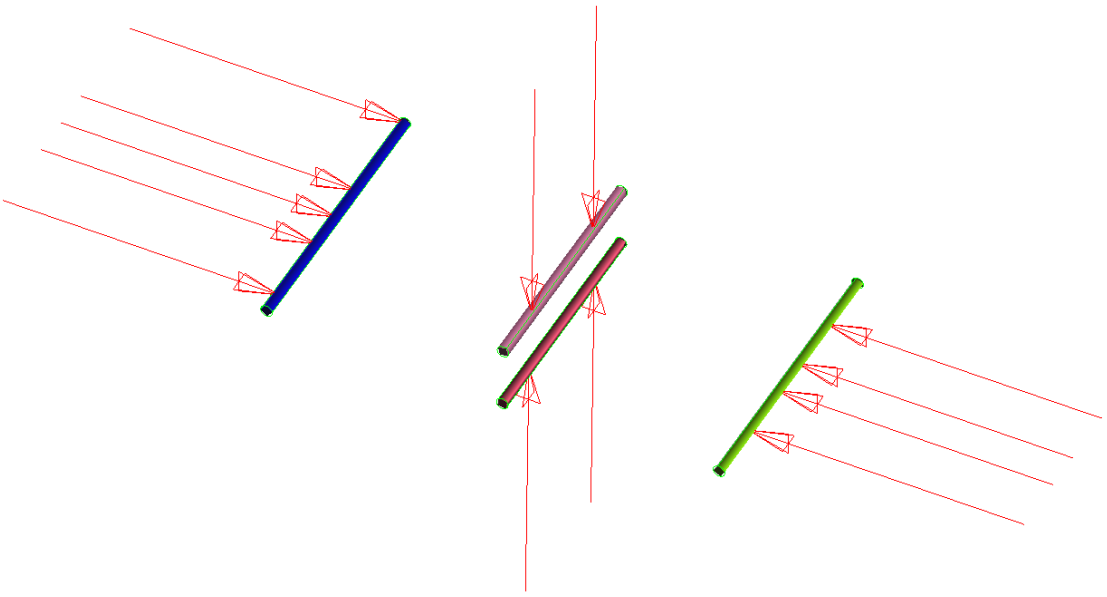

FIGURE 7.12: Kinematic model: Applied forces connections

The SMA forces were implemented using sub-routines. These provided an interface for co-simulation using MATLAB simulink. The load/displacement curve for the SMA material in this project was not, however, suited for application of common SMA models. And since the development of an applicable SMA model was beyond the scope of this project, it was decided that in the current iteration of the project the model would only be solved statically. The desired force distribution could then be found at the mechanisms functional limits. For this, the initial condition of the arm angle was set to that angle that was associated with the maximum force on the actuator arms. The SMA force associated with said arm angle was then also applied in a static manner.

To find the value of this load, a plot of Equation 7.2, the total arms load in quadrant A, is shown in Figure 7.13. Here $F_{act}(F_{aero}$ is the maximum actuator force that was derived in Section 6.6, its expression can be seen in Equation 6.29.

$$F_A = \frac{1}{\sin(\theta_{act})} * \frac{F_{act}(F_{aero})}{2} \tag{7.2}$$

It is clear that the maximum load on the arms would coincide with an arm angle of 8°. This was thus the position in which the actuator was placed at the start of the simulation. In theory, the actuator would be locked in this position until a sufficiently high SMA force was applied, thereafter, a stable equilibrium could not be computed, since there would be a negative force/displacement slope. For this reason, the static simulation was conducted with an applied SMA force slightly smaller than that which would be required to break free from the locked position.

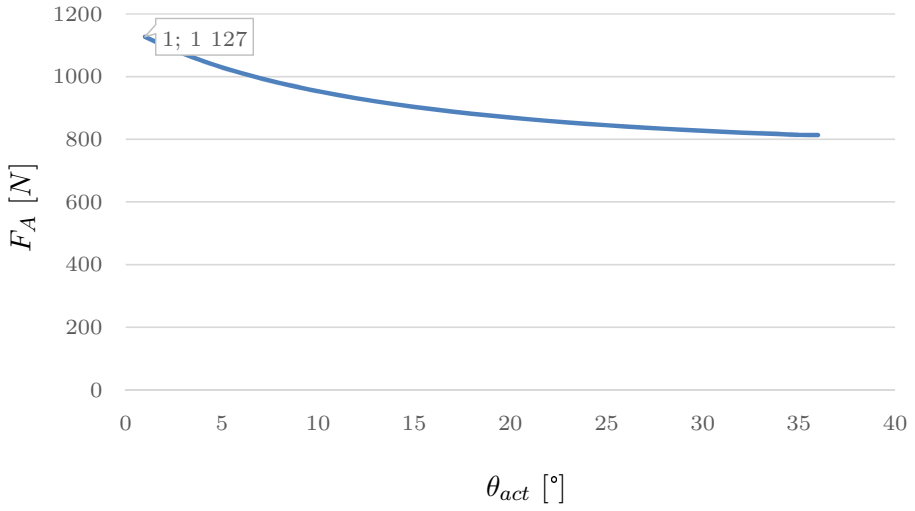

FIGURE 7.13: Arm force in quadrant A plotter against θ_{act}

The "breakout" SMA force would be 2259.6 N. The closest force to this for which a stable solution could be found was 2255 N. This was determined by defining a contact definition between the actuator base and the sliding pins, and determining an SMA force for which the contact force would become zero. In order to avoid numerical instabilities, a stiffness was assigned to the contact. While the exact value of the stiffness was not important, the non-rigid contact definition allowed for linear unloading to occur. The rigid-rigid contact alternative would result in discontinuities, and would not allow the solution to converge.

7.4 Results

In this section the results of the simulation are discussed; the purpose being to validate certain design decisions/assumptions. The first assumption was that all the arms shared the load on them equally. The force distribution results of the simulation were used to show that the variation in loads carried by the arms were within acceptable limits.

The force distribution was then further used to show that the stabiliser arms were effectively applied towards providing lateral stabilisation. The proof of lateral stability was the numerical stability of model itself, while the large variation in load between corresponding pairs of stabiliser arms was considered proof that these arms had the most significant distribution to this lateral stability.

Finally, evidence was shown that supported the use of revolute joints in the kinematic model used. The proof was based on the negligible moment transfer by these arms seen in the results.

For the purpose of this section, the actuator arms and stabiliser arms were grouped into quadrants and numbered to distinguish between different arms. The interfaces (A,

B, C and D) were consistent with those which were used during the design. Their definitions can be seen in Figure 6.4. In each of these quadrants, the arms were then numbered from one to three, and the stabiliser arms were numbered one and two. The numbering convention was such that in Figure 7.10, the number value would increase as one progressed further "into" the page. The progression for any quadrant would then be as follows(quadrant A as example): the first and closest stabiliser arm(Figure 6.4 as reference) would be S_A1; this would be followed by the arms A_A1, A_A2 and A_A3, and finally S_A2 which is the stabiliser arm furthest away from the viewer.

With these viewing directions in place, the results of the previously discussed simulation(Section 7.3) could be plotted. Figure 7.14 shows the axial force for each arm and Figure 7.15 the corresponding bending moment at the sliding pin interface for each arm.

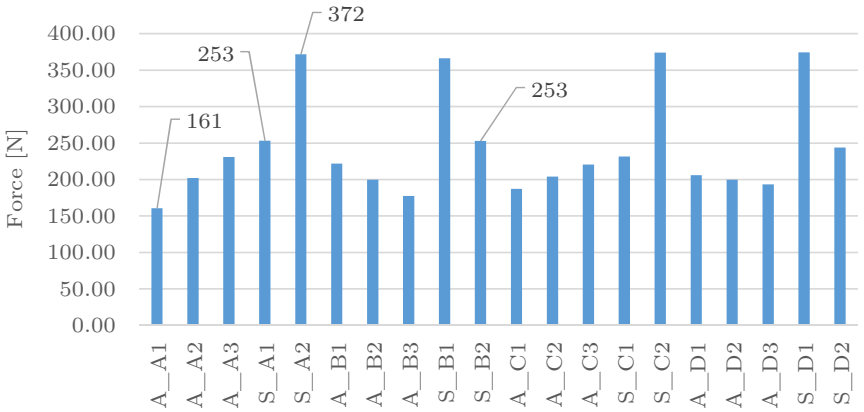

FIGURE 7.14: Kinematic simulation: Force distribution results

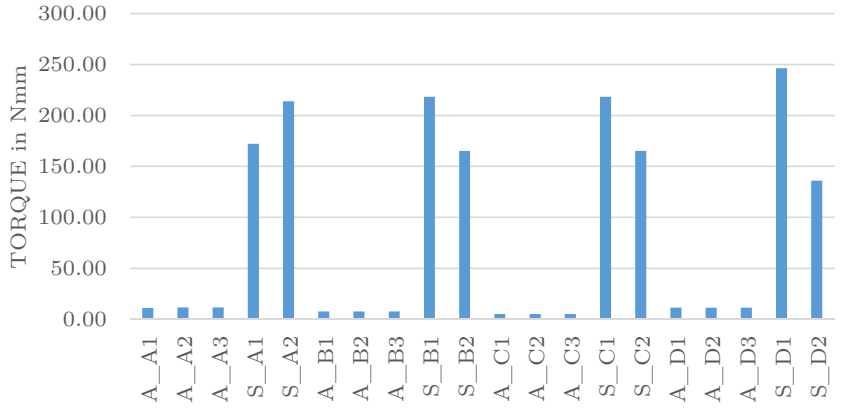

FIGURE 7.15: Kinematic simulation: Torque distribution results

Force distribution:

The results show that the minimum load on any given straight arm is 161 N and the maximum 253 N. The assumption made in the design, was that the force would be shared equally among all the arms. While some deviation from this assumption was expected, such deviation could be tolerated only to a certain extent. To assess whether the design would be valid in spite of this deviation, the parameters used in the design.

The design force used was 228 N, which would yield a design factor of 4. Hence, theoretically, a 400% increase in force could potentially be tolerated. The deviation of the loads found in the simulation from the load that the arms were designed for was a mere 6% for the straight arms, very much an acceptable deviation given the design parameters.

For the stabiliser arms, things looked somewhat different. While the same design force was used, the stabilising functionality was expected to superimpose, on top of this, an unknown amount of additional force. To compensate for this, the cross-sectional area of the stabiliser arms were set to 6 mm^2 instead of 4 mm^2, a 50% increase in cross-sectional area compared to the straight arms. The simulation results indicated a maximum force of 372 N for the stabiliser arms, this was a 56 % increase from the design assumption of 238 N. It is evident that, given the design compensation of 50 % increase in the cross-sectional area, the maximum axial force on the stabiliser arm is once again in the region of 6% larger than that which it was designed for. This 6 % is, however, not a true indication of the stress variation between the design assumption and the simulation, since the bending moment was ignored. This was deemed acceptable, since time constraints did not allow for a FEA to be performed on the stabiliser arm.

Lateral stabilisation:

The concept was discussed in Section 6.4: it came down to a triangular-shaped linkage that would be formed between the straight and the stabiliser arms. The lack of symmetry in distribution of the straight arms was expected to generate moments that would cause a lateral movement of the actuating pins. This triangular linkage would resist such lateral movement by transferring said load to the bottom pin.

The concept was tested by realising that a lack of a lateral bias would mean that all arms would carry equal loads, or, at the very least, any variation in force would be symmetrically distributed about the actuators centre. In reverse, this logic dictated that if forces were not symmetrical about the mid-plane, a lateral bias was indeed present. It then seemed reasonable that if a stable, converged solution existed, the elements that presented the largest deviation in force about the mid-plane could be considered the elements that most strongly resisted the lateral movement. By this reasoning, if the stabilisers worked, it was expected to show the largest variation in force about the centre of all the arms. In other words, the difference in force between the stabiliser arms

on each side of the actuator would be far more pronounced than the variation in force between the straight arms.

Looking at the results in Figures 7.14 and 7.15, it is clear that this requirement is met. There is indeed, in every quadrant, a significant difference in force between the stabiliser arms on opposing sides of the actuator.

Revolute joint validation:

Another conclusion that could be made from the results was that the revolute joints used in the simulation model provided a reasonable representation of reality. While the arms were, in reality, not expected to be capable of facilitating significant transfer of bending moments, revolute joints do allow for such moment transfer to occur. This led to a concern that, numerically, significant moment transfer could occur; hence not simulating the actual behaviour of the mechanism effectively. Since the results showed negligible moment transfer through the arms, this concern was found to be unwarranted, thereby validating the use of revolute joints in the simulation.

Chapter 8

Practical Experiments

The actuator was designed to meet certain high level requirements, which were derived from the goals set out by the customer. To meet these requirements, the actuator was broken down into different subsystems, each of which had a specific role to play in the functionality of the actuator (Chapter 3).

The design process(Chapters 5 and 6) then consisted of intuitive and mathematically motivated decisions, which determined as well as quantified these roles. While testing was required to determine the extent to which the high level requirements were met, it was also useful to determine the performance of each subsystem in terms of its own specifications.

Broadly then, the aims of the experiments were to verify the subsystem interactions. Narrowing the aims down was then an exercise in expanding the functional diagram in a way that it illustrated the design decisions and specifications in a such a way that it facilitated the making of a decision on which of these were important to assess. The diagram, provided in Figure 8.1, is a graphical summary of the designed actuator.

As discussed in Chapter 6, SMA wire coils of two different sizes were used in the actuator. These were grouped into two distinct sets, each driving a different pin in the linkage. Since the coils inside these sets were different sizes, the electrical properties of each set would be different, and therefore the currents required to drive them would be different. From this, two different electrical interfaces (E1 and E2) were identified, as shown in the diagram. The defining parameters at these interfaces were considered to be the driving current and power at each interface. These were parameters that were crucial to the effective testing of the actuator.

The first Experimental Outcome(EO) was thus:

EO 1 - To determine the driving requirements of each wire set

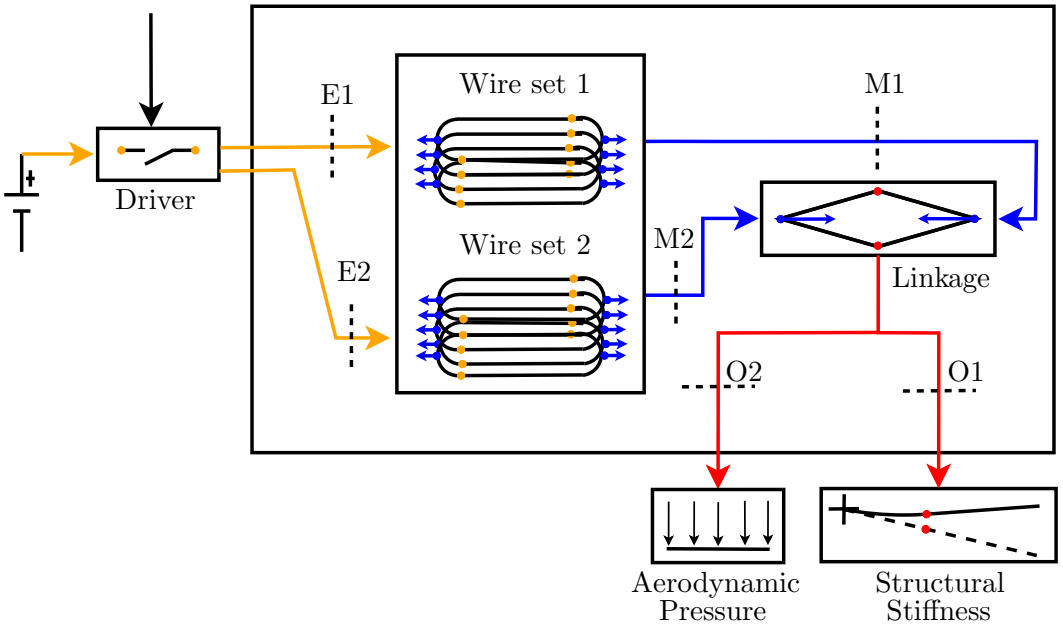

FIGURE 8.1: Subsystem boundary illustration

Once the driving currents were known, they could be applied to the wire sets, thus delivering to it the power it required to perform its functions in the system; these functions being to apply, at the mechanical interfaces M1 and M2, sufficient force and stroke to the pins of the linkage. During actuation this needed to be applied fast enough for actuation to occur in the required period of time. In the case of holding, on the other hand, the force needed to be sufficient for the linkage to remain stationary against the loads applied to it.

In order to test whether these functions could be performed, the next two EOs were defined as follows:

EO 2 - To demonstrate the actuating capabilities of each wire set within the current design

and

EO 3 - To illustrate the holding capability of each wire set under loading

The important variables at M1 and M2 are force and displacement. The force at the output interface would be controlled to match the equivalent aerodynamic loads, as well as structural loads that the actuator would be exposed to. The displacement, on the other hand, had to be measured. Direct measurement of force and stroke at the pins themselves would not be practical, or perhaps even possible. They thus had to be calculated, based on the measurements at the output interfaces (O1 and O2). The rigid nature of the linkage meant that the kinematics of the actuator was fixed, making the relationship between the output and the mechanical interfaces a simple trigonometric one.

Once the performance of the wire sets were verified, the next step was to determine whether or not these wire sets could be operated together. The opposing nature of the two sets meant that they would "pull" against each other, with the strain recovery provided by each wire set super-imposed on the other providing the full actuating stroke. They also needed to be successfully powered in series, since the current required for parallel operations would be massive (somewhere between 60 A and 100 A). The driving voltage in the parallel case would be between 0.5 V and 3 V, which is quite low, considering that the available voltage would be around 100 V.

All of these concerns could be grouped in the final EO as follows:

EO 4 - To assess the stroke capability of the actuator

The discussed interfaces and parameters are listed in Table 8.1, which serves as a summary of the parameters that would need to be measured in order to meet the EO's.

TABLE 8.1: system Boundaries

	Subsystem 1	Subsystem 2	Parameter
E1	Driver	Wire Set 1	Actuating Current Actuating Power Holding Current Holding Power
E2	Driver	Wire Set 2	Actuating Current Actuating Power Holding Current Holding Power Holding Power
M1	Wire Set 1	Linkage	Force Stroke
M2	Wire Set 2	Linkage	Force Stroke
O1	Linkage	Structure	Force Displacement
O2	Linkage	Aerodynamic Pressure	Force

The first three EOs referred to only one wire set at a time, each of which had to be assessed individually. The outcomes themselves, when applied to a specific wire set, were not mutually exclusive. The stroke capability of a wire set could be determined while driving that specific wire-set to determine what a suitable driving current was. The holding capability could then also be determined by applying a suitable current at the end of the actuation phase of a test.

EO 4, on the other hand, referred to the actuator as a whole, and needed to be met in a distinct experiment.

Three experiments were thus conducted. Two similar experiments, as discussed in Section 8.1 were conducted to test each wire set. A third and final run of tests, were defined as experiment 3, and would test the overall functionality of the actuator itself against design specifications, as discussed in Section 8.2.

All of these experiments were conducted using the same assembled actuator, measuring the same variables, and actuating the same subsystems in different combinations. The geometrical and functional similarities between the tests meant that the same test bench and similar test equipment, could be used for all experiments. This test bench is discussed in Section 8.1.1, with Section 8.2.1 highlighting mostly the changes made to said set-up to facilitate the simultaneous actuation of both wire sets.

8.1 Experiments 1 and 2: Wire set tests

The introduction to this chapter discussed in some detail the Experimental Outcomes. It was determined that for each wire-set, the stroke capability was to be determined, as well as the current needed to drive the actuation within the necessary period of time.

It was decided to focus on the study of power requirements. This would be an iterative study, and during the successive actuations in the study, the maximum stroke value could be determined from the same data. The power requirements would also apply to two different phases in the operation of the wire set, with an actuation phase needed before a holding phase could be started. This further meant that actuation and holding could also be assessed during the same run of tests. In such tests, then, the holding capability would be studied by not switching off the supply of current once the wire set had reached its full stroke. A suitable holding current then needed to match the rate of heat loss, so that the temperature of the SMA material did not change.

The experiment used to implement the above-mentioned approach is discussed in Section 8.1.1. The results of the experiment are discussed in Section 8.1.2.

8.1.1 Experimental Setup and Procedures

The experimental procedure followed is depicted graphically in Figure 8.2, with Figures 8.3 and 8.4 depicting the test bench on which this was carried out.

The test bench was made from rectangular tubing, which was strong enough to resist the moments that would be generated during the experiment. Its legs had to be long enough to give the weights used for actuator loading good ground clearance, while providing a

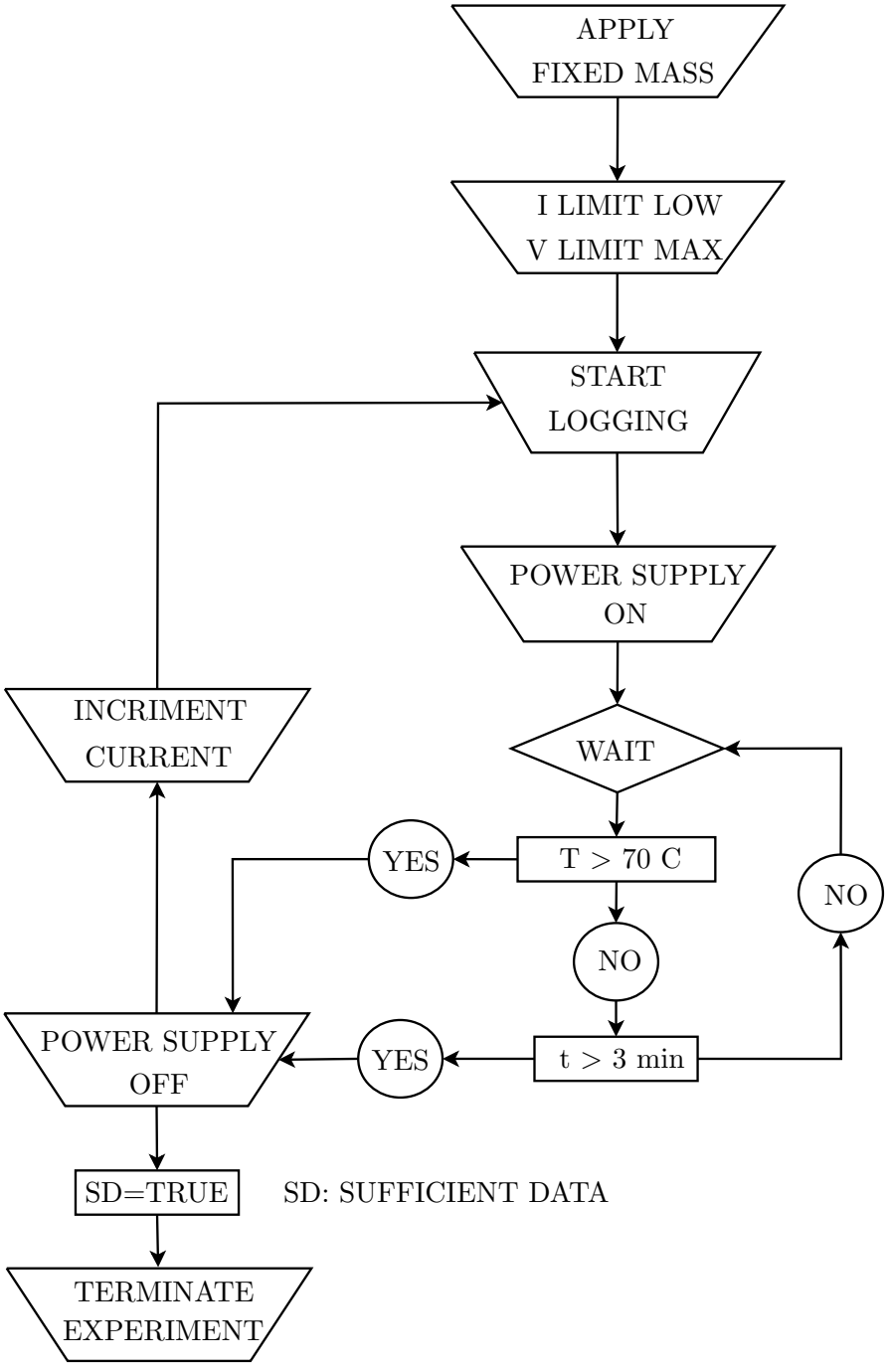

FIGURE 8.2: Wire Set Experimental Procedure

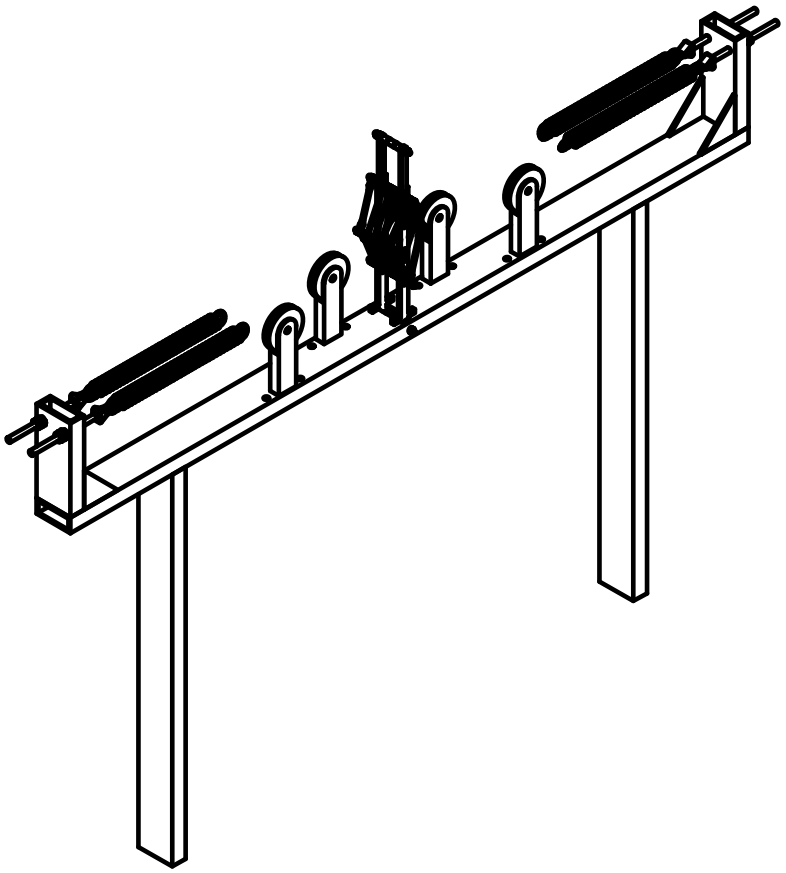

FIGURE 8.3: Universal test bench used for all experiments

comfortable work height for the operator. Four springs, each with a stiffness of 10.9 N/mm were used to simulate the structural force. When placed in parallel, the spring stiffness seen by each side of the actuator would be the 21.8 N/mm specified during the design phase. The springs were also designed to be capable of stretching the necessary 8.2 mm (half the total actuator stroke) without being damaged.

The set-up calibration was done by setting the pre-stress of the springs. To achieve this, eye bolts were used to attach the springs to the test bench chassis, and turn-buckles were inserted between the springs and the actuator. In the case of the wire-set tests, where fixed mass loading was used, the springs were left with enough slack that their contribution to the loading would remain zero throughout the actuator's stroke.

For the mass loading, weights were provided together with 4 ropes, each running on a pulley, from the weight to the force application points. Parachute cords were used due to their high strength (150 kg break strength) and high flexibility (minimum bend radius much smaller than the pulley used). The pulleys that these cords were passed over were made of a low friction coefficient plastic and ran on a smooth pin to avoid result biassing because of friction. The simulated load could be changed from positive to negative by shifting the force application point. A negative aerodynamic pressure would, for instance, be simulated by ropes routed along the blue lines in Figure 8.4 By

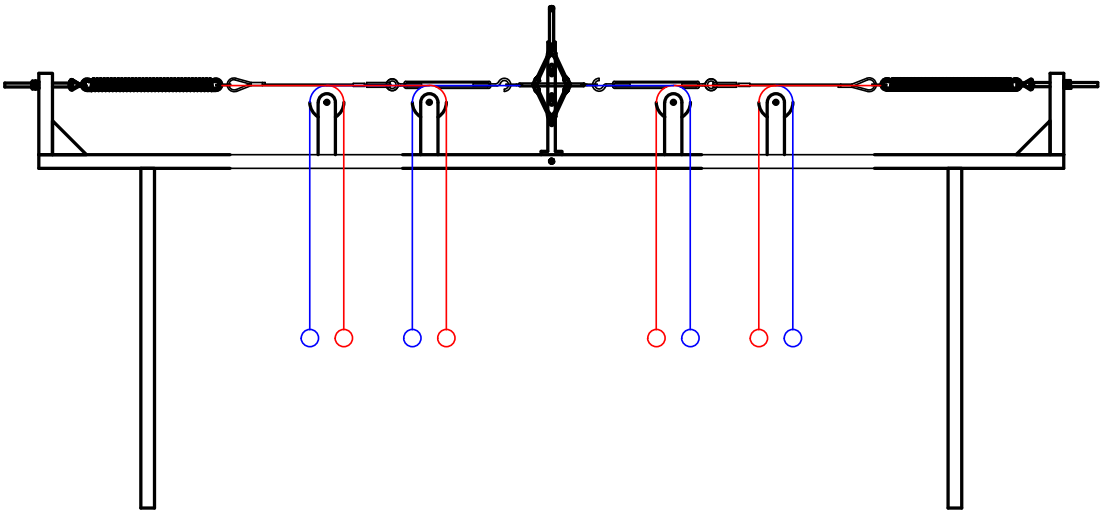

FIGURE 8.4: Universal test bench used for all experiments

rerouting the rope to the spring side attachment points along the red lines, the simulated load would be changed to a positive one.

The actual experimental set-up is shown in Figure 8.5 It includes close-ups of typical attachment points. Note that the rope hooks are attached near, and in line with, the opposing force(spring or actuating point). This is done to avoid errors in the direction of application of the forces.

Note also from this figure the aluminium tube, flattened over the force transfer nodes(FTN, the little triangle containing the attachment points). The tube provided the connection between the LVDT stroke measurement devices and the moving parts of the test set-up. It was connected to the FTN by a pin, and to the LVDT by thread in the other end of the tube. The measurement points were placed exactly midway between the spring attachment points, and in line with the cable that carried the loads between the actuator and the FTN. A convenient result of this arrangement was that the placing of the measurement points did not only allow measurement during the experiment, but also allowed a method by which to measure the spring displacement during calibration. The spring tension could be set by adjusting until the wanted pre-stretch was achieved for the springs on both sides of the actuator. This position would then be used as the reference point for further measurement.

Some other features provided were only used in the full-actuator tests, and therefore does not form part of the current discussion.

The variables listed below were to be measured during the experiment, and Table 8.2 shows the equipment used:

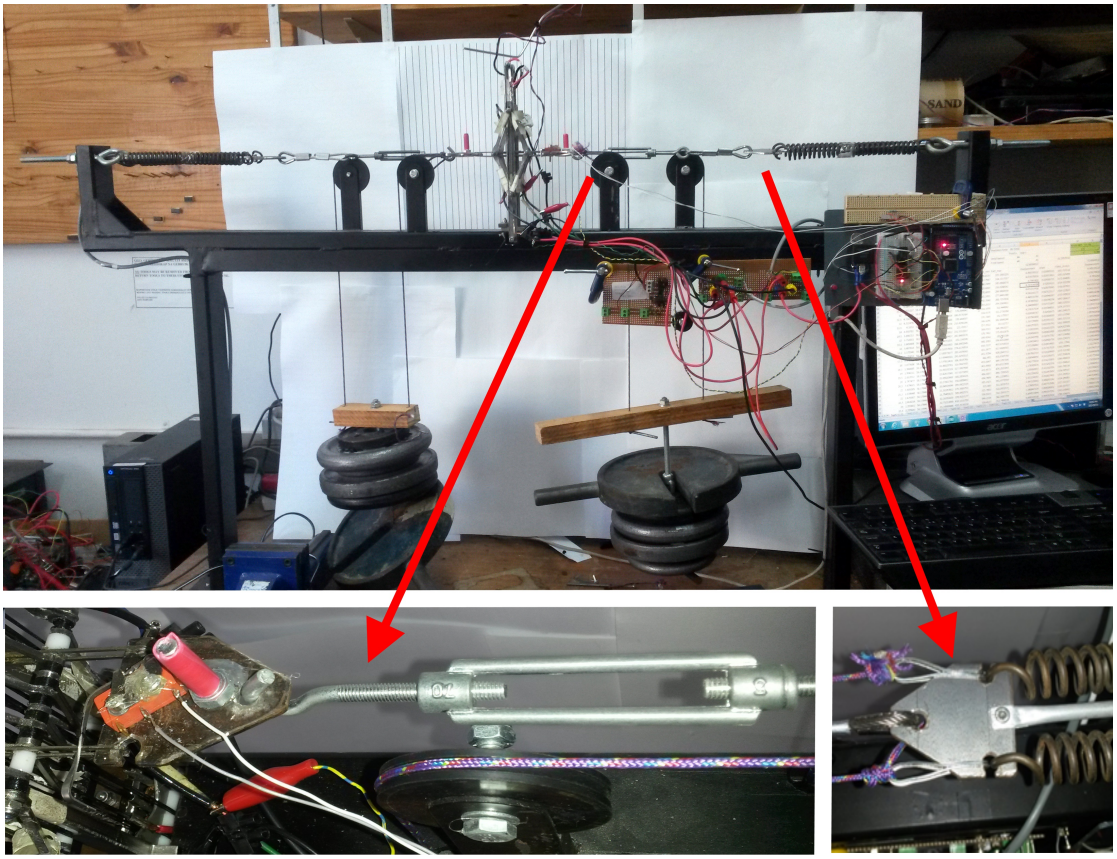

FIGURE 8.5: A photo of the test-bench used

- The current supplied to the wire set
- The voltage across the wire set
- 2 displacements, one on each side of the actuator
- The temperature on at least 2 of the bundles in the wire set

To shed more light on some of the decisions made regarding variables to measure, a short discussion is in order.

Temperature limiting

First it had to be noted that the electrical resistance of the SMA material would increase as the load on it increased. Since $P = I^2R$, in a constant current application such as this, more power would be delivered to the material if it was highly stressed. If the mechanism were to lock up, this could mean that excessive heat had been generated within the material, causing it to heat up to a point where the material lost its shape memory. While this would require a very high temperature, it was nonetheless a worthy concern and something to guard against until the functionality of the actuator had been

TABLE 8.2: Equipment for the experiment

MODEL	CLASS	APPLICATION
AGILENT 34970	Data logger A/D converter	Sensor reading
AGILENT 34901A	Multiplexer	Sensor switching
HP 6274B	Power supply	Actuator driving
	Power supply	Wire bundle driving
HBM AE301	Clip amplifier	LOAD CELL signal conditioning
HBM AE501	Clip amplifier	LVDT signal conditioning
HBM YP WA/50	LVDT	Actuator / Wire bundle displacement
HBM TYP WA/100	LVDT	Actuator displacement
Self constructed	T-type Thermocouple	Temperature measurement
Bare metal 0.2 ohm	Current sense resistor	Current measurement

established. With further design effort, intelligent control could be used to control these risks; however, in the current case a simple temperature limit would suffice.

As noted already, 2 temperatures were measured. This allowed for a reasonable chance to avoid thermal runaway, while not being so intrusive that it significantly affected the heat transfer inside the mechanism.

Displacement measurement

Three possible stroke-measuring strategies are depicted in Figure 8.6.

While one measurement would be sufficient in the direct measurement case, the construction of a device that arched over the mechanism would add unnecessary complexity to the design of the test bench. Another single measurement, the single actuation point measurement, could theoretically be used to determine the overall displacement, due to the symmetrical design of the mechanism. In a non-ideal case, however, the plane of symmetry could shift, due to imperfect loading conditions. This is illustrated in Figure 8.7. This shift in the case of a single measurement would result in an erroneous displacement reading(Equation 8.1), since any movement of the complete actuator would register as part of the actuator stroke.

$$(L_{REF} + \delta y + \delta y_{error}) - L_{REF} = \delta y + \delta y_{error} \tag{8.1}$$

By measuring on both sides, the actuator displacement was measured as both a positive and a negative negative value. The opposing readings would then cancel each other when the displacement readings on both sides were averaged, as shown in Equation 8.2.

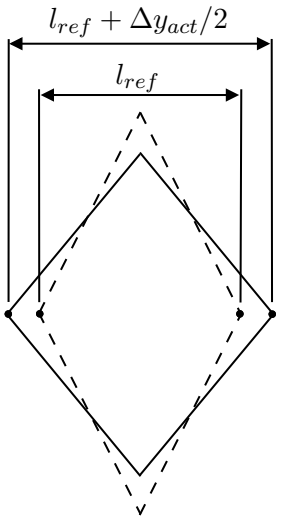

(a) Direct measurement

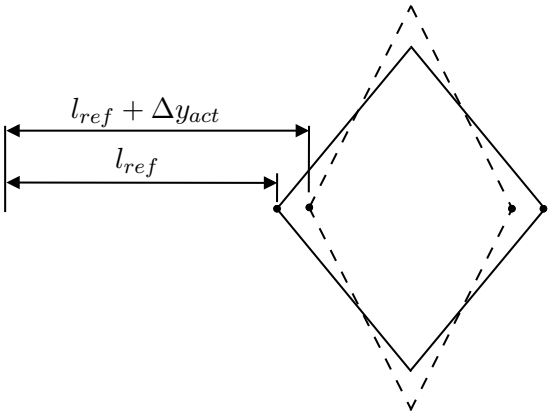

(b) Single point measurement

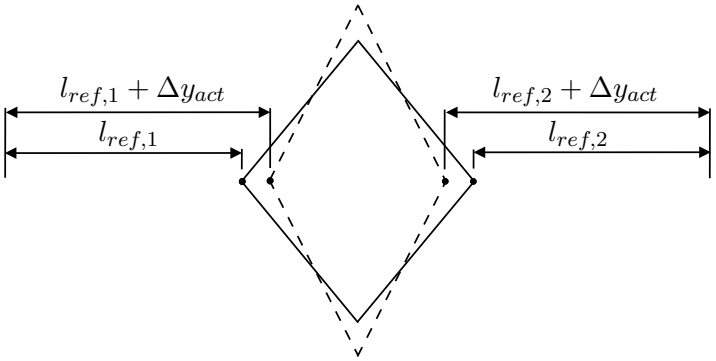

(c) Two point measurement

FIGURE 8.6: Stroke measurement options

$$1/2[((L_{REF,2} + \delta y) - L_{REF,2} + \delta y_{error}) + ((L_{REF,1} + \delta y) - L_{REF,1} - \delta y_{error})] = \delta y \quad (8.2)$$

Fixed mass loading

Realistic loading of the mechanism consisted of a fixed portion, which was meant to simulate the aerodynamic pressure, as well as a linear structural biassing load. Successful testing of the mechanism thus required the application of such forces to it. For the wire set tests, however, the author was more concerned with high level assessment of the wire capabilities than with the exact loading thereof. As a result, a fixed mass loading strategy was adopted. Fixed mass loading posed less risk than a linear one and was easier to implement.

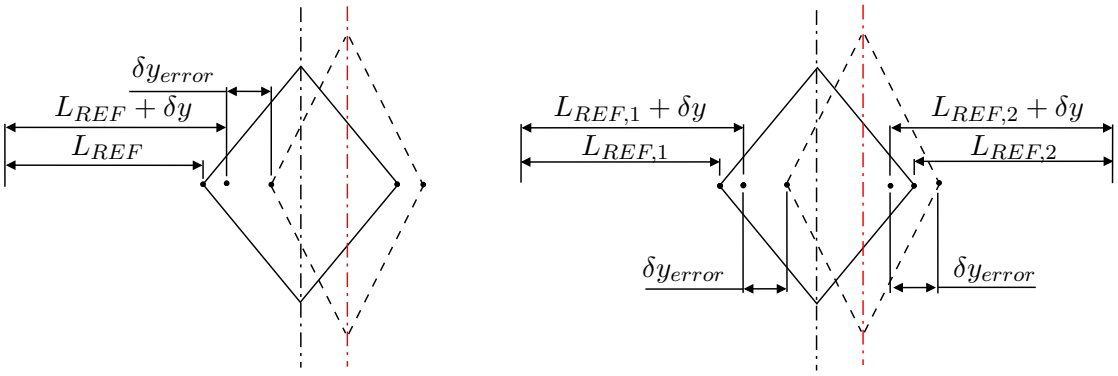

FIGURE 8.7: Stroke measurement error due to a shift in the plane of symmetry

The requirements of such a mass were the following:

- To be high enough that the "starting" stress on the SMA material would be realistic.
- To be large enough to yield the SMA material during reverse actuation so a full stroke could be reached.

Using the kinematic relations and material sizes specified in Sections 5 and 6 a fixed actuator load of 210 N was selected. This load made up a starting stress that was the average between the minimum and maximum estimated starting stresses for the SMA material, and could thus be considered a representative starting stress for a typical actuation.

The predicted SMA stress resulting from this load is shown together with the minimum and maximum design load profiles in Figure 8.8. See Figure 6.18 in Section 6.5 for the definition of θ.

8.1.2 Results

The goals set out for this experiment were:

- To determine the current requirements for each bundle set for a 10 s actuation.
- To determine a suitable holding current for each bundle during holding.

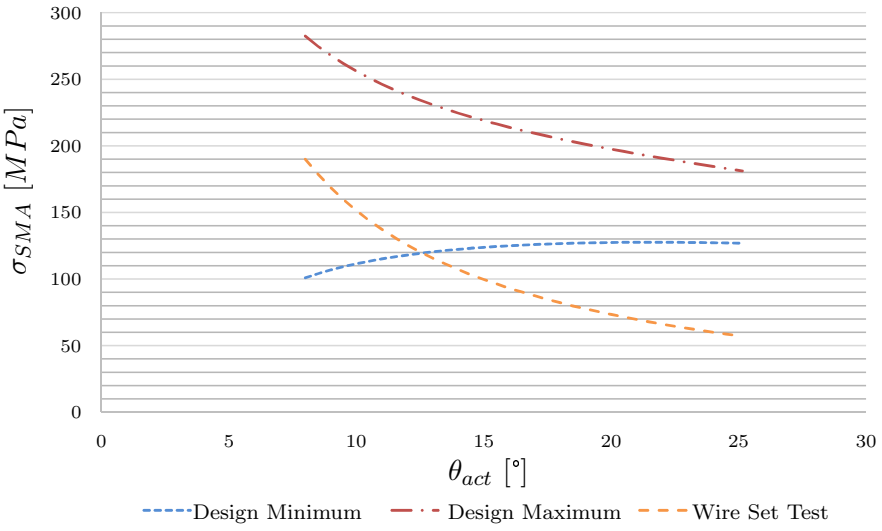

FIGURE 8.8: SMA stress estimate for 210 N fixed actuator loading

- To determine the stroke capability of each wire set.

The approach taken and the test bench used were discussed in Section 8.1.1. Since the experiment was applied to both wire sets the data analysis approach in each case was also identical. As such, the data analysis will be discussed using wire set 2 as an example. The results for wire set 1 will, however, also be given and discussed briefly.

The experiment consisted of successive actuations with a different amount of current applied during each actuation. The time/displacement characteristic of three such actuations is shown in Figure 8.9. From this graph it can be seen that, as expected, the time/displacement was not purely linear. Initially, actuation started up slowly due to the majority of the heat being used to heat the material to a point where the actual phase change starts to occur. Nearing the end of the actuation, on the other hand, a more gradual reduction in actuation tempo can be seen. This decrease in tempo is due to the increased heat transfer as the wire temperature increased, which meant that more of the supplied heat was lost to the surroundings, rather than contributing to actuation. Between these two phases, a reasonably linear actuation phase could be seen. This was the phase during which the majority of the phase change occurred. The author considered this region to be the most suited towards classification and comparison of the different reactions, since the other regions could be compensated for in some manner. The initiation phase, for instance, could be compensated for by pre-heating the wire before the actual actuation, and the slow-down phase would be compensated for by the fact that the majority of the necessary increase in lift would already have been realised by the time this slow-down occurred.

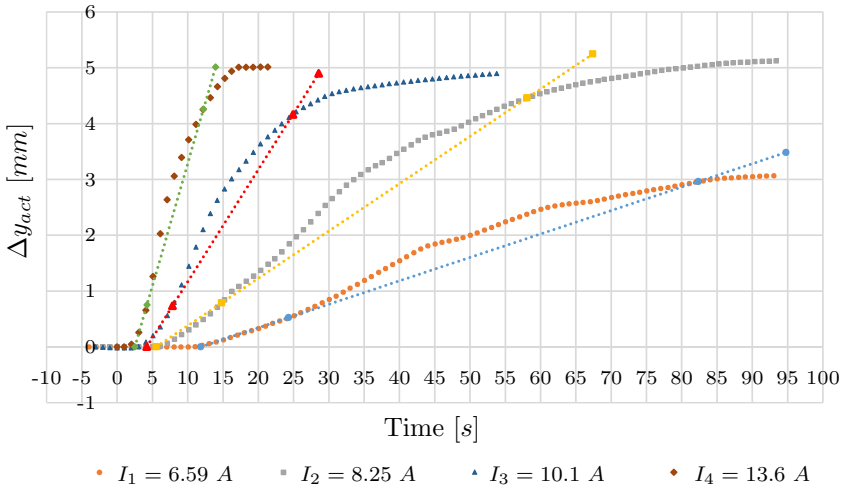

FIGURE 8.9: Bundle set 2(5 Wire) response to different driving currents

A practical difficulty with this was to define the initiation, actuation and slow-down regions. After some consideration, the actuation phase was defined as a linear displacement with its slope set by two points: one where actuation had reached 15% of its maximum value, and the other by where actuation had reached 85% of its maximum value as indicated in Equations 8.3 and 8.4. The time values associated with each of these points were found by linear interpolation of the available data. The calculated slopes were also indicated in Figure 8.9.

$$\Delta y_1 = 0.15 * \Delta y_{max} \tag{8.3}$$

$$\Delta y_2 = 0.85 * \Delta y_{max} \tag{8.4}$$

The required current was calculated based on these slopes. As mentioned before, it was assumed that the plotted lines sufficiently characterised the actuation period, and that the initiation period could be compensated for by pre-heating. Initiation compensated time/displacement curves would then have the same slopes as the ones shown, but these curve would have to pass through the origin. The characteristic equation of such an actuation would have the form:

$$\Delta y = [d(\Delta y)/dt] * t \tag{8.5}$$

By solving for t, and plugging in the previously used maximum displacement, a simplified actuation time could be found for each case. This provided the basis for fitting a curve

(Figure 8.10) of actuation time versus current, and using this simple linear interpolation to estimate a current that would yield the required 10 s actuation.

TABLE 8.3: Driving requirements for 90 W

Property	Unit	Bundle Set	
		Set 2	Set 1
Voltage	V	6.7	8.5
Current	A	13.4	10.6

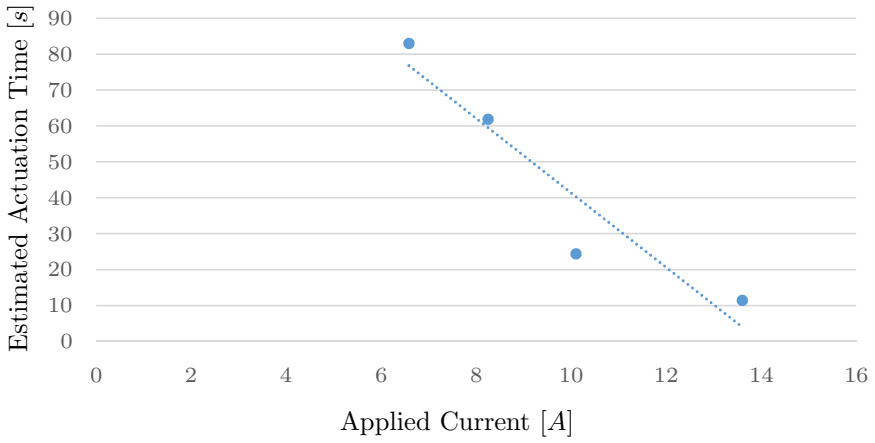

FIGURE 8.10: Bundle set 2(5 Wire) response to different driving currents

The currents identified for the two wire sets are as follows:

- Wire set one: 10 A
- Wire set two: 13 A

The voltages measured over each wire set allowed for the calculation of the power supplied during actuation. All the relevant values are summarised in Table 8.4.

TABLE 8.4: Driving requirements for 10 s actuation

Property	Unit	Bundle Set	
		5 Wire Set	4 Wire Set
Voltage	V	8.5	6.54
Current	A	10	13
Power	W	85	85

A different approach was taken to determine the required holding current. The heat loss during the holding phase, undoubtedly very different at different temperatures, meant that any fixed current would not keep the actuator static at varying environmental

temperatures. As a result, it was decided that the "static" position would rather be held by applying an on-off control strategy with a narrow switching range. A limit switch would detect the end of the actuation phase, after which the actuating current would be switched off, and a lower "holding" current applied. The actuator would then be allowed to relax slightly until some limit is reached, which would trigger the re-activation of the actuating current to return the actuator to its maximum position. The purpose of the holding current would thus be to reduce the rate at which the temperature decreased during this holding phase and, by doing so, limiting the rate of relaxation by the actuator. The result would be on-off cycles with longer switching periods.

The requirement for the holding current would thus be:

To be low enough for actuation to actually stop/reverse, while still being large enough to significantly reduce the rate of the actuators relaxation.

It can be seen, from Figure 8.9, that a current of 6.59 A could not drive the full actuation in a time anywhere close to the required 10 s. From the full data-set (showing the actuation over a longer time scale), however, it was seen that the current still produced continued actuation over a long period of time, until, eventually, the full actuating stroke was reached. This suggested that this current may be close to the current that needed to be identified, especially since the 20 °C temperature at which the experiments were conducted was considered to be reasonably high compared to that which the actuator may be exposed to in flight. Some further data analysis showed that a current of 5 A did not achieve the full actuation even after 3 minutes, and the actuator seemed to reach an equilibrium position at a point about 75% away from the actuators maximum stroke. This applied to both wire sets.

This current value of 5 A was thus chosen as the holding current for the actuator.

The final goal of the experiment was to determine the amount of stroke provided by the wire sets. This was a simple matter of applying the actuator kinematics to the maximum stroke measured during the experiment to determine what wire set stroke would have been needed to provide said stroke.

Equation 8.6 relates the SMA input stroke to the output stroke measured during the experiment, as well as the actuator position before actuation.

$$\Delta x_{SMA} = \sqrt{L_{arm}^2 - (y_{act,1}^2 + \Delta y_{act})^2} - \sqrt{L_{arm}^2 - y_{act,1}^2} \tag{8.6}$$

The starting point was measured in a manner similar to that shown in Figure 8.6a, using a vernier as the measuring device. The starting actuator width, $L_{act,1}$, was found to be:

$$L_{act,1} = y_{act,1}/2 = 23.38\ mm \tag{8.7}$$

thus

$$y_{act,1} = 11.96\ mm \tag{8.8}$$

And Δy was taken to be the maximum stroke achieved during all test-runs, which wass:

$$\Delta y = 5.02\ mm \tag{8.9}$$

Substituting these values together with the arm length of 58.18 mm into Equation 8.6 yielded a stroke capability of:

$$\Delta x_{SMA,ws2} = 3.67\ mm \tag{8.10}$$

This was the case for wire-set 2; the value calculated for Wire-set 1 in a similar fashion is shown in Equation 8.11.

$$\Delta x_{SMA,ws1} = 3.98\ mm \tag{8.11}$$

8.2 Experiment 3: Full Actuator Tests

The intention of this experiment was to verify the performance of the complete actuator. This was to be done by assessing whether the two wire-sets could be used in unison to provide actuation, as well as prevent reverse actuation while the actuator was exposed to realistic loading(holding).

Section 8.2.1 discusses the set-up and equipment, as well as the procedure used to conduct the experiment. This was largely similar to that which was done in the wire-set test, the difference being mainly that linear structural loading was applied in addition to fixed mass loading. Also, in this experiment; a single power supply needed to be used to apply simultaneously to each wire-set the current needed to drive it. The electronic equipment used to facilitate this is also discussed.

The set-up and procedures section is followed by Section 8.2.2, where the results of the experiment are given.

8.2.1 Experimental Set-up and Procedures

The test-bench used was the same as that described in Section 8.1.1, with the addition of electronics used to control the experiment. Also, in this experiment, the springs were

used to apply a linear structural load together with the fixed mass loading such as was used in the previous experiments. It has to be noted that this experiment was conducted in several runs, with two different variables being changed. To avoid any confusion, the following terms are defined to refer to different types of iteration:

Test series: A group of tests for which the spring-calibration is the same, and the fixed mass loading is varied

Test run: A specific iteration within a test series with a specific fixed mass load applied

The applied spring load, defined by the initial pre-stretch of the springs, was controlled by adjusting the turn-buckles, which were already mentioned. The purpose of the structural force would be to bias the actuator in such a way that the SMA material would be stretched during reverse actuation, even though a positive aerodynamic load would counteract the springs force to some extent.

While estimates were provided during the design for what spring forces would be needed, the possibility existed that other spring forces could also achieve a full reverse stroke. If a lower spring force could be identified than that which was estimated, this would prove advantageous, since the full actuating stroke could be achieved with structural components experiencing lower stresses. It could also point towards an alternative starting point in the next iteration of the project, were such an iteration to be conducted.

In order to identify such an alternative spring force, the approach taken during the experiment was to increase the pre-stretch applied to the springs incrementally. With each increase in spring pre-stretch, the strokes achieved would serve as an indication of whether or not a further increase was required to fully bias the SMA material. The full scale pre-stretch was specified in the design as 8.315 mm. Any other pre-stretch used was defined as a portion of this full-scale value. Different values of pre-stretch that were applied to the actuator during the experiment are shown in Table 8.5.

TABLE 8.5: Spring pre-stress values used during the experiment

Spring pre-stretch value $[c_s * \Delta S_{full}]$	Pre-stretch distance $[mm]$
$1/4 * \Delta S_{full}$	2.1
$2/4 * \Delta S_{full}$	4.2
$3/4 * \Delta S_{full}$	6.2

The different fixed masses that were used in each test-run are shown in Figure 8.6. These mass loads were chosen in such a way that the actuator would be tested in several parts of its operational envelope. Since the fixed mass loads were used to simulate the aerodynamic part of the total load, each load corresponded to a certain aerodynamic load. The equivalent aerodynamic pressure coefficient, a coefficient used to represent the aerodynamic load, for each fixed mass is also shown in the table. These coefficients

were scaled between the maximum and minimum aerodynamic loads ($0.2 \geq C_p \geq -0.4$), which were originally specified by the client. $F_{aero,max}$ and $F_{aero,min}$ are the force values associated with each of these coefficients.

TABLE 8.6: Aerodynamic loads simulated during the experiment

Load Number	Applied Force[N]	Corresponding C_p	% Of Full Load
$F_{aero,1}$	71.6	-0.21	105 % of $F_{aero,max}$
$F_{aero,2}$	22.6	-0.066	33 % of $F_{aero,max}$
$F_{aero,3}$	0	0	0
$F_{aero,4}$	-22.6	0.66	17 % of $F_{aero,min}$
$F_{aero,5}$	-71.6	0.21	53 % of $F_{aero,min}$
$F_{aero,5}$	-132.4	0.39	97 % of $F_{aero,min}$

A typical test run consisted of a calibration of the biassing springs and the iterative application of the fixed mass loads, followed by a complete actuation. The currents used to drive this actuation were those determined in the previous experiments. At the end of said actuation, an automated reprogramming of the laboratory power supply reduced the current to the holding currents (also from previous experiments), which was applied for the remainder of a three-minute period. The end of the actuation would be detected by a limit switch. This limit switch was calibrated to do so by adjusting its lever arm.

The discussed test-procedure is shown graphically in Figure 8.11.

A controller was designed to apply the necessary driving currents. See Table 8.3 for the relevant current values.

TABLE 8.7: Driving currents used in the experiment

Property	Unit	Bundle Set	
		Set 2	Set 1
Actuating Current	A	10	13
Holding Current	A	5	5

The control circuit, shown in Figure 8.12, was essentially a constant current supply, with an inner loop capable of tapping a controlled amount of this current off. By tapping off this current, the bundle set requiring the lowest current was partially short-circuited, hence delivering a lower current to it. A suitably biassed transistor was used as the current tap. Also included in this circuit were the bare metal resistors, which were used for the measuring of current in the previous experiments. In this experiment they were applied towards the same end.

The required resistor values were calculated by assuming ideal behaviour from the transistors, and the design was verified by simulating the circuit in LT spice. All relevant component specifications are shown in the table. Note that the resistance values used for the two wire sets were 0.5 Ω and 0.8 Ω. These resistance values were calculated from

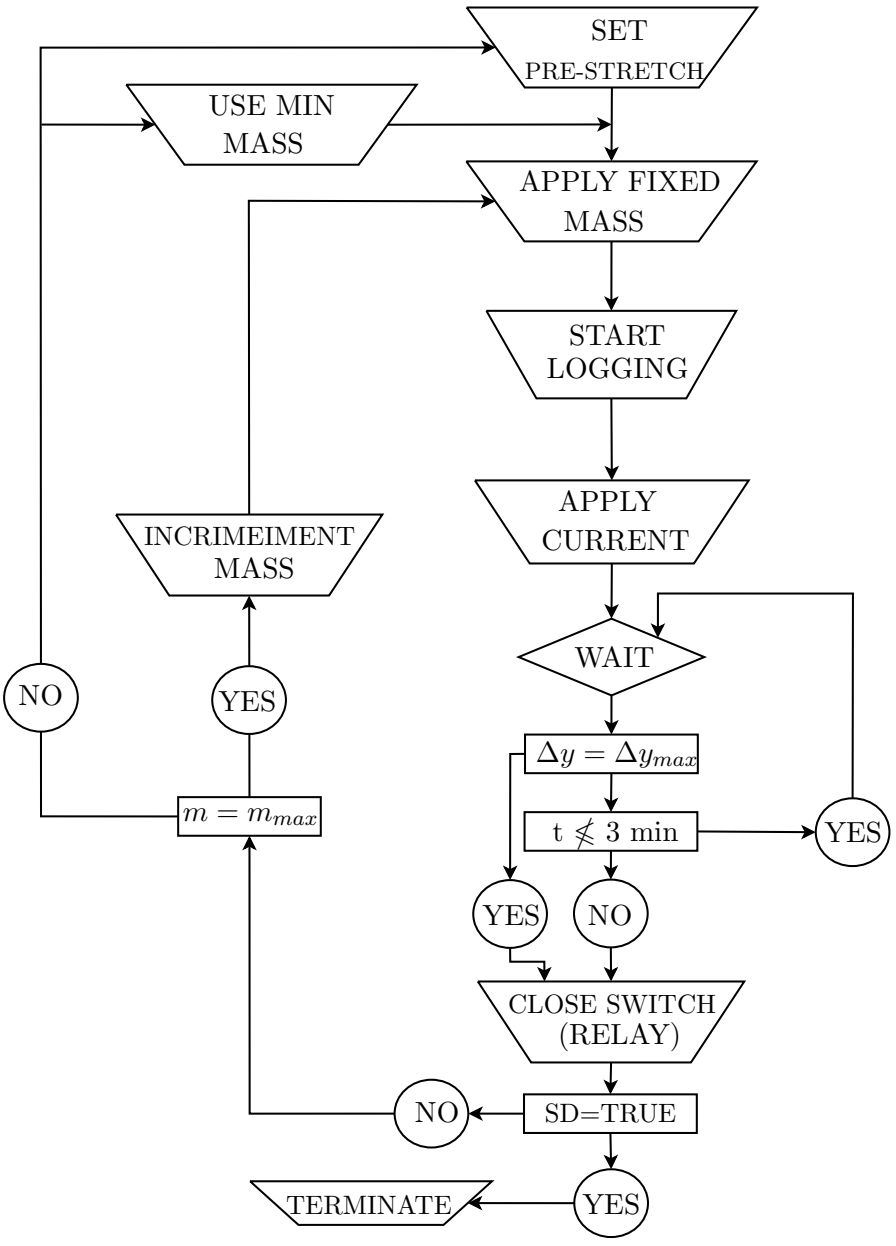

FIGURE 8.11: Full Actuator Experimental Procedure

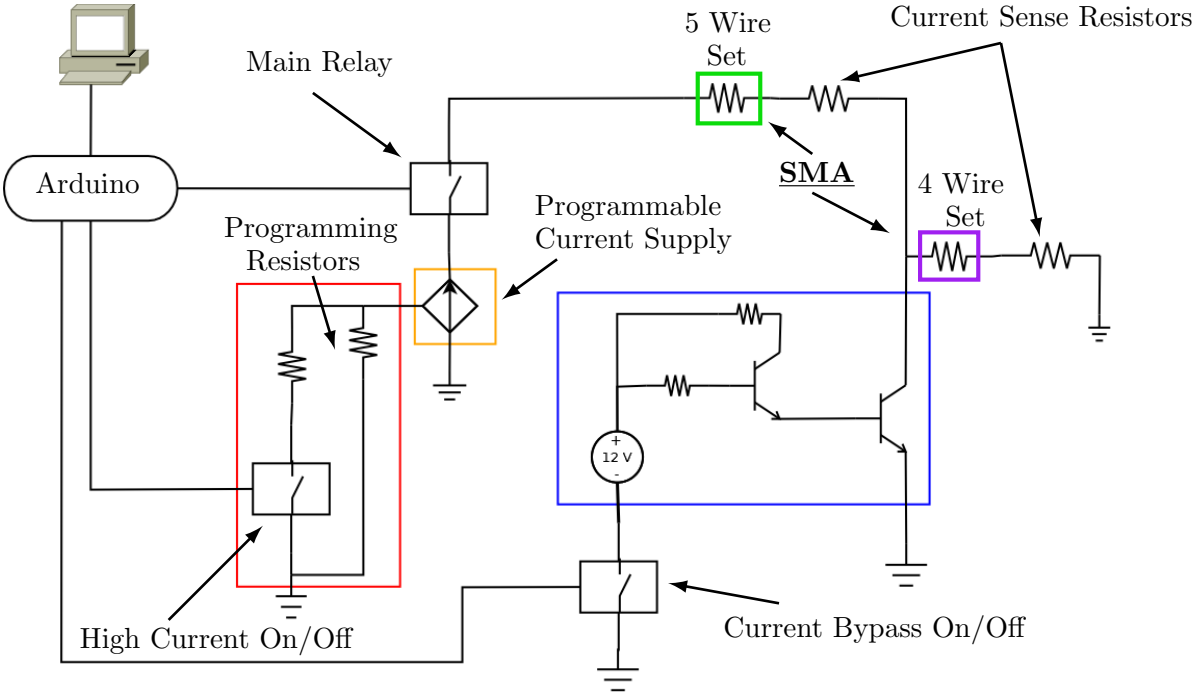

FIGURE 8.12: Control circuit

the voltage and current data in the previous experiments. Although the resistance of the SMA material does not have a fixed value, the average value used here proved a valuable assumption in the design of the circuit.

The algorithm depicted graphically in Figure 8.13 was implemented on an Arduino MEGA 2560 prototyping board to provide the necessary control.

The following mechanisms were used to issue the commands to the controller:

- Actuate Command - Computer Serial Command
- Reset Command - Reset button or computer serial command
- Time limit - Time tracking on controller
- Arduino on - USB connection to computer

8.2.2 Results

The results of the experimental procedure discussed in the previous section are now discussed. The discussion is largely focussed on the extent of actuation and holding capability of the actuator, as verifying the actuation extent of the actuator was the

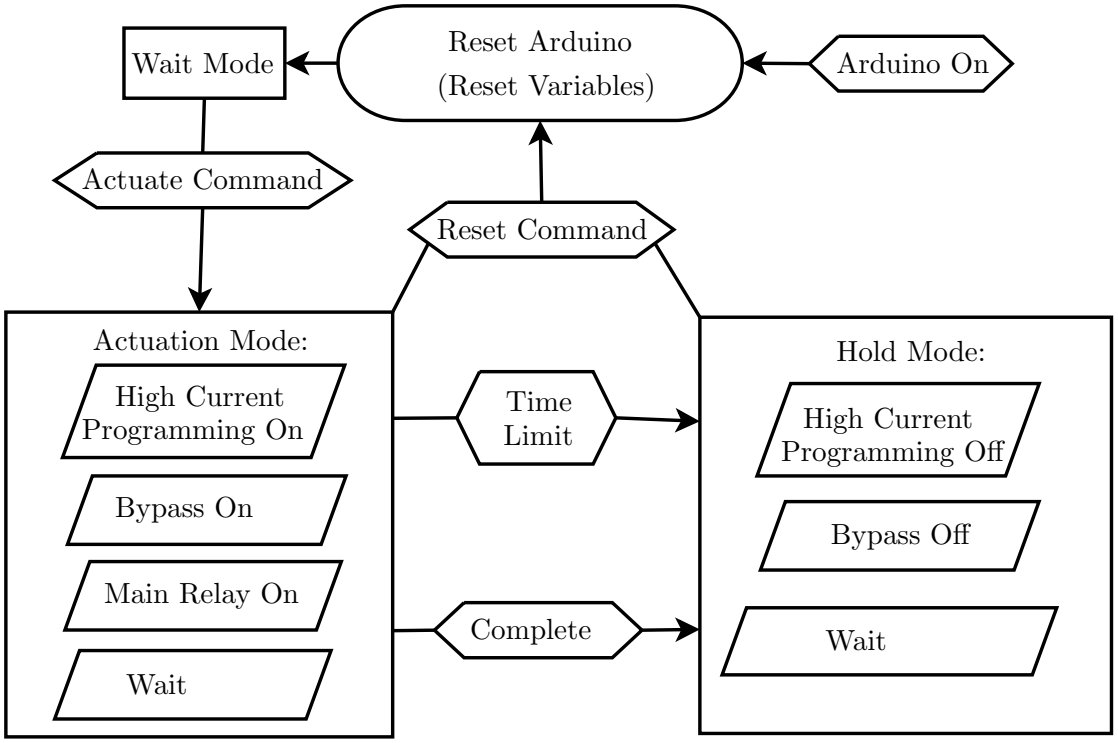

FIGURE 8.13: Control flow on Arduino micro-controller

outcome of this experiment. Some consideration is, however, given also to the time in which the actuation occurred, as well as the effect of spring pre-stretch on the extent of the actuation.

The following graphical definitions(Figure 8.14) of the actuator should serve as a reference for interpreting the results.

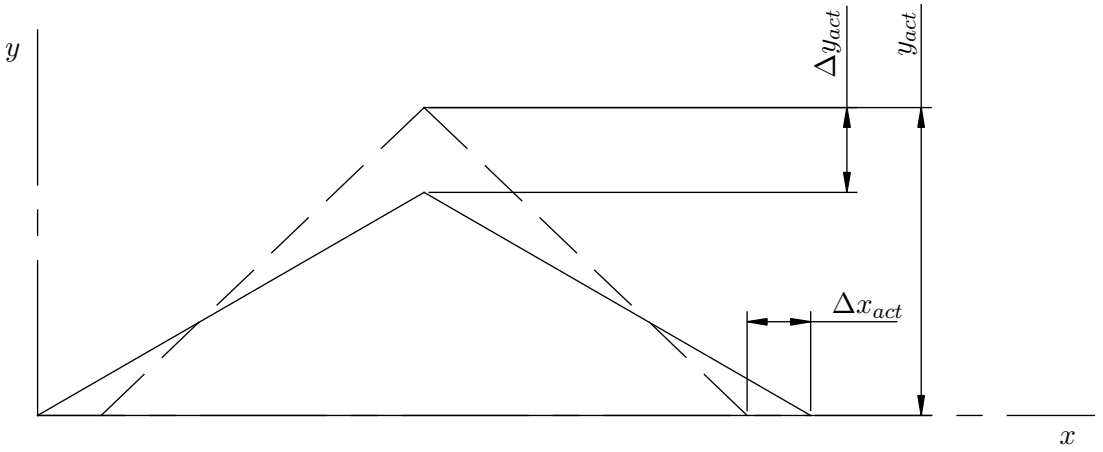

FIGURE 8.14: Result variable definitions

The desired performance of the actuator was as follows:

To provide a stroke of $\Delta y_{act} = 16.63\ mm$ in a period of $t_{act} = 10\ s$

See the time/displacement characteristic typical to the actuator in Figure 8.15. This particular curve was drawn for the case where the spring was pre-stretched to three quarters of the design value. The actuator was exposed to the full aerodynamic load.

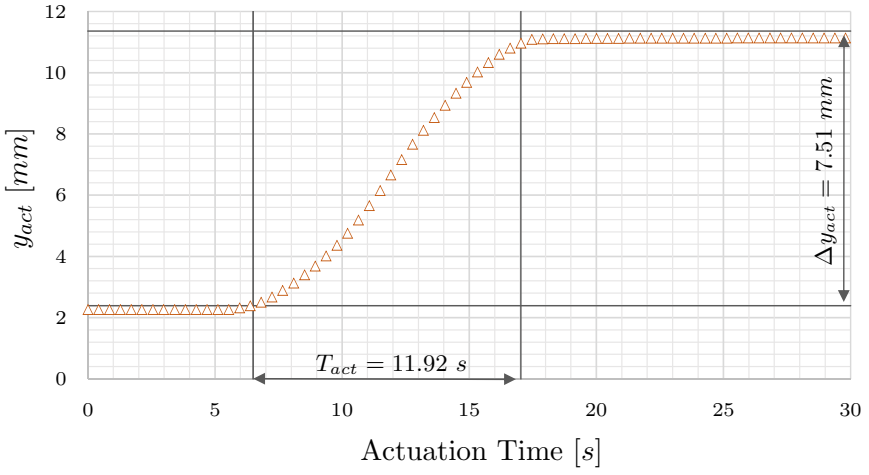

FIGURE 8.15: Actuation with full load and 3/4 spring tension applied

It can be seen that the time taken to complete the actuation was close to the design value of 10 s, but that the stroke achieved was much lower(about half) than the stroke specified in the design. At first glance it seems that the stroke was too small due to the spring pre-stress being set to only three quarters of what it was meant to be. A lower spring tension might then not supply enough stress to the SMA material to strain it sufficiently. To assess the validity of such an assumption, the achieved stroke is plotted in Figure 8.16 for different load scenarios.

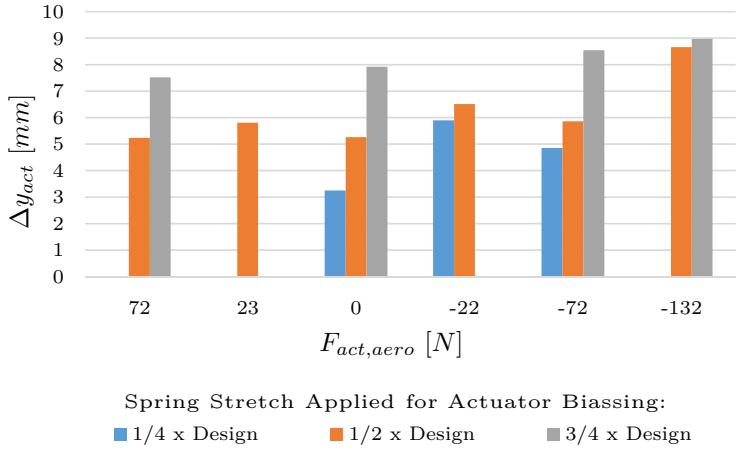

FIGURE 8.16: Actuator performance under various loads

A closer look at the displacements seen in all the test-runs, reveals that the stroke increased with increasing pre-stretch as was expected. It did, however, become somewhat saturated during the $3/4xS\Delta S_{full}$ calibration test-runs. This suggests that some other factor might be at play when it comes to the low stroke output of the actuator. It also indicates that this lower pre-stretch value might be more suited to the task than that which was originally estimated. To shed some more light on a possible cause of the low actuator stroke, consider the graphical representations of the actuation as shown in Figure 8.17. The figure includes actuator positions achieved by the actuator with its biassing spring tensioned to 75% of the full design value, and with the maximum negative aerodynamic load applied. The design intent is also shown in the figure for comparison.

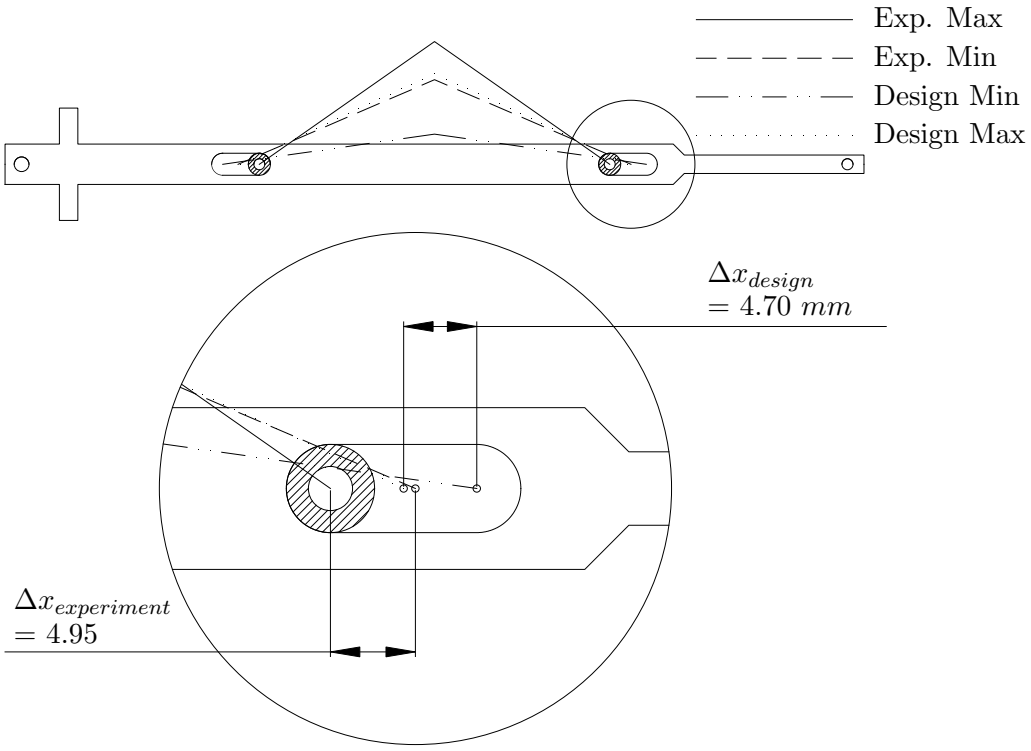

FIGURE 8.17: Graphical comparison between actual and planned actuator positions

From this figure, it is evident that when it comes to the stroke provided by the wire sets, there was not a large discrepancy between the design and the actual values. What did differ substantially from the design were the starting positions of the sliding pins. As a result, the end positions were also affected, together with the actual kinematics of the actuator. Since the stroke output of the actuator was largely dependent on the amplification provided by the mechanism, this change in the actuator kinematics had a significant influence on the relationship between the input and output stroke. The extent of this can be seen by plotting the effect that a change in x has on y.

In order to do this, one has to start with the relationship between x and y:

$$y_{act} = \sqrt{L_{arm}^2 - x_{act}^2} \tag{8.12}$$

The relationship between Δy_{act} and Δx_{act} at any x_{act} is found by taking the derivative of this equation.

$$\frac{dy_{act}}{dx_{act}} = -\frac{x_{act}}{\sqrt{L^2 - x_{act}^2}} \tag{8.13}$$

Figure 8.18 is a plot of this derivative.

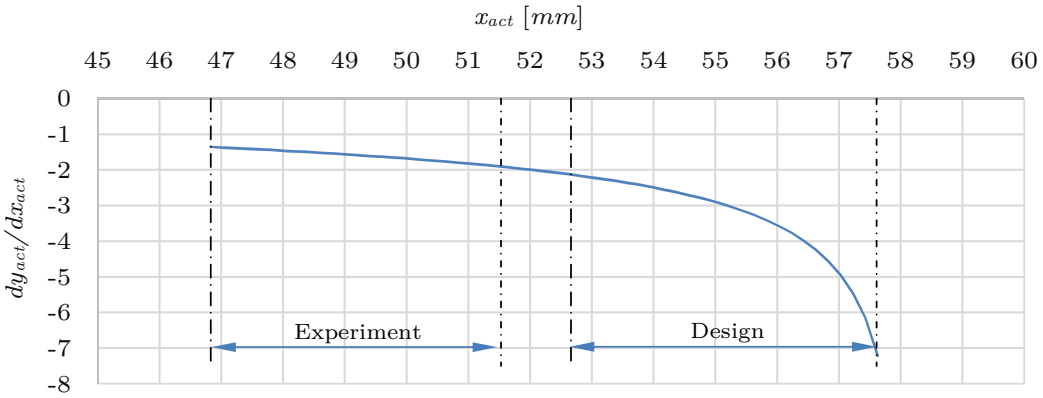

FIGURE 8.18: Input/Output relationship of actuator stroke

It can be seen that between the x-values seen in the experiment, the derivatives values are substantially lower than that which the actuator was designed for. To further quantify this effect, the area under the graph can be calculated.

$$\left(\frac{\Delta y_{act}}{\Delta x_{act}}\right)_{exp} = \int_{x_{act,max}}^{x_{act,min}} -\frac{x}{\sqrt{L^2 - x^2}} = 2.7 \tag{8.14}$$

with:

$$x_{act,max} = 49.36\ mm \tag{8.15}$$

and:

$$x_{act,min} = 53.44\ mm \tag{8.16}$$

This is a 20% decrease from the design value of 3.4.

The forces that acted on the actuator in these two scenarios(experiment and design) are shown in Figure 8.19 together with the resulting stresses on the SMA material. Both

the design and the experimental maximum and minimum curves are shown. On this figure, the difference in actuator starting point is very apparent.

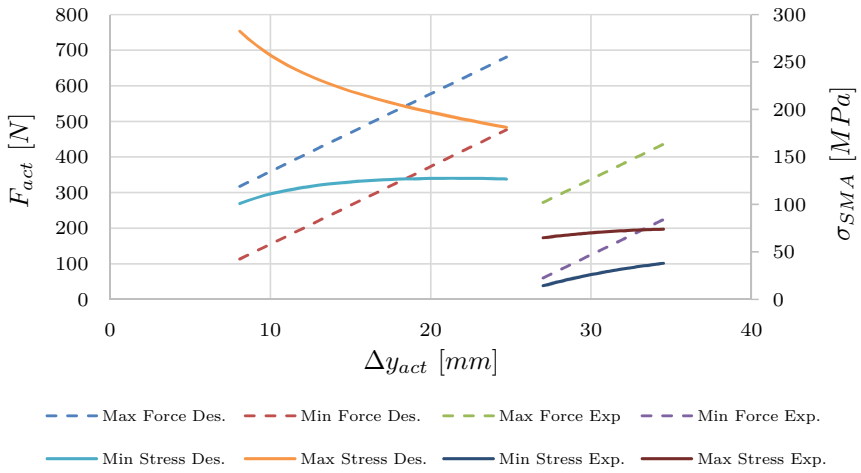

FIGURE 8.19: Actuator forces and stress: Design vs. Experiment

During the experiment, the actuator experienced substantially lower forces than was the design intention. This was accompanied with lower stresses seen by the SMA wires. The design stroke was however reached by the SMA wire bundles, as was shown previously. This was considered an indication that the stresses seen by the SMA material in the experimental case were perhaps better suited to a design of this kind of actuator than the stress estimates that were used in the design. A redesign of the actuator to function at these stresses would mean that a lower stiffness biassing structure could be used, together with smaller and lighter structural components for the actuator. It would, however, require some changes in the actuator, as the current design was already scraping up against the space constraints which were set. Either way, the results were considered a valuable indication of what the operational constraints should be, were a second iteration of the project to be conducted.

8.3 Discussion of Experimental Results

The current requirements of the actuator were determined by interpolating the rate-of-displacement data generated from different applied currents. The identified driving currents(10 A and 13 A) were then effectively applied to the complete actuator. The interpolation technique was effective in that the identified currents, when applied to the complete actuator, resulted in an actuation period of close to the 10 s that was required.

The application of a controlled current effectively managed to keep this actuation period fairly constant regardless of loading. This was counter intuitive, since more energy needed to be delivered to the load during the actuation. The reason for this was that the SMA material experienced an increase in electrical resistivity at higher loading. Since

$P = I^2R$, this meant that at increased loads more power was delivered to the wire. The higher energy requirement at increased loads was therefore partly compensated for, resulting in a self-regulating effect.

During the first experiments it was seen that similar amounts of stroke was achieved by the two wire-sets: 3.67 mm and 3.98 mm for wire set 1 and wire set 2 respectively. This was in the region of 26% lower than the design value of 4.95 mm. This discrepancy, which was not evident in the full actuator tests, was considered to be driven by the lack of a linear biassing stiffness during the experiments. The effective stretching of the wire during the full-actuator tests did, however, negate any concern that this discrepancy may have initially provoked.

The bigger problem here was that the starting value for x_{act} which was different to the planned value. This error meant that the kinematics of the actuator were different to that of the design, which resulted in a 20% lower stroke amplification(2.7 vs 3.4). This in turn resulted in the stroke capability of the actuator to be close to half of the stroke that the design set out to achieve.

While the stroke capability was much lower than the planned value, all was not lost. Through the experimental process followed, it was determined that the minimum reverse actuation stress that was used for the design(100 MPa) was higher than was actually needed. It was seen in the experiment that reverse actuation still happened at stresses as low as 15 MPa. The result of this was that an opportunity was identified for redesign of the actuator with the design requirements in terms of biassing stress being substantially less extreme than that which was used in the design of this iteration of the actuator.

Under these relaxed requirements, the structure's stiffness, which was originally specified to be 21.8 N/mm, could be substantially relaxed. This would have a variety of effects on the design, including less extreme kinematic requirements, lighter structural components and a longer functional life-span for the SMA material.

In the end the changed, "wrong" kinematics seemed to yield a stable, repeatable actuation. The SMA stresses were also more moderate than the huge min/max ratio of the design.

Chapter 9

Conclusions and Recommendations

This chapter serves to round off the project. The project is first summarised, followed by a discussion on the achievements and shortcomings of the project. Next, conclusions and recommendations are made to guide future work.

9.1 Summary

During this project a system was designed by which the trailing edge of a rudder could be thickened in order to increase lift that it generates at low speed flight regimes. The complete system was developed to the point where a detailed concept existed. This included generalised subsystem specifications. The lower level design then focussed on a specific actuator within the system, which was designed in detail, followed by the simulation and testing thereof. This process was aimed at confirming the feasibility of building and operating such an actuator, which would be the fundamental building block of a more complete system. A more detailed account of the mentioned project tasks follows in the rest of this section.

At the onset of the design process, SMA-based technologies and their theoretical suitability for use in the current project was confirmed in a trade-off study, which included a wide range of actuator technologies. The trade-off study was conducted using high level estimates for the performance requirements of such a system. The study included a breakdown of the system into functional blocks, which were then used to generate different system concepts. The trade-off study thus ended with the identification of a system level concept that would be developed further.

Given the high level concept, a system level design could be conducted, during which more detailed requirements were identified. This included the chord-wise placement of

the actuator by treating the system as a multi-stage stroke amplifier, the identification of stroke requirements by conducting a large displacement non-linear FEA of the trailing edge skin and the estimation of the aerodynamic component of the actuator load. The latter was based on the assumption that the force was evenly distributed and that the deformation of the trailing edge could be treated as cylindrical. The results from the FEA supported this assumption. For this iteration of the project, it was decided to distribute 40 actuators along the span of the rudder. This number was chosen arbitrarily as not enough detail existed for an optimised selection.

The next project task was the detailed design of an actuator prototype. The chosen architecture was a car-jack type mechanism where the individual links were replaced by parallel sets of links, referred to as arms. The parallelism was used to create an environment in which forces were transferred in a distributed manner, and where loads were predominantly axial in nature. This would serve to minimise the transfer of moments in the system, which, in turn, would lead to smaller and lighter structural components. To enforce lateral stability on the mechanism, the outside arms (stabiliser arms) were longer than those on the inside in order to form triangular linkages which could resist lateral movements. Within this actuator the active material, SMA wires, was also applied in a distributed manner by using several bundles of SMA wire. The bundles were distributed throughout the actuator in such a way that their forces would be symmetrical about the mid-plane of the actuator.

The design constraints for this actuator were fairly restrictive, which led to actuator kinematics with extreme angles between the arms, which created some difficulty in selecting suitable subsystem specifications.

Regardless of the difficulties, a set of viable specifications could be identified and a prototype could be constructed. This included a physical as well as a digital prototype (a full kinematic model with flexible parts).

The simulation model would allow for the co-simulation of actuator kinematics and models of the SMA material behaviour. A suitable material model could not, however, be identified or developed within the time-constraints of the project. The simulation model could provide a valuable starting point for future iterations of the project. From the static simulations conducted, using the kinematic model, it could be seen that the stabiliser arms effectively provided lateral stabilisation, and that the parallel arrangement of the arms effectively distributed the load.

The physical prototype could be built with reasonable ease, except for the wire bundles for which several difficulties arose. One such difficulty was to construct wire bundles with sufficient accuracy in their lengths; another was difficulty in attaching temperature measurement equipment to the bundles; and a third was the effective crimping of the wire bundles. The space within which the bundles were to be placed did not allow for thick-walled copper crimps as would generally be used, and thin-walled stainless steel

or aluminium ferrules did not provide the necessary clamping force that was needed to resist the large forces that were experienced by the wire bundles. In the end, a type of "knotting" was used to attach the wire ends to each other using small crimps to keep the "knots" in place. This was by no means an elegant or convenient solution, and alternative methods of bundle construction must definitely be explored in future projects.

Testing of the prototype showed that a controlled current was an effective driving method for the actuator, and that the prototype could provide stable and repeatable performance under the loading it was designed for. The inaccuracies of the SMA bundle lengths did, however, alter the planned kinematics, leading to a low stroke output by the actuator. The resulting, "wrong" kinematics and its corresponding force transfer characteristics however indicated that the kinematics of the design were possibly too extreme and that the material constraints used for the SMA material during the design could be somewhat relaxed.

9.2 Conclusions

It was found that SMA technology is very well suited, both theoretically and practically for low frequency actuation in confined spaces. It was also found to function well within the proposed car-jack type actuator, and that some of the architectural decisions made in the project hold great promise in the designing of small, lightweight actuators of high aspect ratio. The car-jack type actuator itself proved to be capable of high stroke amplification, and the axial nature of the loads within it allowed for the use of small structural components. The well-functioning architectural designs were the parallel arms of the actuator, the stabiliser arms, the use of supporting webs on the stationary pins and the push-to-pull conversion by using highly stressed tensile units.

Other architectural decisions proved more restricting and could be improved upon. The first of these was the floating-actuator concept. This proved to be an overly complicated method for establishing degrees of freedom. The problem with this method was that it necessitated a complex arrangement of SMA wire bundles in order for the symmetry of the actuator to be maintained. This complex arrangement also played a major part in the limitation on the length of the actuator.

The extreme actuator kinematics is also not considered to be ideal; this was, however, driven by the length constraint on the actuator and could be adjusted to find a more suitable arrangement. The highly non-linear load/displacement curve that resulted from the kinematics was also the reason why a suitable phenomenological model could not be found for simulation of the SMA.

As far as the SMA material is concerned, the performance of the system was considered to be acceptable. The bundle construction would, however, need to be revisited, as well as the proposed SMA stresses. A minimum SMA stress between 40 MPa and 70 MPa might, for instance, be sufficient.

Overall, the project aims were considered to be successfully met, and the lessons learnt were considered to be valuable. It is believed that the proposed concepts are feasible, and that an SMA-based trailing edge actuation can be successfully implemented. In order to achieve this, however, the design would need to be refined further. It is also believed that, in its current state, this project would provide a valuable context for future iterations thereof.

9.3 Recommendations

A next iteration of the project is recommended. In such an iteration the SMA bundle construction should be refined, as well the operational envelope of the SMA material. Closer attention should be paid to the heat-transfer characteristics of the bundles, and the reverse actuation should be studied further. It should also prove wise to shun the floating actuator concept for a different method of achieving the necessary longitudinal degree of freedom. It is also believed that some scope for optimisation exists for the number of actuators used in the system.

Appendix A

Requirement Calculations

For the trailing edge actuation system that was designed in the SATETH project, the initial technology was based on preliminary estimates of the system requirements. In this appendix the calculation of these requirements are discussed. The requirements, both geometrical(Section A.1) and functional (Section A.2), are based purely on the original problem statement and no details of the operational system are included in the derivations.

A.1 Geometrical Requirements

Since an algebraic expression for the airfoil was not available, the area needed to be calculated through numerical integration of the airfoil coordinates. These coordinates were determined through inspection of the three-dimensional tail-wing model. A linear interpolation was used to place a coordinate point at exactly $x = 0.7c$, which was assumed to be the rudder hinge point. This was done so that the entire rudder cross-section was represented in $A(x_r)$ as can be seen from Figure A.1. The trailing end of the airfoil profile is close to linear; this validated the use of linear interpolation for finding the coordinate point at $x = 0.7c$ as well as the selected integration algorithm which is a simple trapezoidal integration.

The symmetry of the airfoil was also exploited by integrating only the positive y and multiplying it by a factor of 2. The integration is shown mathematically in Equation A.1:

$$A_{rudder}(x_r) = A^{+}_{rudder}(x_r) + A^{-}_{rudder}(x_r) = 2A^{+}_{rudder}(x_r) \tag{A.1}$$

The trapezoidal integration is carried out as shown in Equation A.2.

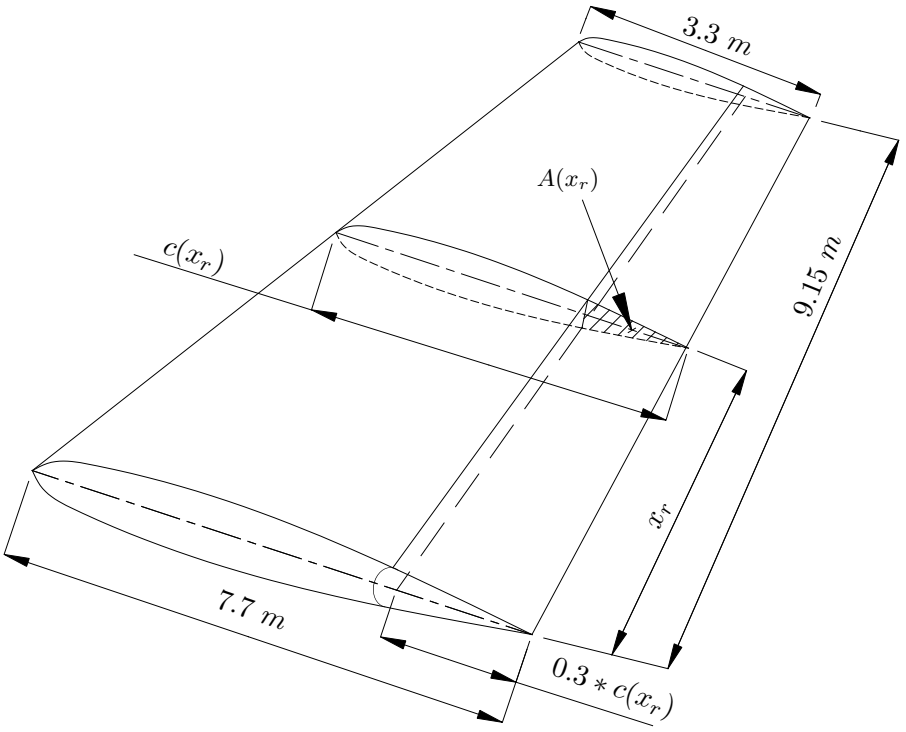

FIGURE A.1: Three dimensional representation of the vertical tail wing

$$A_{rudder}(x_r) = 2 * \Sigma_{n=N_0}^{N_{max}}(1/2)(y_n + y_{n-1})(x_n - x_{n-1}) \tag{A.2}$$

With n being the integer identifier of a discrete point on the rudder skin, and y and x being the coordinates of the point. These values were given by coefficients normalised through the chord length c as is shown in Figures A.3 and A.4.

$$y_n(x_r) = C_n * c(x_r) \tag{A.3}$$

$$x_n(x_r) = D_n * c(x_r) \tag{A.4}$$

If this is substituted into Equation A.2, as shown in Equation A.5, a dimensional expression for cross-sectional area is found. Equations A.6 gives this expression.

$$A_{rudder}(x_r) = 2 * \Sigma_{n=N_0}^{N_{max}}(1/2)(C_n * c(x_r) + C_{n-1} * c(x_r))(D_n * c(x_r) - D_{n-1} * c(x_r)) \tag{A.5}$$

$$A_{rudder}(x_r) = [c(x_r)]^2 * \Sigma_{n=N_0}^{N_{max}}(1/2)(C_n + C_{n-1})(D_n - D_{n-1}) = a * [c(x_r)]^2 \quad \text{(A.6)}$$

with

$$a = \Sigma_{n=N_0}^{N_{max}}(1/2)(C_n + C_{n-1})(D_n - D_{n-1}) \quad \text{(A.7)}$$

By analysing the geometry of the CAD model, a was found to be:

$$a = 0.00479721 \quad \text{(A.8)}$$

Which, together with Equation A.6, could be used to find the cross-section at any height on the tail-wing.

The volume of the rudder could then be found by integrating Equation A.6 over the span of the tail wing, as is shown in Equation A.9.

$$V_{rudder} = \int_0^{9.15} a * [c(x_r)]^2 dx_r \quad \text{(A.9)}$$

Equation A.10 shows the expression for $c(x_r)$ as derived from the CAD model. This led to the calculated rudder volume shown in Equation A.11

$$c(x_r) = 7.7 - 0.5137 * x_r \ [m] \quad \text{(A.10)}$$

$$V_{rudder} = 1.336 \ m^3 \quad \text{(A.11)}$$

The actuation system would need to vary the trailing edge thickness between a blunt and a sharp form. The required geometries of each form are shown in Figure A.2. The trailing edge was assumed to hinge at $x = 0.95c$ and to get thicker towards $x = c$, with x being defined as the distance from the leading edge of the vertical wing along the chord-line. A morphing wing version of this deflected version may ultimately be used in practice, but did not significantly change the current calculations, which were meant to estimate system level requirements to determine the initial constraints.

The unknown dimensions are as follows:

$$d = \sqrt{(0.05c)^2 + (0.0317c/2 - 0.003c/2)^2} = 0.052018c \quad \text{(A.12)}$$

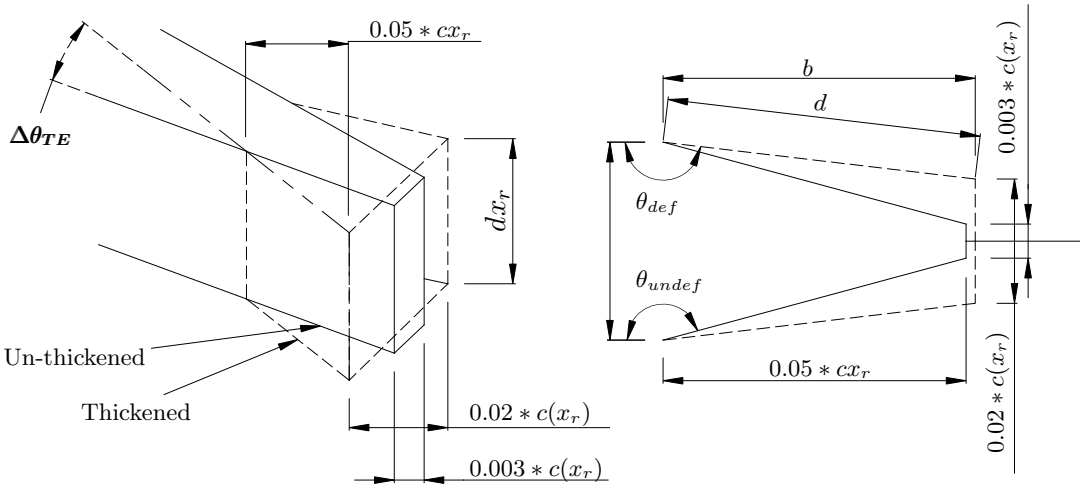

FIGURE A.2: Three-dimensional and two-dimensional representations of the trailing edge thickening geometry

The unknown dimensions were as follows:

$$b = \sqrt{(0.052018c)^2 - (0.0317c/2 - 0.003c/2)^2} = 0.05167c \tag{A.13}$$

$$\theta_{undef} = 90° + sin^{-1}(0.05c/d) = 164.0576 \tag{A.14}$$

and

$$\theta_{def} = 90° + sin^{-1}(b/d) = 173.5416° \tag{A.15}$$

so

$$\theta_{undef \to def} = \theta_{def} - \theta_{undef} = 9.484° \tag{A.16}$$

This is the angular deflection to a specific side, and the total angular deflection would be double that. This is shown in Equation A.17.

$$\Delta\theta_{TE} = 2 * \theta_{undef \to def} = 18.968° \tag{A.17}$$

This is the angle by which the trailing edge would need to be deflected within a 10 s period of actuation.

A.2 Functional Requirements

The initial phases of the SATETH project centred around the selection of a suitable technology with which to build a trailing edge thickening mechanism. For the selection, estimates were needed for the system requirements. This section discusses the first calculations by which such estimates could be found.

The estimates included the force that the actuator would need to exert, the power that the actuator would need to be capable of, and the energy expended during a single actuation stroke. Several intermediate variables were also used in the process, some of which may also be useful in high level studies.

In order to find the actuator force, a differential element was taken from the trailing edge as is shown in Figure A.3. As shown, the force on the centroid of the element was found to represent the load on the element. This was found, as shown in Equation A.18, by multiplying the differential area by the pressure acting on it. Note that the equation also introduced an intermediate variable with which to represent the span-wise load distribution(f_{normal}).

$$dF_{normal} = (p_0 - p_\infty) * 0.05 * c(x_r) * dx_r = f_{normal} * dx_r \tag{A.18}$$

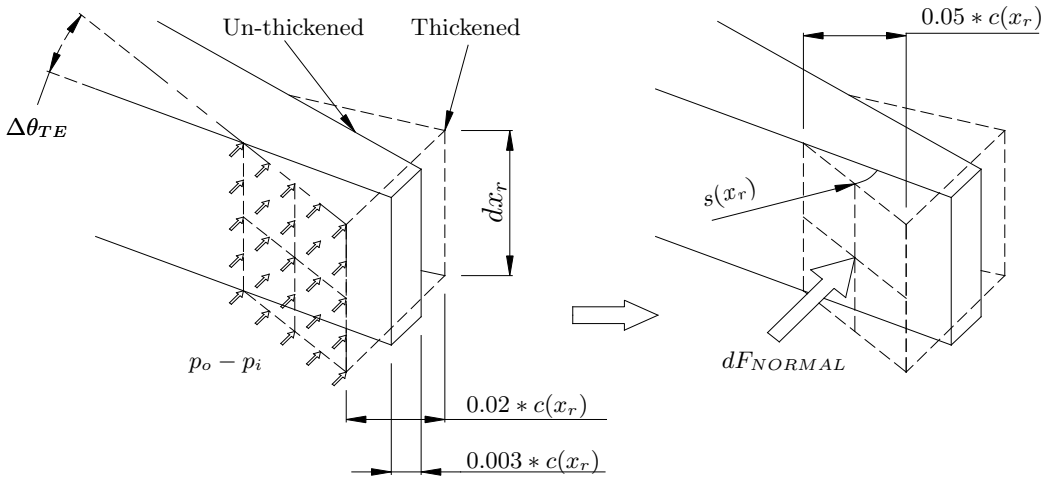

FIGURE A.3: Three-dimensional representation of the trailing edge cross-section with aerodynamic loading

Here f_{normal} is defined as shown in Equation A.19, since $C_p = (p_0 - p_i)/P_{dynamic}$. Note that $P_{dynamic}$ is referred to as the dynamic pressure and is defined as is shown in Equation A.20. In this equation ρ is the density of air, which is equal to 1.799 kg/m^3 if the compressibility of air is considered. V_{air} is the airspeed, given as 103 m/s.

$$f_{normal} = (p_0 - p_\infty) * 0.05 * c(x_r) = C_p * P_{dynamic} * 0.05 * c(x_r) \tag{A.19}$$

$$P_{dynamic} = (1/2) * \rho * V_{air}^2 = (1/2) * 1.799 * 103^3 = 9524Pa \tag{A.20}$$

This distributed load is then integrated to find the full load applied to the trailing edge, as shown in Equation

$$F_{normal} = \int_0^{9.15} f_{normal} * dx_r \tag{A.21}$$

By substituting the relevant variables, the integration results in the force expression are shown in Equation A.22.

$$F_{normal} = 0.05 * c(x_r) * C_p * P_{dynamic} \tag{A.22}$$

By substitution of $C_{p,max} = 0.2$, and $C_{p,min} = -0.5$ the maximum and minimum force values could be found as shown in Equations A.23 and A.24 respectively.

$$F_{normal,min} = F_{normal}(Cp, min) = -11655N \tag{A.23}$$

$$F_{normal,max} = F_{normal}(Cp, max) = 4662N \tag{A.24}$$

These are the forces that would theoretically be exerted by an actuator to overcome the aerodynamic load.

The energy is closely related to force by the multiplication of the distance over which the force is exerted. On the previously defined differential element this would mean that energy is related to the force applied at the centroid of the element, and the arc along which the element moves. This is shown in Equation A.25 in a differential form. Equation A.26 shows the definition for $s(x_r)$

$$e(x_r) = dE_{normal}/dx_r = f_{normal} * s(x_r) \tag{A.25}$$

$$s(x_r) = (1/2) * (0.05 * c(x_r)) * \Delta\theta_{TE,rad} \tag{A.26}$$

with

$$\Delta\theta_{TE,rad} = rad(\Delta\theta_{TE}) = rad(18.968^{\circ}) = 0.331\ rad \tag{A.27}$$

The needed stroke work is determined by integrating A.25 as shown in Equations A.28, A.29 and A.30.

$$E_{normal}(C_p) = \int_0^{9.15} e(x_r)dx_r = 1099 * C_p\ [J] \tag{A.28}$$

$$E_{normal}(C_p, min) = -549.25\ J \approx 550\ J \tag{A.29}$$

During a closing(un-thickening) operation.

$$E_{normal}(C_p, min) = 219.7\ J \approx 220\ J \tag{A.30}$$

During an opening(thickening) operation.

The power requirements were found by assuming that the mentioned energy would be expended at a constant rate over a 10 s period. This is shown in Equations A.31 and A.32.

$$P_{normal}(C_p, min) = E_{normal}(C_p, min)/10\ s = -54.925\ W \approx 55\ W \tag{A.31}$$

During a closing(un-thickening) operation.

$$P_{normal}(C_p, max) = E_{normal}(C_p, max)/10\ s = 21.97\ W \approx 22\ W \tag{A.32}$$

During an opening(thickening) operation.

Bibliography

[1] James Mabe. Variable area jet nozzle for noise reduction using shape memory alloy actuators. *The Journal of the Acoustical Society of America*, 123(5):3871, 2008. ISSN 00014966. doi: 10.1121/1.2935758. URL http://scitation.aip.org/content/asa/journal/jasa/123/5/10.1121/1.2935758.

[2] D J Hartl and D C Lagoudas. Aerospace applications of shape memory alloys. *Proceedings of the Institution of Mechanical Engineers, Part G: Journal of Aerospace Engineering*, 221(4):535–552, jan 2007. ISSN 0954-4100. doi: 10.1243/09544100JAERO211. URL http://pig.sagepub.com/lookup/doi/10.1243/09544100JAERO211.

[3] Righardt Frederick Ehlers. *Feedback Control of a Shape Memory Alloy Actuator for Control Surface Deflection*. PhD thesis, 2012.

[4] D.C. Lagoudas. *Shape Memory Alloys: Modeling and Engineering Applications*. Springer ebook collection / Chemistry and Materials Science 2005-2008. Springer US, 2008. ISBN 9780387476858. URL https://books.google.co.za/books?id=jY-qVrZkqBEC.

[5] a. Manuello Bertetto and M. Ruggiu. Characterization and modeling of air muscles. *Mechanics Research Communications*, 31(2):185–194, March 2004. ISSN 00936413. doi: 10.1016/S0093-6413(03)00088-0. URL http://linkinghub.elsevier.com/retrieve/pii/S0093641303000880.

[6] Bjorn Kiefer and Dimitris C Lagoudas. Phenomenological modeling of ferromagnetic shape memory alloys. In *Smart structures and materials*, pages 164–176. International Society for Optics and Photonics, 2004.

[7] Neil Sclater and Nicholas P. Chironis. *Mechanisms and mechanical devices sourcebook*. McGraw-Hill, New York, volume 3 edition, 2001.

[8] Huixing Zhou, Brian Henson, Andrew Bell, Andrew Blackwood, Andy Beck, and Richard Burn. Linear piezo-actuator and its applications. *University of Leeds*, 2001.

[9] J. E. Huber, N.A. Fleck, and Ashby M.F. The selection of mechanical actuators based on performance indices. *Proceedings: Mathematical, Physical and Engineering Sciences*, 453(1965):2185–2205, 1997. URL http://www.jstor.org/stable/53045.

[10] MSC Software. *MSC Nastran 2012 Superelements User's Guide*. MSC Software, 2012. URL https://simcompanion.mscsoftware.com/infocenter/index?page=content{&}id=DOC10184{&}actp=RSS.

[11] MSC Software. *Motion Workspace Guide*. MSC Software, 2012. URL https://simcompanion.mscsoftware.com/infocenter/index?page=content{&}id=DOC10294{&}cat=1AEYYU{&}actp=LIST.

[12] Eric F Prechtl and Steven R Hall. Design of a high efficiency, large stroke, electromechanical actuator. *Smart Materials and Structures*, 8(1): 13–30, February 1999. ISSN 0964-1726. doi: 10.1088/0964-1726/8/1/002. URL http://stacks.iop.org/0964-1726/8/i=1/a=002?key=crossref.80ad3d6cb2648bb94abb0921d98e5b5f.

[13] J A Rosero, J A Ortega, E Aldabas, and L Romeral. Moving Towards a More Electric Aircraft. *IEEE A&E SYSTEMS MAGAZINE*, (March):3–9, 2007.

[14] Stephen L Botten, Chris R Whitley, and Andrew D King. Flight Control Actuation Technology for Next- Generation All-Electric Aircraft The Benefits of Electric Actuation. pages 55–68, 2000.

[15] S. Croke and J. Herrenschmidt. More electric initiative-power-by-wire actuation alternatives. In *Aerospace and Electronics Conference, 1994. NAECON 1994., Proceedings of the IEEE 1994 National*, pages 1338–1346 vol.2, May 1994. doi: 10.1109/NAECON.1994.332886.

[16] Jan Schrooten, John Parthenios, Georgios C Psarras, Jan Van Humbeeck, Costas Galiotis, and Rolf Gotthardt. Progress on Composites with Embedded Shape Memory Alloy Wires. *Materials Transactions*, 43(Vol. 43 No. 5), 2002.

[17] Peter Konstanzer, Michael Grunewald, Peter Janker, and Stefan Storm. AIRCRAFT INTERIOR NOISE REDUCTION THROUGH A PIEZO TUNABLE VIBRATION ABSORBER SYSTEM. *ICAS 2006*, pages 1–6, 2006.

[18] C Mangeot, B Andersen, and R Hilditch. New actuators for aerospace. 1997, 2000.

[19] Kazeem O. Sanusi, Olukayode L. Ayodele, and Mohamed T.E. Khan. A concise review of the applications of NiTi shape-memory alloys in composite materials. *South African Journal of Science*, 110(7):5–9, 2014.

[20] Benoit Berton. Shape Memory Alloys Application : Trailing Edge Shape Control. *Multifunctional Structures/Integration of Sensors*, pages 13–1 – 13–16, 2006.

[21] T Duerig, a Pelton, and D Stöckel. An overview of nitinol medical applications. *Materials Science and Engineering: A*, 273-275:149–160, 1999. ISSN 09215093. doi: 10.1016/S0921-5093(99)00294-4.

[22] GV Kurdjumov and LG Khandros. First reports of the thermoelastic behaviour of the martensitic phase of au-cd alloys. *Doklady Akademii Nauk SSSR*, 66:211–213, 1949.

[23] István M Ihálcz. FUNDAMENTAL CHARACTERISTICS AND DESIGN METHOD FOR NICKEL-TITANIUM SHAPE MEMORY ALLOY. 45(1):75–86, 2001.

[24] H. Janocha. *Actuators basics and applications*. Springer, Berlin, 2004.

[25] Colin G Cameron and Michael S Freund. Electrolytic actuators: exploring new directions in electrical-mechanical energy transduction. 1(1999), 2001.

[26] M Zupan, MF Ashby, and NA Fleck. Actuator classification and selectionthe development of a database. *Advanced engineering ...*, (12):933–939, 2002. URL http://onlinelibrary.wiley.com/doi/10.1002/adem.200290009/abstract.

[27] a.D. Poole and J.D. Booker. Design methodology and case studies in actuator selection. *Mechanism and Machine Theory*, 46(5):647–661, May 2011. ISSN 0094114X. doi: 10.1016/j.mechmachtheory.2010.12.009. URL http://linkinghub.elsevier.com/retrieve/pii/S0094114X1000234X.

[28] Patcharin Poosanaas, Kazuhiko Tonooka, and Kenji Uchino. Photostrictive actuators. *Mechatronics*, 10:467–487, 2000. URL http://www.sciencedirect.com/science/article/pii/S0957415899000732.

[29] E.M. Purcell and D.J. Morin. *Electricity and Magnetism*. Electricity and Magnetism. Cambridge University Press, 2013. ISBN 9781107014022. URL http://books.google.co.za/books?id=A2rS5vlSFq0C.

[30] Ken Kurosaki, Takehiro Maruyama, Kengo Takahashi, Hiroaki Muta, Masayoshi Uno, and Shinsuke Yamanaka. Design and development of MH actuator system. *Sensors and Actuators A: Physical*, 113(1):118–123, June 2004. ISSN 09244247. doi: 10.1016/j.sna.2004.03.009. URL http://linkinghub.elsevier.com/retrieve/pii/S0924424704001682.

[31] G Lloyd and K Kim. Smart hydrogen/metal hydride actuator. *International Journal of Hydrogen Energy*, 32(2):247–255, February 2007. ISSN 03603199. doi: 10.1016/j.ijhydene.2006.03.014. URL http://linkinghub.elsevier.com/retrieve/pii/S0360319906001807.

[32] Gary Sandrock and Robert C Bowman Jr. Gas-based hydride applications: recent progress and future needs. c:794–799, 2003.

[33] David G. Aliciatore and Histand Michael B. *Introduction to mechatronics and measurement systems*. McGraw-Hill, New York, 1999.

[34] N B Ekreem, A G Olabi, T Prescott, A Rafferty, and M S J Hashmi. An overview of magnetostriction , its use and methods to measure these properties. 191:96–101, 2007. doi: 10.1016/j.jmatprotec.2007.03.064.

[35] Heng Zhang, Tianli Zhang, and Chengbao Jiang. Magnetostrictive actuators with large displacement and fast response. 055014, 2012. doi: 10.1088/0964-1726/21/5/055014.

[36] N. Wavre and X. Thouvenin. Voice coil actuators in space. *European space mechanisms and tribology symposium*, 374(6):227, 1995.

[37] Ching-Chih Tsai, Shui-Chun Lin, Hsu-Chih Huang, and Yu-Ming Cheng. Design and control of a brushless DC limited-angle torque motor with its application to fuel control of small-scale gas turbine engines. *Mechatronics*, 19(1):29–41, February 2009. ISSN 09574158. doi: 10.1016/j.mechatronics.2008.07.003. URL http://linkinghub.elsevier.com/retrieve/pii/S0957415808000986.

[38] Edward Balaban, Prasum Bansal, Paul Stoelting, Abhinav Saxena, Kai F. Goebel, and Simon Curran. A Diagnostic Approach for Electro-Mechanical Actuators in Aerospace Systems. 2009.

[39] Andrew Parr. *Hydraulics and pneumatics a technician's and engineers's guide*. Butterworth-Heinemann, Woburn, 1998.

[40] Frank Daerden and Dirk Lefeber. The concept and design of pleated pneumatic artificial muscles. 1999.

[41] T. Maillard, F. Claeyssen, R. LeLetty, O. Sosnicki, a. Pages, and a. Vazquez Carazo. Piezomechatronic-based systems in aircraft, space, and defense applications. *Proceedings of SPIE*, 7331:73310K–73310K–10, 2009. doi: 10.1117/12.819015. URL http://link.aip.org/link/PSISDG/v7331/i1/p73310K/s1&Agg=doi.

[42] P Jänker, F Claeyssen, B Grohmann, M Christmann, and T Lorkowski. New Actuators for Aircraft and Space Applications. (June):9–11, 2008.

[43] Inderjit Chopra. Review of State of Art of Smart Structures. 40(11):16–19, 2002.

[44] O Söderberg, Y Ge, a Sozinov, S-P Hannula, and V K Lindroos. Recent breakthrough development of the magnetic shape memory effect in NiMnGa alloys. *Smart Materials and Structures*, 14(5):S223–S235, October 2005. ISSN 0964-1726. doi: 10.1088/0964-1726/14/5/009. URL http://stacks.iop.org/0964-1726/14/i=5/a=009?key=crossref.ff4f765d34211f86b88331b29c55fbd5.

[45] Ilkka Suorsa, J Tellinen, E Pagounis, I Aaltio, Kari Ullakko, and AdaptaMat Ltd. Applications of magnetic shape memory alloys. *8th international conference actuator*, 1(June):10–12, 2002.

[46] Bob Williams. An Atlas of Structures , Mechanisms , and Robots. 2014.

[47] R.E. Newnham, a. Dogan, Q.C. Xu, K. Onitsuka, J. Tressler, and S. Yoshikawa. Flextensional "moonie" actuators. *Proceedings of IEEE Ultrasonics Symposium*, pages 509–513, 1993. doi: 10.1109/ULTSYM.1993.339557. URL http://ieeexplore.ieee.org/lpdocs/epic03/wrapper.htm?arnumber=339557.

[48] L. F. Campanile. The "Fish-Mouth" Actuator: Design Issues and Test Results. *Journal of Intelligent Material Systems and Structures*, 15(9-10):711–719, September 2004. ISSN 1045-389X. doi: 10.1177/1045389X04044452. URL http://jim.sagepub.com/cgi/doi/10.1177/1045389X04044452.

[49] Karla M. Mossi and Richard P. Bishop. Characterization of different types of high performance THUNDER actuators. *Symposium on Smart Structures and Materials*, pages 43–52, July 1999. doi: 10.1117/12.352812. URL http://proceedings.spiedigitallibrary.org/proceeding.aspx?articleid=983087.

[50] Maoying Zhou, Yuan Ruan, Weiting Liu, Shuo Huang, and Xin Fu. A bio-inspired piezoelectric motor with simple structured asymmetric stator. *Smart Materials and Structures*, 045003, 2014. doi: 10.1088/0964-1726/23/4/045003.

[51] Kenji Uchino. Piezoelectric ultrasonic motors: overview. *Smart Materials and Structures*, 7(3):273–285, June 1997. ISSN 0964-1726. doi: 10.1088/0964-1726/7/3/002. URL http://stacks.iop.org/0964-1726/7/i=3/a=002?key=crossref.b9de66da754128cebc6ccc8bd723d0fd.

[52] Piezo LEGS Linear Twin 20N. URL http://www.piezomotor.com/app/content/uploads/150020_LT20.pdf.

[53] Alan Poole and Julian D. Booker. Classification and selection of actuator technologies with consideration of stimuli generation. *Proceedings of SPIE*, 6927(Table 1):692728–692728–10, 2008. ISSN 0277786X. doi: 10.1117/12.775426. URL http://link.aip.org/link/PSISDG/v6927/i1/p692728/s1&Agg=doi.

[54] G. Faiella, V. Antonucci, F. Daghia, S. Fascia, and M. Giordano. Fabrication and Thermo-Mechanical Characterization of a Shape Memory Alloy Hybrid Composite. *Journal of Intelligent Material Systems and Structures*, 22(3):245–252, January 2011. ISSN 1045-389X. doi: 10.1177/1045389X10396954. URL http://jim.sagepub.com/cgi/doi/10.1177/1045389X10396954.

[55] P.P. Benham, R.J. Crawford, and C.G. Armstrong. *Mechanics of Engineering Materials*. Longman Group, 1996. ISBN 9780582251649. URL https://books.google.co.za/books?id=R9GoQgAACAAJ.

[56] N.S. Gokhale. *Practical Finite Element Analysis*. FINITE TO INFINITE, 2008. ISBN 9788190619509. URL https://books.google.co.za/books?id=yKTObdhQ66YC.

[57] D.L. Logan. *First Course in the Finite Element Method*. Thomson, 2007. ISBN 9780534552985. URL https://books.google.co.za/books?id=wjr3ArdvAc4C.

[58] D.H. Buckley and Lewis Research Center. *Friction Behavior of 304 Stainless Steel of Varying Hardness Lubricated with Benzene and Some Benzyl Structures*. NASA technical note. National Aeronautics and Space Administration, 1974. URL https://books.google.co.za/books?id=V40W8jzLLj4C.